



Cyclophanes, a bridge between photophysics and supramolecular chemistry

Morgan Auffray

► To cite this version:

Morgan Auffray. Cyclophanes, a bridge between photophysics and supramolecular chemistry. Material chemistry. Université Pierre et Marie Curie - Paris VI, 2017. English. NNT : 2017PA066285 . tel-01707788

HAL Id: tel-01707788

<https://theses.hal.science/tel-01707788>

Submitted on 13 Feb 2018

HAL is a multi-disciplinary open access archive for the deposit and dissemination of scientific research documents, whether they are published or not. The documents may come from teaching and research institutions in France or abroad, or from public or private research centers.

L'archive ouverte pluridisciplinaire **HAL**, est destinée au dépôt et à la diffusion de documents scientifiques de niveau recherche, publiés ou non, émanant des établissements d'enseignement et de recherche français ou étrangers, des laboratoires publics ou privés.

Université Pierre et Marie Curie

Ecole doctorale 397

Institut Parisien de Chimie Moléculaire (IPCM) / Laboratoire de Chimie des Polymères

Cyclophanes, A bridge between photophysics and supramolecular chemistry

Par Morgan AUFFRAY

Thèse de doctorat de Physique et Chimie des Matériaux

Dirigée par André-Jean ATTIAS, David KREHER et Fabrice MATHEVET

Présentée et soutenue publiquement le 9 octobre 2017

Devant un jury composé de :

Pr Anna PROUST	Professeur, UPMC, Paris	Examinatrice
Dr Chantal ANDRAUD	Directrice de Recherche, ENS, Lyon	Rapporteur
Dr Céline FIORINI	Chargé de Recherche, CEA, Saclay	Examinatrice
Dr Jean WEISS	Directeur de Recherche, Unistra, Strasbourg	Rapporteur
Pr André-Jean ATTIAS	Professeur, UPMC, Paris	Directeur de thèse

Remerciements/Acknowledgements

Ce travail a été réalisé au sein de l'Institut Parisien de Chimie Moléculaire (IPCM) dans le laboratoire de Chimie des Polymères dirigé par le Dr. Laurent Bouteiller que je remercie pour son accueil. Je souhaite aussi remercier le Pr. André-Jean Attias pour m'avoir confié ce passionnant sujet de thèse.

Je remercie aussi les Dr. Chantal Andraud, Pr. Anna Proust, Dr. Céline Fiorini et Dr. Jean Weiss d'avoir accepté de juger ces travaux de thèse.

Le manuscrit d'une thèse résume trois ans de la vie d'un doctorant. Il décrit un enchaînement d'hypothèses intelligentes confirmées par de nombreuses expériences à succès, elles-mêmes parfaitement en accord avec des calculs théoriques savants menant indéfectiblement à une unique conclusion dont la qualité certaine ne peut être décrite que par trois mots : du jamais vu. Cela étant dit, il est important de mentionner pour les générations futures qu'un manuscrit représente un doctorat, mais ne le résume pas. Une thèse est en réalité un enchaînement d'hypothèses bizarres un peu bancales que certains accidents expérimentaux finiront peut-être par confirmer. Quant aux calculs savants... disons que le « fit » est au physicien ce qu'est la chimie quantique au chimiste : en modifiant une ou deux variables, ça finit toujours par coller. Et donc quand enfin la théorie est en accord avec la pratique, on cherche rapidement une conclusion viable et on n'y repense plus afin d'éviter le risque de trouver une faille dans le raisonnement...

Mais attention, il ne faut surtout pas être défaitiste pour autant et pour cause, cette thèse n'a qu'un seul auteur mais cet auteur ne serait jamais parvenu à l'écrire sans l'aide de nombreuses personnes que je tiens maintenant à remercier.

En tout premier lieu, il y a bien sur mes deux encadrants de compétition, les docteurs David Kreher et Fabrice Mathevet. Si le monde de la recherche était une entité chimique, David en serait l'état fondamental, calme et patient, et Fabrice en serait l'état excité, dynamique et toujours en mouvement. Ils m'ont toujours apporté les bons conseils aux bons moments, ainsi que la motivation pour poursuivre après les échecs et les réussites. Pour tout leur soutien pendant ces trois ans je les remercie profondément.

Ensuite je souhaiterais remercier ma voisine de bureau, collègue et amie, le Dr. Lydia Sosa-Vargas. Lydia est une personne d'une grande gentillesse qui m'aura apporté son aide ainsi que ses conseils et ses encouragements tout au long de ma thèse. Sans elle, la vie au jour le jour aurait sûrement été beaucoup moins agréable, et mon anglais aurait sûrement été bien pire... Au même titre que Fabrice et David, elle mérite amplement tous mes remerciements.

I also thank all non-permanent members of the team : Dr. Xiaolu Su (I still have the post-it « This is Xiaolu's lab » stuck to my bench), Teng Teng (even if you are always shouting !), Dizheng Liu (fighto fighto ?!), Xiao Liu (the living proof that french is not that hard to learn), Amina Benchohra (la seule et unique personne du laboratoire géolocalisable grâce à son rire) and Dr. Romain Brisse (champion du couplage de Suzuki). Je remercie par la même occasion les stagiaires qui ont participé à ces travaux : Félix qui m'a aidé à terminer mes synthèses en toute fin de thèse, Nils qui m'aura aidé à les commencer et Anissa, une bavarde incontestée qui a toujours su amener le rire dans le laboratoire.

J'aimerais maintenant remercier les docteurs Alaric Desmarchelier, Xavier Caumes et Virgile Ayzac pour les nombreuses soirées à préparer les routes vers Carcassonne, à prendre des Risk avec les « Die Mechaniker » ou partir en quête de stupides gobelins entourés d'un elfe, nain, humain ou demi-portion. Je remercie plus particulièrement Virgile pour une balade en moto mémorable, Xavier pour de nombreuses discussions scientifiques plus qu'intéressantes et Alaric pour ses « trucs et astuces » au laboratoire et ses nombreuses blagues internationales.

Ensuite, pour des pauses café un peu trop nombreuses je remercie Danilo Rosa Nunes et le Dr. André Pontes da Costa, toujours présents pour décompresser, en particulier pendant ma rédaction de manuscrit.

Durant ces trois ans, j'ai aussi eu la chance d'enseigner la chromatographie HPLC ou GC à de pauvres étudiants de licence 2. Je remercie donc le Dr. Laurent Gaillon pour son accueil dans l'équipe d'enseignement de chromato, et bien sur Isabelle et Romain pour leur disponibilité tout au long des travaux pratiques.

Pour ma seconde partie d'enseignement, j'ai eu la chance de pouvoir assister les docteurs Benjamin Isare et François Stoffelbach lors de travaux pratiques de chimie organique. Entre les petites blagues de Benjamin et la bientôt célèbre « poker face » de François, chaque semaine de travaux pratiques s'est avérée être une excellente expérience !

Enfin, je souhaiterais bien sûr remercier tous les membres du LCP que je n'ai pas cités jusqu'à présent et en particulier le Pr. Phillippe Guegan, compatriote breton, pour nos discussions tardives et ses conseils, Georgette Delag pour sa gentillesse et sa disponibilité, Thomas Coustham pour ces trois ans de thèse passés en parallèle, Gaëlle Mellot qui va regretter d'être dorénavant toute seule le matin, Gaëlle Pembouong pour nos encouragements mutuels lors de la rédaction du manuscrit, ainsi que Claire Troufflard pour de nombreuses petites discussions et aussi pour son aide pour enregistrer et dépouiller mes spectres RMN. Je remercie par la même occasion Geoffrey Gontard et Lise-Marie Chamoreau pour leur aide vis-à-vis des expériences en radiocristallographie RX.

Comme mentionné dans le manuscrit, ce travail de thèse a été effectué grâce à de nombreuses collaborations. Je tiens donc à remercier le Pr. Chihaya Adachi pour m'avoir permis de venir travailler dans son laboratoire OPERA à Fukuoka (Japon) et le Dr. Dae Hyeon Kim *alias* Kim-san pour sa disponibilité et pour m'avoir formé aux différents instruments que j'ai eu la chance de pouvoir manipuler. Le Japon étant un environnement totalement différent de ce que moi européen étais habitué, je remercie Fabrice ainsi que le Dr. Jean-Charles Ribierre pour avoir participé à mon éducation sur la culture Japonaise (mon estomac s'en souvient encore) ainsi que sur la photophysique au laboratoire. Je remercie également le Dr. Anthony d'Aléo pour son aide autant pour les manipes que pour la compréhension et la description des phénomènes photophysiques mis en jeu lors des caractérisations, ainsi que Dr. Qisheng Zhang pour avoir effectué et expliqué de nombreux calculs théoriques sur nos molécules cibles.

Je remercie aussi le Dr. Fabrice Charra, et bien sur toute son équipe du LEPO, pour sa gentillesse et pour m'avoir accueilli dans son laboratoire au CEA de Saclay lors de mes expériences par microscopie STM. Je n'ai malheureusement pas eu autant le temps de venir aussi souvent que voulu, mais ça aura été pour moi une excellente expérience de pouvoir observer et étudier mes molécules d'un point de vue autre que celui du chimiste.

Avant de conclure, je souhaite remercier George Lucas pour son inspiration pendant la rédaction, Freddy Mercury pour avoir mis l'ambiance au laboratoire du matin jusqu'au soir et Tyler Bates pour nous avoir offert le magnifique « Awesome Mix vol. 1 ».

Enfin, je souhaiterais remercier ma famille, et plus particulièrement mes parents, mon frère et sa petite famille, ma sœur et bien sur Floriane. Il me semble important de préciser que malgré leur incompréhension quasi-totale de mon sujet de thèse, ils m'ont toujours soutenu, motivé et encouragé. Floriane a aussi du supporter mes horaires décalés, mon réveil sonnant à l'aube et la lumière du salon éclairant la chambre jusque tard dans la nuit. Je dois aussi ajouter que mon caractère, pas forcément facile à vivre d'origine, n'a pas du en être amélioré pendant la période de rédaction. Je vous remercie donc tous pour votre présence et votre indéfectible soutien pendant ces trois années.

“There's something that doesn't make sense. Let's go and poke it with a stick.”

- The Doctor -

Cyclophanes, A bridge between photophysics and supramolecular chemistry

Par Morgan AUFFRAY

Dirigée par André-Jean ATTIAS, David KREHER et Fabrice MATHEVET

TABLE OF CONTENTS

Introduction	17
Chapter 1: Bibliography	21
I. Cyclophanes	21
A. [2.2]paraCyclophane	21
B. Dithia[3.3]paraCyclophane	23
C. Properties and applications of cyclophane derivatives	24
1. Chiral catalysis	24
2. Molecular electronics	26
3. Chromophores and Non-Linear Optics	28
4. Polymer materials	29
II. Supramolecular self-assembly confined on surface	31
A. Scanning Tunneling Microscopy	31
1. Working principle	31
2. Effect of temperature, pressure and environment	32
B. Surface nanostructuration	33
1. Chemisorption	34
a. Substrate	35
b. Head group	35
c. Spacer	35
d. Functional groups	36
e. Conclusion	36
2. Physisorption	37
a. Coordination bond	37
b. Electrostatic bond	39
c. Hydrogen bond	40
d. Halogen bond	41
e. Van der Waals interactions	42
3. Decoupling molecules from the substrate	45
a. Multilayers	47
b. Ultra-thin insulating layers	47
c. Spacers part of the molecule's structure	48
i. Bulky groups	48
ii. Tripodal motif	49
iii. Cyclophane-based pillar	49
III. Thermally Activated Delayed Fluorescence	51
A. Organic electroluminescence	51
1. Principle of luminescence	51
2. Limitations in OLED materials	52
a. Fluorescence-based OLED	52
b. Phosphorescence-based OLED	54
B. Thermally Activated Delayed Luminescence	55
1. First results	55

Strategy B. The halogens game	105
1. Good old fashioned fluoride	105
2. Iodine, you're my best friend	106
3. Bromide rhapsody	107
II. Characterisation of the staggered and eclipsed emitters	110
A. Nuclear Magnetic Resonance and X-ray radiocrystallography	110
1. Nuclear Magnetic Resonance	110
2. X-ray radiocrystallography	113
B. Calculations	114
C. Spectroscopic properties	116
1. Studies in solution	116
a. Steady-state measurements	116
b. Time-resolve measurements	119
2. Studies at the solid state	122
a. Measurements on blends	122
b. Measurements on neat films	123
i. Steady-state measurements	123
ii. Time-resolved measurements	125
iii. Temperature-dependant measurements	127
iv. Potential pathways of deactivation	129
c. Measurements on OLED	130
Conclusion	
General conclusion	137
Appendices	141
Appendix 1: Experimental details	143
Appendix 2: Procedures	145
Appendix 3: E-ecl , NMR experiments	166
Appendix 4: E-sta , NMR experiments	172
Appendix 5: E-sta , X-ray data	177
Appendix 6: Dipole moments calculations	178

INTRODUCTION

Since the discovery of the [2.2]paracyclophane **pCp** (Figure 1) in 1949,¹ this type of derivatives have been the focus of much attention. Indeed, the challenge of synthesising such constricted molecular structure first interested a great number of organic chemists like the Nobel prize laureate Donald J. Cram who even described the [2.2]paracyclophane derivatives as “internally tortured molecules with inherent suicidal tendencies that skirt a fine line between isolability and self-destruction”.² The proximity of the two benzene rings in this system leads to unique structural and electronic properties which have been intensively studied over the past decades. Therefore, in this work we propose to synthesise a series of cyclophane-based molecules in order to exploit the peculiar inter-ring interactions for applications in surface functionalisation and to design new types of fluorophores.

The first part of the Chapter 1 (Bibliography) will be focused on detailing the properties and applications of the [2.2]paracyclophane and their dithia[3.3]paracyclophane analogues (**dtpCp**, Figure 1) in the field of catalysis,³ organic electronics,⁴ optics⁵ and semiconducting polymers⁶. The second and third parts of the same chapter will present the two main topics of this research thesis: the nanostructuration of surfaces by supramolecular self-assembly of three-dimensional tectons and the development of specifically-designed molecules to enhance the efficiency of organic light-emitting diodes (OLEDs).

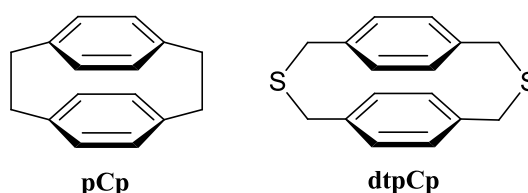


Figure 1: Molecular structure of the [2.2]paracyclophane **pCp** and the dithia[3.3]paracyclophane **dtpCp**

The second chapter will be centred on one of the most investigated research topics in the field of surface science: the nanostructuration of surfaces. Two methods are currently used to control matter at the nano-scale: the *top-down* and the *bottom-up* approaches.⁷ The *top-down* strategy consists in downsizing a bulk material to the nano-scale by using different physical treatments such as lithography or electron-beam writing. In contrast, the *bottom-up* methods are based on the assembly of atomic or molecular building blocks into organised surface structures. One of the most commonly employed strategies in the bottom-up route resides in creating two-dimensional hierarchical structures that exploit the supramolecular interactions between planar molecules. In this context, numerous avenues have been explored to generate highly ordered networks on surfaces by targeting specific supramolecular interactions such as van der Waals forces and hydrogen, coordination and halogen-bonding, etc.⁸ However, by functionalising conducting or semi-conducting substrates (such as metallic surfaces or graphite), the strong interactions that occur between molecules and substrate tend to quench any electronic properties of the molecules.⁹ To overcome this, our group has focused its research on the functionalisation of substrates by using three-dimensional molecules called “Janus-tectons”.¹⁰ Such molecules basically present two “faces” linked by a cyclophane bridge (**pCp** or **dtpCp**) where one face is responsible for the self-assembly on the surface and the second bears an active or “functional” component. The role of the cyclophane core in these tectons is to lift up the

active component and thus allow the electronic decoupling from the metallic surface. The first generation of Janus-tectons permitted the physisorption of supramolecular self-assemblies on graphite and graphene substrates by using molecular clip functions attached to the lower benzene ring of the cyclophane. These clips, composed of alkyl chains, were very efficiently adsorbed on carbon sp^2 -hybridised substrates but became ineffective when applied on pure metallic surfaces such as gold Au(111). Thus the first objective of this thesis is, as reported in chapter 2, the design, synthesis and characterisation of a second generation of Janus tectons. The concept of the non-versatile molecular clip was then abandoned and replaced with the use of pyridine-based units. Such units co-deposited on a surface with the right molecules might allow for multiple supramolecular bonding such as coordination, hydrogen or halogen bonds. The new generation of Janus tectons incorporating such pyridine units is represented in Figure 2 **a** along with the target molecule bearing a benzothiadiazole-based fluorescent moiety in **2b**.

a) **b)**



Figure 2: Molecular structure of the new generation of Janus tecton

The third and last chapter will present the first investigations performed in our lab on new cyclophane-based light-emitting materials developed for third generation OLEDs. Since the pioneering work of Tang and van Slyke,¹¹ and later on of Friend *et al.*,¹² fluorescence-based OLEDs have been intensively studied for applications such as flat-panel displays for TV screens.¹³ However, this first generation of OLED was mainly limited by the proportion of singlet and triplet excited charges injected in the device, resulting in 25 % of singlet and 75 % of triplet excitons. Indeed, due to spin statistics, the electronically-induced fluorescence is basically limited to only 25 % of internal quantum efficiency (IQE), corresponding to the amount of singlet excitons recombining in the device. In contrast, the second generation of OLEDs based on phosphorescent materials were investigated due to the fact that it is possible to harvest both singlet and triplet excitons through heavy atom-enhanced intersystem crossing (ISC), and therefore approach the 100 % of internal quantum efficiency.¹⁴ However, the high cost of such molecules, composed generally of noble metal-based complexes (such as iridium and platinum), drastically hinders the applications of this kind of phosphorescent emitters. This is the reason why recently, a third generation of OLED was proposed, based on thermally activated delayed fluorescence (TADF).¹⁵ This phenomenon is capable of achieving 100% of IQE through up-conversion from the triplet excited state to the singlet excited state. Both singlet and triplet excited states are thus harvested leading to 100 % of fluorescence. It is important to note that the emission is then separated into two different phenomena known as prompt fluorescence (or “classic” fluorescence) and delayed fluorescence (resulting from the up-conversion from the triplet state). This electronic process has been known for decades, but only recent studies have revealed that highly efficient delayed fluorescence can be achieved by optimising the molecular design in order to reduce the energy

difference between singlet and triplet excited states (ΔE_{ST}) whilst maintaining a high electroluminescence efficiency. In general, the key method is to decrease the overlap occurring between the highest occupied and the lowest unoccupied molecular orbitals (HOMO and LUMO, respectively). The HOMO and the LUMO are generally distributed onto the electron-donating and electron-accepting units, respectively. Thus, the common strategy when designing TADF emitters consists in incorporating such electron-donating and electron-accepting groups onto a separating central core. This separation generally occurs by twisting the molecular bonds linking the two acceptor and donor moieties,¹⁶ or by linking the two of them with a σ -bond based structure.¹⁷ The aim of our research is thus to use the dithia[3.3]paracyclophane **dtPCp** as a separator. Indeed, by grafting the donor and acceptor on each opposing benzene ring, the conjugation between them should be highly reduced, but the special interactions between the two opposite benzene rings should allow enough conjugation to achieve good electroluminescent properties. The new type of emitter is represented in Figure 3 along with the target emitter **E**; composed of a cyclophane core with two nitrile units (acting as electron-acceptors) grafted on the lower benzene ring and one ditolylphenylamine (acting as electron-donor) on the opposite benzene ring.

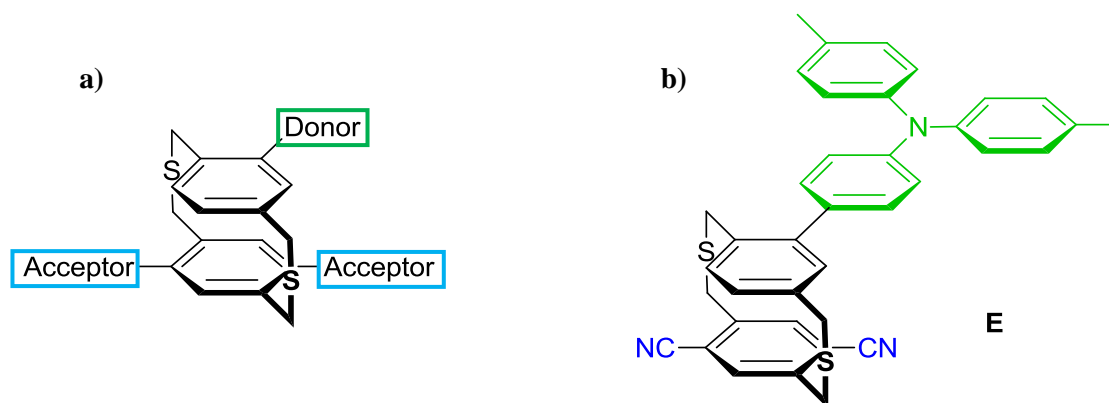


Figure 3: Molecular structure of the new type of emitter (a) and the target emitter **E** (b)

¹ Brown, C. J.; Farthing, A. C. *Nature* **1949**, 164, 915–916.

² Cram, D. J.; Cram, J. M. *Acc. Chem. Res.* **1971**, 4, 204–213.

³ Pye, P. J.; Rossen, K.; Reamer, R. A.; Tsou, N. N.; Volante, R. P.; Reider, P. J. *J. Am. Chem. Soc.* **1997**, 119, 6207–6208.

⁴ Seferos, D. S.; Trammell, S. A.; Bazan, G. C.; Kushmerick, J. G. *Proc. Natl. Acad. Sci.* **2005**, 102, 8821–8825.

⁵ Bazan, G. C. *J. Org. Chem.* **2007**, 72, 8615–8635.

⁶ Morisaki, Y.; Chujo, Y. *Macromolecules* **2002**, 35, 587–589.

⁷ Biswas, A.; Bayer, I. S.; Biris, A. S.; Wang, T.; Dervishi, E.; Faupel, F. *Adv. Colloid Interface Sci.* **2012**, 170, 2–27.

⁸ Kudernac, T.; Lei, S.; Elemans, J. A. A. W.; De Feyter, S. *Chem. Soc. Rev.* **2009**, 38, 402–421.

⁹ Repp, J.; Meyer, G.; Stojković, S. M.; Gourdon, A.; Joachim, C. *Phys. Rev. Lett.* **2005**, 94 (2), 26803.

¹⁰ Bléger, D.; Mathevet, F.; Kreher, D.; Attias, A. J.; Bocheux, A.; Latil, S.; Douillard, L.; Fiorini-Debuisschert, C.; Charra, F. *Angew. Chemie - Int. Ed.* **2011**, 50, 6562–6566.

¹¹ Tang, C. W.; VanSlyke, S. A. *Appl. Phys. Lett.* **1987**, 51, 913–915.

¹² Burroughes, J. H.; Bradley, D. D. C.; Brown, A. R.; Marks, R. N.; Mackay, K.; Friend, R. H.; Burns, P. L.; Holmes, A. B. *Nature* **1990**, 347, 539–541.

¹³ News release of Sony Corporation, 1 October 2007. <https://www.sony.net/SonyInfo/News/Press/200710/07-1001E/>.

¹⁴ Adachi, C.; Baldo, M. A.; Thompson, M. E.; Forrest, S. R. *J. Appl. Phys.* **2001**, 90, 5048–5051.

¹⁵ Adachi, C. *Jpn. J. Appl. Phys.* **2014**, 53, 60101.

¹⁶ Uoyama, H.; Goushi, K.; Shizu, K.; Nomura, H.; Adachi, C. *Nature* **2012**, 492, 234–238.

¹⁷ Nakagawa, T.; Ku, S.-Y.; Wong, K.-T.; Adachi, C. *Chem. Commun.* **2012**, 48, 9580.

CHAPTER 1:

BIBLIOGRAPHY

I. Cyclophanes

“Cyclophane” is a general term to name any cyclic compounds containing aromatic ring(s) as part of their ring structure. As expected, with this definition, a huge amount of molecules can be referenced as cyclophanes. However, our work essentially focused on studying the [2.2]paracyclophanes (**pCp**) and its sulphur-based homologue the dithia[3.3]paracyclophanes (**dtpCp**) (Figure 4).

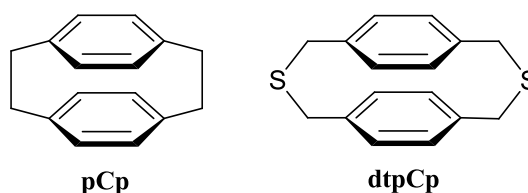


Figure 4: Representation of the [2.2]paracyclophane (**pCp**) and its homologue the dithia[3.3]paracyclophane (**dtpCp**)

A. [2.2]paraCyclophane

The **pCp** was first isolated by Brown and Farthing in 1949 as a by-product of the polymerisation of *p*-xylene by low pressure pyrolysis.¹ Two years later, Cram and Steinberg published an article discussing about a different way to synthesise the **pCp** (by intramolecular Wurtz reactions using metallic sodium on dibromide precursors) and developed a more detailed study of the crystal structure.¹⁸ The X-ray measurements have highlighted an unusual behaviour: the two benzene rings (also named “decks”) have lost their flatness in favour of a more puckered conformation; the carbon atoms bearing the methylene bridges were bent out of the plan of the other four carbon atoms, forming an angle of 12.6° (also known as boat conformation). Moreover, the distance between the two benzene cores was 3.09 Å, which is lower than the ideal π -stacking distance between two organic aromatic entities (3.4 Å, in graphite¹⁹) and thus proving the strong overlap of the two aromatic systems. Finally, the C-C bond of the methylene is slightly longer (1.55 Å) compared to a normal H₂C-CH₂ (between 1.516 and 1.532 Å)²⁰; this confirms the distortion within this molecule, and also the electronic repulsion between the too-close benzene rings. The parameters of the structure are summarised in Figure 5 below.

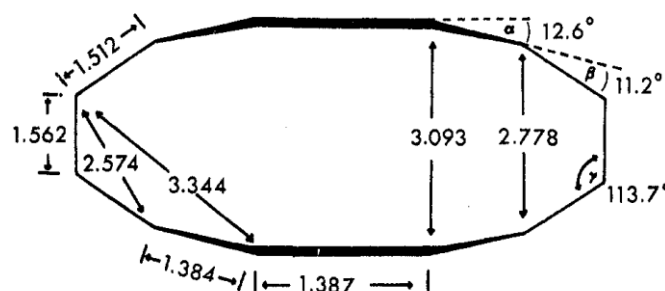


Figure 5: Molecular structure of the **pCp**, by Cram *et al.*²

Furthermore, Cram *et al.* have synthesised several derivatives in order to observe the evolution of the overlap properties *versus* the bridge's length.⁵ Some of these derivatives are represented in Figure 6.

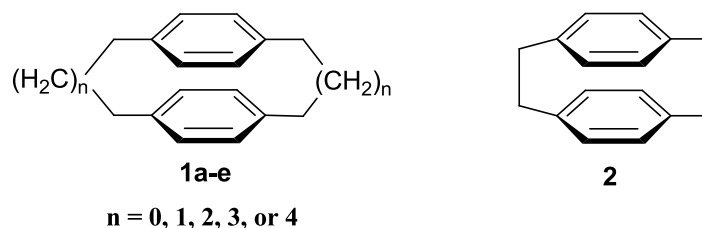


Figure 6: Representation of the pCp derivatives (**1a-e**) and their acyclic analogue (**2**)

They measured the absorption spectra of the different derivatives and compared them with the acyclic molecule acting like a reference. Their measurements have shown several changes in the UV part of the spectra for the lowest bridge's length. Above 5 carbons per chains ($n = 3$), the spectra obtained were almost identical with the spectrum of the acyclic molecule. The conclusion was quite obvious: increasing the number of carbons in the bridge was allowing the benzene rings to recover their normal planarity, and they were thus losing the special interactions they had with each other.

In addition to their atypical electronic behaviour, the two decks of the **pCp** were allowing another property to emerge: the planar chirality. The standard rules of chirality established by Cahn, Ingold and Prelog allow defining the absolute conformation of the cyclophanes.²¹ The most simple carboxylic acid derivated from the [2.2]paraCyclophane is used as an example in Figure 7:

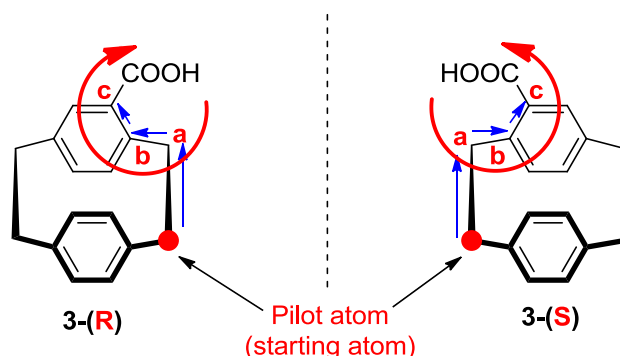


Figure 7: Absolute conformation of the pCp derivatives

The selection rule for planar chirality has been enounced by Cahn, Ingold and Prelog:

*“Of atoms directly bound to atoms in the plane, that most preferred by the Standard Sub-rules, **the pilot atom**, marks the side of the plane from which, under the Chirality Rule, an in-plane sequence is observed; and the sequence starts with the in-plane atom directly bound to the pilot atom (**a**), and continues, to and through other atoms (**b** and **c**), by way of a succession of bonds along that in-plane path, which at each branch leads to the atom more preferred by the Standard Sub-rules”.*

All of these results describe the **pCp** as a distorted but chiral molecule with an interesting electronic communication between the two benzene rings. However, despite the advances in chemistry, the synthesis of the **pCp** and its derivatives remains difficult. On one hand, the cyclisation is currently performed in harsh conditions, using high temperature¹ or strong reagents like metallic sodium¹⁸. In contrast, the post functionalisation was not easily controlled: as described by Cram *et al.* with the dibromination reaction²², a mixture of products is always obtained, as shown in Figure 8.

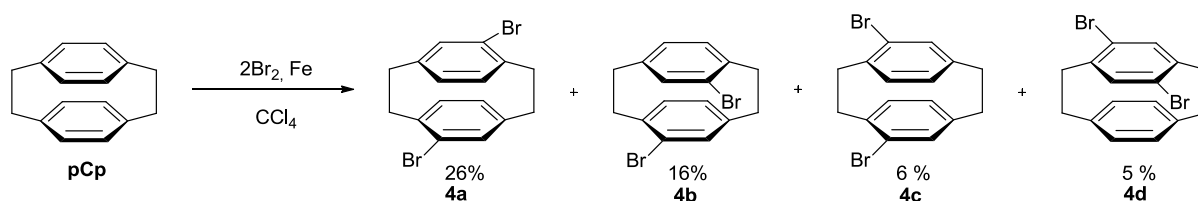


Figure 8: Dibromination of the **pCp** results in the formation of 4 isomeric species

Another pathway mentioned in several articles described an easier synthesis of **pCp**, based on a key precursor: the dithia[3.3]paracyclophane (**dtpCp**). The chemistry around the **dtpCp** and its properties will be discussed in the next part.

B. Dithia[3.3]paraCyclophane

One of the first paracyclophane including sulphur-based bridges was accidentally synthesised by El-Hewehi *et al.* in 1959.²³ They were originally targeting a cyclic diaryl-trithiocarbonate by reaction of potassium trithiocarbonate on 9,10-bis(dichloromethyl)anthracene; but they obtained instead two different cyclophanes **5** and **6** represented in Figure 9. The molecule **6** was an anthracene-based paracyclophane where its two bridges were including one and two sulphur atoms. On the contrary, the cyclophane synthesised by Millar *et al.*²⁴ several years later, represented as **7** (*cf.* Figure 9), was a real [3.3]dithiacyclophane, though still based on anthracene moieties.

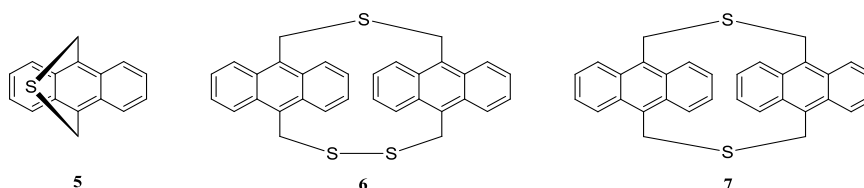


Figure 9: Representations of El-Hewehi's cyclophanes (**5** and **6**) and Millar's (**7**)

The **dtpCp** have been used from the 1970's as a precursor in the **pCp** synthesis. This new route^{25,26} consists in the coupling of 1,4-bis[halogenomethyl]benzene with 1,4-bis(mercaptomethyl)benzene followed by the photodesulphurisation in triethylphosphite, as displayed below in Figure 10.

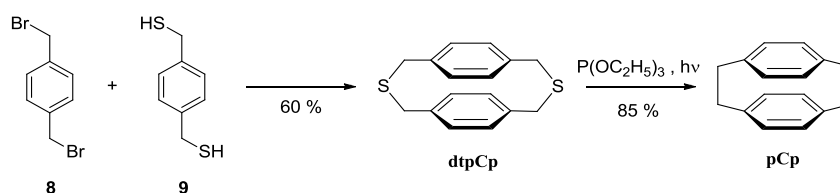


Figure 10: A new route to synthesise the **pCp**, via the **dtpCp**

These reactions not only allow the synthesis of the **dtpCp** under smooth condition (and one step forward, the **pCp**), but also permit the pre-functionalisation of each precursors before coupling them in order to obtain dissymmetric cyclophanes.

A crystal structure of a **dtpCp** derivative bearing two bromides on one side of the cyclophane is given Figure 11.²⁷ The detailed study of this structure showed that the presence of sulphur atoms has a significant impact on the cyclophane architecture. Indeed, the sulphurs act like ball joints and allow a higher mobility of the atoms, leading to the relaxation of a part of the system constraints. More precisely, the distance between the two benzene rings increases from 3.04 Å for the **pCp** to around 3.24 Å in the **dtpCp** and their boat conformation almost disappears as well. Nevertheless, even though

the inter-cycles distance increases to 3.24 Å, this value is still lower than the normal π -stacking distance between two organic aromatic entities (3.4 Å)¹⁹ and consequently the overlap of the π -conjugated systems is still maintained in **dtpCp** derivatives despite the addition of sulphur atoms in the cyclophane bridge.

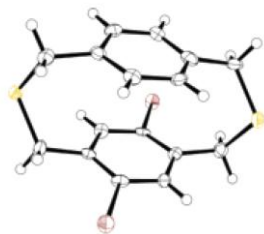


Figure 11: Crystal structure of the *p*-dibrominated **dtpCp**

The work of Wang *et al.*²⁸ on the fluorene-dithia[3.3]paracyclophane copolymers (Figure 12) have also proven the presence of significant transannular π - π interactions in their polymers. It has been essentially demonstrated by comparing two sets polymers (with or without a cyclophane incorporated to the electronic system): emission shifts in solution and in solid state were observed, and also in some case a photoluminescence quantum yield enhancement, which confirmed the overlap of the π -systems.

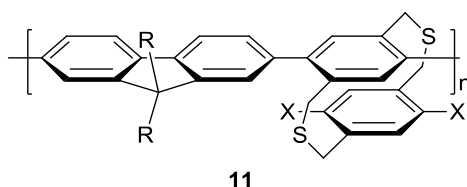


Figure 12: Representation of the fluorene-dithia[3.3]paracyclophane of Wang *et al.*

In conclusion, the **dtpCp** is easily synthesised in comparison with the **pCp**, but the transannular π - π interactions slightly decreases, albeit they are never completely deleted. Thus, in the same way as the **pCp**, the **dtpCp** should have his own load of potential applications.

C. Properties and applications of cyclophane derivatives

The unique properties of the cyclophanes have been studied over the past 50 years and a large amount of articles have been published. Among these, a wide range of applications have been investigated including chiral catalysis, molecular electronics, optoelectronics, polymer materials, ... The followings parts will succinctly describe some interesting results related to those applications.

1. Chiral catalysis

Despite the early discovery of the planar chirality of the **pCp**, its uses in catalysis were almost non-existent until 1990 with the work of Rossen, Pye *et al.* on the 4,12-bis(diphenylphosphino)-[2.2]-paracyclophane, also known as PHANEPHOS, represented in Figure 13.³ Inspired by the good efficiency of the well known 2,2'-bis(diphenylphosphino)-1,1'-binaphtyle (BINAP) ligand²⁹, also planar chiral (Figure 13), they described this new ligand paracyclophane-based, suitable for Rhodium-catalysed hydrogenations.

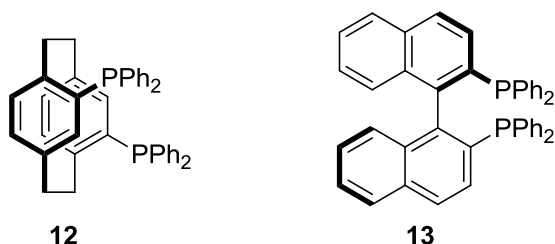


Figure 13: PHANEPHOS (**12**) and BINAP (**13**)

The catalyst, synthesised from $\text{Rh}(\text{COD})_2^+ \text{OTf}^-$ and PHANEPHOS, made possible the hydrogenation of dehydroamino acid methyl esters **14** at -45°C in methanol with very good enantiomeric excess (ee) up to 99% with complete conversion in less than 1 hour. Then, Rossen, Pye *et al.* have successfully investigated several catalyses: the Buchwald-Hartwig coupling with a palladium-based catalyst on a dibromo-**pCp**³⁰ **15** and the hydrogenation of β -ketoesters **16** with a ruthenium-based catalyst.³¹ These three catalyses, summed up in Figure 14, were compared with the BINAP catalyses efficiencies, and the PHANEPHOS ligand has shown at least equivalent performances.

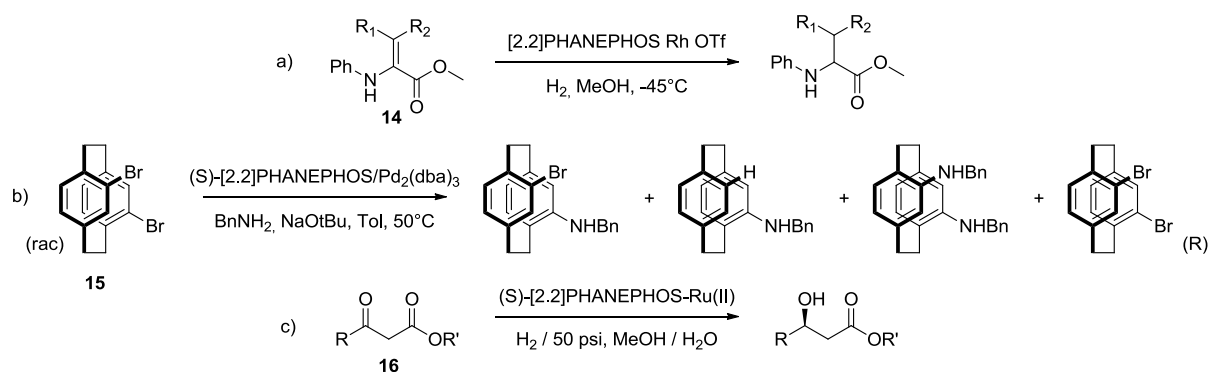


Figure 14: Different uses of PHANEPHOS as catalyst for: a) hydrogenation with rhodium catalyst, b) Buchwald-Hartwig coupling with palladium catalyst and c) hydrogenation with ruthenium catalyst

As the PHANEPHOS was described as the cyclophane-based analogue of the BINAP, Braddock *et al.* decided to apply the same rule for the BINOL, and synthesised the PHANOL in 2002³²; they are both represented Figure 15.

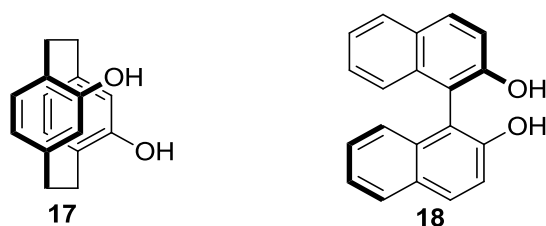


Figure 15: PHANOL (**17**) and BINOL (**18**)

The PHANOL was first used as catalyst of the Diels-Alder reaction between cyclopentadiene and α,β -unsaturated aldehydes or ketones³³. They accurately described the effects of hydrogen bonding within the catalysis, but the results were not satisfying: despite acceptable catalysis efficiency (rate acceleration up to 30 fold), the enantiomeric excess was low (up to 77%) and unpredictable.

Later, the same authors have also published their work on the epoxyde ring-opening catalysis.³⁴ The speed of the reaction increased, but the enantioselectivity of the catalyst was still fickle. We can now assume that PHANOL have never been raised to the enantioselective catalyst status: no article was published since then.

In addition to these two examples, several ligands were designed, based on the paracyclophane backbone. We can quote for instance the N,O-ligand **19** which is very efficient for asymmetric alkenylzinc additions to aldehydes³⁵ and imines³⁶, as represented in Figure 16.

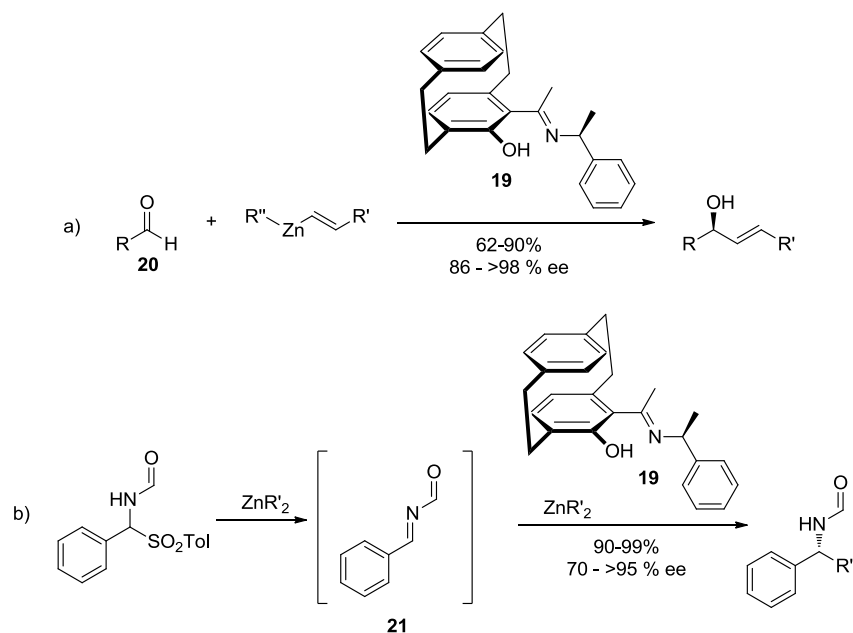


Figure 16: Asymmetric alkenylzinc additions to a) aldehydes, and b) imines

Finally, most of the researches on the cyclophane-based catalyst were done at the end of the 1990's/beginning of the 2000's. But, as proven by Han *et al.*³⁷, new and very efficient ligands are still synthesised: the [2.2]paracyclophane-derived monodentate phosphoramidite ligand **22** have presented high conversion (above 90 %) and high selectivity (up to 95%) for the enantioselective conjugate addition of $ZnEt_2$ to substituted chalcones, as shown in Figure 17.

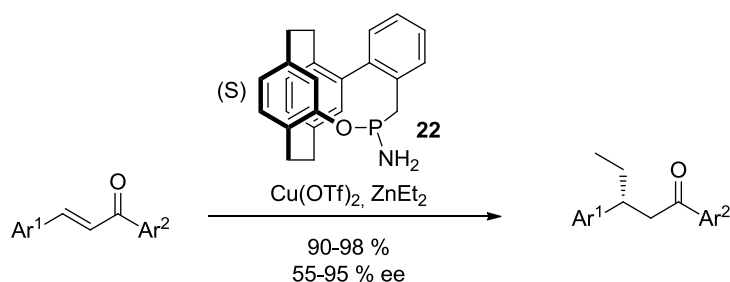


Figure 17: Asymmetric addition to substituted chalcones

2. Molecular electronics

The inter-rings distance within the **pCp** and the **dtPCp** is lower than the ideal π -stacking distance between two aromatic entities, thus interesting electronic interactions can be expected through the cyclophane bridge.

Seferos *et al.* have published several results about the electronic communications through **pCp** by comparing the conductivity of simple cyclophane-based molecule **23** with the benzene analogue **24**, as depicted in Figure 18.⁴

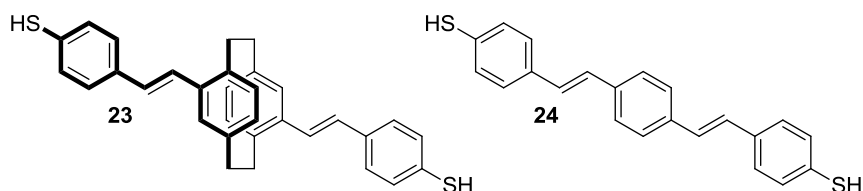


Figure 18: Representation of the molecules (**23**) and (**24**) studied by Seferos *et al.*

By using the terminal thiol, they were able to create a self-assembled monolayer (SAM) of each compound between two electrodes of gold. It appeared that the measured conductivity of the **pCp**-based molecule was only half of that of the benzene-based molecule. Considering that the packing density of **23** was twice that of **24**, a surprising conclusion was deduced: the **pCp** through-space π -interactions are as effective as the simple π -delocalisation in benzene for electron-transport. Later on, they performed some additional experiments under single-molecule conductive atomic force microscopy (C-AFM).³⁸ The conductivity measurements were in total agreement with the previous report.

The electron-transfer through **pCp** bridges has also been studied by Wielopolski *et al.* in molecular wires of different sizes based on donor/acceptor systems.³⁹ In those systems, the donor (fullerene) and the acceptor (zinc-porphyrin) are connected by paracyclophane-oligophenylenevinylene bridges as represented in Figure 19.

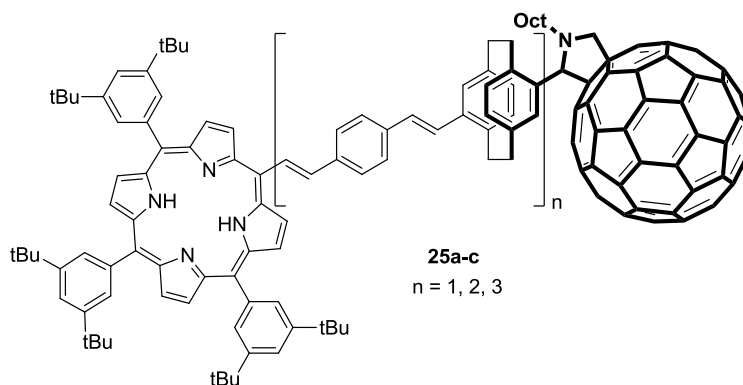


Figure 19: Molecular wires of three different sizes

The molecular modelling studies, and later on the photochemistry experiments, have shown that a charge-transfer was occurring through the bridge: the cyclophanes were able to accept holes and donate electrons, thus leading to an easy charge-transport, successively from the fullerene to the bridge, and then from the bridge to the porphyrin.

Finally, to conclude this topic, the study of **dtpCp**-bridged binuclear ruthenium alkynyl complexes⁴⁰ has highlighted an interesting fact: the non-innocent character of the **dtpCp** moiety. The cyclophane-based complex is represented in Figure 20 with its benzene-based analogue.

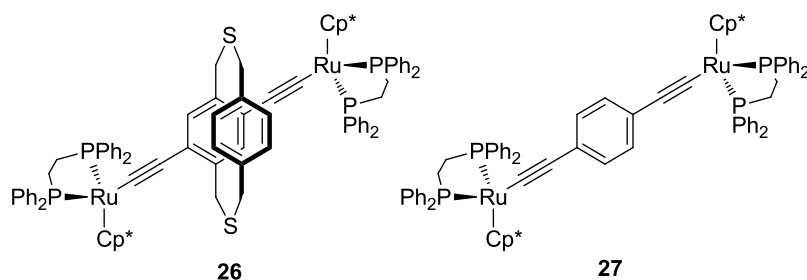


Figure 20: The cyclophane-based ruthenium complex (**27**) and its analogue benzene-based (**28**)

The electrochemistry studies of the analogue have shown that two consecutive one-electron-oxidation processes were localised on the ruthenium moiety. On the contrary, for the **dtpCp**-based complex the oxidations were substantially supported by the alkynyl-cyclophane bridge, thus acting as a non-innocent ligand. In this case, as demonstrated by the Infra-Red studies, relatively intense transitions can be attributed to metal-ligand charge-transfer (MLCT) and also thioether S to bridging ligand charge transfer; in other word, the electronic interactions were, for once, not between the two decks, but mainly directed by the sulphur atoms.

3. Chromophores and Non-Linear Optics

The early work of Bazan *et al.*⁵ on the **pCp**-based chromophores was not first focused on the cyclophane properties by themselves: it was use to study stilbenes in excimer-like conformations⁴¹. The cyclophane's upper and lower decks were grafted with phenylvinylene groups in order to observe their interactions at close range; the designed molecules are represented with the cyclophane-free analogue in Figure 21.

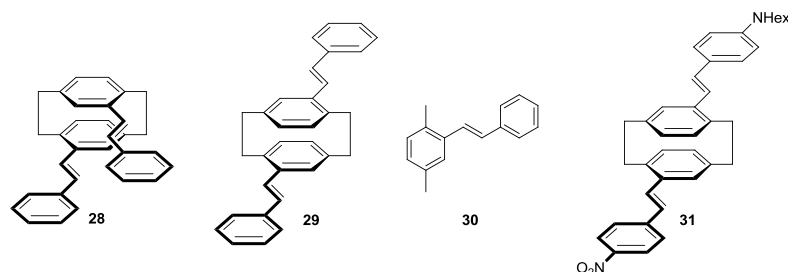


Figure 21: Representation of the **pCp**-based pseudo-excimers (**28** and **29**), the 2,5-dimethylstilbene (**30**) and the push-pull derivative (**31**)

However, as shown *vide supra*, the cyclophane is not a simple bond between two molecular moieties. In **28** and **29**, the absorbance band was split because, unlike excimers, there are ground state electronic interactions between the two units. Moreover, a bathochromic shift can be observed on the emission spectra, easily explainable by the cyclophane's short inter-ring distance (compared with the intermolecular π -stacking of an excimer) leading to a more stable excited state. For a complete study, they decided to synthesise the derivative **31**, expecting from this push-pull molecule to have two-photon absorption (TPA) properties.⁴² The hyperpolarisability β , representing factor of TPA, was measured to be thrice higher than the parallel polar superposition of the two monosubstituted stilbene subunits, once again proving the through-space charge transfer between the two cyclophane's decks.

Carrying on the stilbene-**pCp** derivatives, they designed the molecule **32** represented in Figure 22 which has presented equilibrium between through-bonds conjugation (*i.e.* the stilben parts) and through-space (*i.e.* the **pCp** core)⁴³ in opposition with the molecules represented in Figure 21 where the conjugation was mainly centered on the stilbene moieties. Several donor-acceptor derivatives were synthesised⁴⁴, and their TPA properties studied⁴⁵.

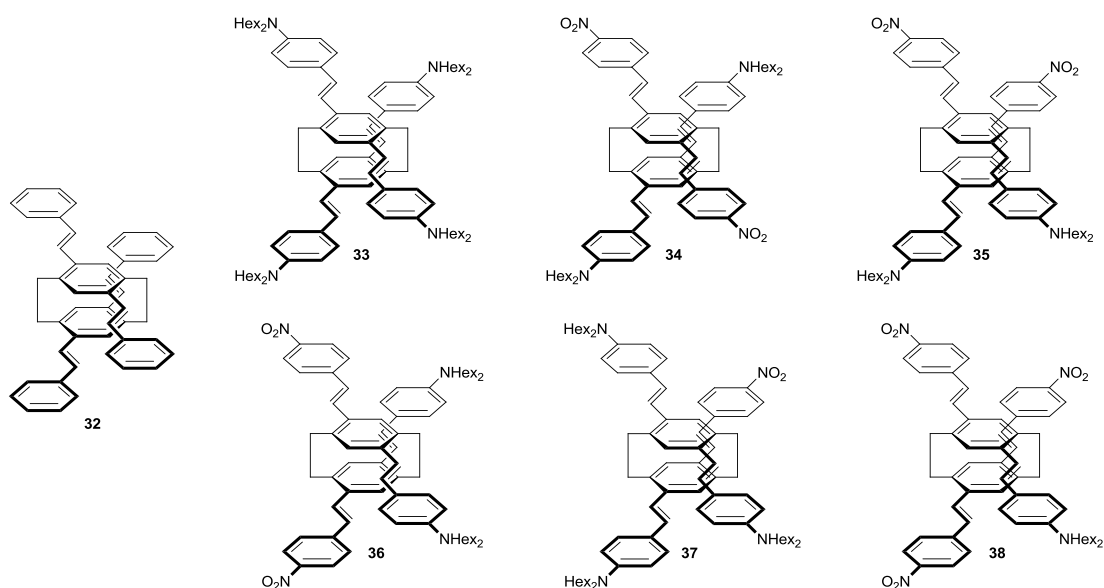


Figure 22: Representation of the multipolar compounds (**33-38**) synthesised by Bazan *et al.*, and their apolar analogue **32**

As represented above, the electron-donor (D) and acceptor (A) groups were organised through different ways: DD/DD (**33**), AA/DD (**34**), AD/AD (**35**), AD/DA (**36**), DD/AD (**37**) and AD/AA (**38**). Such molecules as **34-38** were combining dipolar and octupolar behaviours, in opposition with **33** which were almost only active as octupole. The hyperpolarisability measurements have confirmed the multidirectional through-space character of dipolar and octupolar contributions for all compounds. The **pCp** was thus confirmed to be a good candidate for Non-Linear Optical applications.

4. Polymer materials

The first π -conjugated polymer containing [2.2]paracyclophane was synthesised by Morizaki *et al.*⁶ by Sonogashira coupling. Compared with the model compounds **40** and **41**, the optical properties of the polymer **39** have presented a red shift of the absorption band. These results indicated the extension of the π -delocalisation length *via* the cyclophane through-space interactions. The polymer and its models have been represented below in Figure 23.

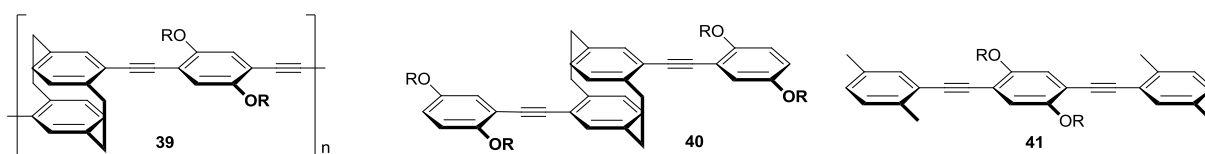


Figure 23: Representation of the first π -conjugated polymer containing [2.2]**pCp** **39**, and its models **40** and **41**, with R = alkyl chain

Morizaki *et al.* followed their investigations by synthesising several new cyclophane-based polymers represented in Figure 24, using Heck coupling and Wittig reaction.⁴⁶ The so-synthesised polymers have shown the same kind of shift on the absorption spectra, and also a very strong fluorescence, confirming their precedent results. They summed up their whole results on those π -conjugated polymers in this review.⁴⁷

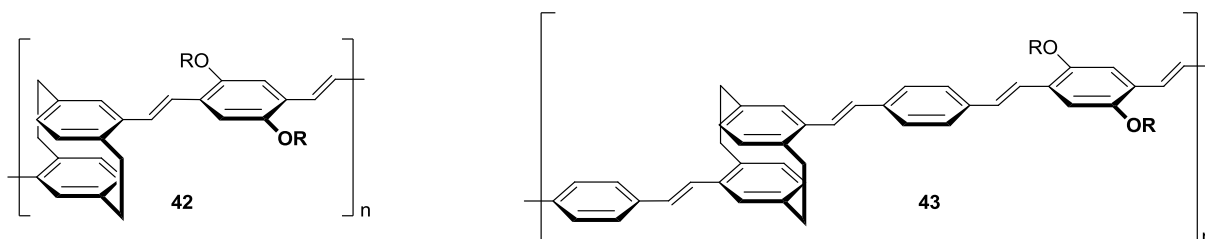


Figure 24: Synthesis of new cyclophane-based π -conjugated polymers, with R = alkyl chain

As mentioned above in part 2), several cyclophane-based polymers have also been synthesised by Wang *et al.*²⁸; each of them are represented in Figure 25. In opposition with Morizaki *et al.*'s work, they first decided to study the dithia[3.3]paracyclophane effects on a fluorine-based polymer. The cyclophane has been kept out of the conjugation length in order to functionalise the outside-deck with donor groups (-OMe) or acceptor groups (-CN), and to measure its impact on the optical properties of the polymer.

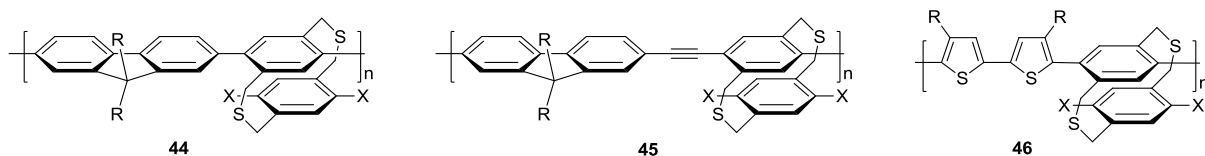


Figure 25: Polymers studied by Wang *et al.*, with R = alkyl chain and X = -H, -OMe or -CN

Once again, they have confirmed the strong transannular π - π interactions through the cyclophane moiety. Indeed, adding donor or acceptor groups on the cyclophane was quenching the fluorescence of the whole polymer⁴⁸, whereas grafting two phenyl or two biphenyl groups was enhancing the photoluminescence properties⁴⁹.

Finally, they have replaced the linker between the cyclophane moieties: ethynylfluorene and bithiophene were used instead of fluorene. Both linkers increased the rigidity of the structure, thus enhanced the conjugation through-bond and decreased the through-space interaction. As a consequence, the copolymers **45** and **46** did not show any difference with or without the introduction of the **dtpCp** moieties inside his structures.

II. Supramolecular self-assembly confined on surface

Surface science plays a crucial role as most emerging nanotechnologies will likely need to be supported on a surface. As a consequence, controlling the spatial arrangement of nano-objects on surfaces attracts considerable attention. The characterisation of such modified substrates requires atomic-scale resolution. It is therefore commonly performed by scanning probe microscopy such as atomic force microscopy (AFM) and scanning tunnelling microscopy (STM). However, the AFM is mainly utilised for topological studies of surface while the STM is centred on measuring the electronic density of nano-objects and is thus the most used technique of surface characterisation.

A. Scanning Tunneling Microscopy

1. Working principle⁵⁰

Scanning tunneling microscopy was invented in 1981⁵¹ by G. Binnig and H. Rohrer who were awarded with the Nobel Prize of physics in 1986.

With this apparatus, a sharp metallic tip is scanned over a surface at a distance of less than ten Ångströms. This tip is hold by a piezoelectric material which will be responsible of its height, thus of the surface-tip distance. If this distance is short enough, applying a bias voltage between tip and sample will cause electrons to tunnel through the vacuum barrier. According to the feedback output voltage, the piezoelectric material can move the tip backward or forward, thus keeping the tunneling current constant during the acquisition (this operation mode is called “constant current mode”). A schematic representation of the apparatus is represented in Figure 26.

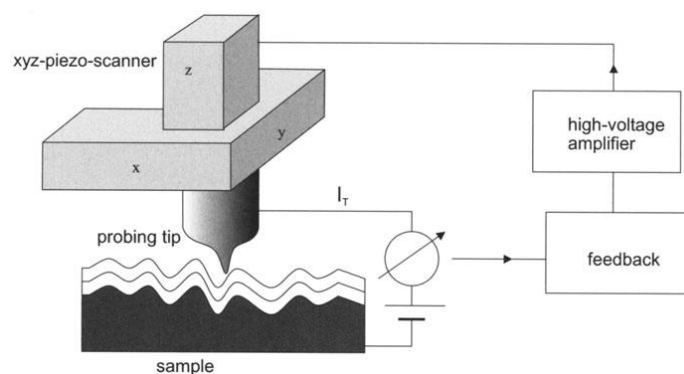


Figure 26: Schematic diagram of the scanning tunneling microscope

The probing tips have to be carefully prepared before any STM experiments. Different ways are possible, the first recipe being an electrochemistry treatment in sodium hydroxide solution, also called “etching”, as showed in Figure 27. Another way consists in carving the tips (platinum or iridium) using simple clippers; not as efficient as the electrochemistry pathway, it is however a very fast method, which roughly gives the same results.

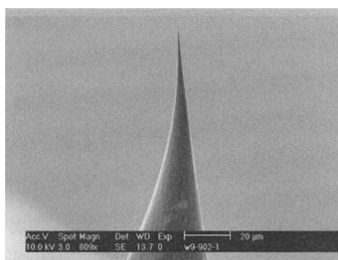


Figure 27: Scanning Electron Microscopy (SEM) picture of a tunneling tip prepared by electrochemical etching technique

Several modes of experiments can be used. To image the surface, under STM for instance, it is possible to work at constant current mode (as mentioned above) which allows the tip to go up and down in order to keep the tunnel current constant. At the constant height mode the tip is forbidden to move upward or downward thus allows the variations of current to be measured (this mode must be chosen only for very plane surface, or the tip may hit some nano-objects). In both experiments, the data (tip height or tunnel current, depending of the mode) are gathered by the computer which gives back an image of the scanned area, as presented Figure 28 with a Cu(111) substrate.

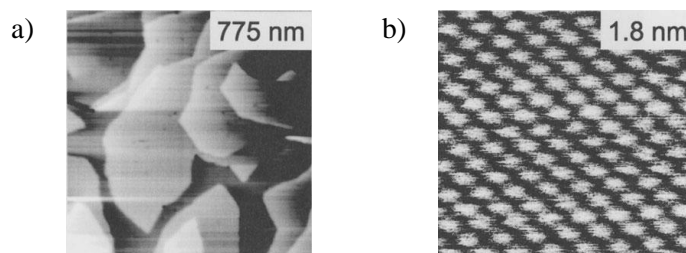


Figure 28: STM images of the Cu(111) surface in constant current mode under ultra-high vacuum. (a) An overview image with some monoatomic steps (775 nm scale) and (b) the atomic resolution of Cu(111) (1.8 nm scale)

Our interest is focusing on the imaging aspect of the STM, however other methods are also available allowing to observe the density of electrons as a function of their energy (spectroscopic modes) or to directly manipulate atoms to create nano-object on surface (manipulations modes).

2. Effect of temperature, pressure and environment

The first STM experiments were performed under ultra-high vacuum (UHV) at ultra-low temperature (Figure 29). Nowadays, it is also possible to analyse samples at room temperature, at the air/solide interface or even in solvents.

Working under UHV conditions allows very high resolution because of the absence of any interference between tip and substrate. Tuning the temperature permits the observation of dynamic behaviour (RT or higher temperature) in contrary with 77K or 4K experiments where the structure is kept still in order to obtain the highest resolution. However, the preparation of such experiments might take days and the cost of the apparatus is very high, that is why numerous studies are performed at room temperature in air or in solvent.



Figure 29: Scanning tunneling microscope, equipped for UHV experiments (CEA Saclay, IRAMIS Group)

At the liquid/solid interface, the molecules observed under the tip are solubilised in a solvent (as apolar as possible, to avoid too much interference). On the surface, the adsorption will be in competition with solvation of the molecule, hence the worst solvent equals to the best adsorption (Figure 30). Finally, the drop of solvent on the substrate must not be volatile: the experiment may last several hours, and the concentration needs to be kept constant. Furthermore, this drop will act as a protection for the tip against the atmosphere, and thus must stay immersed.

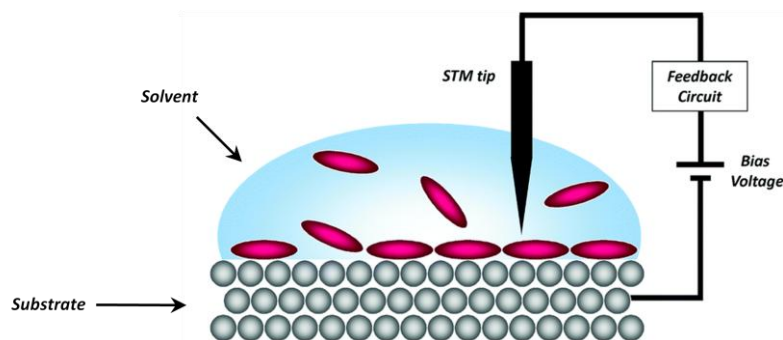


Figure 30: Scheme of Scanning tunneling experiment at the liquid/solid interface

In opposition with this technique, the air/solid interface leaves the tip out in the atmosphere. As a consequence, the tip might get slowly oxidised by the oxygen; thus the imaging might not be constant over several hours. However, this method avoids any solvation problem or any interference from the solvent during the experiment. Moreover, this pathway allows the use of any polar or volatile solvent to solubilise and deposit the molecules on the substrate, the solvent being evaporated before experiment.

B. Surface nanostructuration

In the field of nanotechnology, surface science plays a crucial role as most (nano)devices eventually need to be supported on surface. Therefore, controlling the adsorption on surface is utterly required. Many different approaches exist and it is commonly known that they can be categorised in two contrasting strategies: the top-down and the bottom-up approaches.

On one hand, the top-down approach consists in downsizing bulk material by physical treatment in order to reach the nano-scale. Over the years, several techniques have been developed to create two-dimensional patterns like soft lithography or electron-beam lithography (photolithography). Other

surface treatments can also be performed by using scanning probe microscopy, like local oxidation nanolithography⁵² or dip-pen nanolithography⁵³ technique.

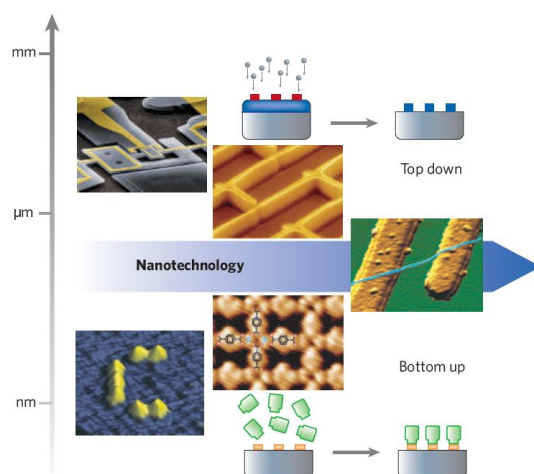


Figure 31: Top-down and bottom-up approaches, by Barth *et al.*⁵⁴

On the other hand, the bottom-up strategy consists in creating a macro-scale object from molecular building blocks. From a simple substrate, two ways are possible in order to obtain new functionalities: the chemisorption and the physisorption. The difference between these two approaches remains in the way that the molecules are “bonded” to the substrate: the chemisorption is based on strong irreversible covalent bonds whereas the physisorption is focused on weaker reversible supramolecular interactions.

1. Chemisorption⁵⁵

Specific strong bonds between a surface and a molecule lead to robust chemisorbed structures. The bonding is typically fully covalent which tends to anchor the molecule to the substrate, generally in a quasi-perpendicular tendency. Moreover, the adsorption is mainly kinetically determined, thus imperfections usually occur. The main example of chemisorbed structures is the self-assembled monolayers (SAMs). The description of the most important characteristics of SAMs follows the representation of their ideal organisation on surface in Figure 32.

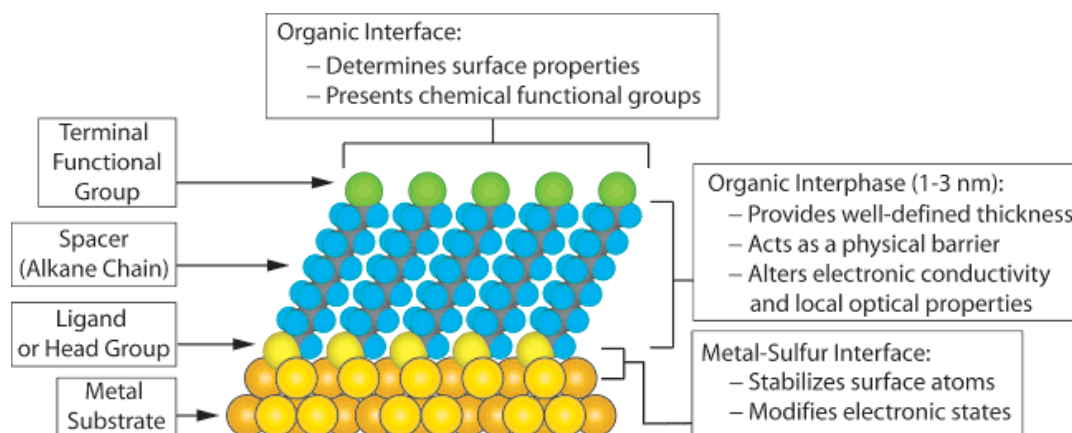


Figure 32: Ideal single-crystalline SAM organisation on metal substrate with alkanethiolate molecules as example⁵⁵

From the bottom to the top, four parameters are essential in the design of self-assembled monolayers: the substrate, the head group, the spacer and the functional group.

a. Substrate

As the bonding process occurs like a non-reversible coordination, the surface needs to be metallic. Most of the common metals can be used for this process: gold, silver, copper, palladium, platinum and even mercury (SAMs on liquid substrate in that case). However, deposition on non-metallic substrate like glass or quartz is also possible: a thin adhesion layer of titanium, chromium or nickel (1-5 nm) is deposited on the insulating substrate, followed by an active layer of metal (10-200 nm). The adhesion layer is used to improve the attachment of the second metallic layer that do not form oxides easily like gold.

Nonetheless, Gold surfaces remain the most studied substrates. Five parameters make it a good choice: first, it is easily obtained by physical vapour deposition or electrodeposition. Second, it is easy to pattern by a combination of lithographic tools. Third, gold is a quite inert substrate: it does not oxidise (below its melting point), does not react with atmospheric oxygen and does not react with most chemicals. Fourth, it is the common substrate used for several spectroscopies and analytical techniques. Finally fifth, gold is compatible with cells without evidence of toxicity.

b. Head group

For coordination to occur on a metallic substrate the molecule has to be a ligand. Numerous functions have been tested (alcohols, acids and carboxylates, amines, nitriles,...) but most of the experiments are carried on using organosulphur derivatives (thiols, disulphides, sulphides).

The organosulphur-based compounds are spontaneously absorbed on materials *via* two main processes: the physical vapour deposition (PVD) and from a dilute solution. The PVD demands an expensive equipment (evaporators, pumps to go down to UHV,...) and raises the problem of post functionalisation of the monolayers, which usually occurs in solution. In contrast, the solution pathway requires control of several parameters: solvent, temperature, concentration and immersion time. SAMs are formed from common solvents (tetrahydrofuran, dimethylformamide, acetonitrile, cyclooctane and toluene) but ethanol is the solvent of choice because it is inexpensive, not (so) toxic, available in high purity and also easily solubilises most of the organosulphur derivatives. The temperature control is also important: above 25°C, the kinetics are improved and the system is allowed to cross the activation barriers for processes such as chain reorganisation and lateral rearrangements. Finally, concentration and immersion time are inversely related: high concentration requires short immersion time.

c. Spacer

With the coordination to the surface, the spacer is also responsible for the packing of the layer. To minimise the free energy, the molecules adopt conformations that allow high degree of van der Waals interactions and sometime hydrogen bonds. Some of the best assemblies can even be adsorbed on the surface in a crystal like structure.

With efficient interactions, the density of the layer increases and as a consequence so does the number of functional groups at the top of the layer. Once again, numerous structures are available: alkanes, alkenes, alkynes, polyaryls,... Considering the case of alkanethiolates on gold for instance, the spacer can be defined by two parameters displayed in Figure 33: its angle of tilt from the surface (α) and its angle of rotation along the long axis of the molecule (β).

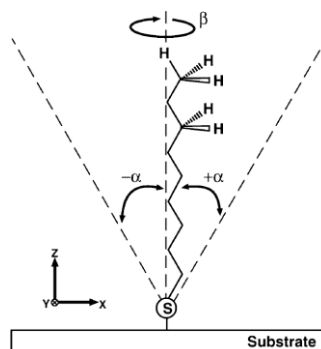


Figure 33: Schematic view of a single chain alkanethiolate absorbed on surface

The angles of the alkanethiolates are very surface-dependent. Concerning the tilt angle, its absolute maximum value is obtained on gold (30°) and its minimum on mercury (0°). About the rotation angle, the average for gold lies near 50° , whereas on other metal the data are generally near 45° .

d. Functional groups

The desired functionalities are generally introduced on the SAMs after adsorption by post-functionalisation on the surfaces. Indeed, the synthesis of functional thiol (or other head groups) is usually laborious especially when the molecules have to be linked to peptides, proteins, metals,... In this perspective, multiple reactive groups, depicted in Figure 34, have been introduced as terminal groups on the SAMs.

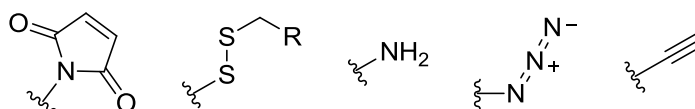


Figure 34: Potential reactive groups for SAMs post-functionalisation

This approach possesses several advantages: it uses common and simple synthetic procedures, it allows the incorporation of functions incompatible with thiol groups, multiple samples can be generated from the same process and it also preserves the underlying structure of the SAM. Nonetheless, this strategy also presents three major inconveniences: the extent of surface coverage remains unknown, the reactions can produce a mixture of functional groups on the surface and the structure of the resulting layer is also unknown (as it is usually unknown with other procedures).

e. Conclusion

The SAMs concept is a very efficient method to functionalise substrates. The resulting network is strongly linked to the surface and it can receive a large range of functionalities. Because of its robustness, it has been the most used method for numerous applications, for example biosensors or captors.

Nevertheless, some inconveniences are restricting its uses: the random post-functionalisation with no means to check the new structure, or the almost exclusive use of alkanethiolates which limits the flexibility of the technique. Furthermore, the chemisorption strategy forbids any molecular dynamics or reorganisations because the bonds with the substrate are too strong to be easily broken. And finally, creating a covalent bond with the surface can modify its entirety, thus may change its intrinsic properties.

2. Physisorption

This strategy is entirely based on the spontaneous organisation of molecules into stable and structurally well-defined networks on surface. In contrast to chemisorption, physisorption occurs by reversible supramolecular bonds between molecules and substrates and is called supramolecular self-assembly. As a consequence, the molecules will tend to lay parallel to the surface, in order to optimise their interactions with it. Moreover, the molecule can have its packing influenced by the surface: the orientations and intermolecular distances may be different from the crystal structure. This behaviour is called epitaxial growth.⁵⁶ It is led by two sets of interactions: molecule/substrate and molecule/molecule interactions.

On the one hand, the supramolecular bond between molecule and substrate depends on the nature of both, for example the van der Waals interactions between alkyl chains and highly oriented pyrolytic graphite (HOPG)⁵⁷ or the coordination-like interactions between π -systems and metallic substrates⁵⁸. On the other hand, the main interactions between molecules (electrostatic bond, halogen bond, hydrogen bond, coordination bond and finally van der Waals interactions) will be described in the following parts.

a. Coordination bond

Metal-organic coordination networks (MOCNs) have been intensively studied because of their high robustness: the strength of the coordination bond can be considered as an intermediary between covalent and non-covalent bond. The self-assembly can be performed by evaporation of the organic molecule and the metal (palladium, copper, iron,...) under UHV condition, or by simple co-adsorption of both derivatives at the liquid/solid interface. Moreover, it is also possible to use the atoms directly from the surface which, incorporated to the network, are called “adatoms”. Most coordination processes can occur on surface, but the studies have mainly focused on carboxylic acid and nitrogen-containing ligands.

The self-assembly of co-adsorbed bis(4-pyridyl)-1,4-benzene **47** and (2,2'-bipyridine)-5,5'-dicarboxylic acid **48**, depicted in Figure 35, on Cu(100) is a good example regarding different kind of bonding on surface.⁵⁹ The two molecules were co-deposited by thermal evaporation under UHV conditions. Using the free copper adatoms present on the surface, the two ligands form a dumbbell-like complex which self-assembles by hydrogen bonds between carboxylate functions and aryl C-H. The obtained network is displayed in Figure 35 with the molecular representation of the different supramolecular bonds.

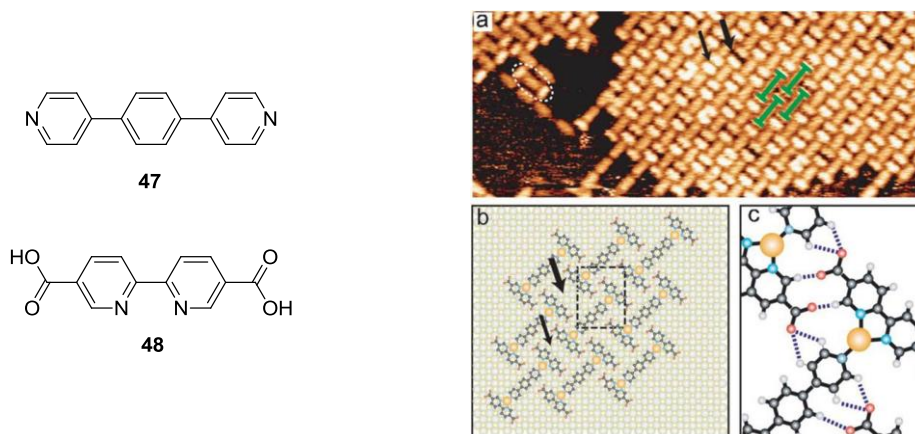


Figure 35: Structure of bis(4-pyridyl)-1,4-benzene **47** and (2,2'-bipyridine)-5,5'-dicarboxylic acid **48** and their co-adsorbed self-assembly on Cu(100) under UHV (33 x 14 nm)

The coordination process can also present several pattern structures, depending of the conditions of the experiment. For example, the terephthalic acid **49** (TPA) depicted in Figure 36, have been well described in the literature, especially by Kern, Barth and co-workers on Cu(111)^{60,61}. The co-adsorption of these carboxylic acids with Fe under UHV can self-assemble in various patterns.

The same procedure was carried on for all experiments: the adsorption of the TPA on the surface, then the Fe atoms at different concentration (compare to the TPA) and finally the annealing. First, the self-assemblies are studied with different ratios of Fe atoms per molecules of TPA(0, 0.3, 0.8 and 1.2), and then they described the influence of the annealing temperature over the networks (400 and 450K).

The TPA self-assembles by itself on Cu(111) by forming well-ordered two-dimensional domains, as represented in Figure 36. It is important to note that in this example, immediate deprotonation occurs on the surface due to the catalytic activity of the substrate.



Figure 36: Structure of the terephthalic acid and its self-assemble network on Cu(111) under UHV

The first MOCN pattern appears as a *cloverleaf phase*, at the concentration of 0.3 Fe atoms per TPA molecules: each Fe atom is surrounded by four TPA molecules. Increasing the concentration of Fe atoms per TPA molecule changes the structure: at 0.8, a *ladder phase* appears where each Fe atoms is linked to three molecules: two double-rows and one spacer. It is interesting to notice that two different types of phase may be distinguished, depending on how the rows are linked by the spacer.

Then a *single-row phase* is observed at the Fe/TPA ratio of 1.2, where the Fe atoms are adsorbed in pairs. Once again two phases are observed, depending on the orientation of the pairs of Fe atoms. Finally, by increasing the temperature of annealing from 400 to 450 K, they observed a new pattern at the 0.9 ratio; an *interlocked phase*. In this case, the surface is saturated, and acts like a broken single-row phase, when TPA makes as much coordination bonds with the Fe atoms as hydrogen bonds with its neighbours. The STM pictures of all four patterns are depicted Figure 37.

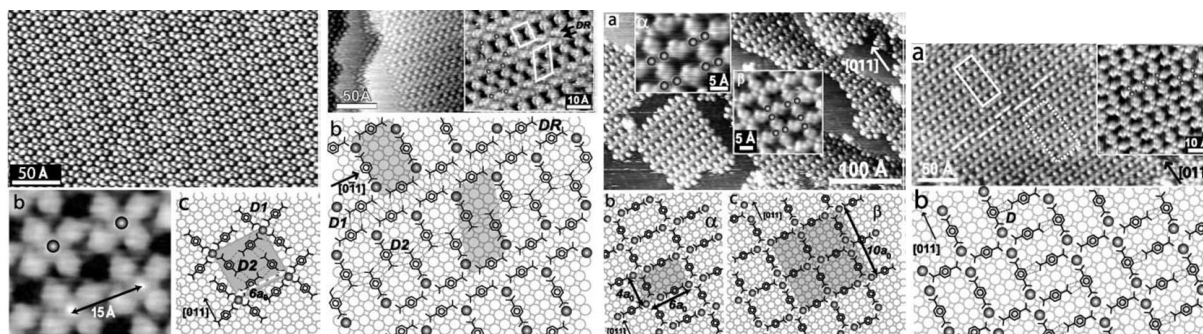


Figure 37: Terephthalic acid patterns on Cu(111) at 400K with different Fe/TPA ratios: 0.3, 0.8, 1.2, and 0.9 after annealing at 450 K (respectively from the left to the right), under UHV

In addition to this polymorphic behaviour, the authors have found a potential application for the *ladder phase* pattern. As depicted in Figure 38, the cavities are large enough to act as host; for example, the fullerene (C_{60}) was successfully adsorbed in the cavities.

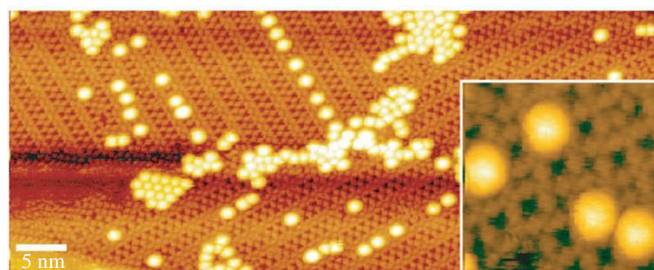


Figure 38: STM image of fullerenes trapped in the TPA network on Cu(111) under UHV

b. Electrostatic bond

After coordination, the electrostatic interactions are the strongest amongst the non-covalent bonds. In this case, the self-assembly mainly occurs by interactions between cationic and anionic species, leading to robust networks on surface.

For example, a family of pseudo-ionic molecules has been intensely studied by Stawasz *et al.*: the squaraines.⁶² These compounds are so named because of the square central carbon ring, as represented in Figure 39.

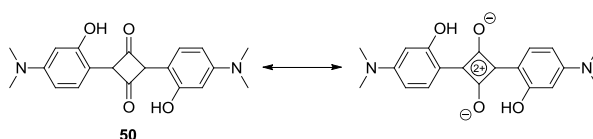


Figure 39: Representation of the squaraine structure **50**, and its zwitterionic behaviour

These molecules possess an interesting Donor-Acceptor-Donor structure leading to the zwitterionic specie represented above. As displayed in Figure 40, the adsorption of **50** on HOPG in phenyloctane leads to several networks. The most stable self-assembly occurs by interactions between the anionic oxygens and the hydrogen atoms born by the dimethylamine donor moieties.

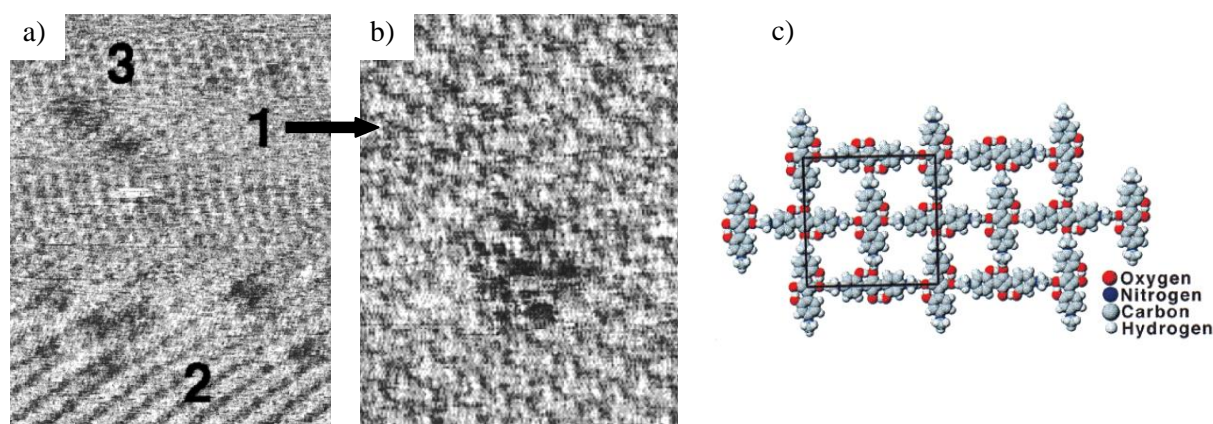


Figure 40: STM images of **50** at the phenyloctane/HOPG interface. **a)** 3 networks are observed (30 x 30 nm), **b)** Zoom on the network **1** (15 x 15 nm) and **c)** the herringbone structure corresponding to **1** as a molecular model

The packing structure of this network gives very interesting information about the nature of the self-assembly: this herringbone pattern implies that the interactions between molecules are so strong that it does not need the underlying hexagonal graphite network to self-assemble.

c. Hydrogen bond

The hydrogen bond (H-bond) is one of the strongest interactions among the non-covalent bonds. Therefore, its use in supramolecular self-assemblies has been widely studied. A large panel of functions can form H-bond on surface (alcohol⁶³, carboxylic acids⁶⁴, amines⁶⁵,...). Like other supramolecular interactions, different parameters can modify or tune the self-assembled network on surface, as presented in the two examples below.

This change of behaviour on surface can be illustrated by the work of Ciesielski *et al.* on 1,3,5-tris(pyridine-4-ylethynyl)benzene **51** (depicted in Figure 41) at the phenyloctane/HOPG interface.⁶⁶ Using both experimental STM imaging and theoretical calculations, they demonstrated the high concentration dependence of the self-assembly: at low concentration (5 to 20. 10^{-3} M), the molecules form the hexagonal porous network represented in Figure 41a while at high concentration (20 to 200 10^{-3} M), the network changes to a more packed supramolecular structure displayed in Figure 41b.

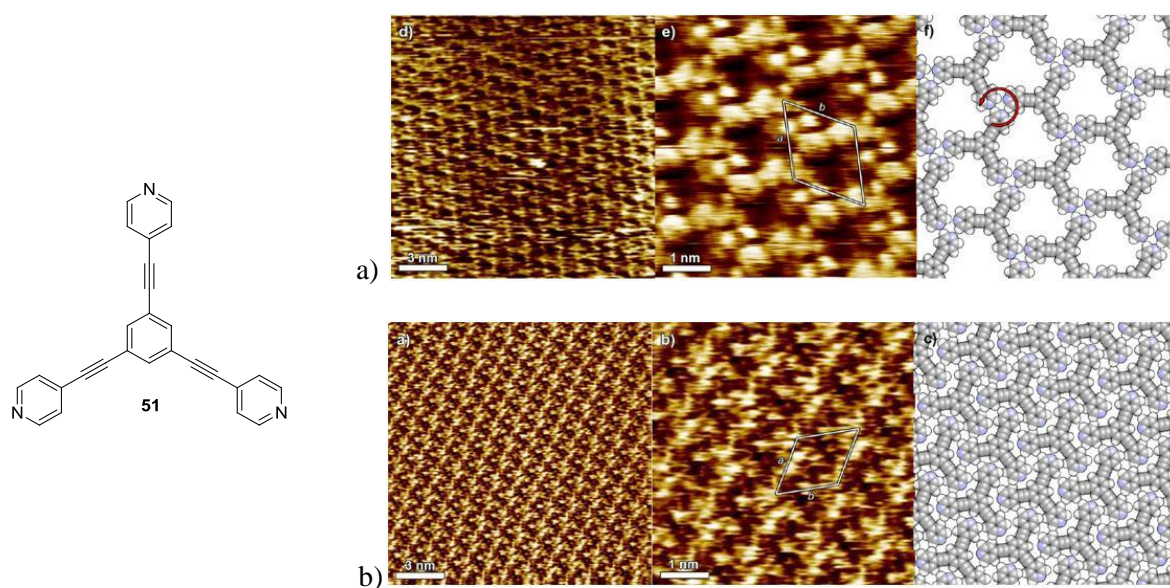


Figure 41: Molecular structure of 1,3,5-tris(pyridine-4-ylethynyl)benzene **51** and its self-assembled network at low (a) and high (b) concentration

Another interesting example have been published by Ruben *et al.* with the benzene-1,3,5-triyl-tribenzoic acid **52** (BTA) as displayed in Figure 42.⁶⁷ The authors studied the supramolecular assemblies at several ranges of temperatures on Ag(111), both by STM under ultra high vacuum (UHV) and by computational modelings.

The BTA molecules were first sublimated on the surface held at 200-250K. The first annealing to 270-300K led to a 2D honeycomb network (Figure 42a); in this assembly, the supramolecular interconnections are simply achieved by symmetric hydrogen bonds of carboxylic acid dimers of neutral BTA. However, increasing the temperature above 320K modified the network to equal-spaced one-dimensional ribbons; in this case, each molecule is singly deprotonated but is still linked to neighbouring molecules (Figure 42b). Finally, heating over 420 K takes off one more proton per

molecule; the acidic hydrogens left are then not sufficient to keep the lead on the network. A closely packed structure is formed, where the H-bond occurs between the pyridines and the aromatic C-H protons of the inner pocket of the molecule (Figure 42c). It is interesting to remark that further increase of temperature does not deprotonate the last acid function: as shown by calculations, the repulsive charges would become too high for the system to remain stable.

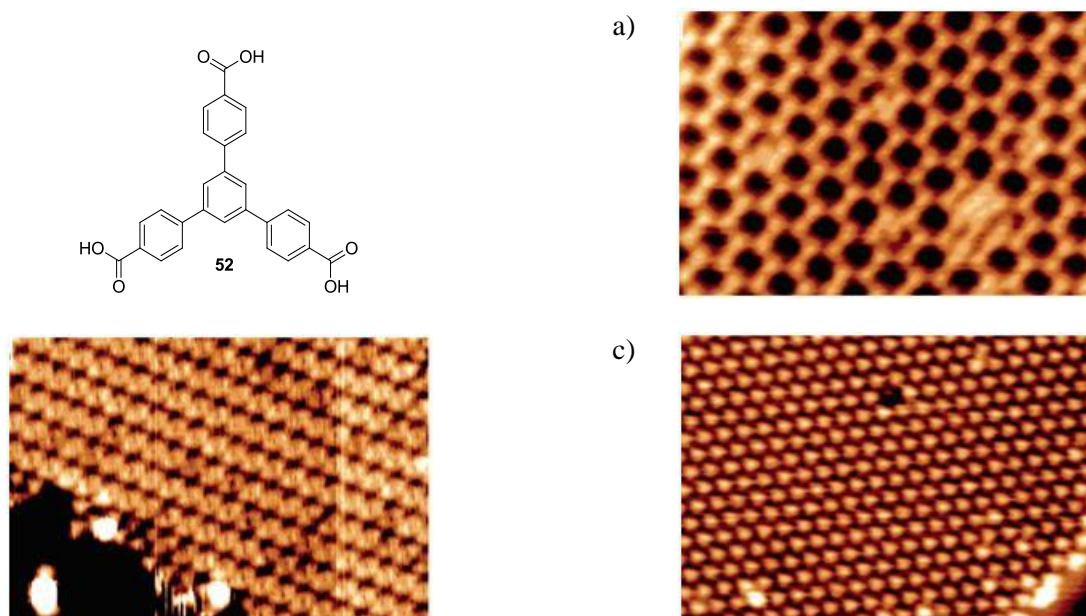


Figure 42: Molecular structure of the benzene-1,3,5-triyl-tribenzoic acid **52**, and STM images of its self-assembly on Ag(111) at 300K (a), 320 K (b) and 420 K (c) (images at 30 x 20 nm)

d. Halogen bond

Despite its important influence on the crystal structure of several molecules⁶⁸, the halogen bond (X-bond) has not yet been intensively studied for the two-dimension self-assembly on surface. Nevertheless, the peculiar behaviour of the halogen atoms should lead to an increase of research on the topic. Indeed, the halogen bond occurs due to polarisation of the halogen atom in a C-X bond resulting in a non-spherical charge distribution. As depicted in Figure 43⁶⁹, the charge depletion of the tip of the halogen atom produces a positive partial charge δ^+ , while an equatorial ring around the C-X bond is partially negatively charged δ^- .

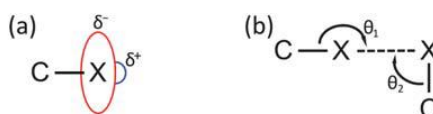


Figure 43: X-bond interaction schemes. Charge distribution in C-X bond (a) and general X-bond interaction (b)

As a consequence, the halogen atom can make bonds with other halogens, but also with any electrophilic or nucleophilic atoms. For example, Chung *et al.* have published their results on supramolecular self-assembly of porous network on Ag(111) under ultra high vacuum (UHV)⁷⁰ at 150K. The adsorption has shown an interesting bonding system of 4,4-dibromo-p-terphenyl (DBPT), following a triangular motif of one $\text{Br} \cdots \text{Br}$ bond and one $\text{Br} \cdots \text{H}$ bond, represented as dotted lines in Figure 44a. This combination of bonds leads to three different networks on surface: square, rectangular and hexagonal, as displayed in Figure 44b. By calculations, Chung and co-workers established that square and rectangular networks were the more energetically favourable to occur. However, the hexagonal lattice covers 70% of the surface (against 20% and 10% for the rectangular and square networks, respectively). As their calculations were not taking into account the effects of the

surface, they concluded that the hexagonal structure may allow more energy gains than others when the molecules are absorbed directly on the hexagonal lattice of Ag(111).

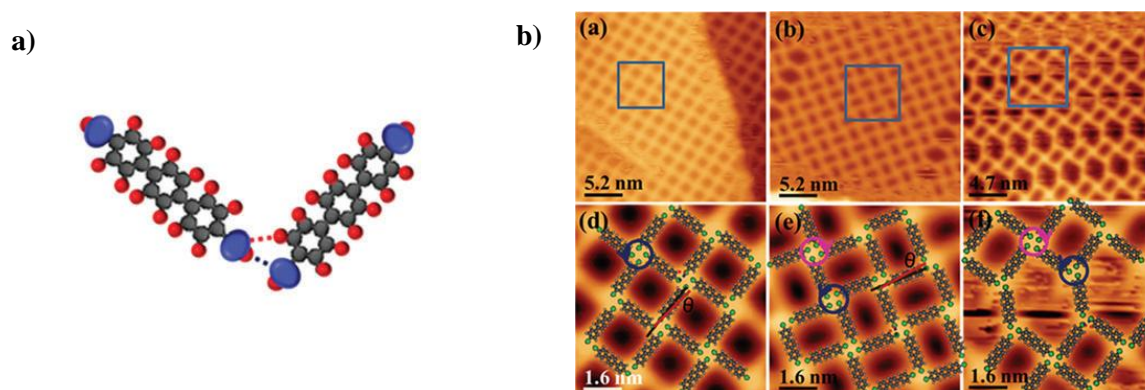


Figure 44: Schematic of a triangular motif bonding two DBTP and STM topography of the three porous networks

One of the main applications of the halogen bond is the possibility of building covalent organic framework (COF) from a supramolecular network. The experiment have been tried several times with 1,3,5-tri(4-bromophenyl)benzene (TBB) under UHV⁷¹ or at the liquid/solid interface⁷². As represented in Figure 45, the molecules were adsorbed on surface. When the self-assembly had occurred, the sample was annealed at 300°C. After heating, the distance between two interconnected molecules was reduced from 1.49 nm to 1.24 nm, proving the creation of the covalent bond by Ulmann coupling⁷³ confined on surface.

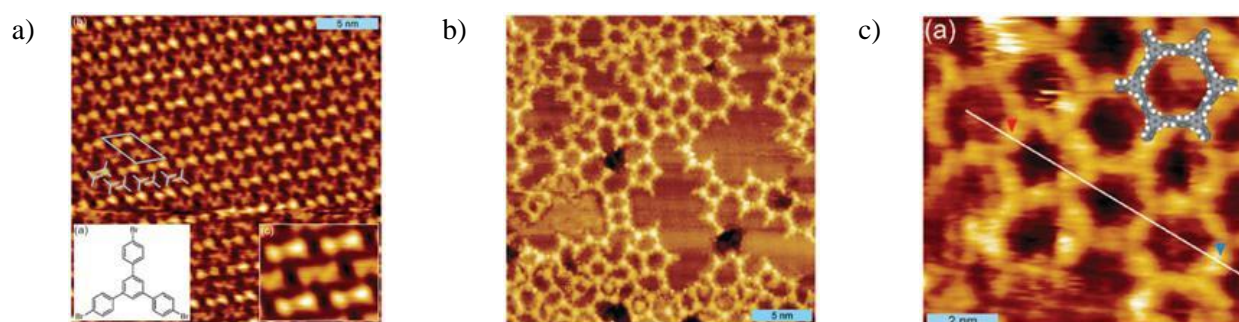


Figure 45: Structure of TBB under UHV on graphite (a), Cu(111) before (b) and after (c) annealing at 300°C

e. Van der Waals interactions

The van der Waals interactions mainly occur between alkyl chains; they are part of the weakest supramolecular interactions. However, the epitaxial adsorption on HOPG compensates the weakness, which results in relatively stable networks. The number and the length of the alkyl chains play an important role: numerous long chains lead to strong bonds between molecules because of the increase of interactions. Thus, the modification of these two parameters can directly impact on the stability of the network or completely change the self-assembly pattern.⁷⁴

The work of Xu *et al.* is a good example to illustrate this aspect. The (E,E,E)-1,3,5-tris[2-(3,4,5-trialkoxyphenyl)ethenyl]benzene **52** depicted in Figure 46 have been synthesised with different chains, deposited on surface in toluene and left to dry.⁷⁵ The STM studies were then performed at the air/HOPG interface.

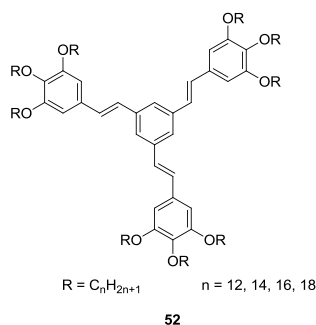


Figure 46: Structure of the (E,E,E)-1,3,5-tris[2-(3,4,5-trialkoxyphenyl)ethenyl]benzenes **52**

Several networks appeared, stabilised by interdigitation of the nine alkyl chains. As represented in Figure 47, the dodecyloxy derivative forms a honeycomb network (a) and the 14-carbons derivative self-assembles with the alkyl chain nearly parallel to each other (b). However, the 16-carbons network was not stable enough to procure an image of the assembly.

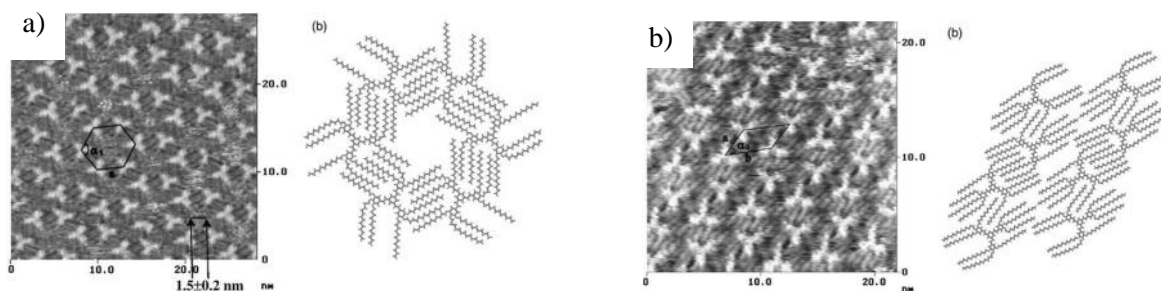


Figure 47: STM images of the self-assembly of (E,E,E)-1,3,5-tris[2-(3,4,5-trialkoxyphenyl)ethenyl]benzenes at the HOPG/phenyloctane interface, a) 12-carbons and b) 14 carbons derivatives (images of 28 x 28 nm)

The early work of Xu *et al.* was presenting different well-defined networks, but the self-assembly was only explained *a posteriori*.⁷⁵ In order to predict the adsorption pattern *a priori*, our group decided to design a new molecular unit acting as a functional linking group able to form strong surface-assisted intermolecular “clips”.⁷⁶ By interdigitation, this clip would strictly mimic the atomically precise organisation of *n*-alkanes on HOPG, as depicted in Figure 48.

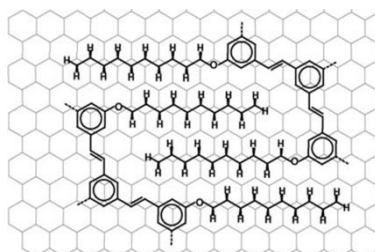


Figure 48: Clip design and principle

This figure shows one of the simplest clip structures using a π -conjugated bis-stilbene-like bridge. Based on these designs, the authors synthesised three molecules, displayed in Figure 49. Those compounds were functionalised with 1, 2 and 3 molecular clips. As proven by the STM images, the

three predicted self-assemblies were obtained on HOPG. The compound (a) was presenting a dimer-like structure, (b) was forming polymers and the last compound (c) was self-assembling as a supramolecular 2D-network (honeycomb) on surface.

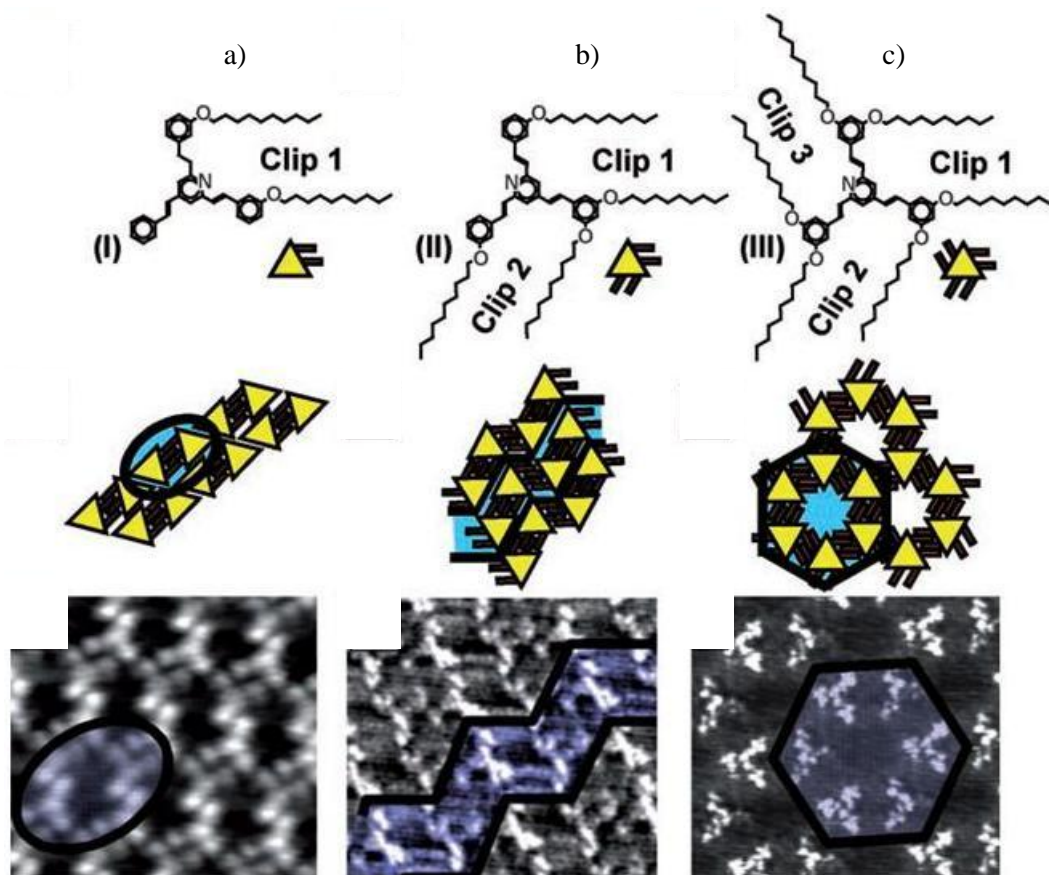


Figure 49: Realisation of dimer-, polymer- and 2D-network-like topologies from a given rigid core with 1 (a, $7.8 \times 7.3 \text{ nm}^2$), 2 (b, $8.1 \times 7.5 \text{ nm}^2$) and 3 clips (c, $8.9 \times 8.3 \text{ nm}^2$) at the HOPG/phenyloctane interface

Later on, the 10-carbons derivative **53** (Figure 50a) was later studied with only 6 alkyl chains in meta-positions by Schull and co-workers at the phenyloctane/HOPG interface.⁷⁷ It appeared that the honeycomb network was a good candidate in the design of host-guest materials. The network confined on surface may act as a sieve to molecule with the proper size. The cavity was 1.3 nm wide, thus for this study the coronene **54** (1 nm) and hexabenzocoronene **55** (1.3 nm) played the role of guest molecules. The STM images presenting the results are displayed in Figure 50.

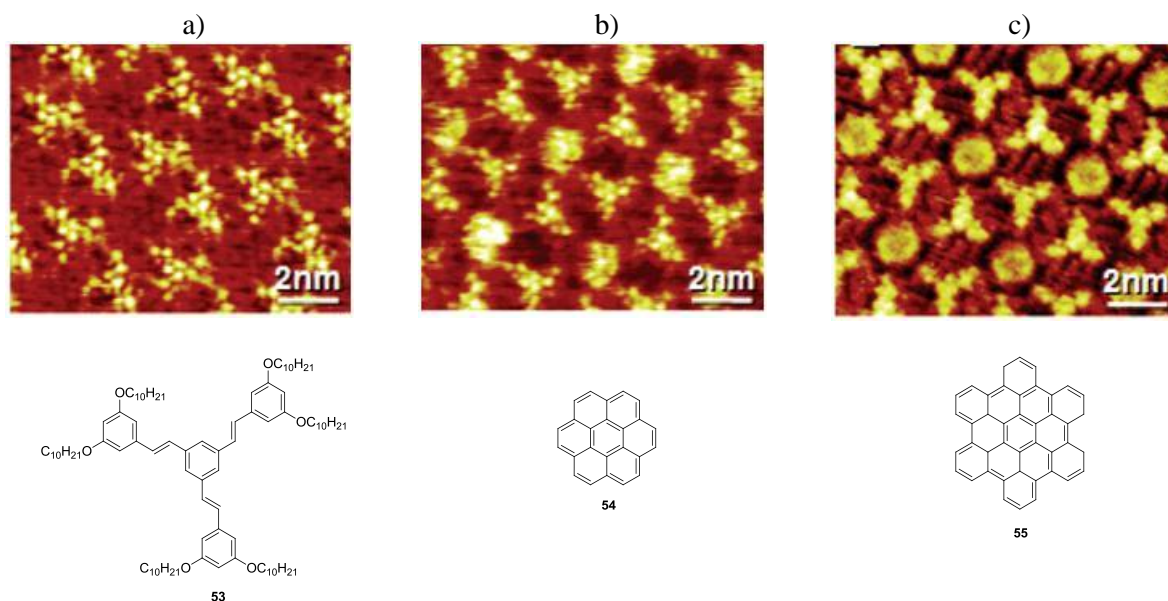


Figure 50: STM images of the host-guest study at the HOPG/phenyloctane interface. The empty honeycomb network (a) and with the guest molecules coronene (b) and hexabenzocoronene (c) are represented.

The efficiency of the molecular sieve is proven by the images above. In addition, the authors also studied the dynamics of the guest diffusion: it was possible to observe the hopping of the guests from one cavity to an empty adjacent one.

Whatever the method, many well-designed self-assemblies have been published, mainly using those five kinds of supramolecular interactions.

However, one problem was still remaining: by using semi-conducting or conducting substrates, charge-transfer and hybridisation between the molecules and the substrate might significantly alter the electronic properties of the adsorbed molecules. As a consequence, the fluorescence is generally quenched. To preserve the electronic properties, the molecule has to be decoupled from the substrate. This is achieved by “lifting” the molecule, as describe in the following part.

3. Decoupling molecules from the substrate

To recover and use the intrinsic electronic properties of an adsorbed entity, a degree of decoupling from the metallic surface must be performed. Indeed, a molecule adsorbed on a conductive or semi-conductive substrate will undergo a hybridisation of its molecular orbitals with those of the surface. As a consequence, in photonics any excited molecule is quickly deactivated by an energy-transfer process. Two electronic phenomena can thus occur: the Dexter⁷⁸ and the Förster⁷⁹ processes.

First, the Dexter energy-transfer follows an electron-transfer mechanism, as displayed in Figure 51. Considering two molecular entities **D** and **A** (**D**onor and **A**ceptor), the Dexter process can occur if the two molecules are close enough for their orbitals to overlap (up to 10 Å). In this case, when **D** is excited (**D***), the electron in the lowest unoccupied molecular orbital (LUMO) can go in **A**'s LUMO, while the reverse process occurs in the highest occupied molecular orbitals.

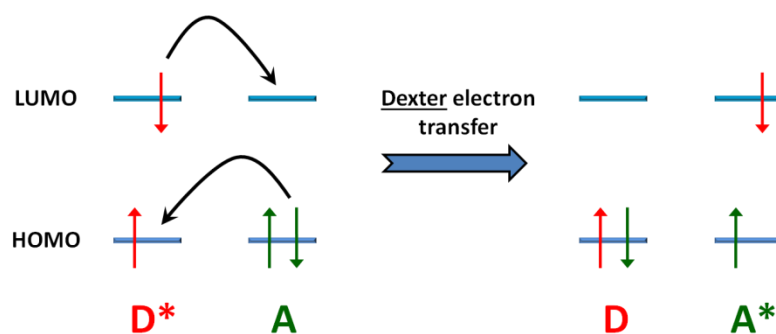


Figure 51: Mechanism of Dexter energy-transfer

In contrast, the Förster energy-transfer, also known as Förster resonance energy transfer (FRET), consists in a dipole-dipole interaction between the two entities **D*** and **A**, as represented in Figure 52. This phenomenon takes place at relatively long range (up to 100 Å) when the emission spectra of **D** overlap the absorption spectra of **A**. Moreover, as it is occurring by classical Coulombic interaction between the two molecules, there is no exchange of electrons: the electron in the LUMO of **D*** comes back in its HOMO while an electron in the HOMO of **A** is excited to its LUMO.

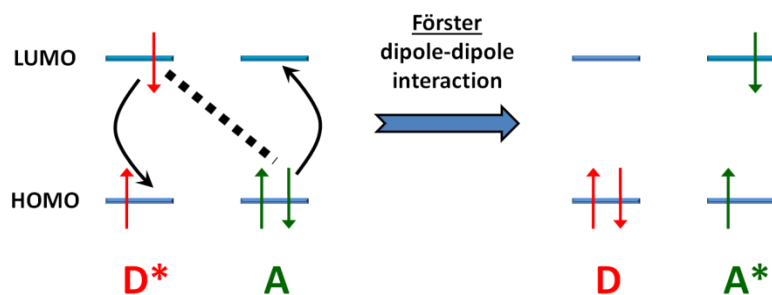


Figure 52: Mechanism of Förster energy-transfer

Those two processes are also viable on metallic surface when **D** corresponds to the adsorbed molecule with its HOMO and LUMO, and **A** to the substrate with its conduction and valence bands (separated by a band gap if semi-conducting). Then, the same mechanisms occur, as represented in Figure 53.

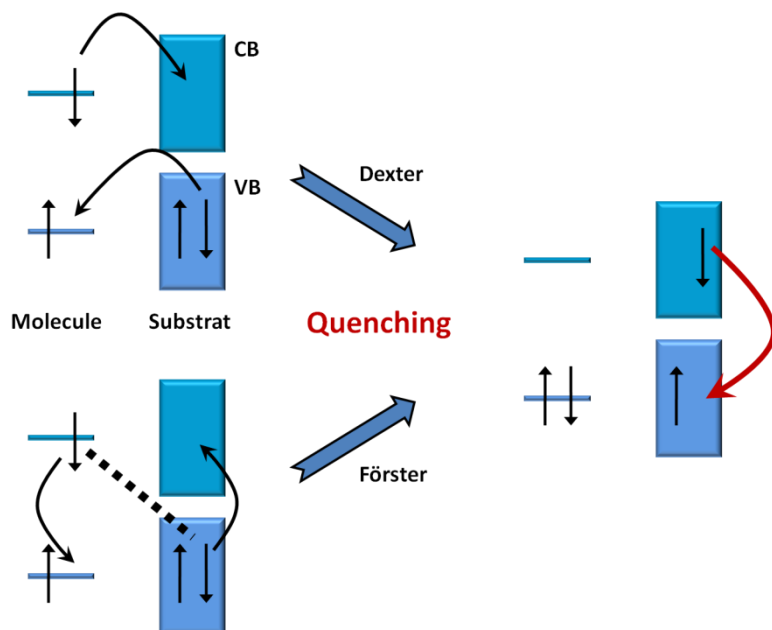


Figure 53: Mechanism of electronic quenching of molecules adsorbed on semi-conducting substrate (**CB**: conduction band, and **VB**: valence band)

Thus, in order to limit these quenching phenomena, the active molecule must be removed from the surface. Effective ways of decoupling have been studied by using multilayers of molecules, ultra-thin insulating layers onto the conducting surface or by chemically modifying the structure of the adsorbed molecule.

a. Multilayers

Insulating molecules from the substrate can be achieved by stacking them high enough for the decoupling to occur. Working on the nanocavity plasmons on Au(111), Dong and co-workers studied the luminescence induced by the STM tip on tetraphenylporphyrins **56** (depicted in Figure 54).⁸⁰ In this case, they had the role of spacer as much as emitter. The STM imaging was first used to monitor the layer-by-layer growth of molecules on the surface. When the stacks had reached 5 layers high, the STM induced luminescence was possible on the well-decoupled top layer, as represented in Figure 54. This method demands expensive apparatus and delicate STM manipulations, but is proven to be effective.

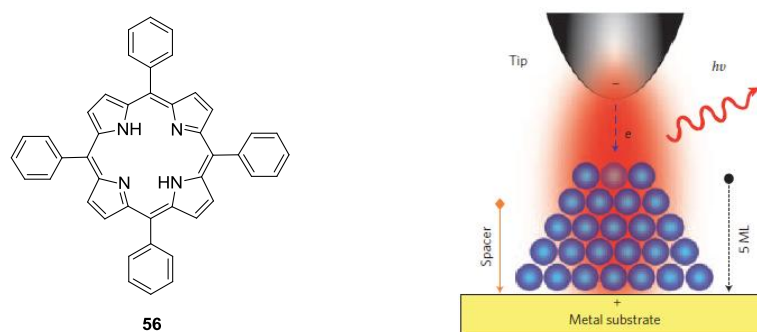


Figure 54: Representation of the tetraphenylporphyrins **56** molecular structure and the schematic of the multilayers stacking under the STM tip

b. Ultra-thin insulating layers

Another way to decouple molecules from surfaces is by using ultra-thin insulating layers deposited on the metallic substrate. A thickness of just a few atomic layer provide sufficient electronic decoupling of the molecules and at the same time still allows the electron to tunnel through, and thus to image by STM. Several examples exist in the literature, like alumina film on NiAl(110)⁸¹ or NaCl on Cu(100) and Cu(111)⁸². This last example perfectly represents the efficiency of the insulating layer. Repp *et al.* were studying the thickness of this layer by imaging pentacene **57** represented in Figure 55a. The experiments were carried on under UHV at 5 K. The NaCl was thermally evaporated to form islands of (100)-terminated NaCl of up to three atomic layers. The pentacene was adsorbed, and the imaging by STM was possible (Figure 55b).

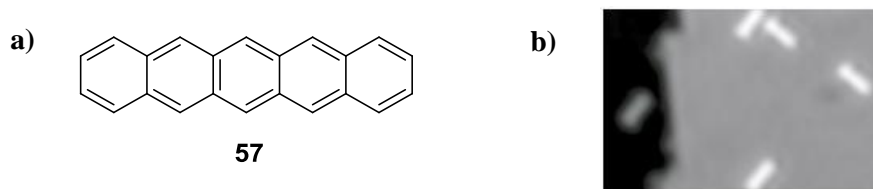


Figure 55: Representation of the pentacene structure and its STM image on NaCl/Cu(111)

One again, this technique requires high cost apparatus, and very good manipulation skills of the microscope. However, the results may be worth it: by picking up a molecule with the tip, they could even use this pentacene-tip to image the HOMO and LUMO of other pentacenes on the surface with very high resolution, as described in Figure 56.

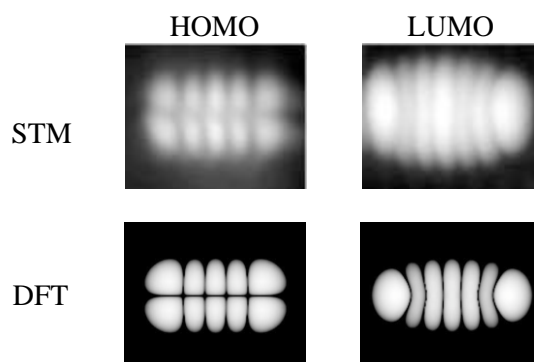


Figure 56: HOMO and LUMO of pentacene observed by STM with a pentacene-tip and calculated by DFT.

c. Spacers part of the molecule's structure

The two first techniques were isolating the active molecules by tuning the parameters of the experiments. This third method aims to chemically modify the active molecule to lift up the active moiety. Several pathways are possible; for example by attaching a bulky group to the molecule, working with a tripodal motif or by using a pillar such as a paracyclophane.

i. *Bulky groups*

Comstock and co-workers wanted to observe the photoisomerisation of azobenzene on Au(111). As for any electronic property, the isomerisation could not occur with the molecule directly in contact with the metallic surface, thus the authors proposed to graft four *tert*-butyl groups on the molecule, as depicted in Figure 57.

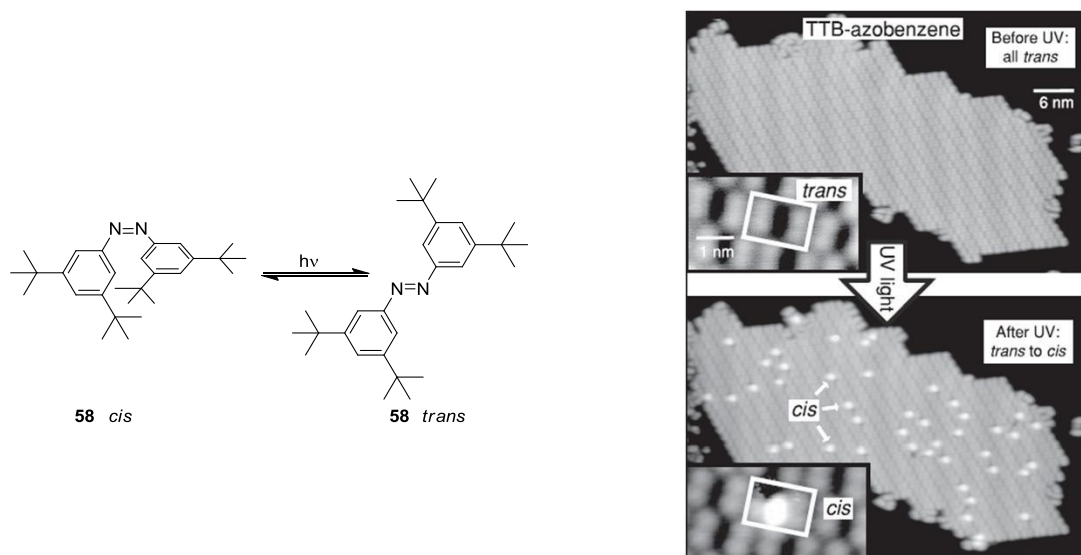


Figure 57: Photoisomerisation of 3,3',5,5'-tetra-*tert*-butyl-azobenzene **58**: chemical process observe on Au(111) at 30 K

The sublimation of the azobenzene derivative **58** on the surface led to islands uniformly composed of the planar *trans* isomer. Upon illumination with UV-light, several molecules underwent the photoisomerisation. As a consequence, the non-planar *cis* compound emerged from the plan, easily identified by bright dots observed under STM, thus proving the efficiency of the decoupling with the surface.

ii. Tripodal motif

This method has been first described for chemisorption by using thiol groups on gold surface⁸³ but Mann *et al.* adapted it to the physisorption pathway on graphene by grafting pyrene feet to the structure, as represented in Figure 58.⁸⁴ The self-assembly was not characterised by STM imaging, but by cyclic voltammetry; the adsorption on a graphene electrode was verified by the effective oxidation/reduction process of the cobalt complex.

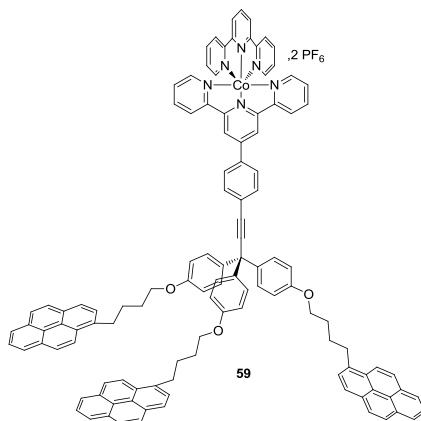


Figure 58: Lift up the active moiety by means of a tripodal architecture

iii. Cyclophane-based pillar

Following the work of the molecular clip, a new kind of three-dimensional molecule was recently proposed by our group: the “Janus tecton”. This molecule is doubly functionalised, exposing two faces linked by a cyclophane-based rigid spacer. One side of this cyclophane derivative is acting like a pedestal and substituted with molecular clips to allow the self-assembly on surface. The other side is supporting the desired active moiety, like a fluorophore (**60**)¹⁰ or a coordinating function (**61**)⁸⁵, as depicted in Figure 59. This molecular design permits the active component to be free from any Dexter energy-transfer process by grafting it far enough from the surface. As the Förster resonance is a long-range process, it is required to finely tune the absorption of our pedestal and the emission of the active moiety in order to avoid the overlapping of the spectra.

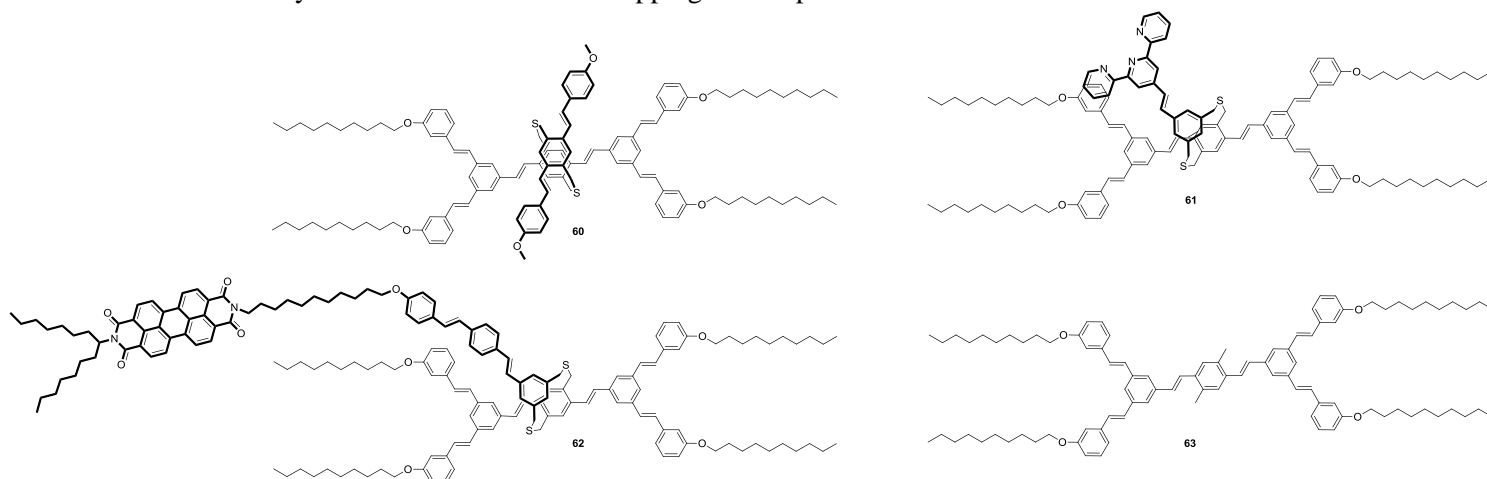


Figure 59: Molecular structures of several Janus tectons **60**, **61**, **62** and the pedestal **63**

A good example of Janus tecton was recently published by Le Liepvre *et al.*, where the fluorophore was a 3,4,9,10-perylenetetracarboxylic diimide (PTCDI), and the substrate was graphene.⁸⁶ The

structure **62** is displayed in Figure 59, with the pedestal **63** (cyclophane-free molecule) on the right. The self-assembly was performed by co-adsorbing the Janus tecton with the pedestal at different ratios. The images displayed in Figure 60 show the evolution of the pattern while the concentration of Janus tecton was increased compared with the pedestal.

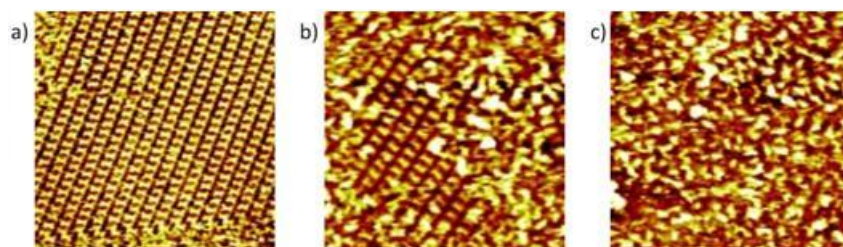


Figure 60: STM images at the liquid/HOPG interface at room temperature. First a 1:4 mixture of Janus tecton and pedestal molecule (60 x 60 nm) (a), then a mixture 1:1 (50 x 50 nm) (b) and finally a pure solution of Janus tecton (50 x 50 nm) (c).

The long alkyl chain linked to the PTCDI allowed a high degree of mobility; thus the molecule tended to move quickly in solution and to aggregate. As a consequence, the photoluminescence studies described the system as mainly aggregated. Nevertheless, the “graphene-dye” hybrid system was emitting light, as proven by the emission spectra displayed in Figure 61.

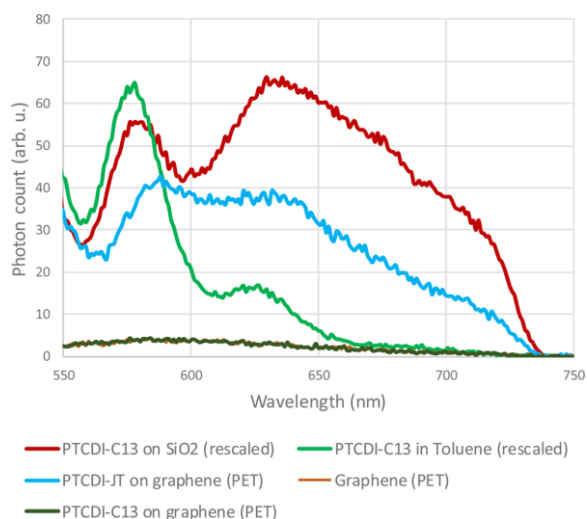


Figure 61: Emission spectra of the self-assembled PTCDI-based Janus tecton (PTCDI-JT) on graphene (blue), compared to the reference compound PTCDI-C13 also on graphene (dark green), in toluene (light green) and at the solid state on SiO₂ (red).

In this figure, the blue spectrum represents the emission of the surface functionalised by the PTCDI-based Janus tectons. This spectrum presents an emission relatively similar to that observed with the reference compound PTCDI-C13 on SiO₂ or in toluene (red and light green spectra). The fluorophore was thus partially emitting, which proves the efficiency of the Janus tecton concept.

III. Thermally Activated Delayed Fluorescence

In the field of organic electronics, the development of highly efficient organic light-emitting diodes (OLED) is one of the trending topics. Recently, a new type of compounds has permitted to drastically enhance the electrically-induced fluorescence efficiency of OLEDs (from 5% to 25% of theoretical external quantum yield). Indeed, the molecular structure of these compounds allows the phenomenon called thermally activated delayed fluorescence (TADF) to occur. Thus in this part, the electroluminescence principle in an OLED will be first describe in order to explain more accurately the changes brought by the TADF mechanism within precisely designed molecules.¹²

A. Organic electroluminescence

The electroluminescence phenomenon was first observed in organic materials by Helfrich and Schneider in 1965 when they applied a high voltage (up to 1000 V) to a 5-millimeter-thick anthracene single-crystal and observed fluorescence.⁸⁷ Despite the great importance of the discovery, the applications were scarce: the difficulties of crystal-growth as well as the large bias necessary were two limiting factor for macroscale development. Later on, Tang and van Slyke bypassed these limitations by making a device by vapor deposition of 8-hydroxyquinoline aluminum (Alq_3) and detected fluorescence at low bias (2.5 V).¹¹ From this point, the concept of OLED started to attract much attention because of their potential lighting applications.

1. Principle of luminescence

The luminescence process can be described as a radiation emitted by a material after absorption of the necessary energy to go to an excited state. Two radiative pathways can be responsible for such emission: the fluorescence and the phosphorescence. The mechanisms of excitation/emission are displayed in the Jablonski diagram⁸⁸ represented in Figure 62.

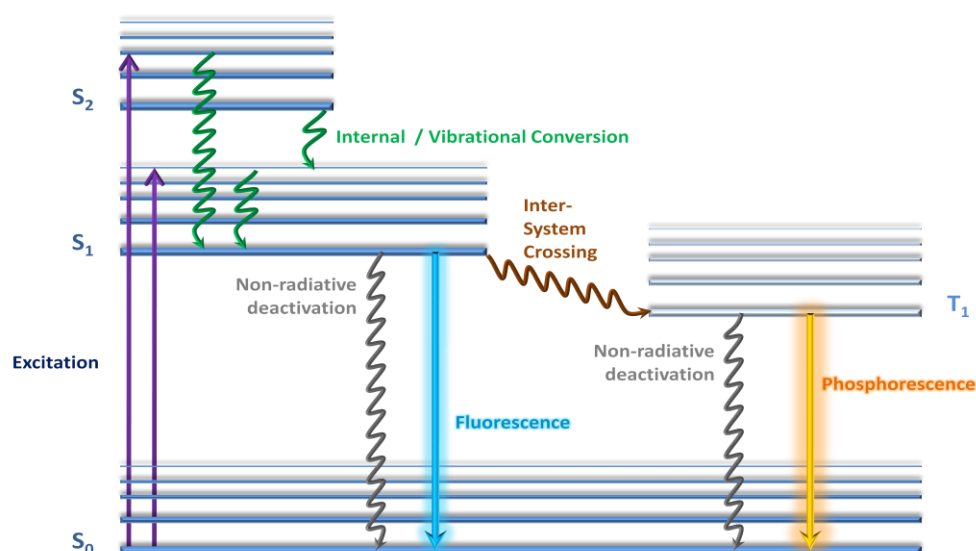


Figure 62: Jablonski diagram of luminescence phenomena

This figure presents the different electronic states of a molecule, each one of them degenerated into several vibrational states. When the molecule undergoes the excitation process, an electron leaves the ground state S_0 to reach the excited singlet state S_1 . The excited electron will then experience several

relaxation processes towards the lower vibrational state of S_1 . From there, several actions can occur. If the electron goes back to the ground state, it can do so *via* a non-radiative way (thermal relaxation), or by emitting a photon *i.e.* by fluorescence. It is also possible for an electron to jump from the singlet to the triplet state T_1 by means of a conversion process named intersystem crossing. From this triplet state, the electron relaxes toward the lowest energy level of T_1 and then either non-radiative deactivation or phosphorescence occurs.

The fluorescence phenomenon have been studied for more than a hundred years, thus a tremendous amount of examples have been discovered. Using photoexcitation, the efficiency of each compound could be determined by the photoluminescence quantum yield (PLQY), which corresponds to the ratio of the number of emitted photons over the number of absorbed photons. At room temperature, PLQYs up to 100% were often measured for fluorescent compounds.⁸⁹

2. Limitations in OLED materials

a. Fluorescence-based OLED

The electroluminescence phenomenon was first observed in organic materials by Helfrich and Schneider in 1965 when they applied a high voltage (up to 1000 V) to a 5-millimeter-thick anthracene single-crystal and observed fluorescence.⁹⁰ Despite the great importance of the discovery, the applications were scarce: the difficulties of crystal-growth as well as the large bias necessary were two limiting factor for macroscale development. Later on, Tang and van Slyke bypassed these limitations by making a device by vapor deposition of 8-hydroxyquinoline aluminum (Alq_3) and detected fluorescence at low bias (2.5 V).¹¹ Shortly thereafter, Friend *et al.* developed a single-layer polymer electroluminescent device represented in Figure 63.¹² From this point, the concept of OLED started to attract much attention because of their potential lighting applications.

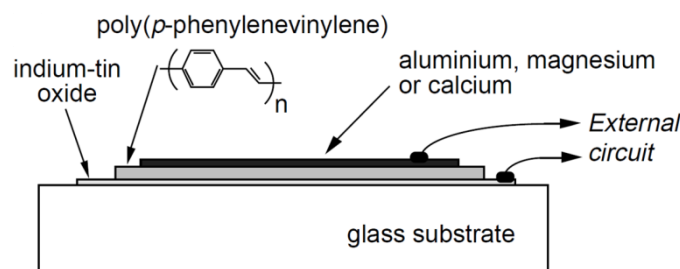


Figure 63: Single-layer polymer electroluminescent device developed by Friend *et al.*⁹¹

Nevertheless, a compound used within an OLED is electrically excited. The charges are injected from the anode and cathode to form polarons. These species migrate through the device in order to meet and then to form the exciton which is able to perform the recombination and thus to emit light. In the device (Figure 64), additional layers are usually incorporated in order to facilitate the injection and the movement of the polarons towards the emitting layer. Thus, the efficiency of the chromophore resides in its ability to effectively recombine the exciton species.⁹²

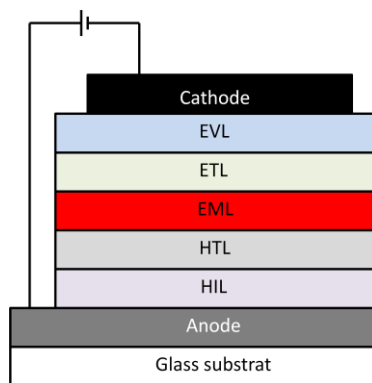


Figure 64 : A typical structure of OLEDs

In such multi-layer structure, the various layers play different key roles. Apart from cathode and anode which inject holes and electrons, the hole injection layer (HIL) and the hole transport layer (HTL) assist the transport of holes from the anode to the emission layer (EML). From the cathode, the electron injection layer (EVL) and the electron transport layer (ETL) are responsible of the transport of electron to the same emission layer. The ideal OLED should transport the polarons (holes and electrons) at the same “speed” in order to quickly recombine the excitons in the EML and thus to maximise the efficiency of the device.

Now, it is necessary to take into account the nature of the spin of both polarons before recombination. It will define the multiplicity of the exciton, and thus determine if the emission will occur from the singlet or the triplet state. Due to the spin statistics represented in Figure 65, the resulting recombination shall potentially emit 25% of fluorescence and 75% of phosphorescence.

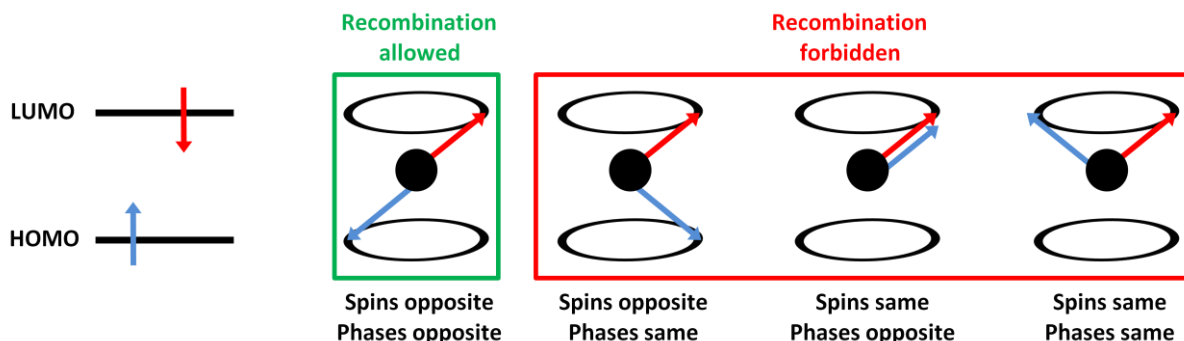


Figure 65 : Spin statistics: the recombinations occur with spins and phases in two potential directions, thus 4 excitons are possible, 1 singlet and 3 triplets

Apart from the spin of the excited state, the light out-coupling efficiency tends to reduce the performance of the device.⁹³ The external quantum efficiency (EQE) of an fluorescence-based OLED can be determined as:

$$EQE = \chi_F \Phi_F \eta_r \eta_e \leq \frac{1}{4} \times 1 \times 1 \times \frac{1}{2n^2}$$

where χ_F is the fraction of recombination that results in singlet excitons, Φ_F represents the intrinsic fluorescence efficiency, η_r is the fraction of polarons that recombines in the emissive layer and η_e corresponds to the light out-coupling efficiency. Thus, as mentioned before, the spin statistics give χ_F as only 25% for fluorescence, and internal quantum yield Φ_F can easily reach 100% for the best molecules. Moreover, considering the advances in the OLED development, the recombination can be ideally performed in the emissive layer with the highest yield of 100%. Finally, the out-coupling efficiency η_e is the fraction of emitted photons that escapes the device. Hence it is limited by the

internal reflexion of the photons and thus is dependent of the reflexion index of the emissive layer. For a glass substrate, the index of reflexion is around $n = 1,5$ which limit the fraction of escaping photons to only 22%. As a consequence, a fluorescence-based and a phosphorescence-based OLED would be limited to 5.5% and 22% respectively of external quantum efficiency.

Fluorescence is still the most used process to achieve suitable OLED because of the high stability of the materials over time and temperature. Every colour has been obtained from fluorescent devices: blue⁹⁴, green⁹⁵, and red⁹⁶ are now achieved with acceptable external quantum efficiency. As a consequence, new devices are nowadays commercialised, based on the concept of OLED.¹³ Examples of emitters are depicted in Figure 66.

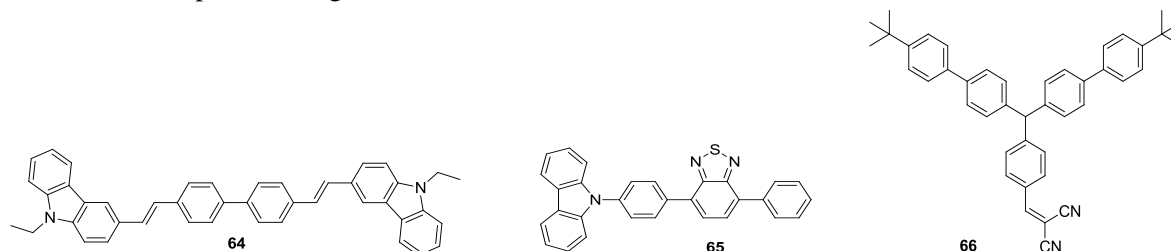


Figure 66 : Molecular structure of blue **64**, green **65** and red emitter **66**

Pure fluorescence-based OLED were widely developed because of their low costs but, apart from exceptions, they are still inconveniently limited around 5 to 6% of EQE.

b. Phosphorescence-based OLED

In contrast with fluorescence, the phosphorescence phenomenon at room temperature was rarely measured because the non-radiative deactivation from the triplet excited state to the singlet ground state becomes dominant by increasing the temperature.⁹⁷ However, by using the intersystem crossing to harvest the 25% of singlet excitons, several organometallic complexes have presented high yield phosphorescence near 100%.¹⁴ As a consequence, phosphorescent-based OLEDs (or PHOLED) can theoretically achieve high EQE near 25%.

The first PHOLED was developed by Suzuki *et al.* by using benzophenone.⁹⁸ The device was only active at low temperature (100 K) but it was a good proof of concept. Later on, Baldo and co-workers published their work on 2,3,7,8,12,13,17,18-octaethyl-21H,23H-porphine platinum **67**.⁹⁹ At room temperature, the device was emitting red light with an EQE of 23% which was a great improvement of efficiency. However, several inconveniences were mentioned, especially the too long life time of emission ($> 10 \mu s$) making the device unsuitable for potential applications. Thereafter, several other materials have been described, mainly presenting iridium complexes like Ir(ppy)₃ **68**, represented in Figure 67.¹⁰⁰

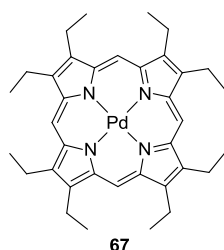


Figure 67 : Structure of phosphorescent platinum- and iridium-based complexes

With these complexes, very high EQE were obtained (up to 19%) with life-time of emission down to 1 μ s. However, there were two main issues in the direct application of PHOLEDs: the relatively short life-time of the device, and the high cost of the emitter based on noble and expensive metals.

As a consequence, combining the high stability of the fluorescence-based OLED and the excellent efficiency of the PHOLED is one of the most studied research topic. Recently, a new type of compounds has been proposed where several finely design molecules have presented delayed emission *via* thermally activated delayed fluorescence (TADF).

B. Thermally Activated Delayed Fluorescence

During the process of electroluminescence, 75% of the excitons are lost in non-radiative processes from the triplet to the ground state. The thermally activated delayed fluorescence is a process harvesting these 75% of triplet exciton in order to convert them into singlets, and thus enhancing the fluorescence towards higher yield.

1. First results

Despite the drastic increase of articles published on TADF molecules for the past 10 years, this “new” pathway toward high-yield fluorescence has been known for more than 70 years. In 1941, Lewis *et al.* have published their study of two different phosphorescence states of fluorescein **69** in boric acid glass.¹⁰¹

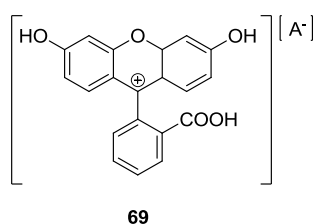


Figure 68 : Fluorescein structure in acid solution

Fluorescein dissolved in acid solutions, as represented in Figure 68, emits strong blue fluorescence at room temperature and pure yellow phosphorescence at low temperature. However, as displayed in Figure 69, the phosphorescence spectrum showed a first strong blue band at room temperature (α band, lifetime $\tau_\alpha = 4$ s) upon which is superimposed a fainter yellow band (β band, lifetime $\tau_\beta = 11$ s). By lowering the temperature, the α band disappears to the benefit of the β band which remains stronger.

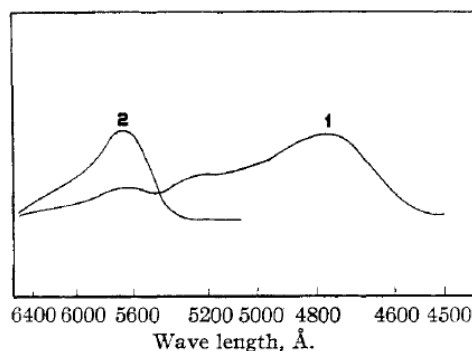


Figure 69: Emission spectra of fluorescein in boric acid depending of the temperature: **1** at 20°C (fluorescence) and **2** at -40°C (phosphorescence)

Using the at-the-time controversial Jablonski diagram, Lewis explained the mechanism of this delayed blue fluorescence by a round trip of the excited electrons from the *fluorescence state* (singlet state) to the *phosphorescence state* (triplet state), whereas the yellow band was attributed to the classic phosphorescence (from the triplet state to the ground state).

The pioneering work of Lewis *et al.* on their long-lived luminescence allowed a better understanding of the phenomenon of delayed fluorescence. However, the first breakthrough only occurred in the 1960s, with Parker and Hatchard's work on eosin, represented below in Figure 70, in glycerol and ethanol.¹⁰²

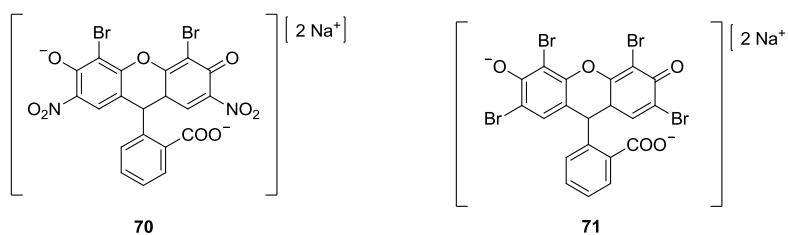


Figure 70 : Structure of Eosin B **70** and Eosin Y **71**, as disodium salts (the type of eosin chosen for the study is not mentioned in the article)

Parker *et al.* have accurately described the unusual long-lived fluorescence of eosin in glycerol and ethanol. The spectra of luminescence were first measured at several temperatures ranging from -70°C to $+70^{\circ}\text{C}$ to prove the presence of a delayed fluorescence: the fluorescence band increases with temperature whereas the phosphorescent band decreases, with a photoluminescence quantum yield up to 87% in ethanol. So, by using a high sensitivity spectrophosphorimeter, Parker *et al.* were the first to describe the parameters of the TADF phenomenon by proving the existence of a reverse intersystem crossing from the triplet state to the singlet state.

Continuing their work on delayed luminescence, Parker and co-workers published several articles on other molecules.^{103,104} The study of aromatic compounds, especially pyrene, has surprisingly shown a different mechanism of delayed fluorescence.¹⁰⁵ When two molecules were excited to the triplet state, a mechanism of “triplet-triplet quenching” was occurring, leading to an excited dimer which dissociated rapidly into excited and ground-state singlet molecules; the excited molecules being responsible for the delayed fluorescence.

In order to make a clear distinction between those two long-live fluorescences, Parker *et al.* have chosen to name these phenomena eosin-type (E-type) delayed fluorescence and pyrene-type (P-type) delayed fluorescence now known as TADF (Thermally Activated Delayed Fluorescence)¹⁰⁶ and TTA (Triplet-Triplet Annihilation)¹⁰⁷ respectively.

Over the years, several examples of TADF molecules have been published: benzyl¹⁰⁸, benzophenones¹⁰⁹, thiones¹¹⁰, fullerene¹¹¹,... However, the properties of delayed fluorescence were still determined *a posteriori*. Thus, the development of TADF-based device required the implementation of rules and methods to design such materials.

2. Description of the TADF phenomenon

Nowadays, the mechanism of thermally activated delayed fluorescence is well established: as represented in Figure 71, an electron is excited from the ground state to the singlet excited state and then undergoes the intersystem crossing toward the triplet state. However, instead of deactivating

through non-radiative or phosphorescence processes, the electron goes back to the singlet state by means of a reverse intersystem crossing, and finally emits fluorescence in order to reach the ground singlet state.

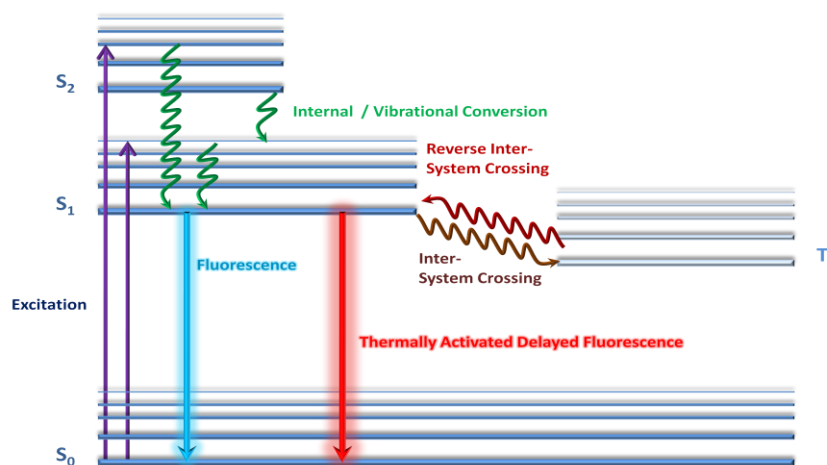


Figure 71 : Simplified energy diagram of the TADF process

Accordingly, as part of an OLED, this mechanism should theoretically allow a molecule to harvest the triplet excitons in order to reach 100% of internal quantum efficiency only with fluorescence. This concept has been first proven by Endo *et al.* in 2009, by incorporating a Sn^{IV} -porphyrin complex **72** (Figure 72a) as emitting layer of an OLED.¹¹² Shortly afterwards in 2010, Deaton *et al.* confirmed the high potential of this new emitting pathway by using a Cu^{I} -complex **73** (Figure 72) to obtain a very efficient OLED with an EQE of 16,1%.¹¹³

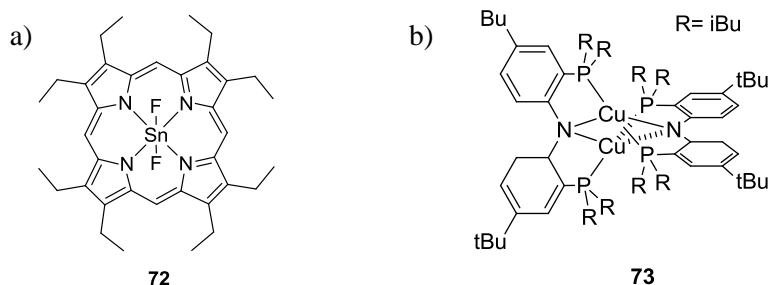


Figure 72 : Representation of the molecular structures of the first two TADF complexes part of OLED: the Sn^{IV} -porphyrin complex of Endo **72** and the Cu^{I} -complex of Deaton **73**

Nonetheless, equal or better performances were already achieved with organometallic materials in PHOLEDs. The significant breakthrough on TADF really occurred when Endo and co-workers published their new OLED based on pure organic materials with an external quantum efficiency of 5,3%, approaching the theoretical limitation of conventional fluorescent devices.¹¹⁴

Despite the low EQE compared with the best PHOLEDs, these results allowed to establish the first rules to obtain TADF properties. On one hand, the gap between singlet and triplet energy levels, so called ΔE_{ST} , has to be as small as possible. One way to achieve this is to reduce the overlap of the highest occupied molecular orbital (HOMO) and the lowest unoccupied molecular orbital (LUMO), thus to separate electron-donating from electron-accepting substituents on the molecule. In contrast, the fluorescence rate must be kept as high as possible by maintaining the whole conjugation effective within the molecule. Because these parameters are conflicting, fine molecular design is required to realise them simultaneously.

The first route to match those two parameters was to induce one or several twists of the molecular structure in order to interrupt the conjugation between donor and acceptor group. For example, Uoyama *et al.* designed and synthesised a series of carbazolyl dicyanobenzene derivatives, the most efficient being the 4CzIPN represented in Figure 73.¹⁶

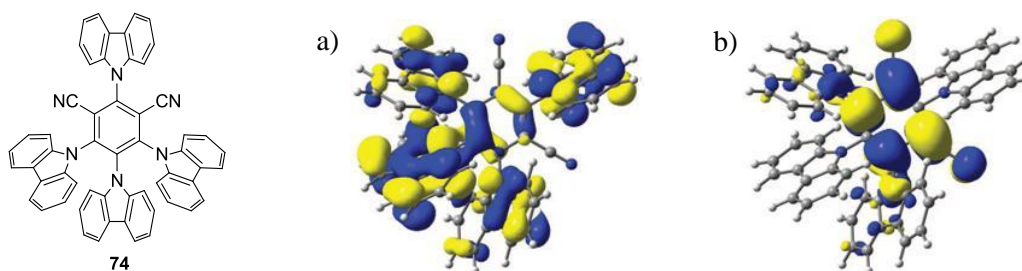


Figure 73 : Molecular structure of 4CzIPN **74** and representation of its highest occupied a) and lowest unoccupied b) natural transition orbitals

In the molecular structure, the electron-donating substituents (carbazol groups) were too bulky to remain plan, thus a twist is induced and the HOMO and LUMO are separated from one another. The DFT calculations of the highest occupied and lowest unoccupied natural transition orbitals¹¹⁵ performed on 4CzIPN were confirming the partial decoupling, as represented in Figure 73 (a and b).

A natural transition orbital analysis is an efficient way to correlate ground and excited state electronic structures *via* diagonalisation of the transition density matrix. In other words, the analysis permits to create unique particle-hole pairs which show where in the system the electron came from and where it went to as a result of the transition.

A small ΔE_{ST} was thus obtained for 4CzIPN (0.27 eV) with a PLQY of 94%. An EQE of 19.3% was measured, which corresponded to the best efficiency of a pure organic-based OLED (metal free).

Numerous examples of twisted TADF molecules have been published showing efficient results. However, another route to separate the HOMO from the LUMO was also recently studied by Nakagawa *et al.*: instead of twisting the donor-acceptor connection, they proposed to physically separate them by means of a spirobifluorene unit.¹⁷ As a consequence, the weak coupling between the electron-donating and electron-accepting groups was mainly due to through-space interactions.

Their best results were obtained by studying the Spiro-CN **75** which is represented in Figure 74 along with the DFT calculations results on the HOMO and LUMO.

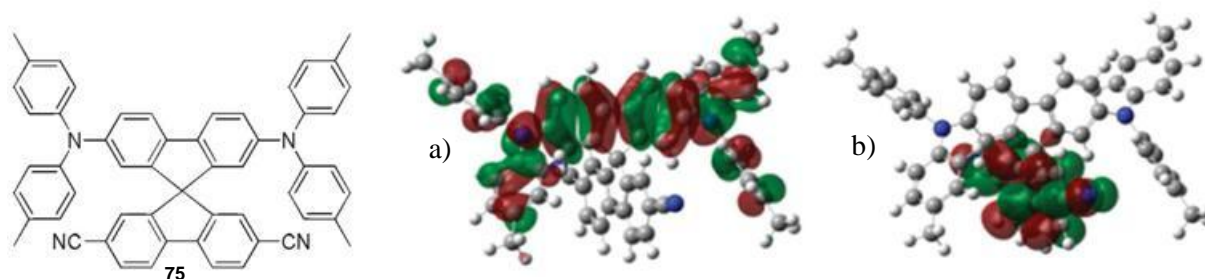


Figure 74 : Molecular structure of Spiro-CN **75** and representation of its highest occupied (a) and lowest unoccupied (b) molecular orbital

A ΔE_{ST} value of 57 meV was calculated and the photoluminescence quantum yield measured at 27%. Finally, with values up to 4.4%, the EQE was largely exceeding the highest EQE values for common fluorescence-type materials with a PL efficiency of 27%.

In conclusion, two effective methods have been proposed to obtain TADF properties from an organic molecule. The twist has allowed to reach high PLQY results whereas the through-space pathway was more efficient in lowering the ΔE_{ST} . Both have presented interesting results, and TADF materials are now catching up with the PHOLEDs efficiencies. However, the research is still focusing on materials with higher quantum yield of fluorescence. As a consequence, new concepts are currently developed in order to facilitate the commercialisation of TADF materials.

3. Extension of the TADF concept

As mentioned above, new materials are always investigated in order to develop further applications of the TADF concept. Indeed, two main research topics have emerged to simplify the potential manufacture of highly efficient OLED. The first method consists in using TADF molecules as dopant of a conventional fluorescent molecule of an OLED in order to transfer the high yield fluorescence to a less efficient emitter. A second pathway aims at synthesising TADF-based polymers which might facilitate the making of devices.

a. TADF materials as dopant

The development of TADF emitters requires a fine tuning of the molecular design in order to obtain high PLQY and low ΔE_{ST} . However, these two parameters are always in conflict, making it difficult to develop high-performance materials. In contrast, various conventional fluorescent molecules with high PLQY are well known to emit light in most of the light spectrum, but are limited by their performance in OLEDs.

Recently, Nakanotani *et al.* proposed a method to enhance conventional fluorescent emitters by using the TADF molecules as assistant dopant of the emitting layer of an OLED.¹¹⁶ As described in Figure 75, the emitting molecule is thus allowed to harvest by Förster process (FRET) the singlet excitons recovered by the TADF mechanism of the dopant, and then to emit fluorescence in high yield.

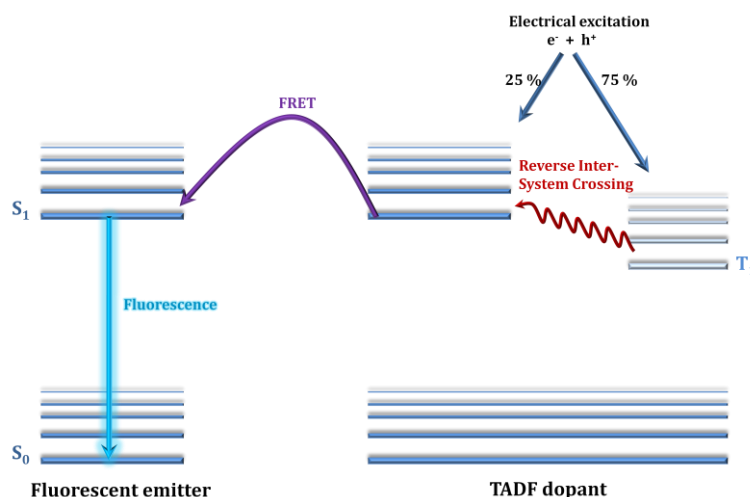


Figure 75: Representation of the Förster process between the TADF dopant and the fluorescent emitter

With this approach, it is thus possible to separately increase the PLQY of the conventional fluorophore and to reduce the ΔE_{ST} of the TADF molecule without any conflicting effects. Moreover, allowing the use of conventional fluorescent molecules drastically expand the panel of available emitters. The authors were then able to develop an OLED based on the TADF molecules **76** and on the emitter **77**, represented in Figure 76. In this figure, the absorption and emission spectrum of the different actors of the emission are also represented.

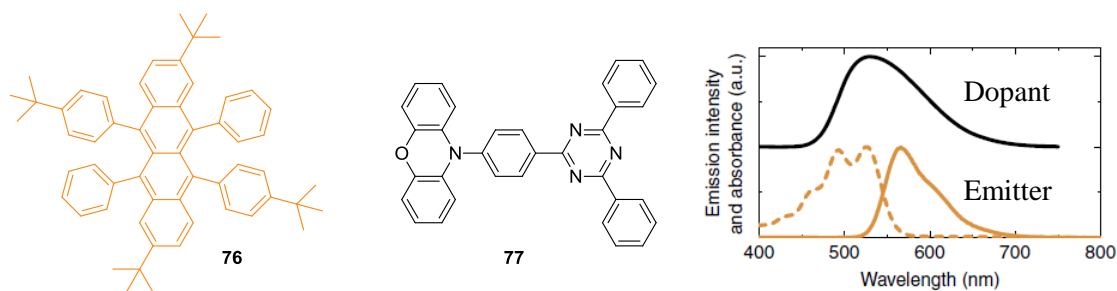


Figure 76: Molecular structures of **76** and **77**, and their absorption/emission spectra

The emitter **77** displays a PLQY of 86% whereas **76** presents a ΔE_{ST} of 0.071 eV. Moreover, the spectra represented in Figure 76 show the overlap of the absorption spectrum of **77** and the emission spectrum of **76**. Thus, the FRET mechanism could take place and the device was built up to afford an EQE of 18 %.

As a conclusion, this pathway allows the use of a large range of conventional fluorophores and still conserves the TADF efficiency. However, some defects of the electronic mechanism can be mentioned: the direct fluorescence of the TADF dopant, and the transfer of the triplet exciton to the emitter by Dexter energy-transfer leading to non-radiative deactivation.

b. Polymer-based TADF materials

Numerous efficient TADF-based fluorophores have recently been published: blue¹¹⁷, green¹¹⁸ and red¹¹⁹ emitters are now obtained with good EQE, respectively 19.5%, 28.5% and 12.5 %. However, the manufacture of such devices requires high cost evaporated deposition process and results in disordered structures. So, to get around this limitation, Luo *et al.* proposed to design a TADF-based polymer.¹²⁰ Indeed, such polymer would permit the use of simpler and cheaper solution-deposition process. Therefore, the authors decided to graft a TADF-emitter onto the side chain of a poly-carbazol as represented in Figure 77.

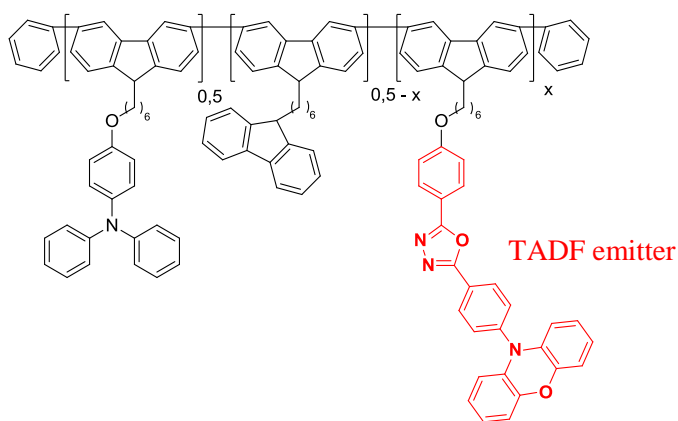


Figure 77: Molecular structure of the TADF-based polymer of Luo *et al.*

The polymer was synthesised by Suzuki cross-coupling, and a PLQY of 33.7% was determined. The polymer light emitting diode (PLED) was made by solution-process deposition and achieved a good EQE of 4.3%. To conclude, the general design strategy to achieve high EQE have been successful, considering the low PLQY measured. Moreover, this new pathway towards TADF-based devices can open access to other solution process depositions, such as the very efficient roll-to-roll process.¹²¹

- ¹⁸ Cram, D. J.; Steinberg, H. *J. Am. Chem. Soc.* **1951**, *73*, 5691–5704.
- ¹⁹ Keehn, P. M.; Rosenfeld, S. M., *Cyclophanes* **1983**, 45-I, Chapt. 3.
- ²⁰ Lide, D. R., *Handbook of Chemistry & Physics* (76th ed.) 1995-1996, p 9-2.
- ²¹ Cahn, R. S.; Ingold, C.; Prelog, V. *Angew. Chemie Int. Ed.* **1966**, *5*, 385–415.
- ²² Reich, H. J.; Cram, D. J. *J. Am. Chem. Soc.* **1969**, *91*, 3527–3533.
- ²³ El-Hewehi, Z.; Runge, F. *J. Prakt. Chem.* **1959**, *9*, 33–42.
- ²⁴ Millar, I. T.; Wilson, K. V. *J. Chem. Soc.* **1964**, 2121–2127.
- ²⁵ Brink, M. *Synthesis (Stuttg.)* **1975**, *12*, 807–808.
- ²⁶ Iwama, A.; Toyoda, T.; Yoshida, M.; Otsubo, T.; Sakata, Y.; Misumi, S. *Bull. Chem. Soc. Jpn.* **1978**, *51*, 2988–2994.
- ²⁷ Tanaka, K.; Hori, T.; Osaka, T.; Noguchi, K.; Hirano, M. *Org. Lett.* **2007**, *9*, 4881–4884.
- ²⁸ Wang, W.; Xu, J.; Lai, Y. H. *Org. Lett.* **2003**, *5*, 2765–2768.
- ²⁹ Noyori, R.; Takaya, H. *Acc. Chem. Res.* **1990**, *23*, 345–350.
- ³⁰ Rossen, K.; Pye, P. J.; Maliakal, A.; Volante, R. P. *J. Org. Chem.* **1997**, *62*, 6462–6463.
- ³¹ Pye, P. J.; Rossen, K.; Reamer, R. A.; Volante, R. P.; Reider, P. J. *Tetrahedron Lett.* **1998**, *39*, 4441–4444.
- ³² Braddock, C. D.; MacGilp, I. D.; Perry, B. G. *J. Org. Chem.* **2002**, *67*, 8679.
- ³³ Braddock, D. C.; MacGilp, I. D.; Perry, B. G. *Synlett* **2003**, *8*, 1121–1124.
- ³⁴ Braddock, D. C.; MacGilp, I. D.; Perry, B. G. *Adv. Synth. Catal.* **2004**, *346*, 1117–1130.
- ³⁵ Dahmen, S.; Bräse, S. *Org. Lett.* **2001**, *3*, 4119–4122.
- ³⁶ Dahment, S. Bräse, S. *J. Am. Chem. Soc.* **2002**, *124*, 5940–5941.
- ³⁷ Han, L.; Lei, Y.; Xing, P.; Zhao, X.-L.; Jiang, B. *J. Org. Chem.* **2015**, *80*, 3752–3757.
- ³⁸ Seferos, D. S.; Blum, A. S.; Kushmerick, J. G.; Bazan, G. C. *J. Am. Chem. Soc.* **2006**, *128*, 11260–11267.
- ³⁹ Wielopolski, M.; Molina-Ontoria, A.; Schubert, C.; Margraf, J. T.; Krokos, E.; Kirschner, J.; Gouloumis, A.; Clark, T.; Guldi, D. M.; Martín, N. *J. Am. Chem. Soc.* **2013**, *135*, 10372–10381.
- ⁴⁰ Xia, J. L.; Man, W. Y.; Zhu, X.; Zhang, C.; Jin, G. J.; Schauer, P. a.; Fox, M. a.; Yin, J.; Yu, G. A.; Low, P. J.; Liu, S. H. *Organometallics* **2012**, *31*, 5321–5333.
- ⁴¹ Oldham W.J., J.; Miao, Y. J.; Lachicotte, R. J.; Bazan, G. C. *J. Am. Chem. Soc.* **1998**, *120*, 419–420.
- ⁴² Zyss, J.; Ledoux, I.; Volkov, S.; Chernyak, V.; Mukamel, S.; Bartholomew, G. P.; Bazan, G. C. *J. Am. Chem. Soc.* **2000**, *122*, 11956–11962.
- ⁴³ Hong, J. W.; Woo, H. Y.; Liu, B.; Bazan, G. C. *J. Am. Chem. Soc.* **2005**, *127*, 7435–7443.
- ⁴⁴ Bartholomew, G. P.; Bazan, G. C. *J. Am. Chem. Soc.* **2002**, *124*, 5183–5196.
- ⁴⁵ Bartholomew, G. P.; Ledoux, I.; Mukamel, S.; Bazan, G. C.; Zyss, J. *J. Am. Chem. Soc.* **2002**, *124*, 13480–13485.
- ⁴⁶ Morisaki, Y.; Ishida, T.; Chujo, Y. *Macromolecules* **2002**, *35*, 7872–7877.
- ⁴⁷ Morisaki, Y.; Chujo, Y. *Bull. Chem. Soc. Jpn.* **2009**, *82*, 1070–1082.
- ⁴⁸ Wang, W. L.; Xu, J.; Sun, Z.; Zhang, X.; Lu, Y.; Lai, Y. H. *Macromolecules* **2006**, *39*, 7277–7285.
- ⁴⁹ Wang, W.; Xu, J.; Lai, Y. H.; Wang, F. *Macromolecules* **2004**, *37*, 3546–3553.
- ⁵⁰ Meyer, E.; Hug, H. J.; Bennewitz, R. *Scanning Probe Microscopy, the lab on a tip*, Advanced Texts in Physics, Springer-Verlag Berlin Heidelberg, **2004**, Vol. 135.
- ⁵¹ Binnig, G.; Rohrer, H.; Gerber, C.; Weibel, E. *Appl. Phys. Lett.* **1982**, *40*, 178–180.
- ⁵² Xu, S.; Liu, G. Y. *Langmuir* **1997**, *13*, 127–129.
- ⁵³ Piner, R. D.; Zhu, J.; Xu, F.; Hong, S.; Mirkin, C. A. *Science* **1999**, *283*, 661–663.
- ⁵⁴ Barth, J. V.; Costantini, G.; Kern, K. **2005**, *437*, 671–679.
- ⁵⁵ Love, J. C.; Estroff, L. A.; Kriebel, J. K.; Nuzzo, R. G.; Whitesides, G. M. *Chem. Rev.* **2005**, *105*, 1103–1170.
- ⁵⁶ Koma, A. *Prog. Cryst. Growth Charact. Mater.* **1995**, *30*, 129–152.
- ⁵⁷ De Feyter, S.; De Schryver, F. C. *J. Phys. Chem. B* **2005**, *109*, 4290–4302.
- ⁵⁸ Müller, K.; Seitsonen, A. P.; Brugger, T.; Westover, J.; Greber, T.; Jung, T.; Kara, A. *J. Phys. Chem. C* **2012**, *116*, 23465–23471.
- ⁵⁹ Lin, N.; Langner, A.; Tait, S. L.; Rajadurai, C.; Ruben, M.; Kern, K. *Chem. Commun.* **2007**, *1*, 4860–4862.
- ⁶⁰ Lingenfelder, M. A.; Spillmann, H.; Dmitriev, A.; Stepanow, S.; Lin, N.; Barth, J. V.; Kern, K. *Chem. - A Eur. J.* **2004**, *10*, 1913–1919.
- ⁶¹ Stepanow, S.; Lingenfelder, M.; Dmitriev, A.; Spillmann, H.; Delvigne, E.; Lin, N.; Deng, X.; Cai, C.; Barth, J. V.; Kern, K. *Nat. Mater.* **2004**, *3*, 229–233.
- ⁶² Stawasz, M. E.; Sampson, D. L.; Parkinson, B. A. *Langmuir* **2000**, *16*, 2326–2342.
- ⁶³ Arado, O. D.; Luft, M.; Mönig, H.; Held, P. A.; Studer, A.; Amirjalayer, S.; Fuchs, H. *Phys. Chem. Chem. Phys.* **2016**, *18*, 27390–27395.
- ⁶⁴ Stepanow, S.; Strunskus, T.; Lingenfelder, M.; Dmitriev, A.; Spillmann, H.; Lin, N.; Barth, J. V.; Wöll, C.; Kern, K. *J. Phys. Chem. B* **2004**, *108*, 19392–19397.

- ⁶⁵ Ruiz-Osés, M.; Kampen, T.; González-Lakunza, N.; Silanes, I.; Schmidt-Weber, P. M.; Gourdon, A.; Arnau, A.; Horn, K.; Ortega, J. E. *ChemPhysChem* **2007**, *8*, 1722–1726.
- ⁶⁶ Ciesielski, A.; Szabelski, P. J.; Rziysko, W.; Cadeddu, A.; Cook, T. R.; Stang, P. J.; Samorì, P. *J. Am. Chem. Soc.* **2013**, *135*, 6942–6950.
- ⁶⁷ Ruben, M.; Payer, D.; Landa, A.; Comisso, A.; Gattinoni, C.; Lin, N.; Collin, J.; Sauvage, J.; De Vita, A.; Kern, K. *J. Am. Chem. Soc.* **2006**, *128*, 15644–15651.
- ⁶⁸ Mukherjee, A.; Tothadi, S.; Desiraju, G. R. *Acc. Chem. Res.* **2014**, *47*, 2514–2524.
- ⁶⁹ Gutzler, R.; Fu, C. Y.; Dadvand, A.; Hua, Y.; MacLeod, J. M.; Rosei, F.; Perepichka, D. F. *Nanoscale* **2012**, *4*, 5965–5971.
- ⁷⁰ Chung, K.-H.; Park, J.; Kim, K. Y.; Yoon, J. K.; Kim, H.; Han, S.; Kahng, S.-J. *Chem. Commun.* **2011**, *47*, 11492–11494.
- ⁷¹ Gutzler, R.; Walch, H.; Eder, G.; Kloth, S.; Heckl, W. M.; Lackinger, M. *Chem. Commun.* **2009**, *29*, 4456–4458.
- ⁷² Russell, J. C.; Blunt, M. O.; Garfitt, J. M.; Scurr, D. J.; Alexander, M.; Champness, N. R.; Beton, P. H. *J. Am. Chem. Soc.* **2011**, *133*, 4220–4223.
- ⁷³ Ullmann, F.; Bielecki, J. *Berichte der Dtsch. Chem. Gesellschaft* **1901**, *34*, 2174–2185.
- ⁷⁴ Groszek, A. J. *Proc. R. Soc. A Math. Phys. Eng. Sci.* **1970**, *314*, 473–498.
- ⁷⁵ Xu, S.; Zeng, Q.; Lu, J.; Wang, C.; Wan, L.; Bai, C.-L. *Surf. Sci.* **2003**, *538*, L451–L459.
- ⁷⁶ Bléger, D.; Kreher, D.; Mathevet, F.; Attias, A. J.; Schull, G.; Huard, A.; Douillard, L.; Fiorini-Debuisschert, C.; Charra, F. *Angew. Chemie - Int. Ed.* **2007**, *46*, 7404–7407.
- ⁷⁷ Schull, G.; Douillard, L.; Fiorini-Debuisschert, C.; Charra, F.; Mathevet, F.; Kreher, D.; Attias, A. J. *Nano Lett.* **2006**, *6*, 1360–1363.
- ⁷⁸ Dexter, D. L. *J. Chem. Phys.* **1953**, *21*, 836–850.
- ⁷⁹ Förster, T. *Ann. Phys.* **1948**, *437*, 55–75.
- ⁸⁰ Dong, Z. C.; Zhang, X. L.; Gao, H. Y.; Luo, Y.; Zhang, C.; Chen, L. G.; Zhang, R.; Tao, X.; Zhang, Y.; Yang, J. L.; Hou, J. G. *Nat. Photonics* **2009**, *4*, 50–54.
- ⁸¹ Qiu, X. H. *Science* **2003**, *299*, 542–546.
- ⁸² Repp, J.; Meyer, G.; Stojković, S. M.; Gourdon, A.; Joachim, C. *Phys. Rev. Lett.* **2005**, *94*, 26803.
- ⁸³ Drew, M. E.; Chworos, A.; Oroudjev, E.; Hansma, H.; Yamakoshi, Y. *Langmuir* **2010**, *26*, 7117–7125.
- ⁸⁴ Mann, J. A.; Rodríguez-López, J.; Abruña, H. D.; Dichtel, W. R. *J. Am. Chem. Soc.* **2011**, *133*, 17614–17617.
- ⁸⁵ Du, P.; Jaouen, M.; Bocheux, A.; Bourgogne, C.; Han, Z.; Bouchiat, V.; Kreher, D.; Mathevet, F.; Fiorini-Debuisschert, C.; Charra, F.; Attias, A.-J. *Angew. Chemie Int. Ed.* **2014**, *5*, 10060–10066.
- ⁸⁶ Le Liepvre, S.; Du, P.; Kreher, D.; Mathevet, F.; Attias, A.-J.; Fiorini-Debuisschert, C.; Douillard, L.; Charra, F. *ACS Photonics* **2016**, *3*, 2291–2296.
- ⁸⁷ Helfrich, W.; Schneider, W. G. *Phys. Rev. Lett.* **1965**, *14*, 229–231.
- ⁸⁸ Jablonski, A. *Nature* **1933**, *131*, 839–840.
- ⁸⁹ Brouwer, A. M. *Pure Appl. Chem.* **2011**, *83*, 2213–2228.
- ⁹⁰ Helfrich, W.; Schneider, W. G. *Phys. Rev. Lett.* **1965**, *14*, 229–231.
- ⁹¹ Friend, R. H.; Gymer, R. W.; Holmes, A. B.; Burroughes, J. H.; Marks, R. N.; Taliani, C.; Bradley, D. D. C.; Santos, D. A.; Dos; Bredas, J. L.; Logdlund, M.; Salaneck, W. R. *Nature* **1999**, *397*, 121–128.
- ⁹² Kodan M. *OLED, displays and lighting*, Wiley-IEEE press, **2016**.
- ⁹³ Smith, L. H.; Wasey, J. A. E.; Samuel, I. D. W.; Barnes, W. L. *Adv. Funct. Mater.* **2005**, *15*, 1839–1844.
- ⁹⁴ He, S. J.; Wang, Z. B.; Wang, D. K.; Jiang, N.; Lu, Z. H. *Appl. Phys. Lett.* **2013**, *103*, 83301.
- ⁹⁵ Wang, C.; Li, X.; Pan, Y.; Zhang, S.; Yao, L.; Bai, Q.; Li, W.; Lu, P.; Yang, B.; Su, S.; Ma, Y. *ACS Appl. Mater. Interfaces* **2016**, *8*, 3041–3049.
- ⁹⁶ Forget, S.; Chenais, S.; Tondelier, D.; Geffroy, B.; Gozhyk, I.; Lebental, M.; Ishow, E. *J. Appl. Phys.* **2010**, *108*, 64509.
- ⁹⁷ Hirata, S.; Totani, K.; Zhang, J.; Yamashita, T.; Kaji, H.; Marder, S. R.; Watanabe, T.; Adachi, C. *Adv. Funct. Mater.* **2013**, *23*, 3386–3397.
- ⁹⁸ Hoshino, S.; Suzuki, H. *Appl. Phys. Lett.* **1996**, *69*, 224–226.
- ⁹⁹ Baldo, M. A.; O'brien, D. F.; You, Y.; Shoustikov, A.; Sibley, S.; Thompson, M. E.; Forrest, S. R. *Nature* **1998**, *395*, 151–154.
- ¹⁰⁰ Baldo, M.; Lamansky, S.; Burrows, P. E.; Thompson, M. E.; Forrest, S. R. *Appl. Phys. Lett.* **1999**, *75*, 4.
- ¹⁰¹ Lewis, G. N.; Lipkin, D.; Magel, T. T. *J. Am. Chem. Soc.* **1941**, *63*, 3005–3018.
- ¹⁰² Parker, C. A.; Hatchard, C. G. *Trans. Faraday Soc.* **1961**, *57*, 1894.
- ¹⁰³ Parker, C. A.; Hatchard, C. G. *Proc. Chem. Soc.* **1962**, June, 147.
- ¹⁰⁴ Parker, C. A.; Hatchard, C. G. *J. Phys. Chem.* **1962**, *66*, 2506–2511.
- ¹⁰⁵ Parker, C. A.; Hatchard, C. G. *Trans. Faraday Soc.* **1963**, *59*, 284–295.

-
- ¹⁰⁶ Yang, Z.; Mao, Z.; Xie, Z.; Zhang, Y.; Liu, S.; Zhao, J.; Xu, J.; Chi, Z.; Aldred, M. P. *Chem. Soc. Rev.* **2017**, *46*, 915–1016.
- ¹⁰⁷ Zhao, J.; Ji, S.; Guo, H. *RSC Adv.* **2011**, *1*, 937.
- ¹⁰⁸ Parker, C. A.; Joyce, T. A. *Chem. Commun.* **1968**, 1421, 1421.
- ¹⁰⁹ Wolf, M. W.; Legg, K. D.; Brown, R. E.; Singer, L. a.; Parks, J. H. *J. Am. Chem. Soc.* **1975**, *97*, 4490–4497.
- ¹¹⁰ Maciejewski, A.; Szymanski, M.; Steer, R. P. *J. Phys. Chem.* **1986**, *90*, 6314–6318.
- ¹¹¹ Berberan-Santos, M. N.; Garcia, J. M. M. *J. Am. Chem. Soc.* **1996**, *118*, 9391–9394.
- ¹¹² Endo, A.; Ogasawara, M.; Takahashi, A.; Yokoyama, D.; Kato, Y.; Adachi, C. *Adv. Mater.* **2009**, *21*, 4802–4806.
- ¹¹³ Deaton, J. C.; Switalski, S. C.; Kondakov, D. Y.; Young, R. H.; Pawlik, T. D.; Giesen, D. J.; Harkins, S. B.; Miller, A. J. M.; Mickenberg, S. F.; Peters, J. C. *J. Am. Chem. Soc.* **2010**, *132*, 9499–9508.
- ¹¹⁴ Endo, A.; Sato, K.; Yoshimura, K.; Kai, T.; Kawada, A.; Miyazaki, H.; Adachi, C. *Appl. Phys. Lett.* **2011**, *98*, 10–13.
- ¹¹⁵ Martin, R. L. *J. Chem. Phys.* **2003**, *118*, 4775–4777.
- ¹¹⁶ Nakanotani, H.; Higuchi, T.; Furukawa, T.; Masui, K.; Morimoto, K.; Numata, M.; Tanaka, H.; Sagara, Y.; Yasuda, T.; Adachi, C. *Nat. Commun.* **2014**, *5*, 4016.
- ¹¹⁷ Zhang, Q.; Li, B.; Huang, S.; Nomura, H.; Tanaka, H.; Adachi, C. *Nat. Photonics* **2014**, *8*, 326–332.
- ¹¹⁸ Kim, B. S.; Lee, J. Y. *Adv. Funct. Mater.* **2014**, *24*, 3970–3977.
- ¹¹⁹ Zhang, Y.; Zhang, D.; Cai, M.; Li, Y.; Zhang, D.; Qiu, Y.; Duan, L. *Nanotechnology* **2016**, *27*, 94001.
- ¹²⁰ Luo, J.; Xie, G.; Gong, S.; Chen, T.; Yang, C. *Chem. Commun.* **2016**, *52*, 2292–2295.
- ¹²¹ Søndergaard, R.; Hösel, M.; Angmo, D.; Larsen-Olsen, T. T.; Krebs, F. C. *Mater. Today* **2012**, *15*, 36–49.

CHAPTER 2:

SUPRAMOLECULAR CHEMISTRY ON SURFACES

One objective of this work is to create supramolecular self-assemblies on different kinds of metallic surfaces. As presented earlier, the supramolecular functionalisation of carbon sp^2 -hybridised substrates (highly oriented pyrolytic graphite (HOPG) and graphene) has already been performed in our lab by using planar molecules equipped with clip functions self-assembling in stable and well-organised networks. The concept was even extended to three-dimensional (3D) molecules called Janus tectons in which an active component is grafted on the upper deck of a **dtpCp** while molecular clips are borne by the lower deck. To date, the evolution of our molecules' designs is displayed in Figure 78 with both their structures and their behaviours on surface. From now on, the aim of this thesis is to prepare a 3D-tecton able to work on various substrates by replacing the molecular clips with functional groups targeting supramolecular interactions like halogen bonds, hydrogen bonds or coordination bonds.

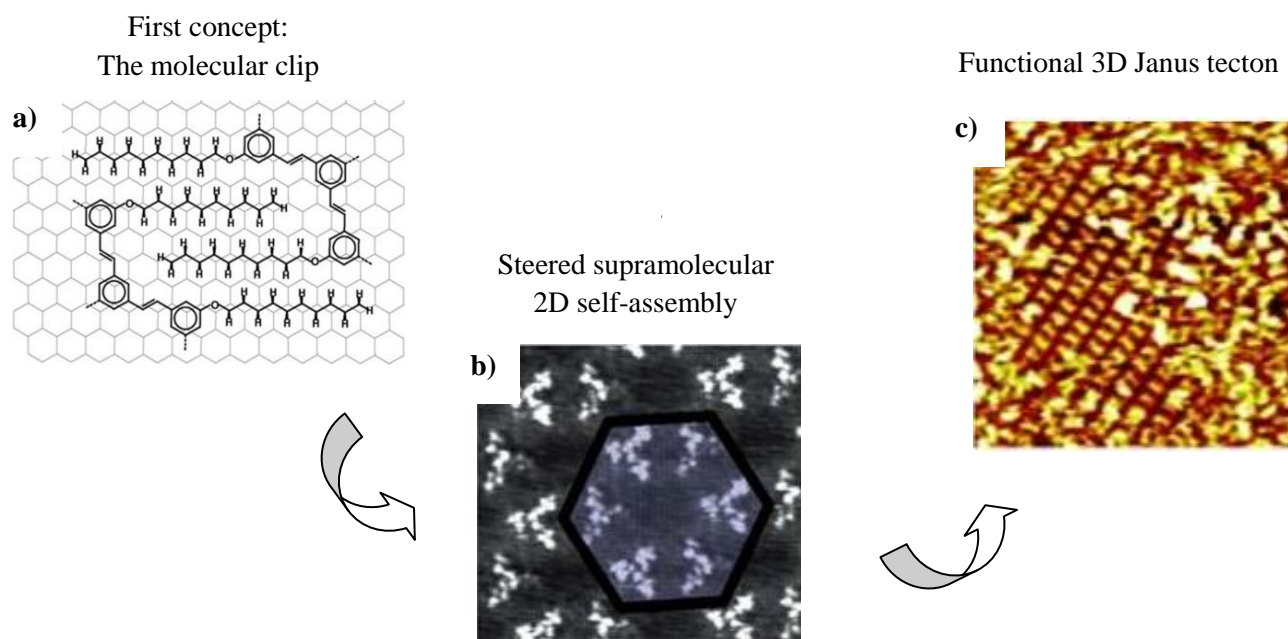


Figure 78: Evolution of the molecular designs developed in our group over the years, with the corresponding STM images (a: $8.9 \times 8.3 \text{ nm}^2$, b: $50 \times 50 \text{ nm}^2$)

The first part of this chapter will present the synthetic pathways used over the years to obtain functionalised **pCp** and its derivative **dtpCpB**, from its first characterisation by Brown and Farthing¹ to the recent work done in our lab⁸⁶. Then, the second part will focus on the different syntheses carried out during this PhD thesis and will discuss the different routes tested to obtain the target molecules. Finally, the third and last part will present the characterisations on these molecules (Nuclear Magnetic resonance, Infra-red, UV/Vis and fluorescence spectroscopy) and the first images of supramolecular self-assemblies on surface.

I. Paracyclophane's chemistry

The chemistry related to the paracyclophane derivatives will be presented in the following two grand axes: the cyclisation of the molecule leading to the cyclophane moiety, and the different pathways developed in our lab to functionalise or post-functionalise this synthon.

A. Synthetic step toward cyclophanes

Since its discovery by Brown and Farthing in 1949,¹ the chemists have described several synthetic routes towards the paracyclophane (**pCp**). The first one ever published was definitely developed by the discoverers of the molecule, and was based on the pyrolysis of *p*-xylene at low pressure as represented in Figure 79. The pyrolysis of *p*-xylene led to the *p*-xylylene monomer **A1**, highly reactive and thus polymerised immediately. Apart from several polymers, the reaction also gave different by-products including the **pCp** with very low yield. The **pCp** was also obtained as a by-product with very low yield by Errede *et al.* who tried to slow down the polymerisation of *p*-xylene monomer by radical initiation (down to -78°C).¹²²

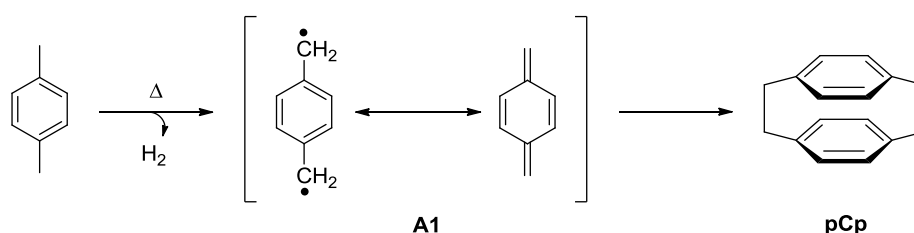


Figure 79: Synthesis of **pCp** by pyrolysis of *p*-xylene.

Later on, Cram *et al.* proposed an alternative way to synthesise the paracyclophane.¹⁸ As represented in Figure 80, a Grignard reaction was first accomplished by action of metallic magnesium on benzyl chloride to afford **A2**. The bromomethylation of this biphenyl derivative **A2** was then carried on with bromic acid and formic acid to afford the dimethylbromide compound **A3**. Finally, an intramolecular Wurtz reaction was performed at high dilution in *p*-xylene with metallic sodium to lead to the **pCp** in less than 1% of overall yield. This pathway was however interesting because it was henceforth possible to modify the length of the alkyl bridges.

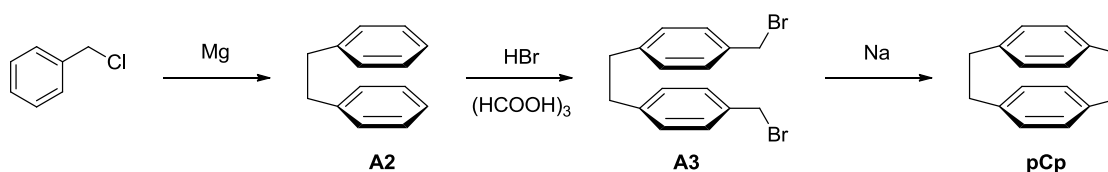


Figure 80: Synthesis of **pCp** with tunable alkyl bridges

An easier pathway was subsequently developed by Hopf to overcome the extremely low yield of Cram's synthesis.¹²³ The reaction was based on a [2+4] cycloaddition between a diene and an alkyne in benzene at 65°C. As shown in Figure 81, the alkyne had to be substituted with two dienophiles (esters groups) in order to favour the [2+4] addition over the [2+2] on the allene group. The **pCp** was obtained as a *syn*- or *anti*- tetra-ester isomer in 32% yield.

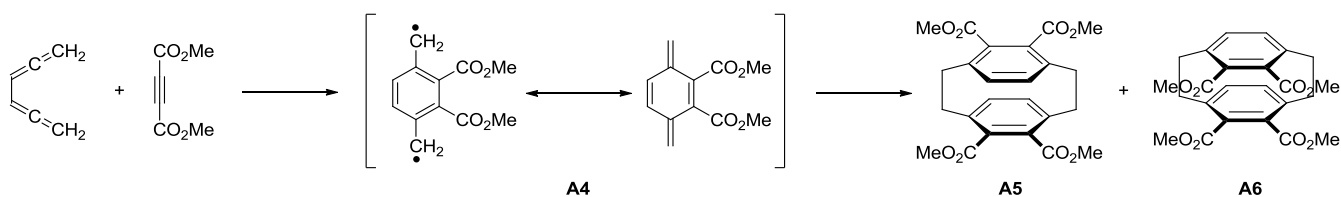


Figure 81: Hopf's route based on a [2+4]-cycloaddition leading to **pCp** derivatives

Shortly after, Winberg and Fawcett developed an alternative route towards **pCp** based on a two-steps reaction represented in Figure 82.¹²⁴ The first step was implying the nucleophilic substitution of trimethylamine on the bromobenzyl derivative and second a 1,6-Hofmann elimination leading to the **pCp** with the acceptable yield of 17 to 19%. This yield was lower than that of the Hopf's pathway, however the choice of reactants is wider because of the simplicity of the mechanism compared to the cycloaddition.

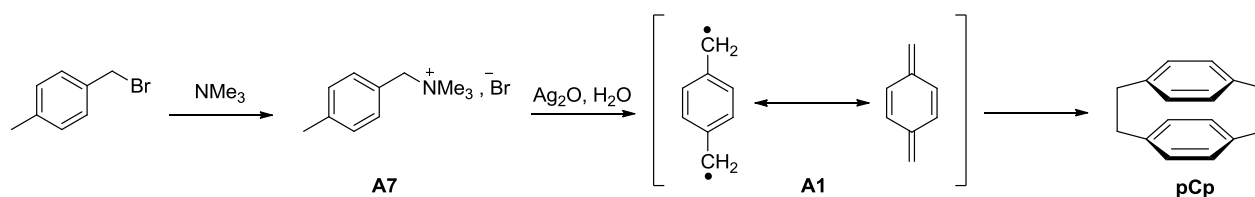


Figure 82: Winberg and Fawcett's pathway towards the **pCp** synthesis, *via* an Hofmann elimination

The last route to synthesise **pCp** is based on the prior preparation of the dithia[3.3]paracyclophane (**dtpCp**). This new approach was first proposed by Vögtle for the synthesis of the metacyclophane depicted in Figure 83. He developed two possible pathways: either by using 1,3-bis(bromomethyl)benzene **A8** and sodium sulphide to synthesise the symmetrical dithia[3.3]metacyclophanes **A10**, or from 1,3-bis(bromomethyl)benzene **A8** and 1,3-bis(mercaptomethyl)benzene **A9** for the asymmetrical cyclophanes.¹²⁵ The extrusion of the sulphur atoms was then described as an oxidation of the dithiacyclophane with hydrogen peroxide followed by a pyrolysis at 350°C. This pathway led to the metacyclophane **A11** with a global yield lower than 2% .

Figure 83: Vögtle's routes towards metacyclophanes, *via* dithia[3.3]metacyclophane intermediate

Finally, the most efficient pathway was published by Brink in 1975: inspired by Vögtle's work on dithia[3.3]metacyclophane, the **dtpCp** was simply synthesised from the 1,4-bis(bromomethyl)benzene **A12** and 1,4-bis(mercaptomethyl)benzene **A13**, followed by the photodesulphurisation using triethylphosphite with an overall yield of 51%.²⁵ This synthetic route, described in Figure 84, was not only efficient but was hence allowing the synthesis of asymmetric **pCp**.

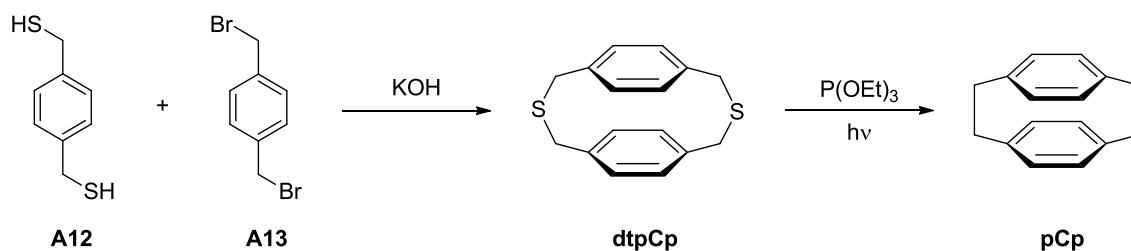


Figure 84: Brink's efficient pathway toward **pCp**

B. Janus tectons: state of the art

As mentioned in the first chapter, our group focused on functionalising sp^2 -hybridised carbon surfaces by physisorption of organic materials.⁸⁶ In our case, the cyclophane has been used as a mean to electronically decouple the active moieties (attached to the upper deck) from the surface in order to limit the fluorescence quenching induced by the substrates. Thus, the cyclophane unit represents the central pillar of our molecules on which the upper deck is functionalised with the active component while molecular clips grafted on the lower deck are responsible for the self-assembly on HOPG or graphene. The whole molecule is called a “Janus tecton”, and a schematic representation is depicted in Figure 85. The **pCp** and **dtpCp** molecular architectures have both been tested but to decrease the number of synthetic steps as well as to avoid too much through-space interactions, our group mainly centred its studies on the **dtpCp** derivatives.¹²⁶

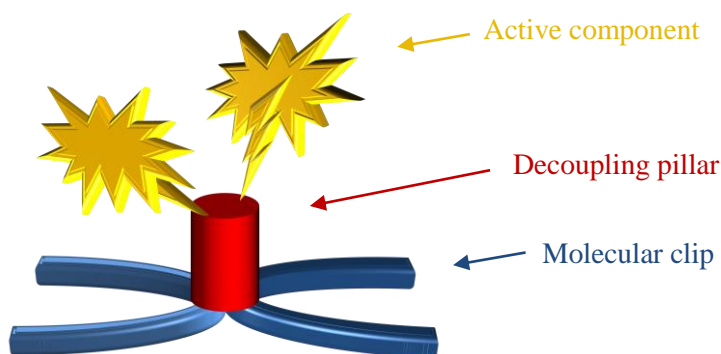


Figure 85: Original design of the Janus tecton

The synthesis of these three-dimensional tectons can be described in two main steps: the preparation of the cyclophane core and then its functionalisation.

The best strategy to synthesise the **dtpCp** core was developed by Bakhma *et al.*¹²⁷ and consisted in building up the dibromo-**dtpCp**-dialdehyde **B4** as represented in Figure 86. On one hand, the 1,4-dibromo-2,5-*p*-xylene was first brominated by NBS to form the dibromo derivative **B1** and then turned into the bis-thiol **B2** by action of thiourea and potassium hydroxide. On the other hand, six steps were necessary to synthesise the dialdehyde **B3** from the *p*-xylene. Finally, the cyclisation of **B2** and **B3** to give the cyclophane **B4** occurred by nucleophilic substitution of the **B3** bromides by the bis-thiolate obtained after deprotonation of **B2** under basic conditions. This last step was carried on at very high dilution in order to avoid polymerisation side reaction and to favour the **dtpCp** formation.

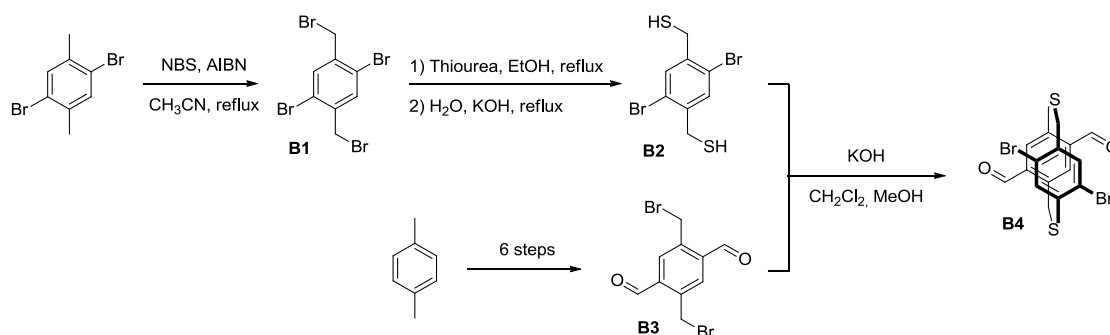


Figure 86: Synthesis of **B4** according to Bakhma *et al.* strategy

Therefore, the dibromo-**dtPcP**-dialdehyde **B4** has been used as a molecular building block on which different components were grafted. As represented in Figure 87, the distyrylbenzene phosphonate unit (molecular clip for absorption on surface) was added on the cyclophane by using the Wittig-Horner reaction while the active entity was added *via* palladium-catalysed cross-couplings: Stille coupling for the oligothiophene¹²⁷ (**B5**) and Suzuki coupling for the styrylbenzene derivative¹⁰ (**B6**).

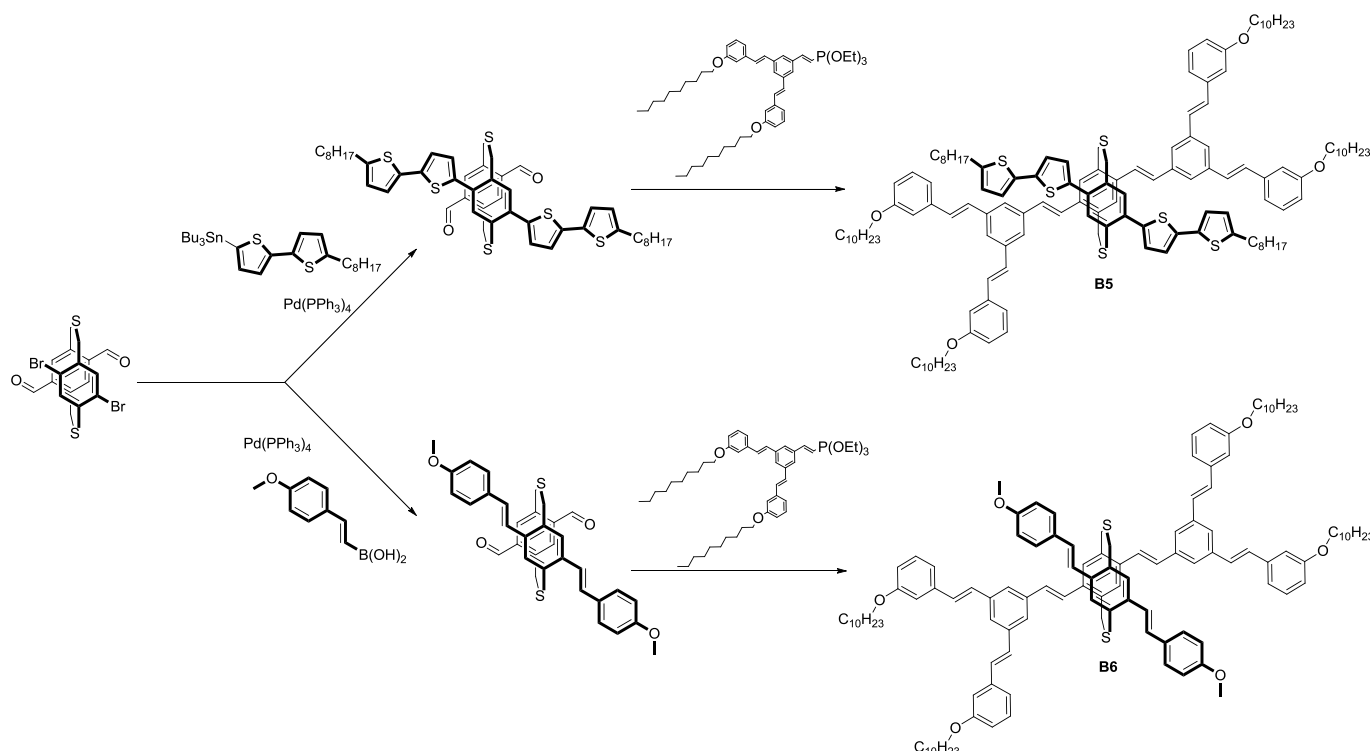


Figure 87: Functionalisation of **dtPcP** for HOPG-confined self-assembly

Several Janus tectons were synthesised with acceptable overall yields up to 20%. The design was proven quite efficient: highly stable self-assembled networks were obtained on HOPG. However, this approach based on molecular clips is only viable for sp^2 -hybridised carbon substrates such as graphite or graphene. Therefore, to move on toward new types of substrates such as metals, the molecular clip must be replaced by a more suitable function and drastic modifications of the tecton's structure are thus required. A new design of the cyclophane's lower deck is therefore needed to allow the adsorption on such surfaces.

II. Designing new cyclophane-based molecules

As previously discussed, the molecular design of the first generation of Janus tectons must be modified to allow their self-assembly on larger variety of substrates such as HOPG, gold,... The van der Waals interactions are not viable for metallic substrates, the adsorption should thus occur by π -interactions with the metal atoms in a coordination-like process.

As a consequence, we proposed to design a new type of 3D Janus tectons suitable for different kind of supramolecular interactions on surface such as coordination, halogen bond or hydrogen bond. The schematic representations of the new target molecular architectures are represented in Figure 88.

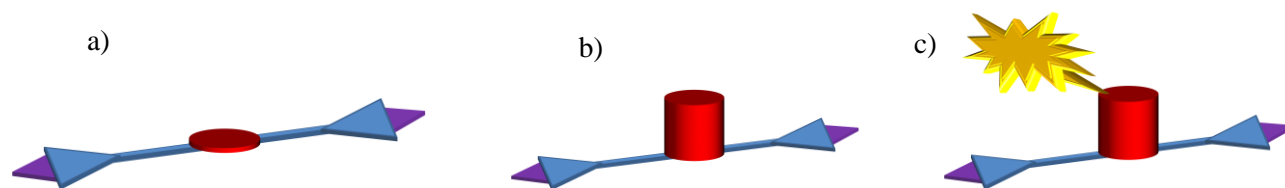


Figure 88: Schematic representations of our three molecular architectures: **(a)** pedestal, **(b)** naked pillar and **(c)** new 3D Janus tecton

The first architecture **(a)** represents the pedestal (only) to demonstrate the proper self-assembly of the molecules on surfaces. Then, the second architecture **(b)** named “naked pillar” represents the pedestal incorporating a cyclophane core to verify that the presence of a central nanopillar does not change the self-assembly on the substrate. Finally, the third molecular architecture **(c)** represents the new generation of Janus tecton incorporating an active unit (emitter) at the upper deck of the cyclophane. This latter architecture should self-assemble on several surfaces and should also be able to emit light from the decoupled active moiety.

We based our molecular design on functional units already known to self-assemble on metallic substrates such as pyridine groups. As described by Tait *et al.* on copper¹²⁸ or by Surin *et al.* on HOPG¹²⁹, the pyridine can be used as a function of coordination on surface. Such units can also make hydrogen-bonds with carboxylic acid derivatives¹³⁰ or halogen bonds with compounds bearing iodide atoms¹³¹. The chemical structures of these new pyridyl end-capped molecules are given in Figure 89. The synthesis of each molecule will be described afterwards in the following parts.

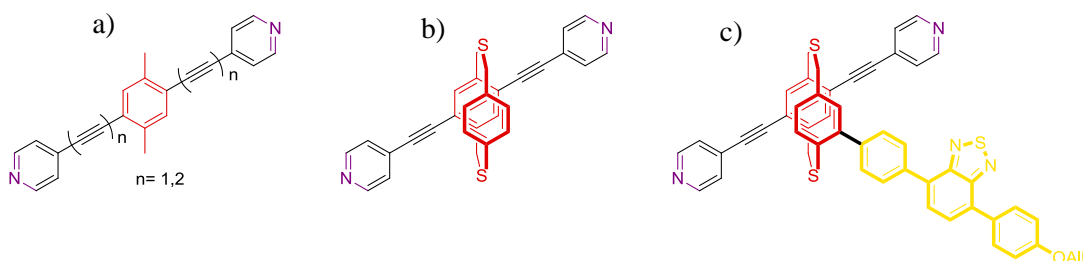
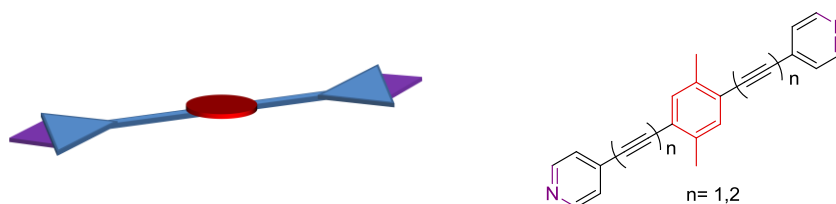


Figure 89: Chemical structures of our target pyridyl end-capped molecules: **(a)** pedestals, **(b)** naked pillar and **(c)** Janus tecton

A. Synthesis of the pedestal



The pedestal molecule must replicate the lower deck (base) of our 3D Janus tecton responsible for the self-assembly on surface. Thus, the *p*-xylylene moiety acts as the core of the molecule and pyridine units are linked to it by means of alkyne spacers. The synthetic route of this molecule is described in Figure 90.

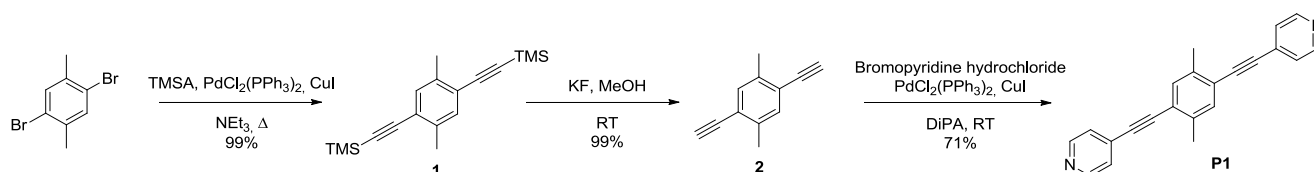


Figure 90: Synthetic route of the pedestal molecule **P1**

The Sonogashira cross-coupling¹³² between 1,4-dibromo-*p*-xylene and a large excess of trimethylsilylacetylene (TMSA) by using a palladium catalyst ($\text{Pd}(\text{PPh}_3)_2\text{Cl}_2$) and copper iodide (CuI) in triethylamine led to the compound **1** in 99% yield. Then, the quantitative deprotection of the trimethylsilyl group by potassium fluoride¹³³ gave the intermediate **2** and finally a second Sonogashira coupling in diisopropylamine (DiPA) using the $\text{Pd}(\text{PPh}_3)_2\text{Cl}_2/\text{CuI}$ catalyst was carried out with *p*-iodopyridine to form the target pedestal **P1** with a yield of 71%.

Furthermore, the option of the alkyne unit as spacer was first decided because of the simplicity of the Sonogashira cross-coupling. However, another interest resides in its tunable length. Indeed, from the compound **2**, it is also possible once to couple it again with TMSA by Glaser-Hay coupling^{134,135} in order to obtain butadiyne derivatives. The synthesis is then the same as that with the ethynyl spacers. Thus, we took advantage of the versatility of this synthetic route to prepare a longer pedestal **P2** as described in Figure 91.

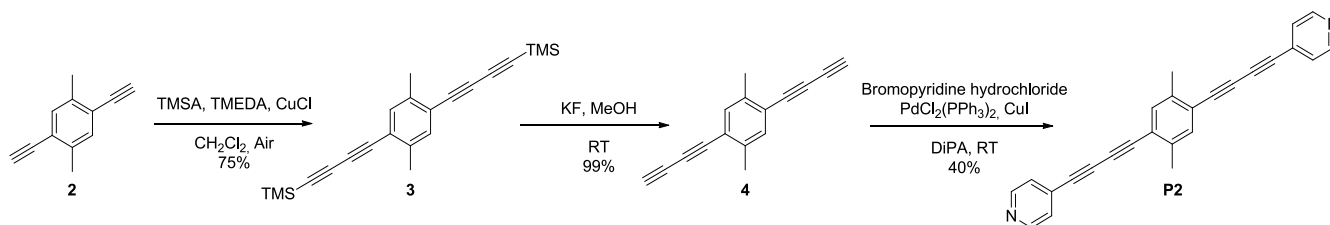


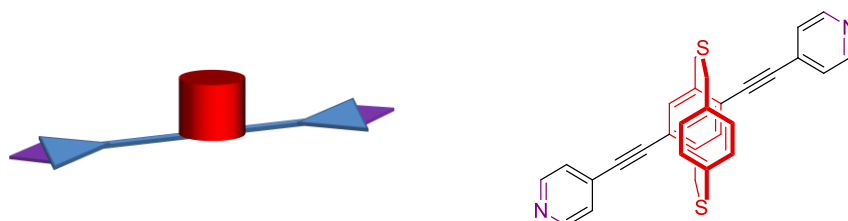
Figure 91: Synthetic route of the pedestal **P2**

The Glaser-Hay coupling occurred in dichloromethane by action of a copper chloride-tetramethylethylenediamine (TMEDA) catalyst on **2** and TMSA (in large excess) to afford the compound **3** in 75% yield. For this reaction, oxygen was bubbled into the reaction mixture in order to

regenerate the catalyst at each cycle. Then, as for the ethynyl derivative, the compound **3** is deprotected with potassium fluoride to afford **4** in quantitative yield. However, the so-obtained compound **4** imperatively needs to be kept in an oxygen-free environment: its high unstability makes it turned from pure white to dark grey after few seconds of exposition to air. Finally, the palladium-catalysed Sonogashira coupling of *p*-iodopyridine and **4** led to the pedestal **P2** in 40% yield.

It is worth noticing that the synthesis of compounds of different length (**P1** and **P2**) would also allow us to tune the network lattice size on the surface, or eventually to use bulkier active components on the top of the pillar without risks of changing the underlying network. Nonetheless, before testing several active moieties, it was important to develop the chemistry on a pedestal molecule incorporating a naked cyclophane as discussed in the next part.

B. Synthesis of the naked pillar



Numerous reactions have been attempted in order to obtain the desired naked cyclophane. Five different strategies were tested and the main intermediary products are represented in the retrosynthetic pathways depicted in Figure 92.

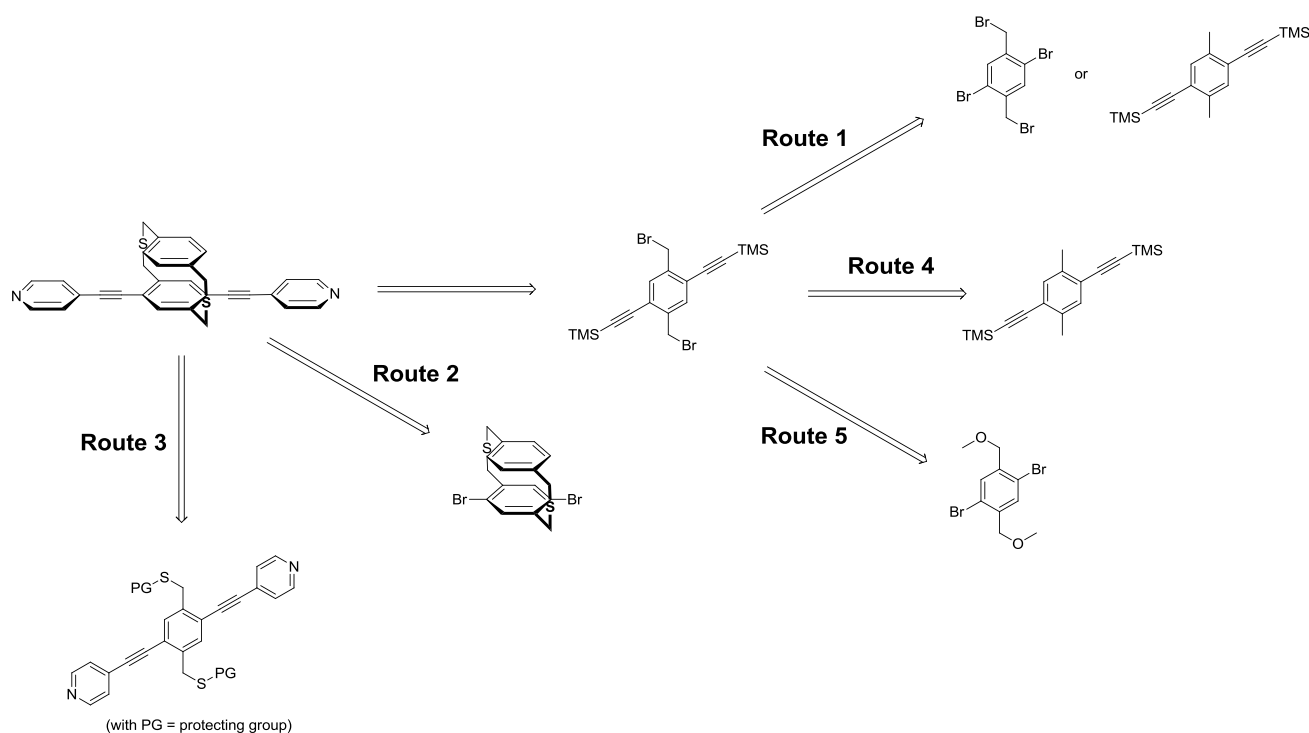


Figure 92: Retrosynthetic pathways toward the naked pillar

1. The bromide menace (Route 1)

The aim of the first pathway was to graft the alkyne moieties to the *p*-xylene core before “closing” the cyclophane. As represented in Figure 93, starting from the 1,4-dibromo-*p*-xylene, two synthetic routes are possible: either to first synthesise the compound **1** by Sonogashira cross-coupling and then to brominate the methyl groups with NBS, or to start with the bromination and then to carry on with the palladium catalysed coupling to connect the alkyne moieties.

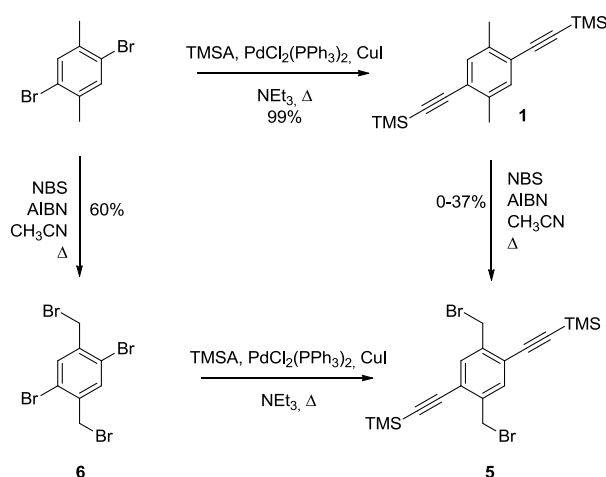


Figure 93: Representation of the two different routes towards the building block **5**

First developed by Wohl and Ziegler¹³⁶, the bromination reaction with NBS follows a radical pathway where AIBN is the radical initiator. The compound **1**, previously synthesised by Sonogashira coupling (Figure 90), was bis-brominated in these conditions to afford the derivative **5** in very variable yields: the first reaction of bromination gave **5** with a yield of 37 %, and then any other attempt never gave the product with more than 12% yield. The main reason for these low yields is the multiple by-products afforded by the radical reaction. Indeed, it was possible to isolate multi-brominated compounds (the methyl groups being able to support 1 or 2 bromides each). In addition, several other unidentified by-products were observed, supposedly coming from the bromination of the alkyne groups, as discussed by Jin *et al.*¹³⁷.

On the other hand, the bromination of the 1,4-dibromo-*p*-xylene afforded the compound **6** in reasonable yield of 60%. However, the Sonogashira coupling carried out on **6** never gave the expected product **5**, but a mixture of unknown compounds impossible to separate. Indeed, this cross-coupling is known for its high reactivity on halogens borne by Csp² carbons, but the benzylic positions (-CH₂-Br) are also activated enough to participate to the coupling. Therefore, the mixture of numerous products was certainly due to four reactive sites on the molecule, instead of the two Csp²-Br initially expected.

In conclusion, the prior grafting of the alkyne moieties appearing to be ineffective, another pathway was proposed based on the prior synthesis of the cyclophane core before performing the addition of the rest of the pedestal.

2. Attacks on the cyclophane (Route 2)

Based on previously reported syntheses (Figure 86), the cyclophane was synthesised in 4 steps, as described in Figure 94.

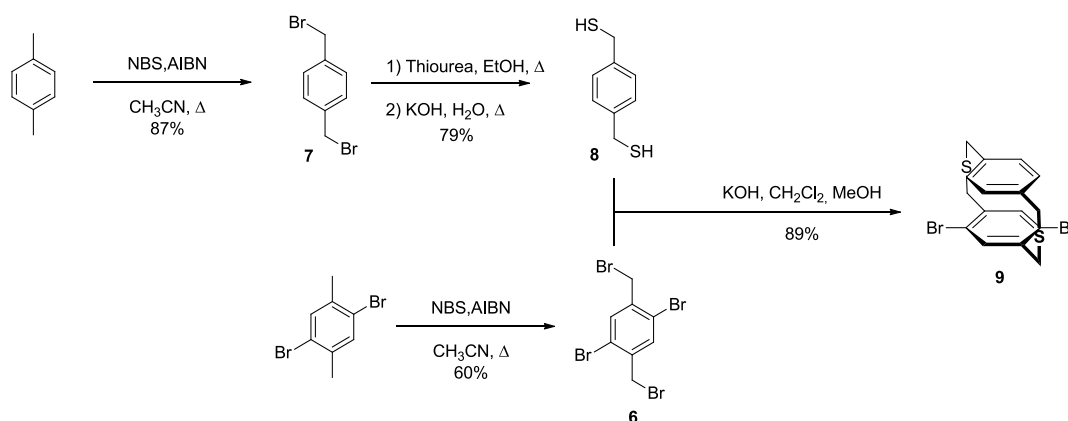


Figure 94: Synthesis of the cyclophane building block **9**

The *p*-xylene was first brominated in the same condition as previously described for **6** to give the derivative **7** with a good yield of 87%. Then, thiourea was added on **7** in boiling ethanol and the intermediary bis-isothiuronium salt was obtained. This salt was solubilised in a solution of potassium hydroxide in refluxing water to form the bis-thiolate compound, and then the medium was acidified to obtain the product **8** in 79% yield.¹³⁸ The compounds **6** and **8** were then solubilised in dichloromethane and slowly added to a highly diluted solution of potassium hydroxide in methanol to afford the cyclophane derivative **9** with a very good yield of 89%. It is noteworthy that the high dilution parameter is very important in order to limit unwanted polymerisation side-reactions of the reactants, as represented in Figure 95.

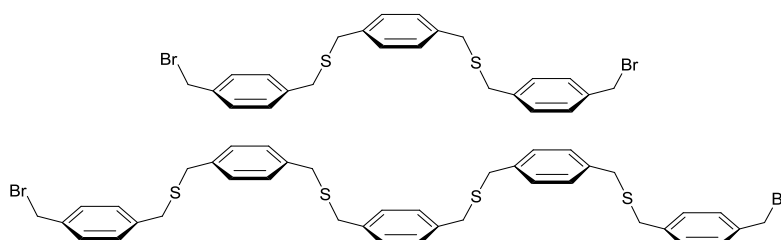


Figure 95: Examples of oligomer by-products possibly formed during the reaction of cyclisation

Several attempts of Sonogashira coupling were then carried on the cyclophane **9** and TMSA by using the usual conditions (palladium catalyst $\text{Pd}(\text{PPh}_3)_2\text{Cl}_2$ and copper iodide in triethylamine) to prepare the derivative **10**, as depicted in Figure 96. However, even by adding toluene to increase the solubility of the starting materials, the yield of the reaction never went above 10%, and the cyclophane derivative **10** could not be separated from the mono-substituted compound.

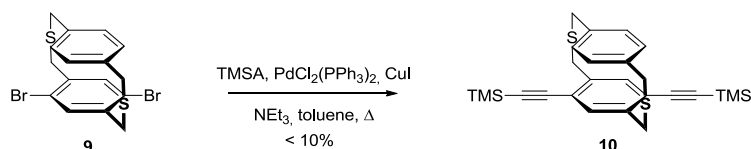


Figure 96: Sonogashira coupling on the cyclophane **9**

As a conclusion, the Sonogashira coupling could not be efficiently performed either before or after the closure of the **dtpCp**. This reaction might still be improved by tuning the catalyst, but additional tedious tests would have been necessary to study the effects of other ligands. Thus, we decided to move to another strategy based on the preparation of the bis-thiol derivative from the compound **6**, and the protection of the sulphur in order to perform the cross coupling.

3. Revenge of the thiol (Route 3)

As the two first strategies were not working, we decided to try another pathway based on the insertion of the thiol functions on the bottom of our pillar. The sulphurs were then protected in order to achieve the Sonogashira coupling. Thus, the bis-thiol derivative **11** have been synthesised according to the previous procedure used to prepare **8**: thiourea was first added on **6**, then the intermediary salt was recovered and subsequently treated by potassium hydroxide and sulphuric acid in order to obtain the bis-thiol compound **11**. The synthesis of **11**, as well as the different tested protection reactions of the thiol units are represented in Figure 97.

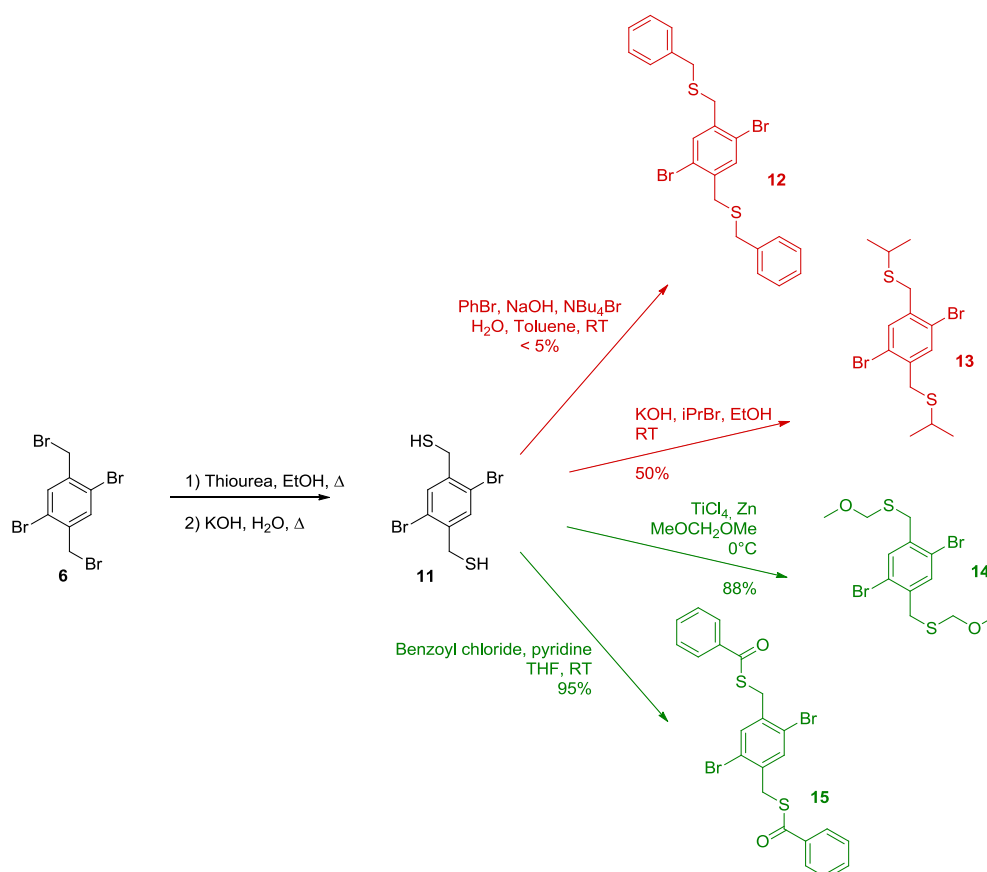


Figure 97: Synthesis of **11**, and the four different attempts to protect the thiol units

In this figure, four successful protections are presented using different groups: benzyl¹³⁹ **12**, isopropyl¹⁴⁰ **13**, methoxymethyl (MOM)¹⁴¹ **14** and benzoyl groups¹⁴² **15**. Among those, benzyl was not considered as a good candidate because of the very low yield of reaction, and isopropyl was not selected either because it was impossible to cleave the function after protection. Thus, the next reactions were carried out with both MOM and benzoyl groups.

a. Protection with the MOM group

The MOM has been commonly used to protect alcohol functions, and then has been successfully adopted here for thiols. The protection was carried on **11** in 88% yield by using low-valent titanium species prepared by addition of TiCl₄ on metallic zinc in methoxymethyl ether to give the protected derivative **14** with a quantitative yield. The TMSA was then grafted on **14** by Sonogashira coupling as described earlier to form the derivative **16** (84% yield) and the trimethylsilyl groups were then removed by potassium fluoride to obtain the bis-alkyne **17** with a yield of 64%. The

second Sonogashira coupling of **17** and *p*-iodopyridine was then carried out and **18** was recovered in 67% yield. The reaction pathway is reported in Figure 98.

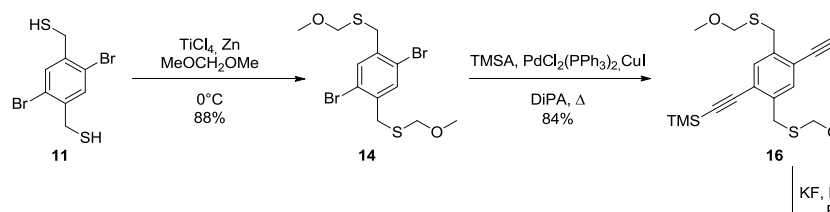


Figure 98: Reaction pathway using MOM as a protecting group

The last key step before cyclisation was the deprotection of the MOM groups to obtain the bis-thiol building block **19**. According to the literature,¹⁴⁰ the treatment of **18** with hydrochloric acid 2M in methanol at room temperature should lead to the thiol units. The expected mechanism of deprotection is described in Figure 99.

Figure 99: Expected mechanism of deprotection of the building block **18** with hydrochloric acid and methanol

However, despite the increase of temperature or acid concentration, the deprotection completely failed. Inspired by the deprotection of alcohol functions, several other reagents were tried like trifluoroacetic acid, boron trifluoride and hydrobromic acid in methanol or acetonitrile without any recovery of the thiol functions.¹⁴⁰ As the sulphur atom is a less effective attractor than oxygen, we can suppose that the S-CH₂-O moiety was less activated than O-CH₂-O in the alcohol protected function, and thus was preventing the deprotection of the thiol.

In conclusion, the MOM was not the best protection for the thiol group or our building block **19**; we thus decided to change it for a benzoyl groupement.

b. Protection with the benzoyl group

The use of benzoyl as a protection group for thiol was first described by Fowelin *et al.* on anthracenethiol derivatives.¹⁴² The procedure was successfully adapted to our synthesis as depicted in Figure 100: the compound **11** was added to a solution of benzoyl chloride and pyridine in THF to obtain the bis-thioester **15** in 95% yield.

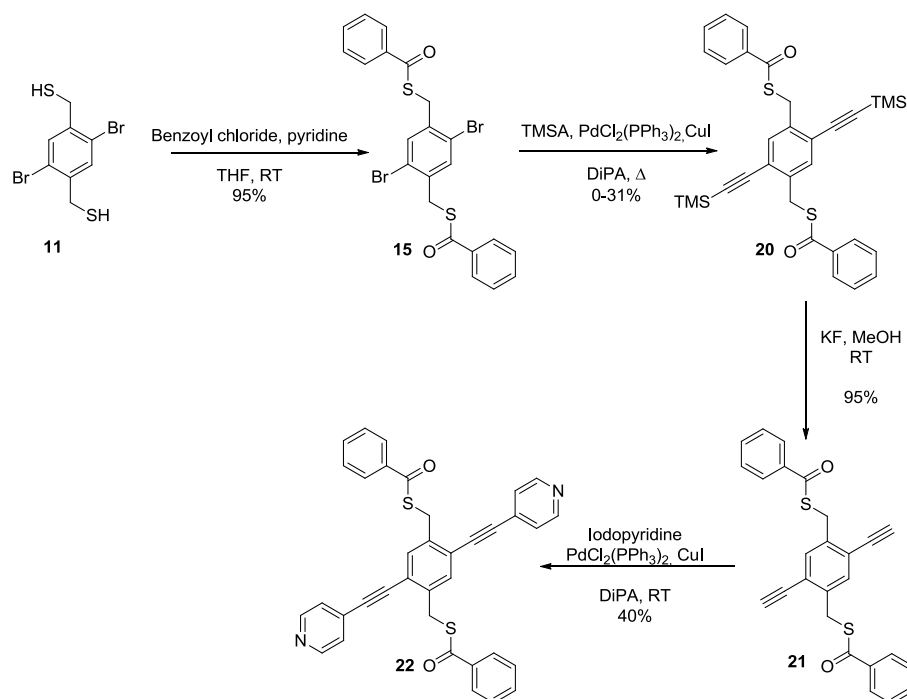


Figure 100: Reaction pathway using benzoyl as a protecting group

The Sonogashira cross-coupling was then performed on **15** with TMSA to afford the derivative **20** in low yield: the best results were 31%, but most of the reactions were giving less than 10% yield. The deprotection was nonetheless performed with potassium fluoride to obtain the bis-alkyne **21** with the very good yield of 95%. Finally, the second Sonogashira coupling with *p*-iodopyridine gave the thioester **22** in 40% yield. The deprotection of **22** was then attempted with sodium methanolate to afford a low quantity of a red insoluble powder. Unfortunately, this red product could not be characterised by common spectroscopic techniques like NMR because of its absence of solubility in any solvent.

In conclusion, the strategy of the thiol protection appeared as an unproductive way to prepare the building block **19**. Thus we decided to come back to the first route to prepare the derivative **5**, and tried several modifications to improve the low yield of the reaction.

4. A new solvated hope (Route 4)

As mentioned before, the first attempts to synthesise **5** were affording the desired compounds with erratic yields. The reaction was then performed in various conditions: changing the solvent from acetonitrile to chloroform or dichloromethane and thus modifying the temperature of the refluxing mixture, modulating the amount of NBS from 2 to 5 equivalents, switching from AIBN to BPO (dibenzoylperoxide) as radical initiator or tuning the duration of the reaction... Unfortunately, no relevant improvement was observed: the yields were still low and the purification still painful because of the presence of different by-products. Finally, the real breakthrough occurred by using carbon tetrachloride as solvent of the reaction and DBO as radical initiator. The CCl_4 is commercially hard to obtain because of its high toxicity for the humans as much as for the environment, but it is also the solvent of choice for a reaction of bromination. Inspired by Hennrich *et al.*¹⁴³, the reaction depicted in Figure 101 was carried out with a better yield (52 % *versus* 37 %).

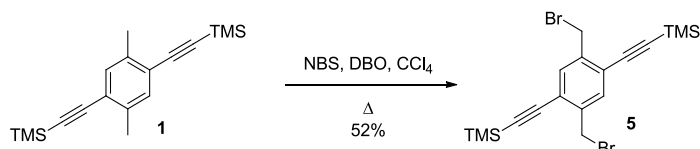


Figure 101: Successful bromination of **5** with 52% yield.

However, the reaction presented good yield for the three first attempts (above 40%), before backing down to 10% yield for the next ones. The first three reactions were carried out by using the carbon tetrachloride from an old container, while the next ones were using a newly ordered bottle. We thus assumed that over the years, part of the solvent evolved into Cl_2 species which might have catalysed the reaction or prevented secondary reactions to occur.

A solution of compounds **5** and **8** in dichloromethane was then slowly added to potassium hydroxide in methanol to afford the cyclophane **23** with a yield of 43%. It is interesting to note that two reactions were performed in the same reacting mixture: the cyclisation of the **dtbCp** and the deprotection of the alkyne units. Then, as displayed in Figure 102, the compound **23** was finally added to a mixture of *p*-iodopyridine, $\text{Pd}(\text{PPh}_3)_2\text{Cl}_2$ and copper iodide in diisopropylamine to carry out the Sonogashira coupling and afford the naked pillar **NP** in 44% yield.

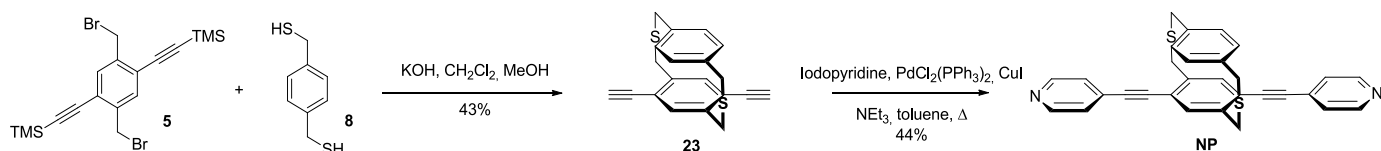


Figure 102: Final steps of the synthesis of the naked pillar **NP**

The desired naked cyclophane was finally obtained in 4 steps with an overall yield of 9%. However, as previously discussed, the reaction of bromination is still giving irregular results. This overall yield can thus fluctuate from 2 to 9%. As a consequence, another pathway was proposed in order to increase and stabilise the efficiency of the synthetic route.

5. The bromide strikes back (Route 5)

This last synthetic part is focused on obtaining the cyclophane **23** with a better yield by increasing the efficiency of synthetic route toward the bis-brominated derivative **5**. As depicted in Figure 103, we decided to start from the compound **6**, and the benzylic positions were first protected with methoxy units. The reaction was carried out in methanol, and sodium methanolate was added on **6** to afford **24** in quantitative yield. The Sonogashira coupling was then performed with the usual mixture of catalysts and TMSA to afford the protected derivative **25** in 84% yield.

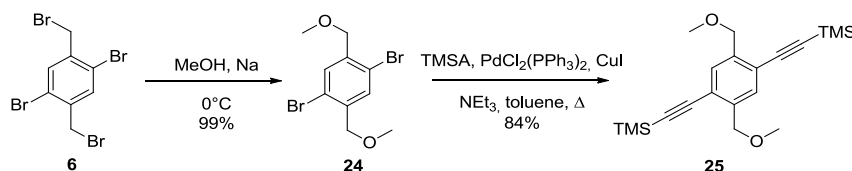


Figure 103: Protection of the benzylic position by adding methoxy units, and the following Sonogashira coupling

The deprotection lately occurred by slowly adding boron tribromide (BBr_3) to a solution of **25** in dichloromethane at 0°C .¹⁴⁴ However, the BBr_3 reagent was not only efficient in substituting the methoxy units to form **26**, it also started to partially deprotect the TMS groups of the alkynes chains.

As a consequence, we decided to proceed to the deprotecting step directly on the crude. The reaction was carried out in a solution of potassium fluoride in methanol to afford the bis-alkyne **27** with an overall yield on the two reactions of 47%. The cyclisation was finally performed as usual by adding the bis-brominated compound **27** and the di-thiol **8** to a solution of potassium hydroxide to afford **23** with a yield of 81%. These last few steps are represented in the following Figure 104.

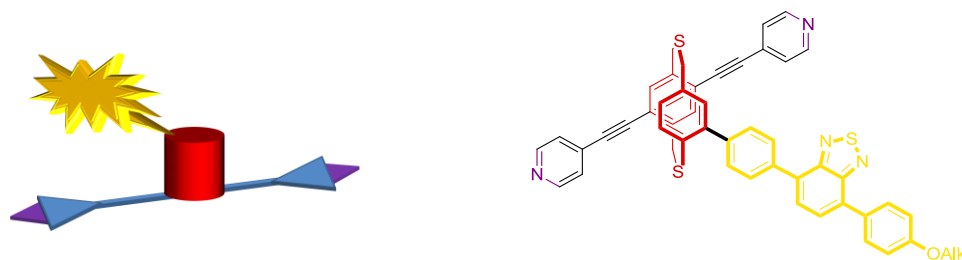


Figure 104: Synthesis of the cyclophane derivative **23** starting from **25**

The final Sonogashira coupling was then performed on the cyclophane building block **23** to conclude the synthesis of the naked cyclophane **NP**, as presented before (Figure 102).

In conclusion, this new synthetic pathway successfully led to the final product **NP** with an overall yield of 8% for seven steps. The previous strategy was erratically affording **NP** with various global yields of 2 to 9% (depending on the quite uncertain success of the bromination step). Thus by using this novel and more reliable strategy, the synthesis of the final product in 8% yield was definitely insured. The synthesis of the functionalised cyclophane, so-called Janus Tecton, was then investigated.

C. Synthesis of the Janus tecton



The synthesis of the naked pillar **NP** provided guidelines to develop the Janus Tecton's synthetic pathway. However, the incorporation of the active function atop of the cyclophane may alter the established course of the previous reactions. Thus, a new strategy was proposed where the first step consisted of synthesising a **NP** derivative which would allow the grafting of any desired active component. Then the second step was to prepare the fluorophore **F** able to react with the pillar. Finally, the third step was centred on the last reactions to synthesise and graft **F** to the cyclophane, and thus to obtain the Janus tecton **JT**.

1. Return of the cyclophane

Considering the structure of the **NP**, adding a bromide atom atop of the cyclophane would have perfectly fit with the syntheses previously develop. Moreover, it would have also authorised an organometallic cross-coupling to graft the active component. However, as detailed in the second

strategy above, couplings like Sonogashira's are not so effective on the **ntpCp**. As a consequence, an alternative pillar **nsNP** (not so Naked Pillar) was proposed, where the bromide atom is separated from the cyclophane by a spacer phenyl ring, as represented in Figure 105.

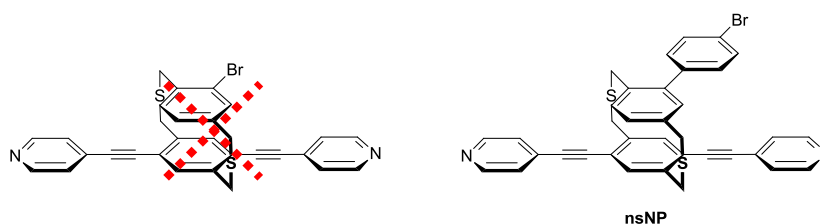


Figure 105: Representation of the not so Naked Pillar (**nsNP**)

The synthesis of **nsNP** is a 5 steps pathway starting with the palladium catalysed Suzuki-Miyaura cross-coupling between the 2-iodo-*p*-xylene and the 4-bromophenylboronic acid. The reaction was carried on in a solution of $\text{Pd}(\text{PPh}_3)_2\text{Cl}_2$ and K_2CO_3 in a mixture of dioxane and water to afford **28** in 94% yield. It is important to note that a precise equal amount of reactants is needed in order to avoid multiple Suzuki couplings on the bromide unit. A bromination reaction was then performed with NBS and AIBN in acetonitrile to obtain **29** in a surprisingly good yield of 90%: note that very few multi-brominated by-products were recovered. Later on, the thiolation was carried out as usual by addition of thiourea in ethanol and then potassium hydroxide in water to afford **30** in 83% yield. These three first steps are presented in Figure 106.

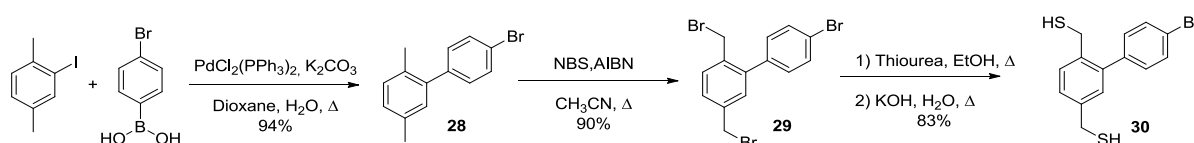


Figure 106: First steps towards the synthesis of the **nsNP**

As depicted in Figure 107, the cyclisation of the cyclophane was achieved by slow addition of a solution of **27** and **30** in dichloromethane to a large volume of a potassium hydroxide solution in methanol to afford **31** in 60% yield. Finally, the Sonogashira cross-coupling between **31** and *p*-iodopyridine was performed with the usual catalyst $\text{Pd}(\text{PPh}_3)_2\text{Cl}_2$ and CuI in DiPA to afford **nsNP** in 84% yield. It is important to note that both **31** and **nsNP** were obtained as a mixture of two structural isomers, the staggered (**sta**) and the eclipsed (**ecl**) derivatives.

Figure 107: Final steps of the **nsNP** synthesis, obtained as a mixture of two structural isomers **nsNP-sta** and **nsNP-ecl**

The **nsNP** was mainly synthesised in very good yield. The next step consisted in preparing the active component with the right grafting function allowing Suzuki or Stille cross-coupling reactions with **nsNP**.

2. The fluorescence awakens

The target fluorophore was chosen according to recent article from the literature,¹⁴⁵ and also from recent work in our lab. A benzothiadiazole derivative was thus chosen for its very small size which should prevent any perturbation of the underlying self-assembled network on surface. Moreover, despite its small size, it also presents an efficient fluorescence in the yellow area of the spectra.

Two molecules were thus targeted: the model fluorophore **F** and its derivative **Fp** which corresponds to the precursor that will be grafted atop the cyclophane core of the **nsNP**; both molecules are represented in Figure 108.

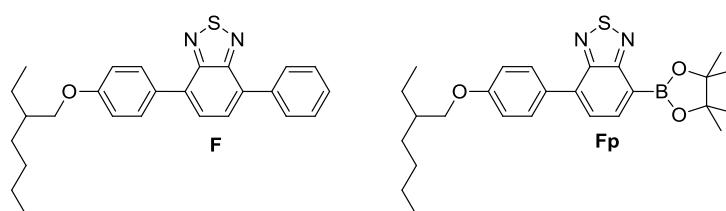


Figure 108: Representation of the fluorophore **F** and the fluorophore precursor **Fp**

The preparation of the targeted fluorescent molecules was performed by using two similar and successful synthetic routes. As represented in Figure 109, the route **A** first consisted in a Williamson reaction between the *p*-bromophenol and the ethylhexylbromide in refluxing DMF. The addition of potassium carbonate afforded the derivative **32** with a yield of 77%. Later on, the bromide was substituted by a pinacolborane function by cross-coupling reaction, using a [1,1'-bis(diphenylphosphino)ferrocene]dichloropalladium ($\text{Pd}(\text{dppf})\text{Cl}_2$) catalyst in a solution of potassium acetate and bis(pinacolato)diboron in dry dioxane to afford the compound **33** with 86% yield. It is important to note that using a dry solvent is mandatory to avoid the homocoupling due to Suzuki cross-coupling between the reactant **32** and the product **33** during the preparation. The intermediate **33** was then grafted on the dibromobenzothiadiazole **34** (prepared by brominating the commercial benzothiadiazole) by Suzuki coupling using $\text{PdCl}_2(\text{PPh}_3)_2$ and potassium carbonate to afford the building block **35** in 76% yield.

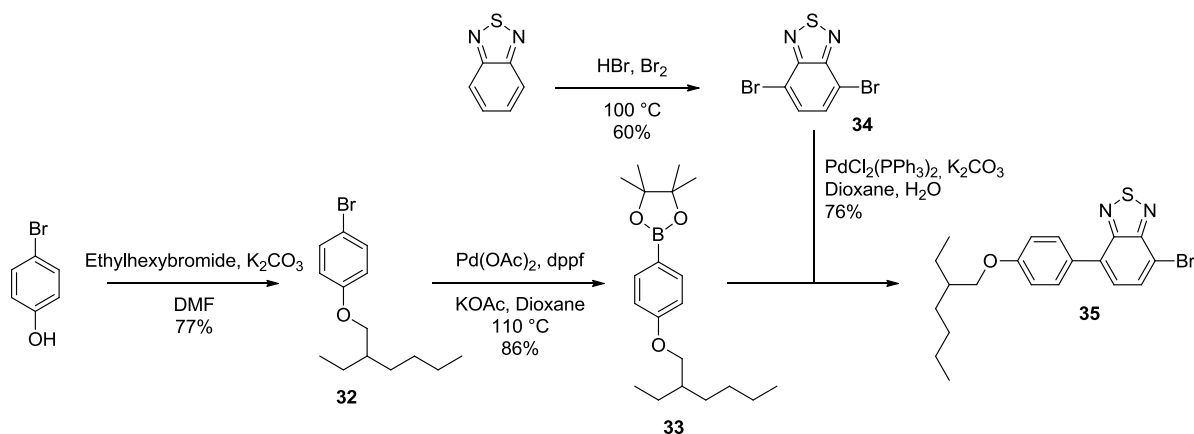


Figure 109: Synthetic route **A**

The Suzuki coupling leading to **35** was carefully carried out in order to avoid the functionalisation of both bromide units. After several attempts, the reaction was successfully carried out to obtain **35** with a yield of 76%.

The route **B** was directly focused on the Suzuki cross coupling with the dibromobenzothiadiazole **34** and *p*-hydroxyphenylboronic acid as depicted in Figure 110. The reaction was carried out using $\text{PdCl}_2(\text{PPh}_3)_2$ and potassium carbonate to afford **36** with a yield of 59%. The Williamson reaction was then performed on **36** using the ethylhexylbromide and potassium carbonate in DMF. This reaction was tried several times before obtaining the derivative **35**, the key parameter being the temperature: at room temperature the reaction was not happening, under reflux ($T_{\text{eb}} = 153\text{ }^\circ\text{C}$) the reactant **36** was decomposing. As a consequence, using DMF at 110°C led to **35** with a good yield of 76%.

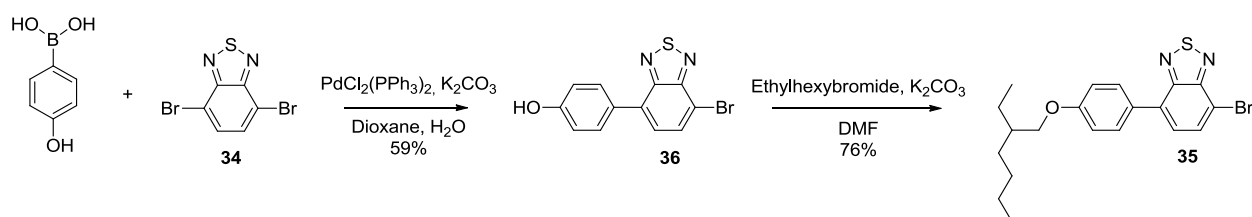


Figure 110: Synthetic route **B**

The two synthetic pathways allowed to obtain the product **35** with overall yield of 50% for **A** (3 steps) and 45% for **B** (2 steps).

However, the synthesis of the fluorophore **F** has not been performed yet, but a simple Suzuki coupling between **35** and phenylboronic acid should be carried out soon. Indeed, the synthon **Fp** was recently obtained in 88% yield by substituting the bromide unit of **35** with a pinacolborane with the same procedure as before ($\text{Pd}(\text{dppf})\text{Cl}_2$ and potassium acetate in dioxane), as displayed in Figure 111.

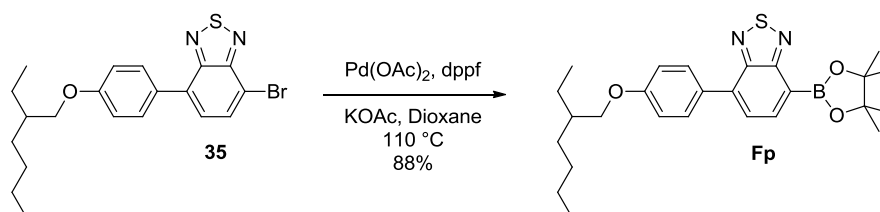


Figure 111: Synthesis of the fluorophore precursor **Fp**

Unfortunately, the final step consisting of grafting **Fp** on **nsNP** could not be performed yet because of time issues. Nonetheless, the final step being a common Suzuki cross-coupling, the reaction should be successful. The whole synthesis of the Janus tecton seems thus ready and will be finalised soon.

To summarize this part, the pedestal and the naked pillar were successfully synthesised, according to the synthetic pathway represented Figure 112 (a and b, respectively). Moreover, the synthetic route towards the Janus tectons is now effective and ready to be ended, as depicted in the Figure 112c. The next part will thus be focused on the characterisation of the so-synthesised molecules **P1** and **NP**.

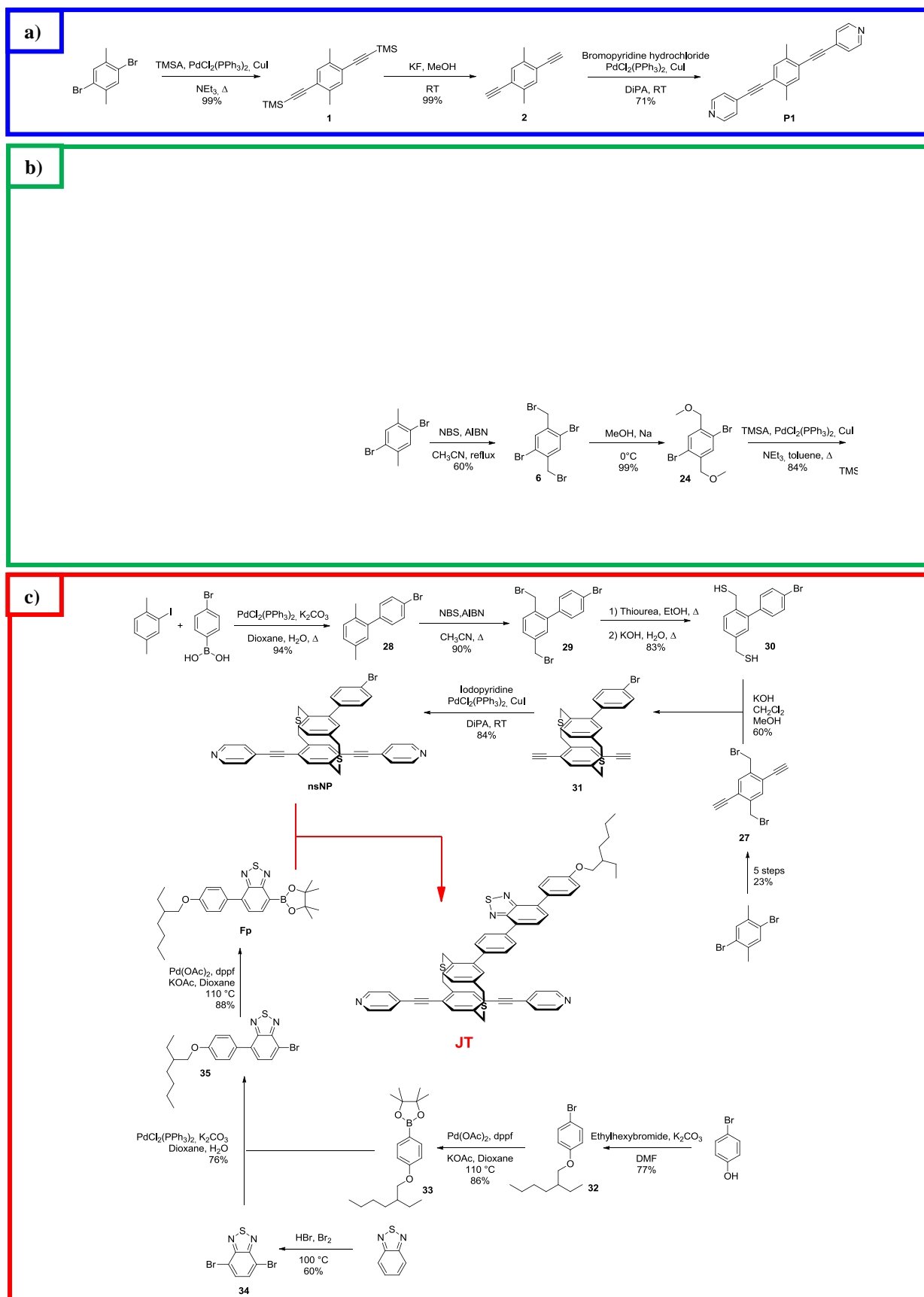


Figure 112: Representation of the definitive synthetic pathways of the pedestal (**a**), the naked pillar (**b**) and the unfinished Janus tecton (**c**)

III. Characterisations

This third and last part will focus on the characterisation of the target molecules **P1** and **NP**. On the one hand, the properties of these molecules were studied by various spectroscopic methods: NMR, IR, UV-vis and fluorimetry. On the other hand, further experiments were performed on surface by using different techniques of scanning probe microscopy (STM, AFM) in order to study the supramolecular self-assembly of the molecules on different substrates.

A. Spectroscopic studies

1. Nuclear Magnetic Resonance

The NMR spectrum of **P1** was then recorded in deuterated chloroform, as displayed in Figure 113.

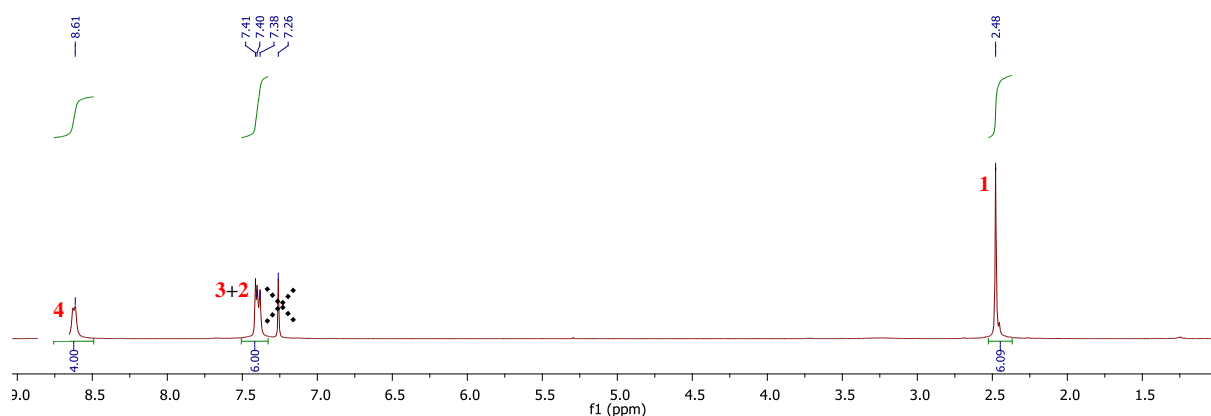


Figure 113: NMR spectrum of the pedestal **P1** in chloroform, on a 300 MHz spectrometer

On this simple spectrum, in addition to the peak of the solvent at 7.26 ppm, four other signals are displayed. The first peak at 2.48 ppm integrating for 6 corresponds to the methyl groups **1**. Then the singlet at 7.38 ppm and the doublet at 7.40 ppm correspond to the protons **2** and **3**, respectively, both integrating for 6. Finally, the last doublet at 8.61 ppm is attributed to the 4 protons **4** close to the nitrogen and thus deshielded.

The NMR spectrum of **NP** was then recorded in deuterated chloroform and is depicted in Figure 114.

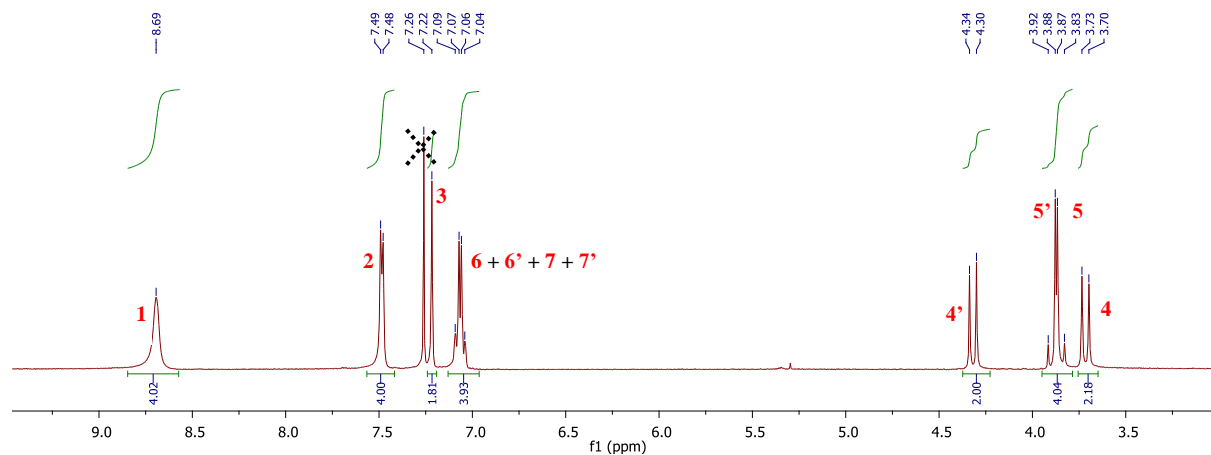


Figure 114: NMR spectrum of the pedestal **NP** in deuterated chloroform, on a 300MHz spectrometer

The attribution of the aromatic part of this spectrum was made easy by the previous study of the pedestal's NMR spectrum. Thus, the pyridine's protons **1** and **2** respectively correspond to the wide singlet at 8.69 ppm and to the doublet at 7.48 ppm, both integrating for four protons. Then the protons **3** borne by the lower deck of the cyclophane are represented by a peak at 7.22 ppm, integrating for 2. Finally, **6**, **6'**, **7** and **7'** are attributed to the close pair of doublet with a chemical shift of 7.06 ppm integrating for 4 protons. These signals are undergoing a "roof-top effect" which indicates the second order coupling occurring between **6** and **6'**, and between **7** and **7'**. This slight coupling might occur because in each pair, one is located above the alkyne (**6** and **7'**) and the other above a simple proton (**6'** and **7**). As a consequence, the deshielding of the alkyne would slightly affect one of each pair, making them lightly different. A representation of the deshielding area of the alkyne is represented in Figure 115.

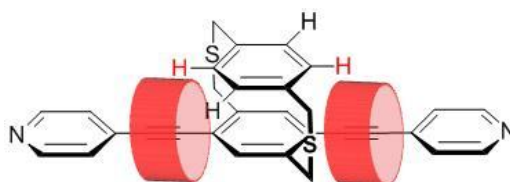


Figure 115: Deshielding effect of the alkyne unit in the naked pillar **NP**

The attribution of the second part of the spectrum, concerning the CH₂ protons of the cyclophane-bridge, is entirely based on second order couplings. Four doublets with a roof-top shape can be observed at the chemical shifts of 4.32, 3.90, 3.85 and 3.70 ppm, integrating for 2 protons each. The protons **4'** and **5'** should thus be deshielded compared to their homologues **4** and **5**. However, since **4'** is closer to the alkyne than **5'**, the effect would be enhanced. As a consequence, **5** and **5'** are respectively attributed to the pair of doublets located at 3.85 and 3.90 ppm, **5'** being slightly more deshielded than **5**. The protons **4** are the more shielded of all, and correspond to the doublet at 3.70 ppm. Finally **4'**, the most deshielded of all, is located at 4.32 ppm.

2. Infra-red

The infra-red analysis was then carried out on **P1** at the solid state, in attenuated total reflectance mode (ATR); the spectrum is displayed in Figure 116.

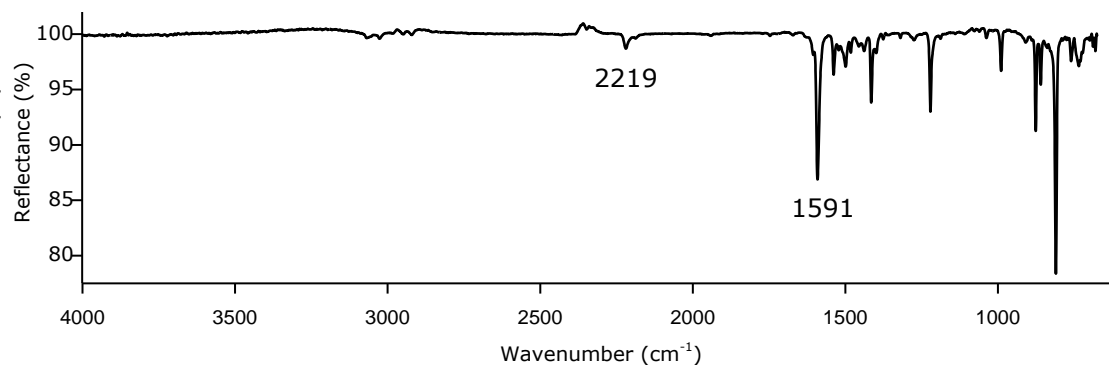


Figure 116: Infra-red spectrum of **P1** in ATR

In this spectrum, two main stretching bands are representative of the pedestal: $\nu = 2219\text{ cm}^{-1}$ corresponds to the alkyne bonds stretching whereas $\nu = 1591\text{ cm}^{-1}$ is attributed to the C-N bond stretching in the pyridine units.

The infra-red analysis was then carried out on the naked pillar **NP** at the solid state (ATR), and the spectrum is displayed in Figure 117.

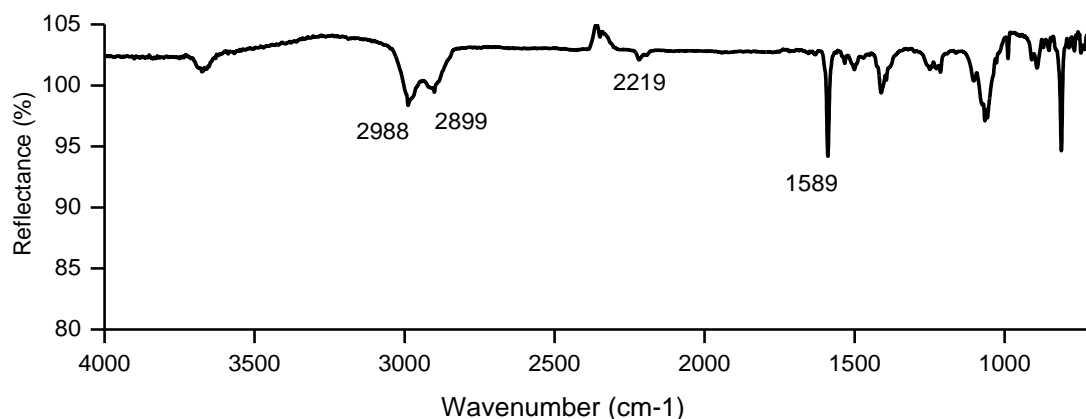


Figure 117: Infra-red spectrum of **NP** in ATR

In this spectrum, several stretching bands are representative of the naked pillar **NP**, such as $\nu = 2219\text{ cm}^{-1}$ and $\nu = 1589\text{ cm}^{-1}$ which respectively correspond to the alkyne bonds and C-N bonds' stretching bands, respectively. The incorporation of the cyclophane core did not imply much changes in these stretching bands compared to the pedestal ($\nu_{\text{alkyne}} = 2219\text{ cm}^{-1}$ and $\nu_{\text{C-N}} = 1589\text{ cm}^{-1}$). However, the bands representing the stretching of the $\text{C}_{\text{sp}^3}\text{-H}$ bonds within the cyclophane bridge are clearly visible at $\nu = 2988$ and 2899 cm^{-1} .

3. UV-Vis and fluorimetry

Later on, the absorption spectra of the pedestal **P1** and the naked pillar **NP** were recorded in dichloromethane as represented Figure 118.

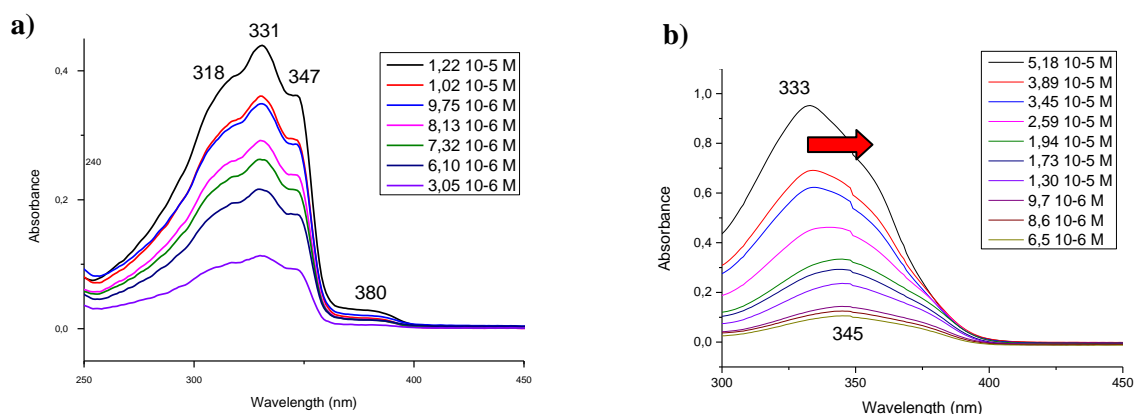


Figure 118: Absorption spectra of **P1** (a) and **NP** (b) in dichloromethane at different concentrations

In Figure 118a, the absorption spectra of **P1** were measured at different concentrations in order to calculate the molar attenuation coefficient ϵ of this compound. The spectra presented four transition bands at 318, 331, 347 and 380 nm and the band at $\lambda_{\text{max}} = 331$ nm was used to estimate the ϵ (35 500 L.mol⁻¹.cm⁻¹).

The Figure 118b presents the spectra of absorption at several concentration from $5.18 \cdot 10^{-5}$ to $6.5 \cdot 10^{-6}$ mol.L⁻¹. However, the maximum of absorption is not constant over the concentration and a redshift can be observed from 333 nm (at $5.18 \cdot 10^{-5}$ M) to 345 nm (at $1.94 \cdot 10^{-5}$ and lower concentrations). An aggregation thus takes place at concentrations above $1.94 \cdot 10^{-5}$ M. The molar attenuation coefficient was then calculated at $\lambda_{\text{max}} = 345$ nm from the low concentrations to give $\epsilon = 18\,000$ L.mol⁻¹.cm⁻¹.

The incorporation of the cyclophane core to the pedestal seems to reduce the molar attenuation coefficient from 35 500 to 18 000 L.mol⁻¹.cm⁻¹ without any significant effects on the maxima of absorption value ($\lambda_{\text{max}}^{\text{P1}} = 331$ nm and $\lambda_{\text{max}}^{\text{NP}} = 345$ nm).

The emission spectra of both pedestal **P1** and naked pillar **NP** were then recorded, as represented in the Figure 119, along with the absorption spectra.

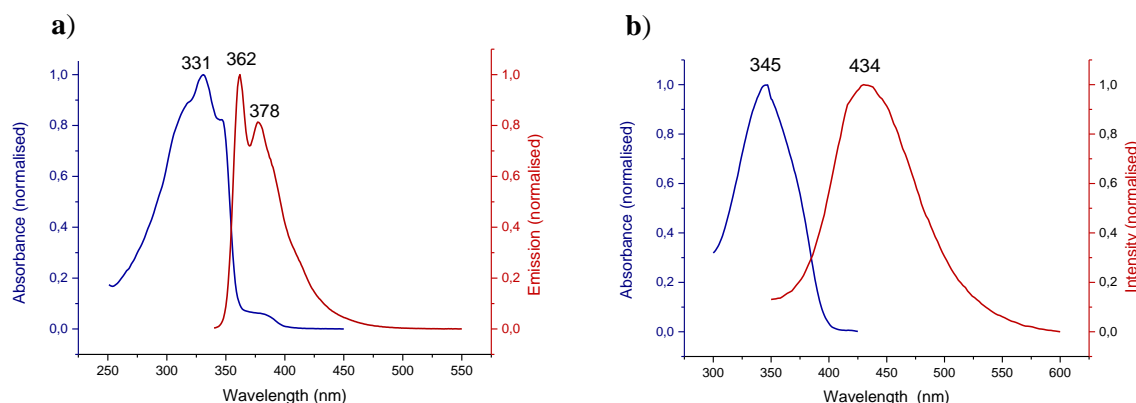


Figure 119: Absorption and emission spectra of **P1** (a) and **NP** (b) in dichloromethane

As displayed in the Figure 119a, the pedestal **P1** emits in blue with a λ_{max} of emission at 362 nm. The Stoke's shift value (difference between maxima of emission and absorption) was thus 31 nm (1100 cm⁻¹).

The emission spectrum of the naked pillar **NP** was measured at low concentration ($5.9 \cdot 10^{-6}$ M) in order to avoid any concentration effects (Figure 119b). The fluorescence of the naked pillar is redshifted from the pedestal ($\lambda_{\text{max}} = 378$ nm) and emits at $\lambda_{\text{max}} = 434$ nm. This redshift is in accordance with the increase of conjugation due to the cyclophane core. However, the Stokes shift value of 89 nm (5900 cm⁻¹) was calculated, which indicates a higher degree of reorganisation of the naked pillar **NP**'s excited state in comparison with that of the pedestal **P1** (1100 cm⁻¹).

a. Concentration-dependent emission of NP

Due to concentration effects previously observed on the absorption spectra of the naked pillar **NP**, additional concentration-dependent fluorescence studies were also carried out, as displayed in Figure 120.

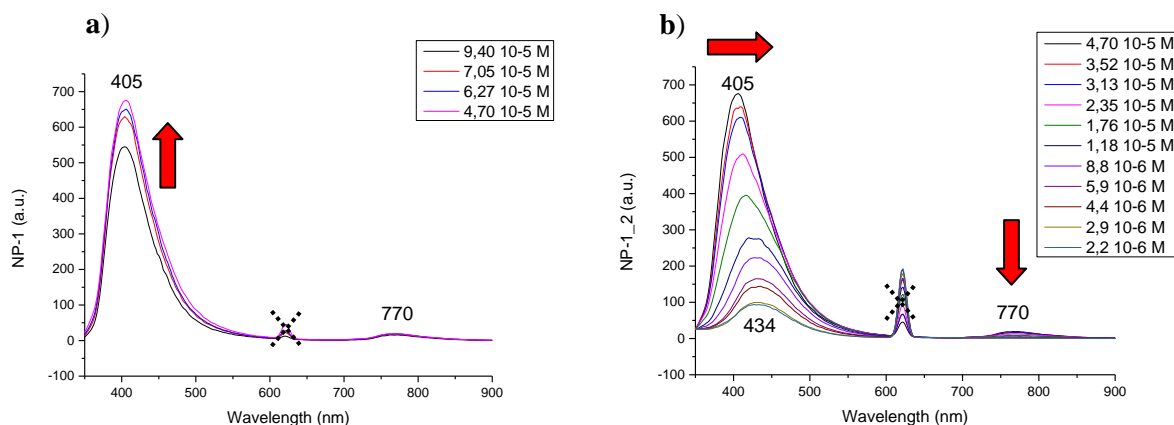


Figure 120: a) Spectra of emission from $9.40 \cdot 10^{-5}$ to $4.7 \cdot 10^{-5} \text{ mol.L}^{-1}$, b) Spectra of emission from $4.70 \cdot 10^{-5}$ to $2.2 \cdot 10^{-6} \text{ mol.L}^{-1}$. The peak at 620 nm corresponds to the second harmonic of excitation

In the first series of spectra ranging from $9.40 \cdot 10^{-5}$ to $4.7 \cdot 10^{-5} \text{ M}$ and depicted in Figure 120a, the dilution induced an increase of the intensity of fluorescence at the wavelength of 405 nm while an additional band was observed at 770 nm. Decreasing the concentration reduced the emission intensity and redshifted the maximum of emission from 404 to 434 nm where it stabilised for $5.9 \cdot 10^{-6} \text{ M}$ and lower concentrations, as displayed in the Figure 120b. Moreover, the dilution also impacted on the second band of emission which was diminished until full disappearance at the same concentration of $5.9 \cdot 10^{-6} \text{ M}$.

This behaviour suggests that at the highest concentrations, the spectra were measured on the aggregated molecules: the proximity of the molecules would then induce a blueshift of the absorption. By diluting, the concentration quenching is reduced and the fluorescence enhanced (Figure 120a). Then, the dilution slowly diminishes the aggregation and thus the spectra are shifted toward the spectrum of the isolated molecule. At $5.9 \cdot 10^{-6} \text{ M}$ (Figure 120b), the molecule could be considered as isolated, and the intensity decreases with the concentration at the same maximum of emission $\lambda = 434 \text{ nm}$.

The second emission has not been clearly identified: it can be attributed either to the formation of an excimer, slowly disappearing with the dilution, or to an artefact of the spectrometer because it corresponds to *ca.* twice the wavelength of the main emission. Anyhow, the aggregation would thus occurred for concentrations higher than $5.9 \cdot 10^{-6} \text{ M}$ which is in accordance with the previously values calculated from the absorption studies ($6.5 \cdot 10^{-6} \text{ M}$).

b. pH-dependent absorption and emission of **P1**

The pyridine units are commonly used as bases in organic reactions, thus addition of acid in the medium should protonate the pyridines and thus modify the absorption and emission spectra. A pH-dependent study was carried out (in dichloromethane) by successive additions of a solution of trifluoroacetic acid (TFA) in dichloromethane. Each addition corresponded to 0.1 equivalent of **P1** in the quartz cell, and the results are represented in Figure 121.

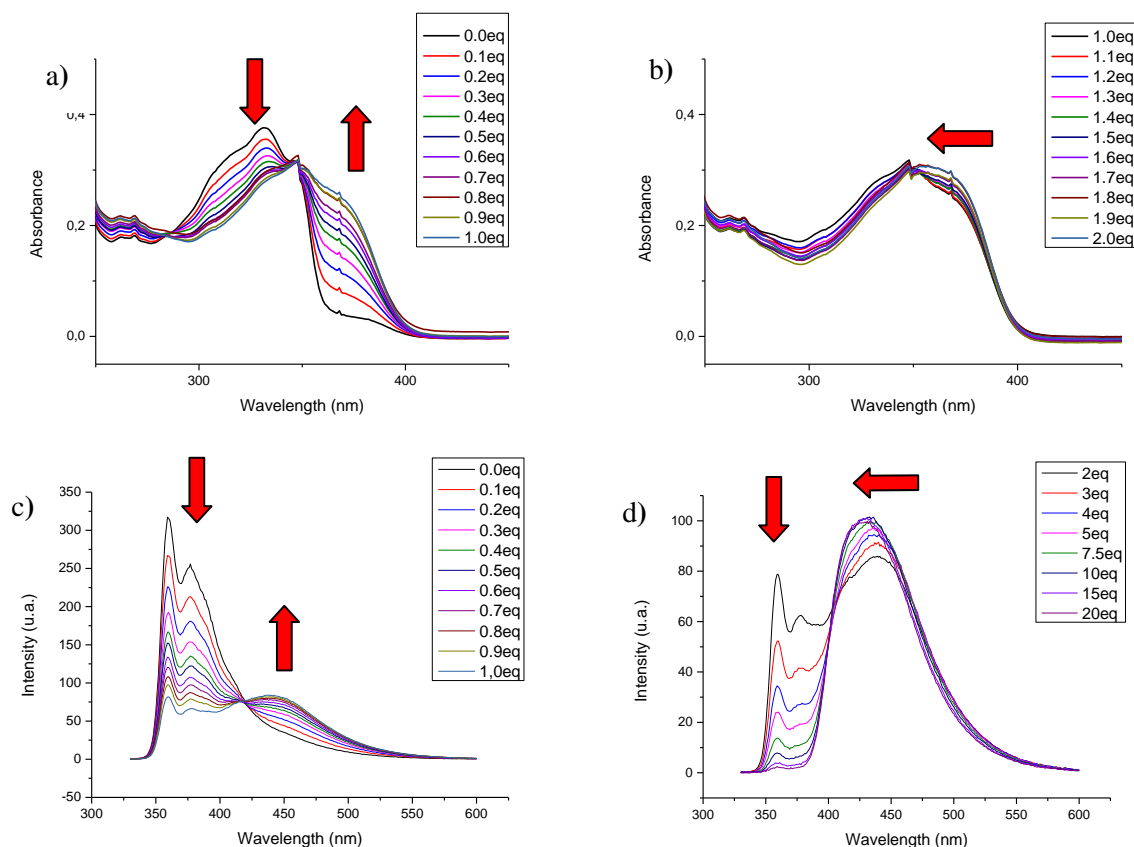


Figure 121: pH-dependent study of **P1** with (a) the spectra of absorption from the addition of 0 to 1 equivalent of TFA and (b) from 1 to 2 equivalents. (c) represents the emission spectra from the addition of 0 to 1 equivalent of TFA, and (d) from 2 to 20 equivalents

The addition of acid in the solution drastically increased the absorption band intensity at 380 nm and also reduced the two bands at 318 and 331 nm (Figure 121a) with the isobestic point located at 350 nm. Then, the increasing addition of acid allowed observing a slight blueshift of the absorption maximum from 380 to 360 nm. This hypsochromic shift was attributed to the second protonation (Figure 121b).

In the Figure 121c, the addition of acid quenched the emission of the neutral pedestal at both wavelengths 362 and 378 nm in favour of a new redshifted band at $\lambda = 439$ nm corresponding to the molecule mono-protonated. In this case, the isobestic point was located at $\lambda = 419$ nm. In accordance with the study on the absorption, the Figure 121d presents the apparition of a bis-protonated specie with a slight blueshift of the maxima of emission from 439 to 427 nm.

As expected, the protonation of the pyridine units have a strong impact on the absorption and emission spectra of the molecule. Later on, it could be interesting to study the effect of such protonation on surface at the liquid/solid interface. The addition of acid might favour or modify the supramolecular self-assembly of the pedestal **P1**.

4. Study of the pedestal **P1** as part of a supramolecular system

As mentioned before, the aim of this work was to create self-assemblies based on the co-adsorption of **P1** with different additives, depending of the targeted interaction. Therefore, preliminary studies on bulk materials were performed. The hydrogen bonding (H-bond) was expected with the terephthalic acid (**TPA**) while the coordination was tried with the bis(benzonitrile) palladium (II)

chloride (**Pd^{II}**). Finally, the attempts of halogen bonding (X-bond) were performed using 1,4-diiodobenzene (**IPhI**). All three expected supramolecular entities are represented in Figure 122 along with the predicted supramolecular bonds with the pedestal **P1**.

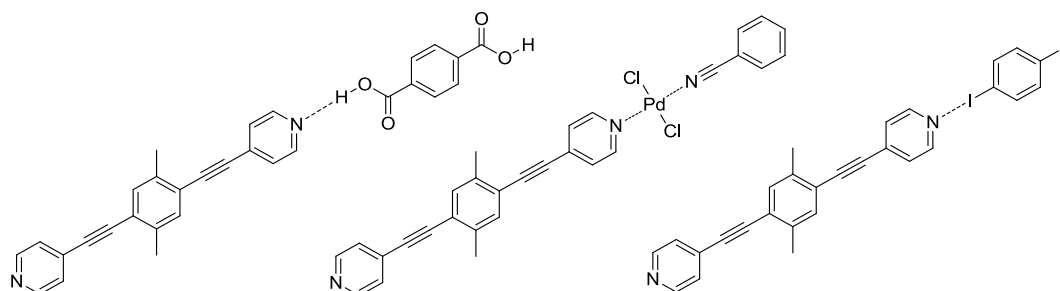


Figure 122: Expected supramolecular bonds between the pedestal **P1** and a) terephthalic acid **TPA** (H-bond), b) bis(benzonitrile) PdCl_2 **Pd^{II}** (coordination bond) and c) 1,4-diiodobenzene **IPhI** (X-bond)

The synthesis of each supramolecular assembly was performed using equimolar quantities of both reactants. **P1** and **TPA** were heated under reflux for 30 minutes in tetrahydrofuran (THF). The solution was then evaporated *in vacuo* to directly afford the supramolecular entity **P1-TPA**. The preparation of **P1-Pd^{II}** was carried out by simple addition of **Pd^{II}** to a solution of **P1** in dichloromethane. The immediate precipitation of the desired complex allowed recovering the product by simple filtration. Finally, the **P1-IPhI** was obtained by simple evaporation *in vacuo* of a solution of dichloromethane containing both precursors.

Unfortunately, the common characterisation of the supramolecular assemblies by NMR could not be performed: **P1** and **TPA** were only both soluble in polar solvent such as THF or methanol, which favoured the breaking of the H-bonds. The coordination complex **P1-Pd^{II}** was completely insoluble which limited the choice of characterisation techniques. Finally, even if **P1-IPhI** was easily solubilised in most common solvent, the pyridine unit is not a very strong acceptor of X-bond and thus hardly detected by NMR.¹⁴⁶ As a consequence, the simplest way to study the supramolecular bonds was to carry out the Infra-red analyses on bulk materials by ATR.

The IR spectra were then recorded as reported in Figure 123 along with the spectrum of the pedestal **P1** alone.

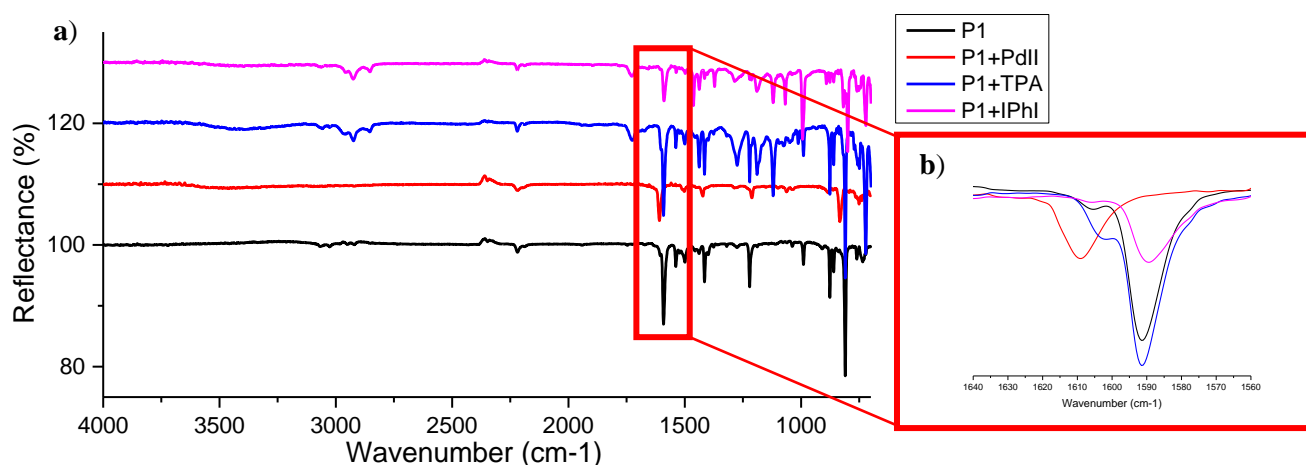


Figure 123: a) Infra-red spectra of **P1**, **P1-Pd^{II}**, **P1-TPA** and **P1-IPhI**, and b) zoom in on the C-N bond stretching

In this figure, the peak representative of the C-N stretching (1519 cm^{-1} for **P1**) within the pyridine unit is shifted in the different supramolecular assemblies. Thus, as described for different coordination

complexes in the literature,¹⁴⁷ it was possible to observe and measure the relative strength of the supramolecular bonds in each system. The values of the C-N stretching for each supramolecular entity are reported in the Table 1.

	P1	P1-Pd^{II}	P1-TPA	P1-IPhI
$\nu_{\text{C-N}} \text{ (cm}^{-1}\text{)}$	1591	1609	1591	1589

Table 1: Values of the C-N bond stretching for each supramolecular system

The stretching bond value of the C-N bond is shifted of 18 cm^{-1} in the **P1-Pd^{II}** compared to the pedestal alone. We can thus conclude to the effective formation of the coordination bonds. However, considering the weak evolution of the stretching bond value in **P1-IPhI**, the halogen bonding is only suspected. Unfortunately, the hydrogen bond in **P1-TPA** could not be observed. There are two possible explanations for this absence of shift: first, the procedure to prepare the compound may not be efficient and thus the expected supramolecular product was not obtained. Second, the pedestal may naturally display hydrogen bonds between the pyridine unit and the methyl group of its *p*-xylene core. As a consequence, the pedestal alone could already present the signal of a hydrogen bonded pyridine. This second hypothesis would be in accordance with the negative shift for the halogen bond (weaker than the H-bond) and the positive shift of the coordination bond (stronger than the H-bond).

The observation of the supramolecular entities at the liquid/solid interface should be carried out by STM in order to confirm the presence of hydrogen-bonding in **P1-TPA** and also to observe the potential self-assembly of **P1-Pd^{II}** and **P1-IPhI** on surface.

B. Scanning probe microscopy

1. Self-assembly of the pedestal **P1** on HOPG

The scanning tunneling microscopy (STM) was first used to observe the self-assembly of the pedestal **P1** at the liquid/solid interface. The experiments were performed in collaboration with Dr. Fabrice CHARRA at the CEA of Saclay. A solution of **P1** was first prepared at a concentration of $10^{-3} \text{ mol.L}^{-1}$ and was then deposited on the surface. The sample was heated at 80°C for ten minutes and then a drop of phenyloctane was added onto the dried sample before starting the experiments. This last drop of phenyloctane was necessary to keep the tip of the microscope inside the solution and avoid its oxidation by the air. A clear picture of the self-assembly on surface is depicted in Figure 124.

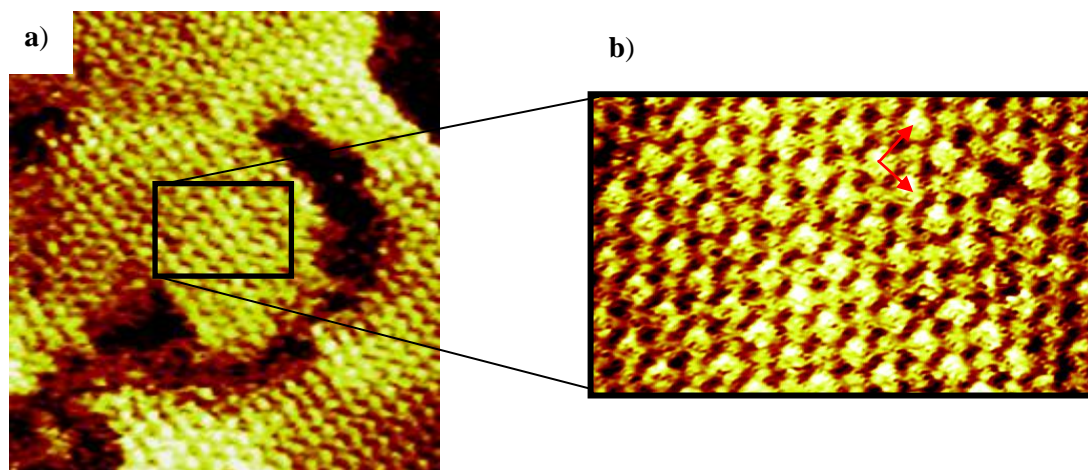


Figure 124: STM pictures of **P1** on HOPG. a) $50 \times 70 \text{ nm}$, $V_{\text{bias}} = 670 \text{ mV}$, $I = 14 \text{ pA}$, b) $25 \times 15 \text{ nm}$, $V_{\text{bias}} = 1370 \text{ mV}$, $I = 14 \text{ pA}$

The Figure 124a shows ordered 2D domains formed by assembly of the pedestal **P1**. The bright dots represent the molecules organised as quasi-square unit cells. The lattice could be observed more accurately by zooming on the monolayer as depicted by Figure 124b. The unit cell dimensions are $a = 2.1$ nm, $b = 2.2$ nm and the angle $\alpha = 94^\circ$.

In Figure 125a, the space-filling molecular model of **P1** self-assembly is stacked to the previous STM image in order to have a better view of molecular organisation on HOPG. In contrast, the Figure 125b represents the molecular structures superimposed on the graphite's first layer.

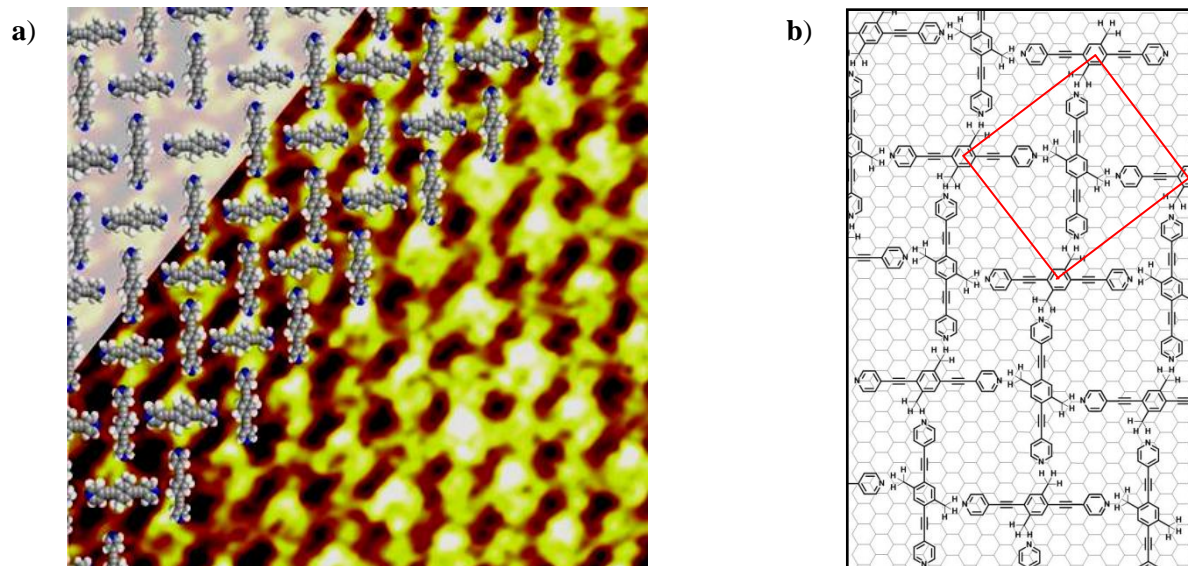


Figure 125: a) Space-filling molecular model of **P1** self-assembly superimposed to the STM image, and b) representation of the pedestal's network on HOPG

As presented by the Figure 125a, the horizontal pedestals are easily detectable as bright yellow dot. However, the vertical molecules are almost indiscernible. This phenomenon can be explained by looking at the Figure 125b where the graphite structure is represented below the network of **P1**. The horizontal molecules are well stacked on the underlying structure in contrast with the vertical ones which seem to be adsorbed without any special interactions with the surface. As a consequence, when the tip of the STM scanned the surface, the horizontal molecules were conducting the current in a better manner than their vertical homologues and thus the signal was stronger, as proven by the brightness of the dots.

Considering the organised system absorbed on the surface, the network seems to be driven by hydrogen bonds between the pyridine units and the methyl groups on the core of the molecule. Moreover, due to the squared-lattice, the 2D-structure does not follow the hexagonal underlying network of the graphite. This suggests that the self-assembly is stable enough to occur without additional assistance of the substrate. This type of behaviour has already been observed in other type of molecules such as the squaraines, mentioned before (Chapter 1, Figure 37).⁶² These molecules represented in Figure 126a are known to self-assemble in the same manner due to strong hydrogen bonds between its proton-donor extremities and its negatively charged core. The model of the 2D network based on squaraines is depicted in Figure 126b.

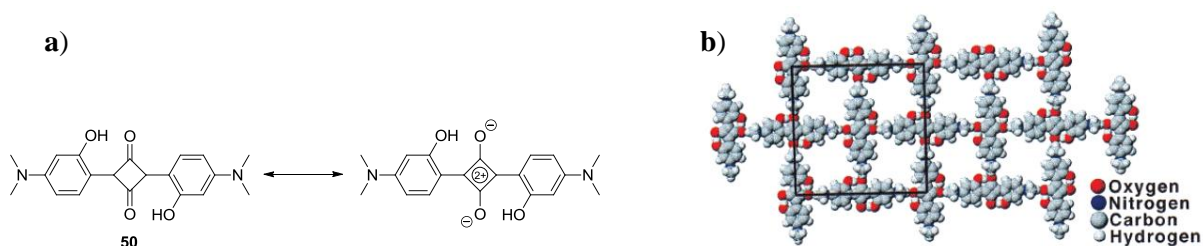


Figure 126: a) Molecular structure of the dimethyl hydroxylated squaraines and b) Molecular model of the herringbone structure

The pedestal **P1** is thus self-assembling as 2D-monolayered domains on HOPG by hydrogen bonding without any assistance of the substrate. This behaviour indicates the presence of strong intermolecular interactions and thus the self-assembly pattern might not be affected by the substrate.

Later on, the supramolecular entity **P1-Pd^{II}**, previously studied by infra-red spectroscopy, was deposited on HOPG. However, the necessity of solubilising the molecules before deposition on surface has complicated the preparation of the samples. The on-surface complexation was then attempted by the successive additions of **P1** and then **Pd^{II}**, separately dissolve in dichloromethane. However, until now, no clear picture of 2D-monolayers could be recovered.

2. Self-assembly of the naked pillar NP on Au(111)

Several attempts of supramolecular self-assembly of the naked pillar **NP** were performed on Au(111) surface. Based on the previous results using the pedestal **P1**, the concentration of the **NP** solution was precisely calculated for one drop to correspond to a monolayer of molecules on surface ($1.8 \cdot 10^{-6}$ M). We have then carried out preliminary studies of the self-assembly by Atomic Force Microscopy (AFM) in collaboration with Dr. Imad Arfaoui in the Monaris laboratory (UPMC).

The AFM studies are commonly carried out to observe the topography of a substrate. In the case of organic molecules, an ultra-thin tip had to be used in order to detect such fragile layer on top of the Au(111) substrate. The first picture so-obtained are represented in Figure 127.

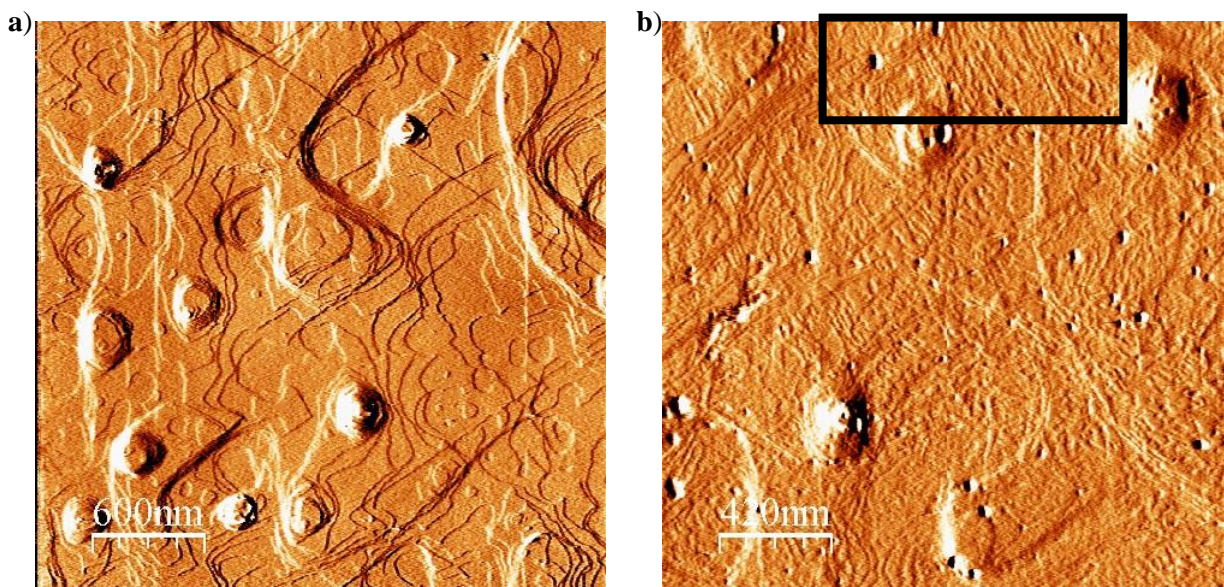


Figure 127: AFM picture of a) the Au(111) surface and b) the same surface after deposition of the **NP** solution using an ultra-thin tip (65 kHz, 0.5 N/m).

The Figure 127a depicts the Au(111) surface before deposition of the organic layer. The resolution allows observing the different mono-atomic layer terraces of the substrate. On the second figure, the same substrate was imaged after deposition of the **NP** layer. The topography of the surface drastically changes and the terraces are no longer observable. The layer of naked pillar is definitely adsorbed on the surface but the self-assembly is hardly observable. The black square drawn on the Figure 127b presents some parallel lines which could not be attributed to the underlying substrate. Moreover, the height of these lines reaches 0.4 Å, which corresponds to the height of the cyclophane core (0.3-0.4 Å). The resolution of the AFM was not high enough to observe these objects at the atomic scale. However, these images are consistent with the presence of a supramolecular self-assembly on Au(111). Additional studies by STM will be carried out to confirm this hypothesis.

Conclusion

In this chapter, we designed and synthesised new molecular architectures based on the 3D Janus tecton concept, suitable for self-assembly on surface by supramolecular interactions such as coordination, halogen bond or hydrogen bond. We proposed three different pyridyl end-capped molecules: the pedestal **P1**, the pedestal incorporating a cyclophane core **NP** and the Janus tecton **JT** incorporating an active unit at the upper deck of the cyclophane. After the attempt of several synthetic routes, the pedestal **P1** and the naked pillar **NP** were finally obtained in four and nine steps with an overall yield of 71% and 8%, respectively. The synthesis of the Janus tecton **JT** could not be achieved in time to report the final step which will be carried out soon.

The pedestal **P1** was then characterised by NMR and infra-red spectroscopies, and the absorption and emission properties were then studied. The maxima of absorption and emission were measured at 331 nm and 362 nm, respectively. The pH-dependent absorption and emission were also studied on the pedestal. The first protonation of the pyridine unit could be easily observed as a redshift of the maxima of the absorption (331 → 380 nm) and the emission (362 → 439 nm) with an isobestic point at 350 and 419 nm, respectively. The second protonation was then detected as a slight blueshift of the absorption (380 → 360 nm) and the emission (439 → 427 nm) but the isobestic point could not be accurately estimated.

The complexation of **P1** with complementary entities (palladium II dichloride, terephthalic acid and 1,4-diiodobenzene) to form supramolecular network was also investigated by infrared spectroscopy in solid state. As a conclusion, the coordination with **Pd^{II}** was observed by a strong shift of the C-N bond stretching of the pyridine unit compared to the pedestal alone (1591 → 1609 cm⁻¹). The halogen bond interactions with 1,4-diiodobenzene were slightly observed (1591 → 1589 cm⁻¹) which would be consistent with the very weak character of such bond. Finally no shift of the stretching bond could be observed from the hydrogen-bond, which would imply the absence of such supramolecular interactions or more probably that the pedestal already makes hydrogen bonds with itself in solid state.

The naked pillar **NP** was also studied by NMR and infra-red spectroscopies. The NMR studies presented an interesting deshielding of the protons located directly above the alkyne groups on the upper deck of the cyclophane core. The absorption and emission spectra of **NP** presented the maxima at 345 and 434 nm, respectively. However, by increasing the concentration, and aggregation induced hypsochromic shift of the maxima of absorption (345 → 333 nm) and emission (434 → 405 nm) was observed, as well as an additional emission band at 770 nm attributed to the emission of an excimer of **NP**.

Finally, different attempts of supramolecular self-assemblies were carried out on surface. The behaviour of the pedestal **P1** was first investigated by STM at the liquid/solid interface. The arrangement of the molecules on HOPG presented a quasi-square lattice ($a = 2.1$ nm, $b = 2.2$ nm, $\alpha = 94^\circ$) self-assembled by hydrogen bonds between the pyridine unit and the methyl groups borne by the *p*-xylene core. The quasi-square lattice was indicating strong intermolecular interactions between the molecules **P1** leading to a supramolecular self-assembly independent of the underlying HOPG structure.

Second, the naked pillar **NP** was deposited on gold substrate (Au(111)) and some preliminary observations were performed by AFM. The supramolecular self-assembly could be assumed by meticulous study of the images and the observation of small domains of long parallel lines.

To conclude, the first results of self-assembly on surface of both pedestal **P1** and naked pillar **NP** on HOPG and Au(111), respectively, are encouraging. We are thus confident that the future Janus tecton **JT** might also self-assemble on the same substrates.

In the perspective of future work, the synthesis of both naked pillar **NP** and Janus tecton **JT** allows the easy tuning of the function responsible of the self-assembly. The pyridine units could therefore be replaced by a benzoic acid derivative for example. The main objective of such replacement would be the co-adsorption of both acid- and pyridine-derived Janus tectons, leading to a well-defined 2D-alternating copolymer on surface. Then, the grafting of electron-donor and acceptor groups atop of the pyridine- and acid-derivatives, respectively, would allow the well-defined alternation of donor and acceptor groups upon the surface, as represented in Figure 128. Surface quenching being limited by the design of the Janus tectons, the electronic properties of such copolymers could be studied, like on-surface intermolecular charge transfer.

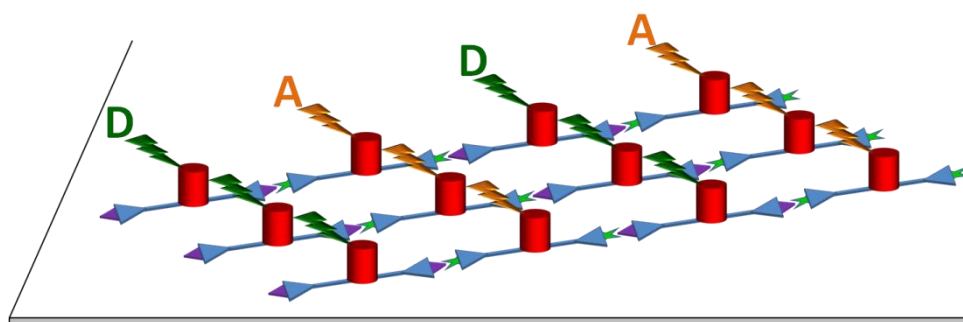


Figure 128: Towards well-defined alternation of donor/acceptor (D/A) groups upon surface

- ¹²² Errede, L. A.; Gregorian, R. S.; Hoyt, J. M. *J. Am. Chem. Soc.* **1960**, *82*, 5218–5223.
- ¹²³ Hopf, H. *Angew. Chemie Int. Ed.* **1972**, *11*, 419–420.
- ¹²⁴ Winberg, H. E.; Fawcett F. S. *Org. Synth.* **1962**, *42*, 83.
- ¹²⁵ Vögtle, F. *Angew. Chemie Int. Ed.* **1969**, *8*, 274–274.
- ¹²⁶ Bléger, D.; Kreher, D.; Mathevet, F.; Attias, A. J.; Arfaoui, I.; Metgé, G.; Douillard, L.; Fiorini-Debuisschert, C.; Charra, F. *Angew. Chemie - Int. Ed.* **2008**, *47*, 8412–8415.
- ¹²⁷ Bakhma, A.; Laboratory of Polymer Chemistry (LCP), Pierre and Marie Curie University (UPMC), Paris, France. Thesis, 2012, January.
- ¹²⁸ Tait, S. L.; Langner, A.; Lin, N.; Stepanow, S.; Rajadurai, C.; Ruben, M.; Kern, K. *J. Phys. Chem. C* **2007**, *111*, 10982–10987.
- ¹²⁹ Surin, M.; Samorì, P.; Jouaiti, A.; Kyritsakas, N.; Hosseini, M. W. *Angew. Chemie - Int. Ed.* **2007**, *46*, 245–249.
- ¹³⁰ Adam, W.; Grimison, A.; Hoffmann, R.; Zuazaga de Ortiz, C. *J Am Chem Soc* **1968**, *90*, 1509–1516.
- ¹³¹ Fan, H.; Eliason, J. K.; Moliva A., C. D.; Olson, J. L.; Flancher, S. M.; Gealy, M. W.; Ulness, D. J. *J. Phys. Chem. A* **2009**, *113*, 14052–14059.
- ¹³² Sonogashira, K.; Tohda, Y.; Hagihara, N. *Tetrahedron Lett.* **1975**, *16*, 4467–4470.
- ¹³³ Carpino, L. a.; Sau, A. C. *J. Chem. Soc., Chem. Commun.* **1979**, *11*, 514–515.
- ¹³⁴ Glaser, C. *Chem. Ber* **1869**, *2*, 422–424.
- ¹³⁵ Hay, A. S. *J. Org. Chem.* **1962**, *27*, 3320–3321.
- ¹³⁶ Djerassi, C. *Chem. Rev.* **1948**, *43* 271–317.
- ¹³⁷ Jin, Z.; Lu, Y.; Li, S.; Li, Z. *Synth. Commun.* **2014**, *44* (1), 82–88.
- ¹³⁸ Stacy, G. W.; Papa, A. J.; Villaescusa, F. W.; Ray, S. C. *J. Org. Chem.* **1964**, *29* (3), 607–612.
- ¹³⁹ Gray, B. D.; Jeffs, P. W. *ChemInform* **1988**, *19*, 454–456.
- ¹⁴⁰ Wuts, P. G. M.; Greene, T. W., *Greene's protective groups in organic chemistry (4th ed.)* **2007**, 651.
- ¹⁴¹ Jeong, H. J.; Yoon, E. Y.; Kim, M. K.; Lee, J. H.; Yoon, Y. J.; Lee, S. G. *Bull. Korean Chem. Soc.* **2003**, *24*, 1689–1691.
- ¹⁴² Fowelin, C.; Schüpach, B.; Terfort, A.; Schupbach, B. *European J. Org. Chem.* **2007**, *2007*, 2–11.
- ¹⁴³ Hennrich, G.; Lynch, V. M.; Anslyn, E. V. *Chem. - A Eur. J.* **2002**, *8*, 2274–2278.
- ¹⁴⁴ Hudson, H. R.; Kinghorn, R. R. F.; Murphy, W. S. *J. Chem. Soc. C.* **1971**, 3593–3596.
- ¹⁴⁵ Heiskanen, J. P.; Vivo, P.; Saari, N. M.; Hukka, T. I.; Kastinen, T.; Kaunisto, K.; Lemmetyinen, H. J.; Hormi, O. E. O. *J. Org. Chem.* **2016**, *81*, 1535–1546.
- ¹⁴⁶ Dumele, O.; Wu, D.; Trapp, N.; Goroff, N.; Diederich, F. *Org. Lett.* **2014**, *16*, 4722–4725.
- ¹⁴⁷ Perelygin, I. S.; Klimchuk, M. A. *J. Appl. Spectrosc.* **1976**, *24* (1), 43–46.

CHAPTER 3:

TOWARD CYCLOPHANE-BASED TADF MATERIALS

As previously mentioned, the TADF concept aims at enhancing the electroluminescence of a molecule by harvesting both singlet and triplet excitons (Chapter 1, Figure 71). This phenomenon may occur if two main prerequisites are gathered: a high photoluminescence quantum yield (PLQY) and a low electronic gap between first excited singlet and triplet state ($\Delta E_{ST} < 0.4$ eV). These conditions are usually fulfilled by using finely tuned donor-acceptor molecules where the overlap of the HOMO and LUMO is reduced by separating the electron-donor from the acceptor of the molecule. However, the low overlap of the frontier orbitals contributes to lower the oscillator strength f of the absorption transition, leading to an ineffective absorption and thus to a low brightness (defined as the product of the absorption capability by the PLQY). As a consequence, finely tuning the molecular structure of the TADF emitter is required in order to have a balance between high PLQY and low ΔE_{ST} . This objective is usually achieved by using different structural approaches for the design of molecules; for example the twist of the carbazolyl units in the multi-carbazolyl dicyanobenzene of Uoyama *et al.*¹⁶, or the σ -bond in the spirobifluorene of Nakagawa *et al.*¹⁷, both represented in Figure 129.

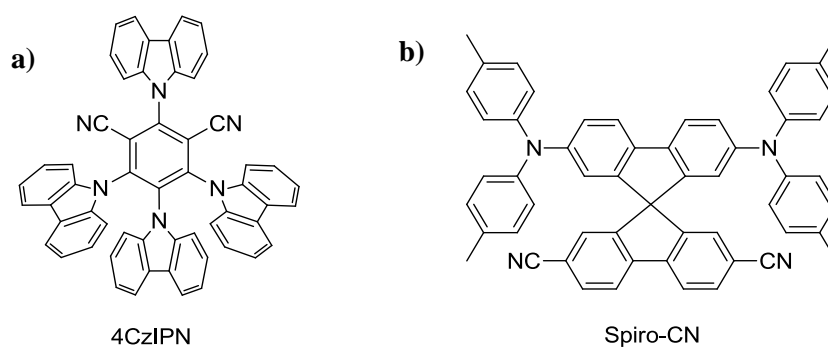


Figure 129: Representation of the molecular structure of Uoyama¹⁶ (a) and Nakagawa¹⁷ (b) TADF molecules

In this context, we propose to test the cyclophane as key unit to induce small energy gap between singlet and triplet states in donor-acceptor molecules to try to obtain TADF property: indeed, our previous work on surface demonstrated the effective decoupling of one deck of the cyclophane from the other (Chapter 1, Figure 59) while other articles from the literature illustrate through-space conjugation between the two phenyls (Figure 18). Thus, by grafting donor and acceptor units on different decks of the cyclophane, we expected to separate HOMO and LUMO while maintaining a slight conjugation between the two entities through the cyclophane unit. The design of the target molecule has been first intensively studied by theoretical calculations by tuning the nature of the electron-donor and acceptor in order to reach the lowest theoretical ΔE_{ST} . One of the best candidates was then chosen as the emitter **E** depicted in Figure 130a. One deck of the cyclophane core is bearing the donor moiety (ditolylphenylamine unit) whilst the opposite deck bears the nitrile functional groups acting as acceptors. In this molecule, the frontier orbitals (HOMO and LUMO) are efficiently separated as represented by the Figure 130b.

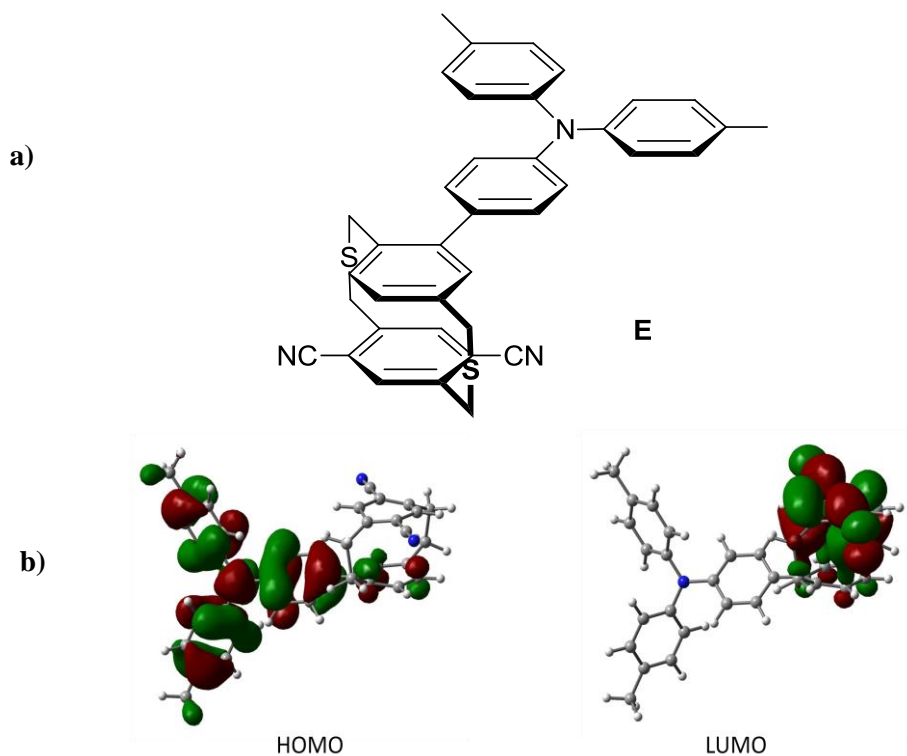


Figure 130: Structure of the emitter **E** with its calculated HOMO and LUMO representations

From these structures a high reverse inter-system crossing (RISC) was expected because of the very low ΔE_{ST} (estimated at 0.02 eV). The full synthetic pathway is developed in the first part of this chapter. Then, the second part describes the characterisations (NMR, X-ray and photophysics studies) and the theoretical calculations carried out on the molecule.

I. Design and synthesis

The synthesis of the emitter **E** has not been straightforward: several synthetic pathways were attempted before finally succeeding. The chemistry routes can be regarded as two main strategies **A** and **B** detailed in the following pages: the first one was using palladium cross-coupling catalyses on different synthons in order to graft the donor moiety on the top of the cyclophane core. The second strategy consisted in playing with halogen substituents (fluoride, bromide and iodide) to attach the donor unit on the rest of the molecule. Both strategies are depicted in Figure 131.

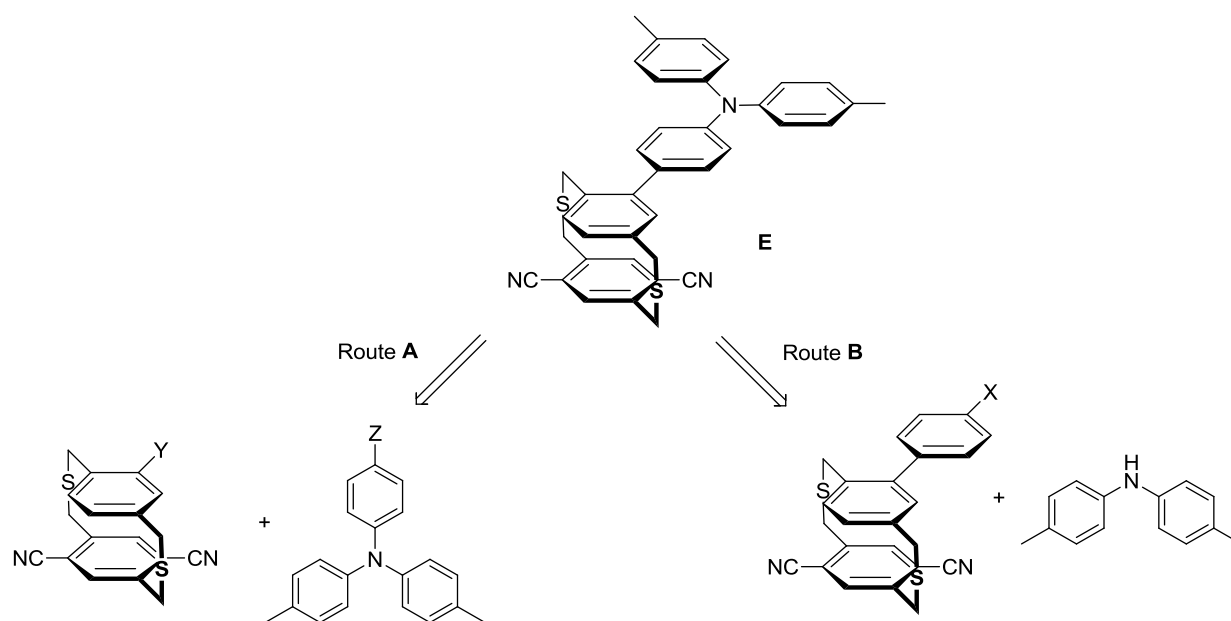


Figure 131: Retrosynthetic pathways towards the emitter **E** (Y= Br or SnBu₃, X= I, Br, or F, Z= Br, SnBu₃ or B(OH)₂)

Strategy A. Palladium forever

This first strategy can be divided in two parts: on one hand, the synthesis of the cyclophane core and in a second stage the use of palladium cross-coupling reactions to make the donor moiety and to finally graft it onto the core to form the target emitter **E**. Following the route **A**, the synthetic pathway towards the desired cyclophane core can be described by a succession of four steps: the preparation of the lower deck, then the upper deck before closing the cyclophane, and finally the synthesis of the electron-donor moiety and its grafting to the rest of the molecule.

1. Synthesis of the lower deck building block

The synthesis of the lower deck started by the cyanation of the 1,4-dibromo-*p*-xylene with copper cyanide in refluxing DMF, as represented in Figure 132.¹⁴⁸ Iron trichloride in diluted hydrochloric acid was then added to quench any trace of copper cyanide. Later on, we first followed the procedure described in the literature consisting in a painful extraction of the compound with ethyl acetate and a washing with water before purification by chromatography to afford the compound **37** in 30 to 50% yield. However, simply pouring the solution into a large amount of water was enough to make the desired compound to precipitate. The mixture was thus filtered off, and the crude solubilised in dichloromethane and washed with water to afford **37** in 91% yield.

The next step depicted in the same figure was targeting the bis-brominated derivative **38**. As studied by Huang *et al.*, this reaction is known to give a mixture of the mono-, bis-, and tris- brominated derivatives in various yields and hard to separate.¹⁴⁹

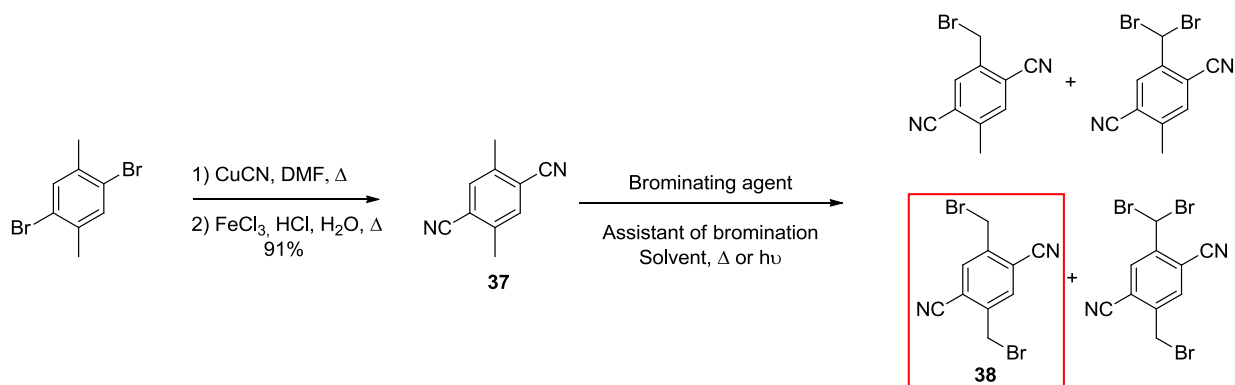


Figure 132: Synthesis of the lower deck **38**, with the by-products of the bromination of **37** by Huang *et al.*

According to Huang and co-workers, the desired bis-brominated compound was obtained with a HPLC yield of 30%, in the best conditions depicted in the first line of the following Table 2. However, after purification by chromatography, **38** was isolated in 10 to 20% yield. Thus, several conditions were tried in order to optimise the efficiency of the reaction. The results of the conditions screening are summarised in the Table 2.

Bromide source	Number of equivalents	Assistant of bromination	Percentage of assistant	Solvent	Conditions	Yield (%)
NBS	2.1	BPO	5	CCl ₄	Reflux	10-20
NBS	2.5 to 5	AIBN	5-10	CHCl ₃ or CH ₃ CN	Reflux	0 to 40
NBS	2,2	TiCl ₄	10 to 80	CH ₂ Cl ₂	Reflux	0 to 4
NBS	2.5+2.5	-	-	CHCl ₃	Reflux	20
Br ₂	5 to 12	-	-	1,2,4-trichlorobenzene	Reflux	0 to 20
NBS	2.5	AIBN	5	CHCl ₃	UV	10
NBS	2.5	-	-	CHCl ₃	UV	6 to 37
NBS	2+1.5	-	-	CHCl ₃	UV	14 to 23
NBS	2.5+2.5	-	-	CHCl₃	UV	10 to 52

Table 2: Reaction conditions of the bromination of **37** into **38**

In this table, most reactions were carried out using NBS as source of bromides because pure bromine has never given any viable results. The NBS amount was either directly added when the reaction was initiated, or in two small portions at the beginning and in the middle of the reaction. Some assistant of bromination were first used like AIBN, BPO (benzoyl peroxide) or TiCl₄ but it seemed that the NBS did not need any additional activation: the reflux or the UV radiations were enough.

In conclusion, the highest yields were obtained in a sealed Schlenk tube under UV, using **37** in chloroform without radical initiator and by introducing NBS at the beginning and in the middle of the 1 hour-reaction under UV irradiation. **38** was then recovered in variable yields, from 10 to 52%; by this method, higher but irregular yields were obtained but this new pathway was also affording an additional tetrabromo-substituted by-product. Nevertheless, careful chromatography purification afforded the pure product **38** and thus the next steps could be carried out.

The third and last step of synthesis of the lower deck of **E** was the thiolation. The reaction was performed as previously mentioned by using thiourea, then potassium hydroxide and sulphuric acid to afford **39** in 90 % yield, as depicted in Figure 133. However the extremely low solubility of **39** made any further reaction difficult to carry on, thus it was decided to mainly use the derivative **38** to form the cyclophane with the thiol derivative of the upper deck yet to synthesise.

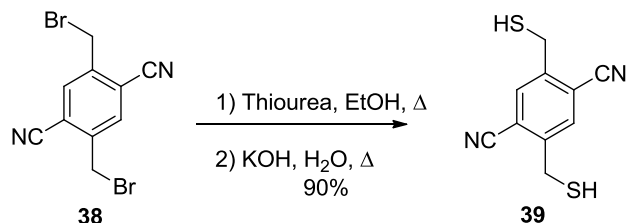


Figure 133: Synthesis of **39**

2. Synthesis of the upper deck building block and cyclophane formation

The synthetic route for the preparation of the upper deck was using classic reactions previously developed: first the bromination with NBS and AIBN in refluxing acetonitrile affording **40** in 72% yield, and then the thiolation with thiourea and potassium hydroxide giving the bis-thiol **41** in 50% yield. These two reaction steps are depicted in Figure 134.

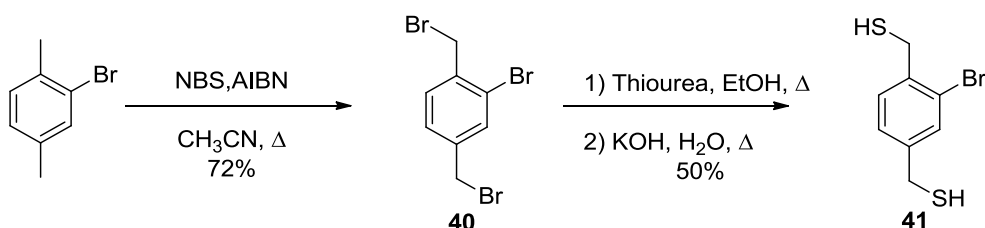


Figure 134: Synthesis of the upper deck of the cyclophane core

The cyclophane is then obtained by adding dropwise the bis-brominated compound **38** and the bis-thiol derivative **41** into a large volume of a solution of potassium hydroxide in methanol to afford the cyclophane **42** as a mixture of two structural isomers (staggered **42-sta** and eclipsed **42-ecl**) in 82 % yield, as represented in Figure 135. The cyclophane **42** was finally attacked at low temperature by *n*-butyl lithium followed by tributyltin chloride to afford **43** (**sta** and **ecl**). These tin-derivatives will be useful to try the palladium catalysed Stille reaction. As the products were used for the next step without further purification, the yield was not calculated but estimated to be quantitative.

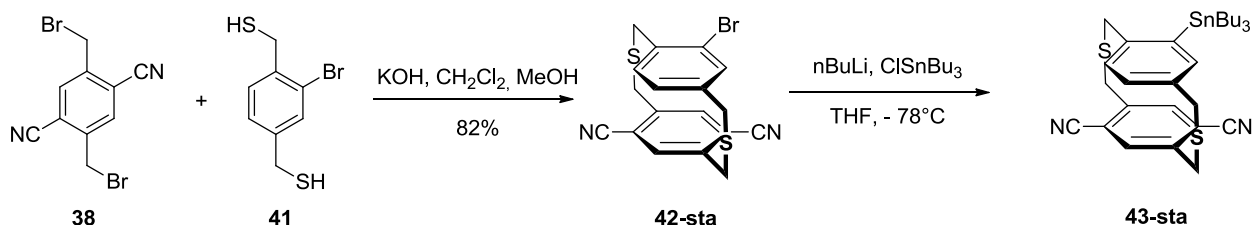


Figure 135: Cyclisation of the cyclophane **42**, and preparation of the tributyltin derivative **43**. (only the staggered isomers are represented)

The next steps concern the synthesis of first the ditolylphenylamine donor and then the final grafting on the cyclophane previously synthesised. These reactions were carried out by organometallic couplings using copper chloride or palladium (II) derivatives as catalysts.

3. Synthesis of the electron-donor ditolylphenylamine building block

As previously mentioned in the Chapter 1, the reactivity of the cyclophane derivatives is reduced by the steric hindrance of the benzene rings π -stacking. As a consequence, several donor units were synthesised in order to investigate different synthetic pathway (Ullmann, Still and Suzuki couplings) towards the final molecule **E**.

The first synthons was prepared from ditolylamine and 1-bromo-4-iodobenzene by using a copper-phenanthroline catalyst and potassium hydroxide in a Ullmann-type reaction to afford the brominated amine **44** (67% yield). Then, the treatment of **44** by *n*-butyl lithium and tributyltin chloride afforded the stannane derivative **45** in quantitative yield, as presented in Figure 136. Finally, the boronic acid synthon **46** was synthesised from ditolylamine and *p*-iodophenylboronic acid once again by Ullmann-type reaction in 25% yield.

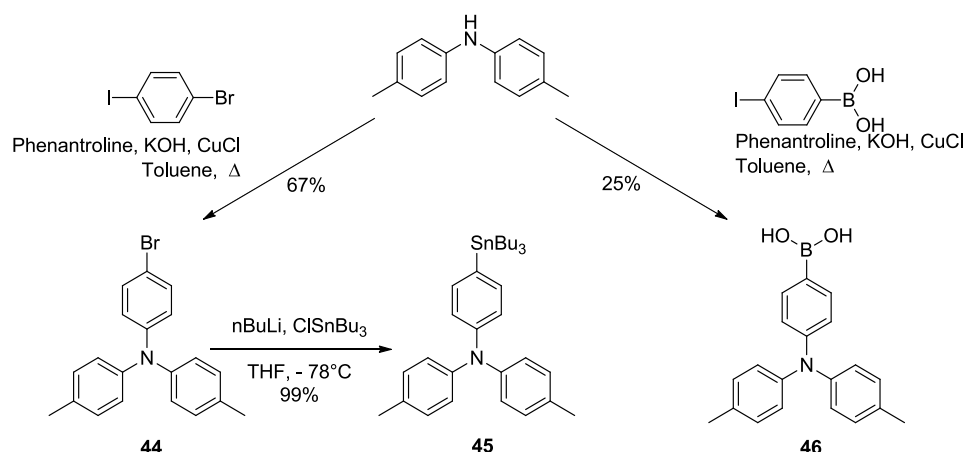


Figure 136: Preparation of the different electron-donor units **44**, **45** and **46**

4. Disappointing cross-couplings

Once the last synthons were prepared, we tried to couple them in order to obtain **E**. The different tested cross-coupling reactions are summarised in Figure 137.

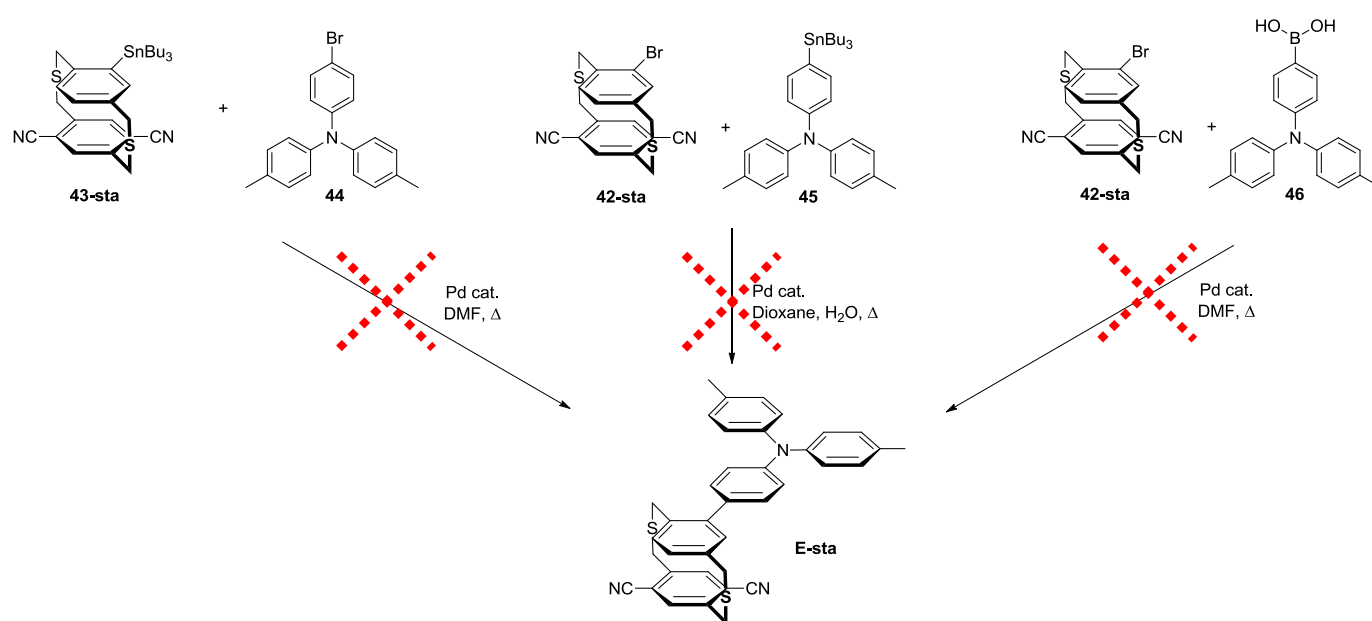


Figure 137: Palladium catalysed cross-coupling toward **E** (only the staggered isomers of **E**, **42** and **43** are represented)

The reaction of Stille was first tried between the derivatives **42** and **45** using $\text{PdCl}_2(\text{PPh}_3)_2$ or $\text{Pd}(\text{OAc})_2 + \text{PPh}_3$ as catalyst in THF or toluene without any success: thin layer chromatography was showing rainbows of fluorescent products, but the ^1H NMR analyses were not giving any clear information about the structure of the so-obtained molecules. The only identified compound recovered was the product of homocoupling of the ditolylphenylamine represented in Figure 138.

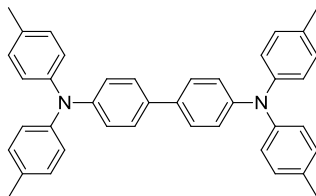


Figure 138: Homocoupling product of the Stille reaction

The second coupling, once again of Stille type, between **43** and **44** showed equivalent results: numerous fluorescent products, but in too little quantity to really characterise them. However, some reactant **44** was recovered after purification by chromatography.

Finally, the Suzuki coupling of **42** and **46** in a mixture of dioxane and water allowed us only to recover half of the reactant **42** introduced for the reaction.

To conclude, what was proven in the Chapter 2 is also confirmed here: the cyclophane derivatives are not good candidates for direct organometallic couplings. Thus, a second route was proposed in order to avoid doing cross-coupling reactions directly on the upper deck of the molecule.

Strategy B. The halogens game

As introduced above in the retrosynthetic scheme in Figure 131, this strategy aims at removing the reactive site from the upper deck by inserting the phenyl spacer before finally grafting the ditolylamine on the molecule. This final step could be performed using several reactions: nucleophilic aromatic substitution, Ullmann-type reaction or palladium-catalysed Buchwald-Hartwig coupling. One halogen derivative was thus chosen according to the targeted reaction, as described in the following parts.

1. Good old fashioned fluoride

Using the nucleophilic aromatic substitution reaction, some TADF-molecules were synthesised by direct attack of the electron-donor amines on the molecule's core substituted by fluorides.¹⁶ The same procedure was thus attempted to obtain the target molecule **E**. Therefore the synthesis of the upper deck had to be modified from the beginning to introduce the fluorophenyl unit as presented in Figure 139.

The compound **47** was first obtained in quantitative yield by Suzuki coupling between 2-bromo-*p*-xylene and *p*-fluorophenylboronic acid using $\text{PdCl}_2(\text{PPh}_3)_2$ as catalyst. The bromination of **47** was then carried out in acetonitrile using NBS and AIBN to afford **48** in 66% yield. Later on, the thiolation was performed as usual, using thiourea, potassium hydroxide and diluted sulphuric acid to afford the bis-thiol **49** in 73% yield. Finally, **38** and **49** were dissolved in dichloromethane and slowly added to a large volume of potassium hydroxide in methanol to afford the cyclophane **50** as a mixture of two inseparable positional isomers **50-sta** (staggered) and **50-ecl** (eclipsed) in 52% yield.

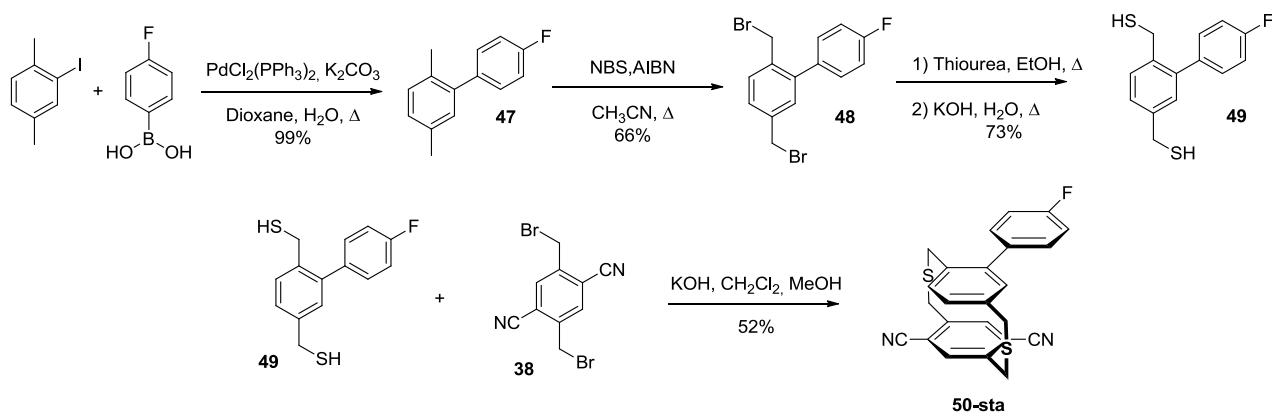


Figure 139: Synthesis of the cyclophane **50** (only the staggered isomer of **50** is represented)

Finally, the compounds **50** (**sta** and **ecl**) were added to a solution of ditolylamine and sodium hydride (NaH) in dimethylformamide, as depicted in Figure 140. However, no trace of the cyclophanes **50** or the target emitter **E** was observed at the end of the reaction. We thus concluded that the cyclophane may not be able to endure such aggressive environment of NaH in solution.

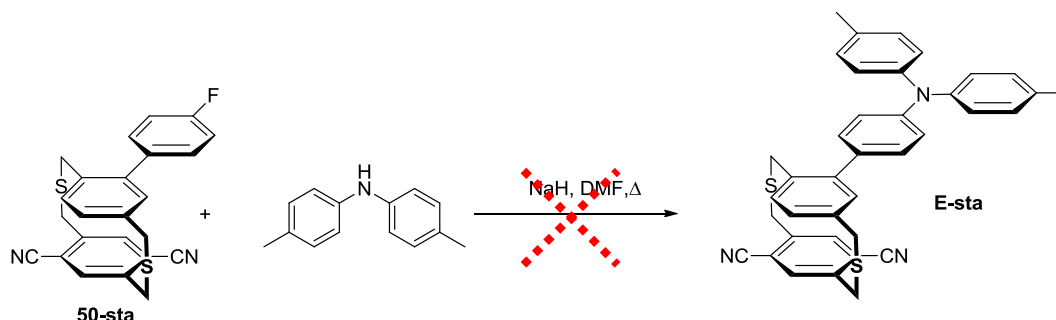


Figure 140: Final step: nucleophilic aromatic substitution on the cyclophane **50** (only the staggered isomers of **50** and **E** are represented)

As the nucleophilic aromatic substitution seemed not effective enough, another pathway was proposed by using an Ullmann-type reaction, as described in the next part.

2. Iodine, you're my best friend

The Ullmann-type coupling was already successfully used in the first strategy (preparation of **44** and **46**, Figure 136): it consists of the coupling between an aromatic derivative bearing a halogen (commonly iodide) and an amine, catalysed by copper (I) (commonly copper chloride). Thus the synthesis of the cyclophane derivative similar to **50**, and bearing an iodide instead of a fluoride, was tested in order to increase the chances of success of the Ullmann-type reaction.

However, grafting the phenyliodide instead of phenylbromide was not possible because of selectivity problems of the Suzuki coupling. As a consequence, the bromide derivative **28** was first synthesised using 2-iodo-*p*-xylene and *p*-bromophenylboronic acid in quantitative yield (Chapter 2, Figure 106). The trans-halogenation reaction was then carried out in diethylether at 0°C using *n*-butyl lithium and iodine to afford **51** in quantitative yield. The bromination of the methyl groups was then performed using the common procedure (acetonitrile, NBS and AIBN) to obtain **52** in 74% yield.

Later on, the next step of thiolation was performed as usual (thiourea, potassium hydroxide and diluted sulphuric acid) but the product was not recovered. The reaction was tried several times: the first

reaction of thiourea on **52** was proven effective. However, the conversion of the bis-isothiouronium salt into bis-thiolate and then bis-thiol was unsuccessful, and the product could not be isolated.

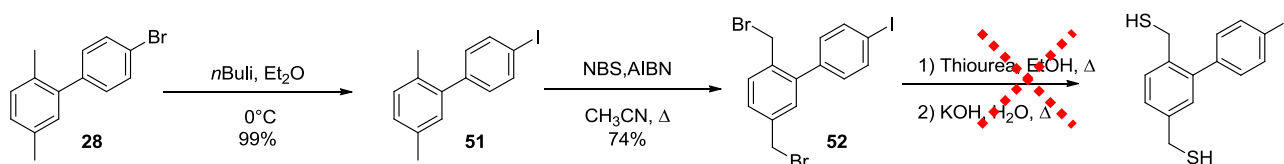


Figure 141: Synthesis of the iodide derivatives

As the iodide derivative could not be synthesised, we thus proposed to start from the bromide derivative **28** to graft the ditolylamine on the cyclophane. However, as the Ullman-type reaction is not very efficient with bromide derivative, another type of reaction was then chosen: the Buchwald-Hartwig reaction.

3. Bromide rhapsody

The last pathway towards the target molecule **E** includes the use of the palladium-catalysed Buchwald-Hartwig cross-coupling. This reaction is mainly used to couple aryl halides (mainly bromides) and amines. In contrast with the Ullmann-type reaction, the conditions are currently smoother and the selectivity should be higher.

First, the bis-thiol upper deck **30** was synthesised according to the procedures previously developed and was obtained from 2-iodo-*p*-xylene and *p*-bromophenylboronic in 3 steps with an overall yield of 75%. The cyclisation to form the cyclophane **53** was then performed in high dilution using **30** and **38** in 42% yield. The complete synthesis is represented in Figure 142.

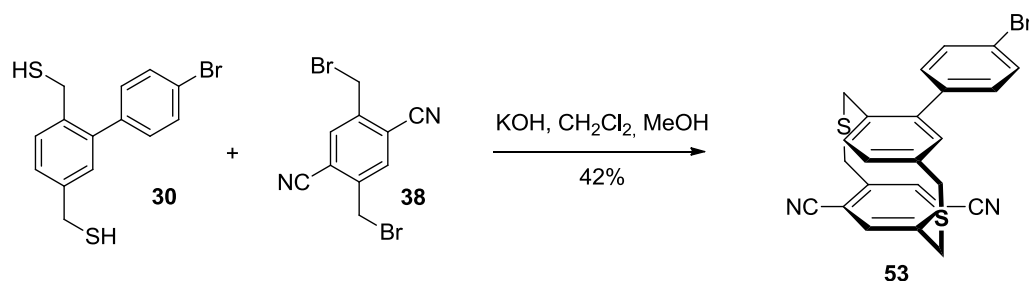


Figure 142: Synthesis of the cyclophane **53**

The cyclophane **53** was recovered as a mixture of two structural isomers which were separated by chromatography to afford the eclipsed (**ecl**) and the staggered (**sta**) in respectively 12% and 30% yields. These isomers were then used separately for the final step as **53-ecl** and **53-sta**, as depicted in Figure 143.

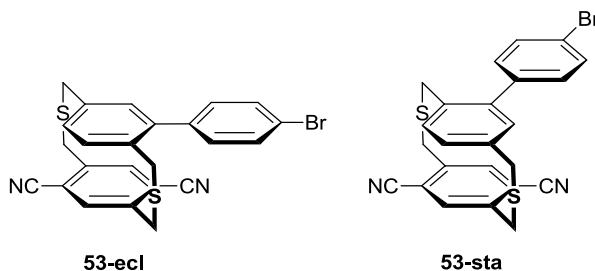


Figure 143: Representation of the structural isomers of the cyclophane **53** (eclipsed and staggered)

The last step was a Buchwald-Hartwig coupling between **53** (**ecl** or **sta**) and ditolylamine. This coupling is very efficient when strong electron-donor ligands are used with a strong base. The best conditions were thus first evaluated by coupling ditolylamine and bromobenzene: the palladium acetate was tested with the ligands tri-*tert*-butylphosphine ($\text{P}(\text{t-Bu})_3$) and diphenylphosphinoferrocene (dppf), and also with different bases : potassium *tert*-butoxide and cesium carbonate.

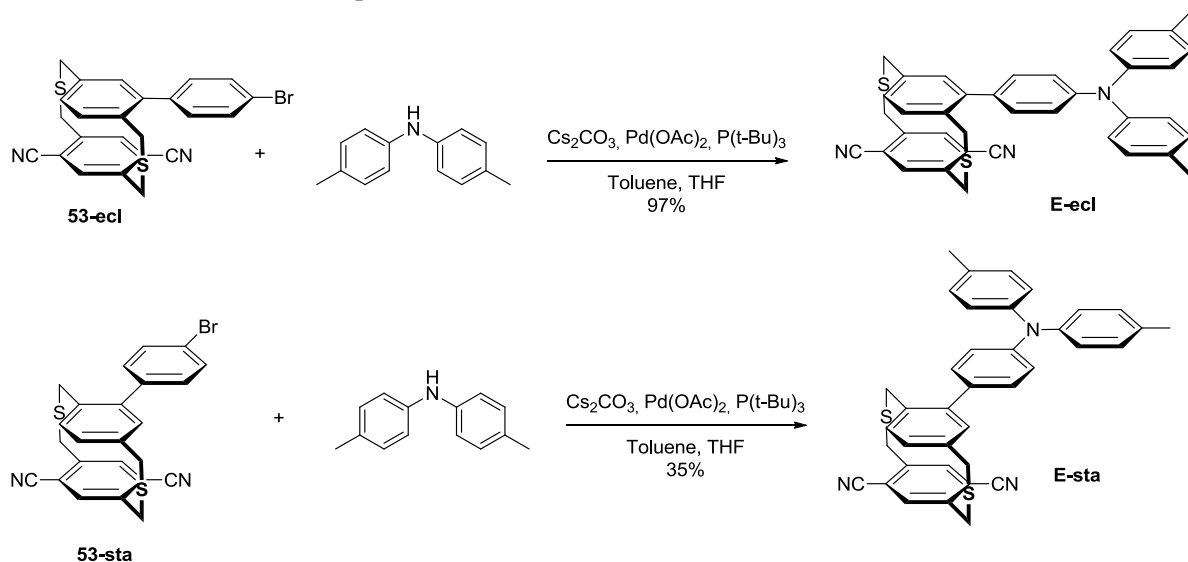


Figure 144: Buchwald-Hartwig coupling between **53** and ditolylamine

As represented in Figure 144, the reaction between **53** (**ecl** or **sta**) and ditolylamine was successfully carried out in a mixture of tetrahydrofurane and toluene, using palladium acetate and tri-*tert*-butylphosphine as catalyst and cesium carbonate as base to afford **E-sta** in 35% yield and **E-ecl** in 97% yield.

The emitter **E** was finally synthesised, as represented in Figure 145, with an overall yield of 5% and 5.5% for **E-sta** and **E-ecl**. This yield is mainly limited by the bromination step of **37** (Figure 132), and also by the cyclophane synthesis affording **53** as two isomers. So, these two reactions might need further works to optimise the whole synthesis. The characterisations of the photophysical properties of both emitter **E-ecl** and **E-sta** will be carried out in the next part of this chapter.

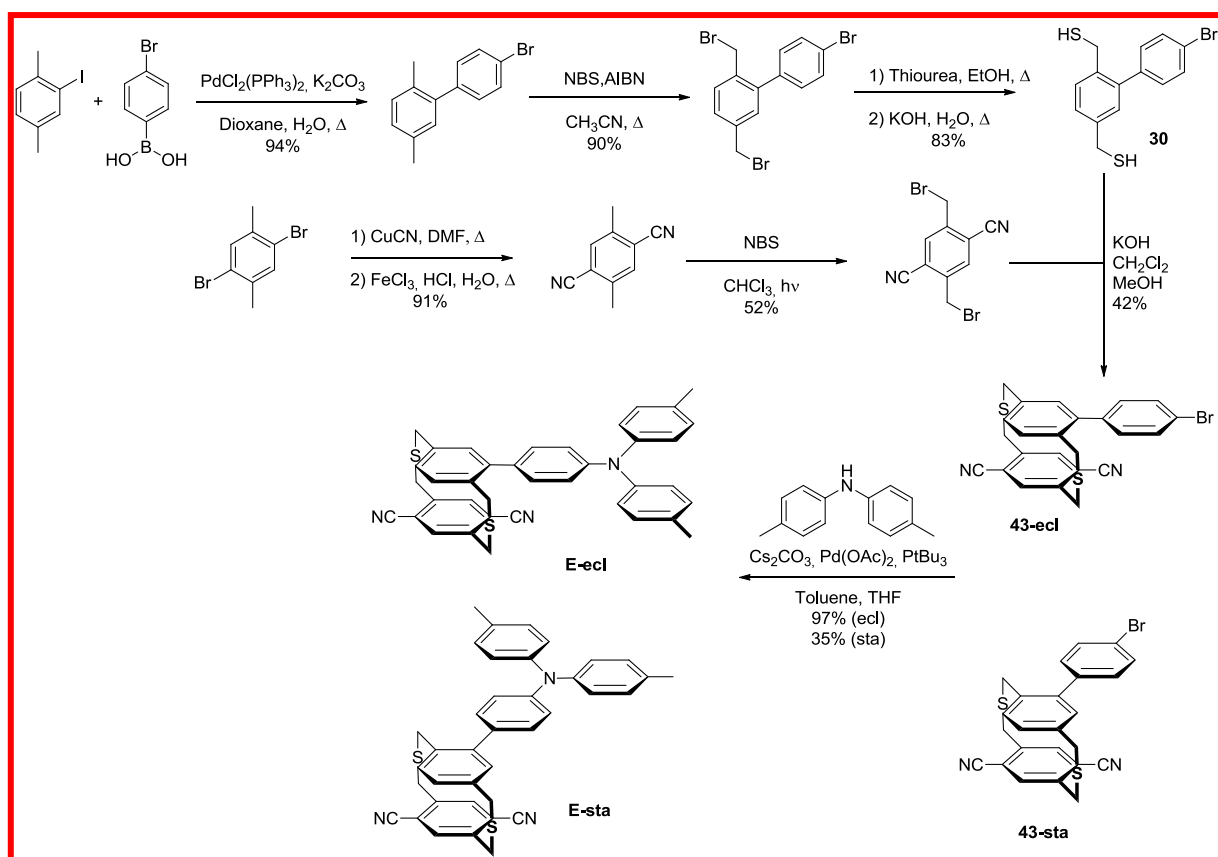


Figure 145: Definitive synthesis of the emitter **E-ecl** and **E-sta**

II. Characterisations of the staggered and eclipsed emitters

The preparation of the two positional isomers **E-ecl** and **E-sta** offered the opportunity to study the effects of the cyclophane core isomerisation on the electronic and luminescence properties.

In this section, we first characterised the two isomers by Nuclear Magnetic Resonance (NMR) and X-ray radiocrystallography. Then we performed theoretical calculations to determine some important parameters before studying the photophysic properties of both isomers in solution and in the solid state.

A. Nuclear Magnetic Resonance and X-ray radiocrystallography

1. Nuclear Magnetic Resonance

The first interest of the NMR is here to truly identify the emitters as eclipsed and staggered compounds. The two NMR spectra (recorded in deuterated dimethylsulfoxide (DMSO)) are displayed in Figure 146.

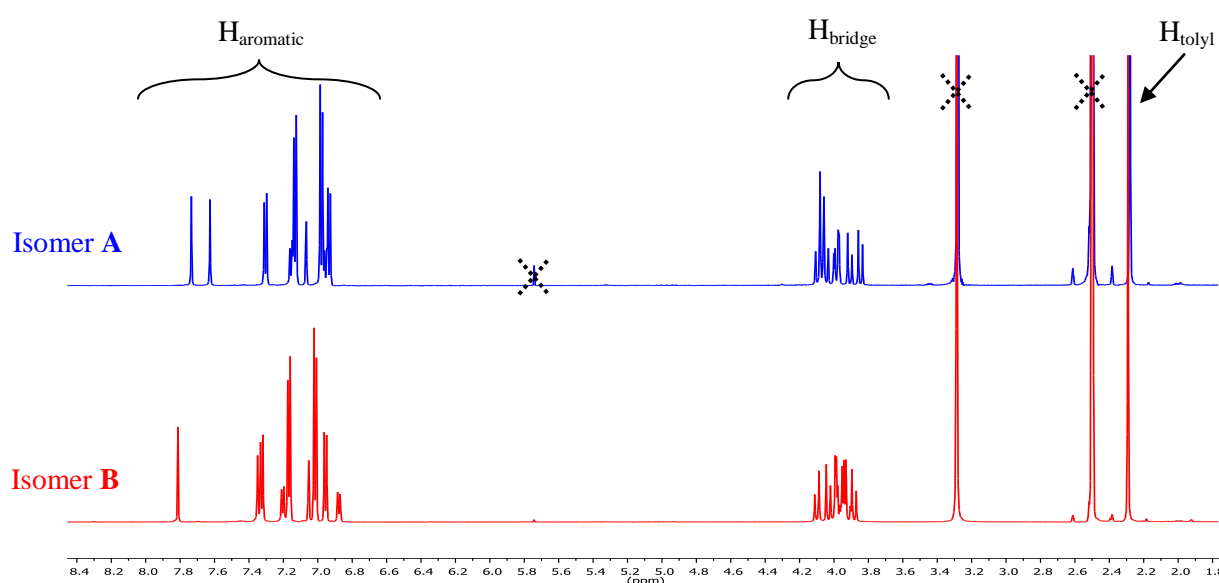


Figure 146: ¹H NMR spectra of the isomers **A** and **B**, in deuterated DMSO on a 600 MHz spectrometer (the crosses indicate the residual solvent and water traces)

Apart from the peak of the NMR solvent (2.50 ppm) and of some traces of residual solvents (water at 3.33 ppm and dichloromethane at 5.76 ppm), the spectra can be divided in three parts. First, the peak at 2.28 ppm represents the six protons borne by the tolyl groups of the donor. Then, we can observe eight protons of the CH₂-S-CH₂ cyclophane's bridges from 3.29 to 4.11 ppm. Finally, the aromatic area (6.87 to 7.81 ppm) shows the signals of the different phenyl groups (17 protons).

The assignment of each spectrum to its eclipsed or staggered structure was performed by looking at the aromatic signals, more precisely the protons of the cyclophane's lower deck. However, the complexity of the aromatic system first demands to assign each peak to its proton(s), as displayed in Figure 147.

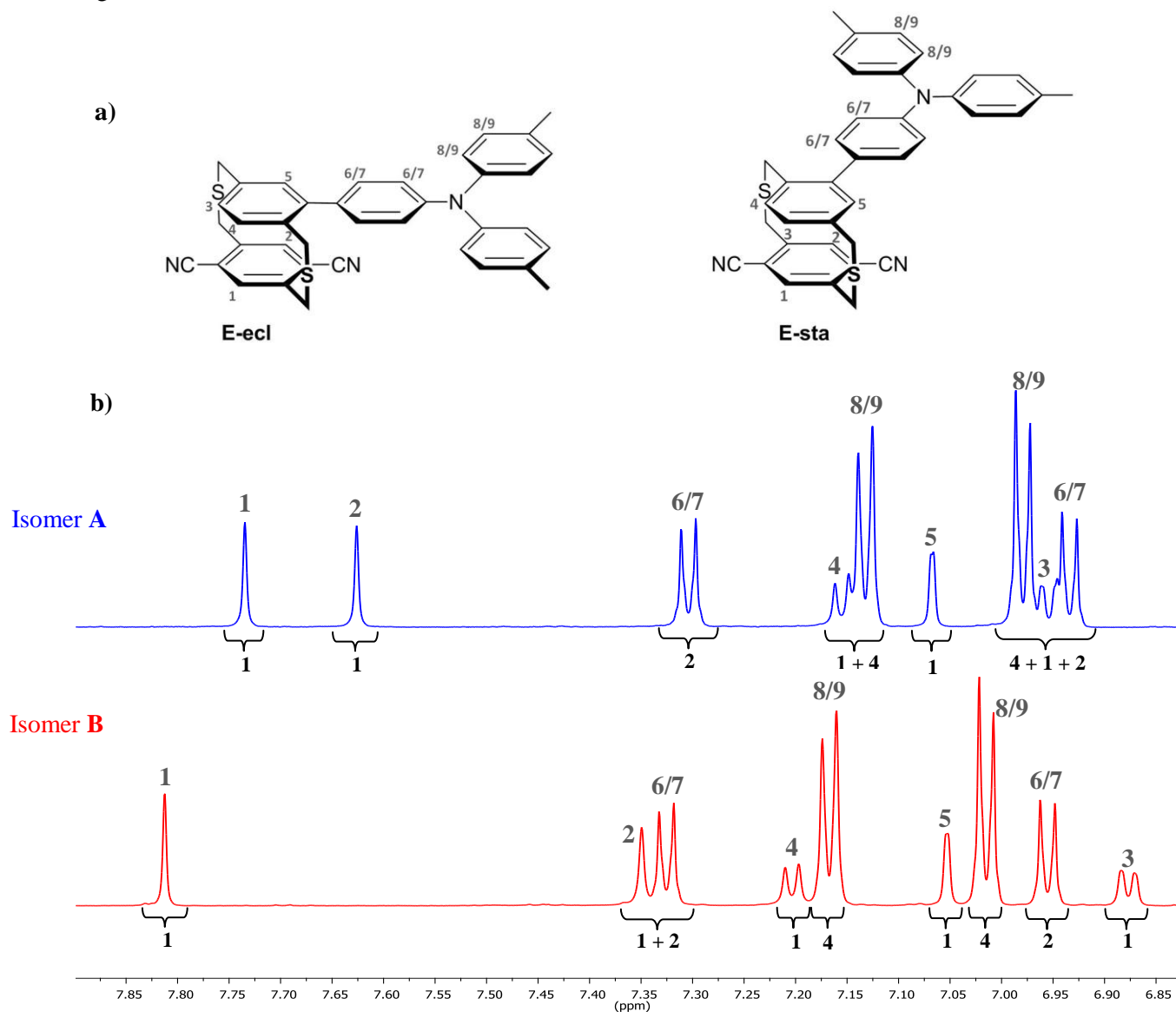


Figure 147: a) Representation of the emitter's structures and b) zoom on the aromatic part of the ¹H NMR spectrum of the two isomers **A** and **B**

In these spectra, the protons **8** and **9** can only correspond to the two doublets integrating for 4 protons each. Then the two doublets integrating for two are attributed to **6** and **7**. The three protons of the upper deck are then identified by their coupling constants *J*: the lonely **5** corresponds to the doublet with a *J*-constant near zero (1.3 Hz), then **3** is a simple doublet and finally **4** is a doublet of doublet

with the same J-constant as **3** and **5** (the near-zero constant is almost not observable on the figure). The last two aromatic protons **1** and **2** are easily identified as two singlets integrating for one each.

In the spectrum **B**, the proton **2** is shielded compared to the same proton in the spectrum **A** (7.35 ppm in B versus 7.63 ppm in A). This spectrum **B** is thus attributed to the staggered isomer, in which the proton **2** is located directly under the phenyl ring. As represented in Figure 148, in this position the proton is directly localised under the shielding cone of the upper phenyl unit; as a consequence, its chemical shift is reduced.

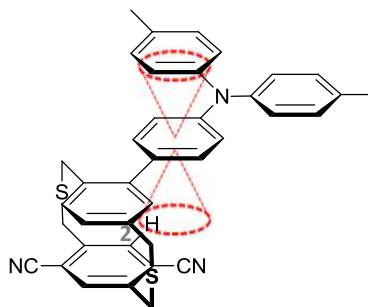


Figure 148: Shielding cone in the staggered derivative

We can thus definitely assign the spectrum **A** to the emitter **E-ecl** and the spectrum **B** to **E-sta**. The full attribution of each signal is hence possible. However, considering the complexity of the spectra (especially the protons from the cyclophane-bridges), different two-dimensional NMR experiments were carried out.

These additional 2D-NMR analyses were carried out in collaboration with Claire Troufflard (research engineer at the IPCM): correlation spectroscopy (COSY, shows the proton-proton couplings), heteronuclear single quantum coherence spectroscopy (HSQC, shows the 1J couplings between carbon and hydrogen atoms), heteronuclear multiple bond correlation (HMBC, shows the 2J and 3J couplings between carbon and hydrogen atoms) and nuclear Overhauser effect spectroscopy (NOESY, shows the through-space interactions between protons). These 2D-NMR spectra are given in the Appendices 4 and 5 and the resulting attributions of the protons' signals are depicted in Figure 149.

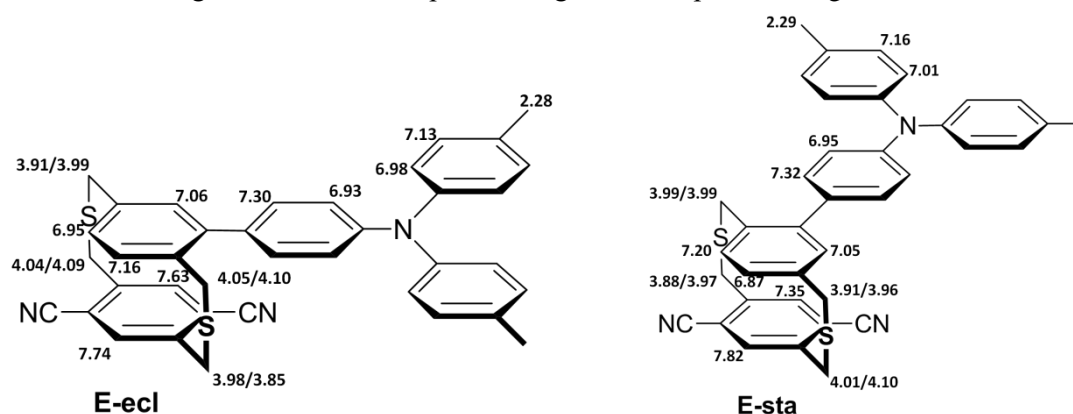


Figure 149: Full attribution of the ^1H NMR spectrum, deduced from ^{13}C NMR, COSY, HSQC, HMBC and NOESY experiments

Every proton could be attributed to its signal. Moreover, the multitude of second order couplings in the cyclophane core confirms the high rigidity of such structure, where every proton is almost fixed in only one position.

2. X-ray crystallography

The structure of the staggered emitter **E-sta** was investigated by X-ray diffraction on monocrystals obtained by slow evaporation of a solution of compound in a mixture of isopropyl alcohol and *n*-hexane (1/1). The crystal structure is represented in Figure 150, and additional parameters are reported in Appendix 5.

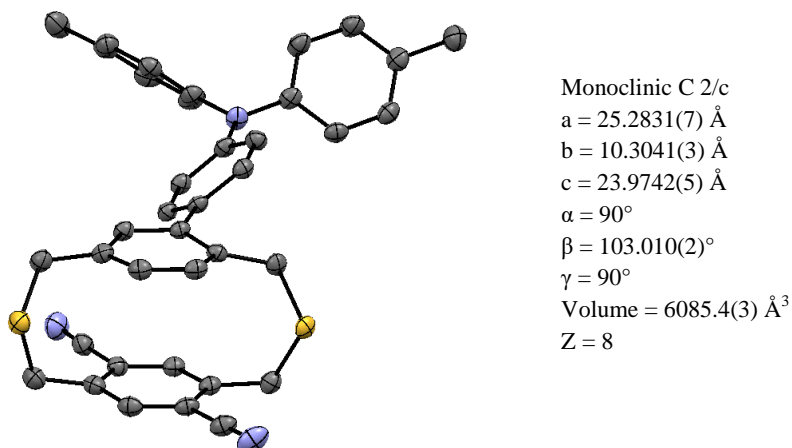


Figure 150: X-ray crystal structure of **E-sta** represented as an ORTEP drawing

The structure shows that the distance between the two parallel decks of the cyclophane is about 3.35 \AA , which is slightly higher than that usually observed within the “naked” dithiacyclophane (3.24 \AA) as described in the chapter 1 (Figure 11). This difference could be attributed to the functionalisation of the cyclophane’s benzene rings with bulky groups such as the ditolylphenylamine for instance. However, this distance is smaller than the ideal π -stacking distance between two aromatic entities (3.40 \AA , in graphite)¹⁹ and therefore a slight overlap of the molecular orbitals between the upper and lower decks could be expected. Nevertheless, the benzene rings are not entirely planar: the carbon atoms bearing the methylene bridges are bent out of the plan of the other four carbon atoms, forming an angle of 3° to 8° . The distorted structure of the cyclophane is thus confirmed by the benzenes’ boat conformation.

The 3D packing of the molecules is displayed in Figure 151.

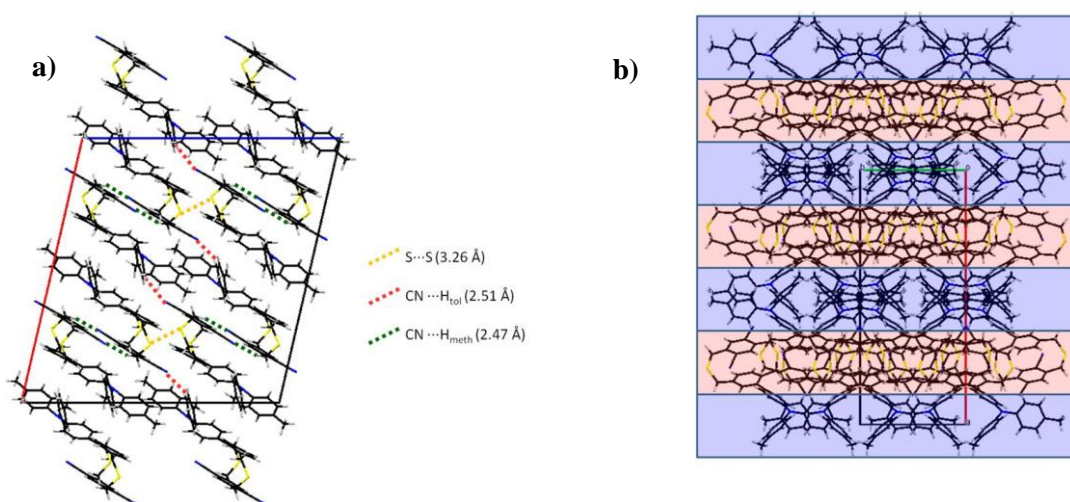


Figure 151: Representation of the packing structure of **E-sta** where (a) depicts the intermolecular interactions (H_{tot} : hydrogen borne by the tolyl unit and H_{meth} : hydrogen borne by the methylene bridge) along the **b** axis and (b) depicts the bilayer structure along the **c** axis.

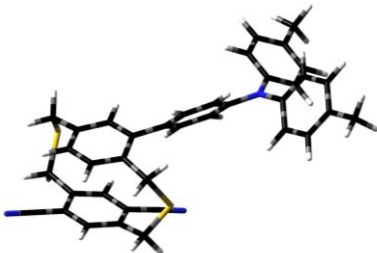
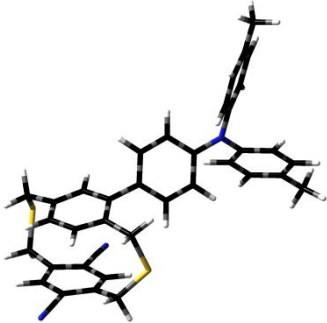
The emitter **E-sta** crystallised in a monoclinic crystal system, space group $C2/c$, and the density was calculated to be 1.296. Each cyclophane moiety is linked to its neighbours by strong interactions as displayed by the view along the **b** axis represented in Figure 151a. The shortest intermolecular S...S distance between two cyclophane entities equals to 3.26 Å, which is smaller than twice the van der Waals radius of the sulphur atom (1.8 Å) and thus indicates a strong overlap of the atoms' orbitals. Moreover, each nitrile unit displays strong interactions with the hydrogens of the nearest methyl bridge (close by 2.47 Å) and of the nearest tolyl unit borne by the amine group (close by 2.51 Å), both corresponding to strong hydrogen bonding (2.2 to 2.5 Å)¹⁵⁰.

The sum of these interactions induces a bilayer structure within the crystal by alternating electron-acceptor (nitrile-functionalised lower deck) and donor units (ditolylphenylamine groups), as shown by the view along the c axis given in the Figure 151b.

B. Calculations

The theoretical calculations were performed on **E-ecl** and **E-sta** derivatives in collaboration with Pr. Q. Zhang at Zhejiang University to evaluate their properties. First, density functional theory calculations (DFT) with the most popular functional B3LYP were used to simulate the ground-state geometries. Then the TD-DFT/B3LYP (time-dependent DFT) calculations were performed to estimate various electronic parameters related to the excited states. However, the results of these common calculations are not always accurate when predicting the energy levels of complex excited states like in TADF molecules. Thus, other calculations were performed by mixing TD-DFT with a certain amount of the older but more accurate Hartree-Fock theory (HF). The resulting calculations are part of the hybrid functional BMK (Boese-Martin for Kinetics) where the optimised parameters are carefully chosen by tuning the percentage of HF theory within the simulation.¹⁵¹

The use of hybrid functional is not common because of its complexity and its time-consuming calculations. However, this technique allows a rather sharp determination of the percentage of charge-transfer in the singlet state, and also the energy levels of the locally-excited (LE) and charge-transfer (CT) triplet states. The results of these calculations are summarised in the Table 3 along with the HOMO and LUMO representations.

	E-ecl	E-sta
Molecular structure		
CT amount (%)	93	94
OHF (%)	39.1	39.5
LUMO (eV)	-1.74	-1.74
HOMO (eV)	-5.56	-5.50
$\Delta E_{\text{HOMO-LUMO}}$ (eV)	3.82	3.76
$\mu_{\text{Ground State}}$ (Debye)	1.100	1.280

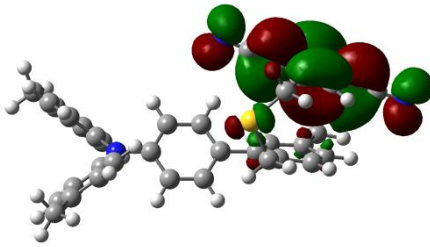
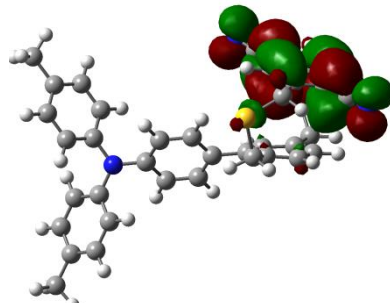
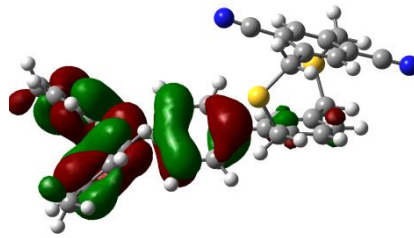
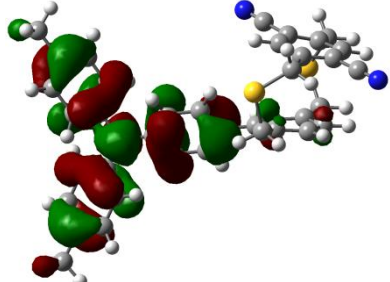
$S_1(^1\text{CT})$ (eV)	2.63	2.74
$S_2(^1\text{LE})$ (eV)	3.55	3.52
$T(^3\text{CT})$ (eV)	2.61	2.73
$T(^3\text{LE})$ (eV)	2.75	2.72
ΔE_{ST} (eV)	0.02	0.02
f	0.019	0.000
HOMO		
LUMO		

Table 3: Results of theoretical calculations performed by BMK on the emitters **E-ecl** and **E-sta**, CT: charge-transfer percentage, OHF: Optimised Hartree-Fock parameter, $\mu_{\text{Ground State}}$: dipole moment, $S_1(^1\text{CT})$ = charge-transfer singlet excited state, $S_2(^1\text{LE})$ = locally-excited singlet state, $T_1(^3\text{CT})$: charge-transfer triplet excited state, $T_1(^3\text{LE})$: locally-excited triplet state, ΔE_{ST} : electronic gap between first singlet and triplet state ($= S_1 - T_1$), f : oscillator strength of the $S_0 \rightarrow S_1$ transition

In this table, the CT amount depicts the estimated percentage of charge-transfer in the singlet state which is, considering the results, almost completely in a CT configuration. The OHF parameter (Optimised Hartree-Fock) represents the percentage of HF theory within the hybrid functional BMK; it is an important factor for the reproducibility of the calculation.¹⁵² The HOMO and LUMO energy levels were also estimated and the electronic gaps imply that both isomers should be green emitters. Small values of dipole moments of the ground state were obtained and it will be interesting to compare those values with the ones of the excited state. The calculated excited states are represented in the energy diagram depicted in Figure 152.

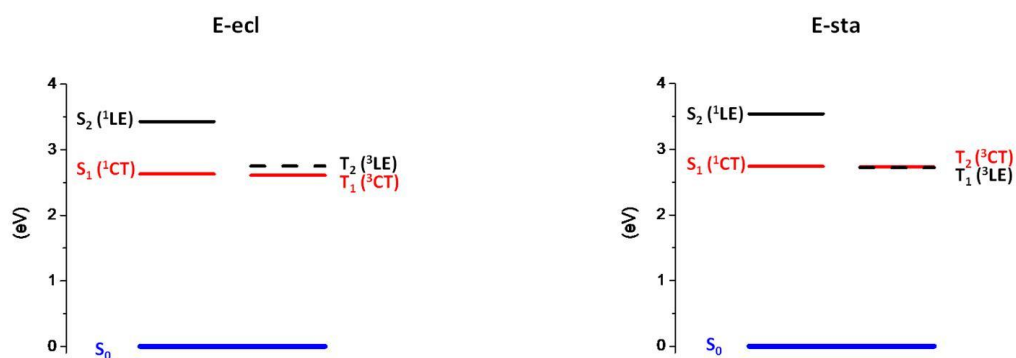


Figure 152: Energy diagrams representing the calculated energy levels of the excited states of both isomers **E-ecl** (a) and **E-sta** (b)

The simulation of the excited states announces a small ΔE_{ST} of around 0.02 eV for both isomers which is smaller than the theoretical limit of 0.4-0.3 eV generally observed to obtain TADF. However, according to the literature¹⁵³, the staggered's lowest triplet state is locally-excited (LE) which might prevent efficient RISC towards the charge-transfer (CT) singlet state S_1 , and thus reduce the potential delayed emission. The calculated oscillator strengths f are quite low, especially for **E-sta** which is around zero. Therefore we can expect a low absorption efficiency of the emitters and thus the brightness might be limited to low values. Finally, the HOMO and LUMO representations display a small overlap, which is consistent with the low oscillator strengths previously mentioned. Based on these results, and more particularly the small calculated ΔE_{ST} , we could assume that both derivatives may present TADF properties and could be good candidates to prove the potential interest of the cyclophane unit in the design of a new type of TADF emitter.

C. Spectroscopic properties

The steady-state and the time-resolved fluorescence of the two emitters **E-sta** and **E-ecl** were studied in solution using different solvents and in the solid state (thin films). These experiments were performed in collaboration with the OPERA laboratory of Pr. Chihaya Adachi of Kyushu University.

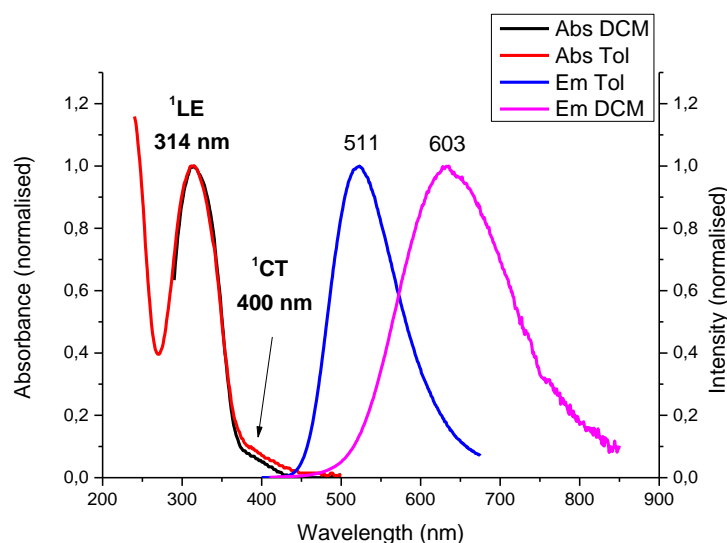
1. **Studies in solution**

E-ecl and **E-sta** are both donor-acceptor molecules, also named “push-pull” molecules. As a consequence, solvatochromic effects usually occur; it is thus interesting to study the compounds in different solvents (polar and apolar).

a. Steady-state measurements

The absorption and emission spectra of both emitters were first recorded in two solvents of opposite polarities: toluene (apolar) and dichloromethane (polar), as depicted in Figure 153.

a) **E-ecl**



b) E-sta

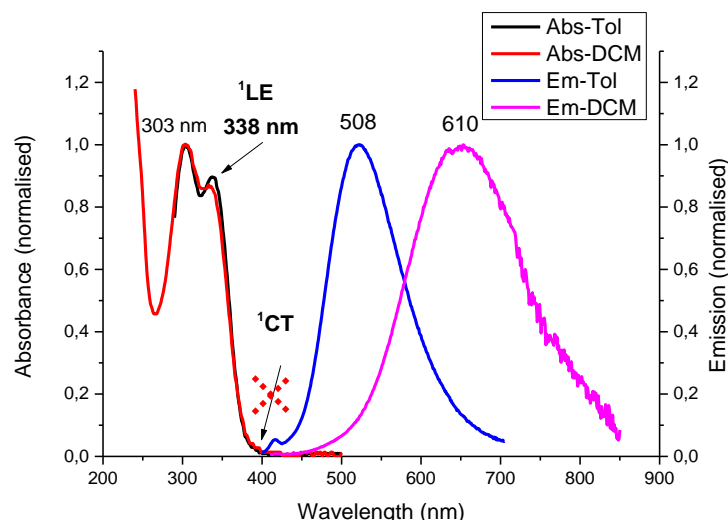


Figure 153: Spectra of absorption (Abs) and emission (Em) of **E-ecl** (a) and **E-sta** (b) in toluene (Tol) and dichloromethane (DCM)

Both emitters' absorption were recorded at different concentrations in order to calculate the molar absorption coefficient ϵ of the compounds, evaluated at $23\,000\text{ L.mol}^{-1}\text{.cm}^{-1}$ for both of them. **E-ecl** presents one large absorption band at $\lambda_{\text{max}} = 314\text{ nm}$ corresponding to the local transition from HOMO to LUMO+1, and a very small band at *ca.* 400 nm corresponding to the charge-transfer (CT) transition from HOMO to LUMO (attributions based on theoretical calculations). This small CT-band is consistent with the calculated small oscillator strength for the transition $S_0 \rightarrow S_1$ ($f = 0.019$). In the case of **E-sta**, the spectra display two close absorption bands at $\lambda_1^{\text{max}} = 303\text{ nm}$ and $\lambda_2 = 338\text{ nm}$. Based on the calculations, the band at $\lambda_2 = 338\text{ nm}$ could be attributed to the local transition HOMO to LUMO+1. However, no CT-band was observed experimentally which is consistent with the predicted calculations. Indeed, the f was calculated to be 0 which seems to indicate that this transition is forbidden (*i.e.* explaining the absence of absorption).

The fluorescence spectra of **E-ecl** presented a first emission band in toluene at 511 nm which is strongly redshifted in dichloromethane (603 nm). In the same way, the emission of **E-sta** was detected at 508 and 610 nm in toluene and dichloromethane. The Stokes shift was thus calculated for both emitters in both solvents. The values of 197 nm (12200 cm^{-1}) and 289 nm (15200 cm^{-1}) for **E-ecl**, and 205 nm (9900 cm^{-1}) and 307 nm (12900 cm^{-1}) for **E-sta** were respectively determined in toluene and dichloromethane. The Stokes shift values thus depend on the polarity of the solvent, which is consistent with the donor-acceptor character of the emitters.

The photoluminescence quantum yields (PLQY) were then studied in the presence of oxygen and in oxygen-free solvents. Indeed, the oxygen would quench the triplet excited state emission (by collisional quenching since the oxygen ground state is a triplet) and the reverse intersystem crossing from triplet to singlet state (if **E-ecl** and **E-sta** are TADF emitters). The measured PLQYs are reported in the Table 4.

Solvents	E-ecl		E-sta	
	λ_{max} (nm)	PLQY (%)	λ_{max} (nm)	PLQY
Dichloromethane	632	0.8	650	0.8
Degassed dichloromethane		2.0		0.8
Toluene	520	16.6	522	0.8
Degassed toluene		61.1		2.0

Table 4: PLQY and maxima of emission of **E-ecl** and **E-sta** in toluene and dichloromethane

The staggered isomer **E-sta** presents a low PLQY in both solvent, slightly increased by the degassing. In contrast, despite the low efficiency in dichloromethane, the eclipsed compound shows significant exaltation of its emission in toluene with values of 16.6 and 61.1 % in non-degassed and degassed solvents, respectively. The emission properties are thus dependent of the oxygen present in the medium which indicates that the triplet states are involved in the luminescence process. This behaviour is therefore in accordance with the potential TADF property of both emitters.

The effect of solvent polarity was then investigated in more detail and the absorption and fluorescence spectra were recorded in a large range of solvents as reported in Figure 154. At the low concentration used (*ca.* 1.10^{-6} M), no aggregation was observed.

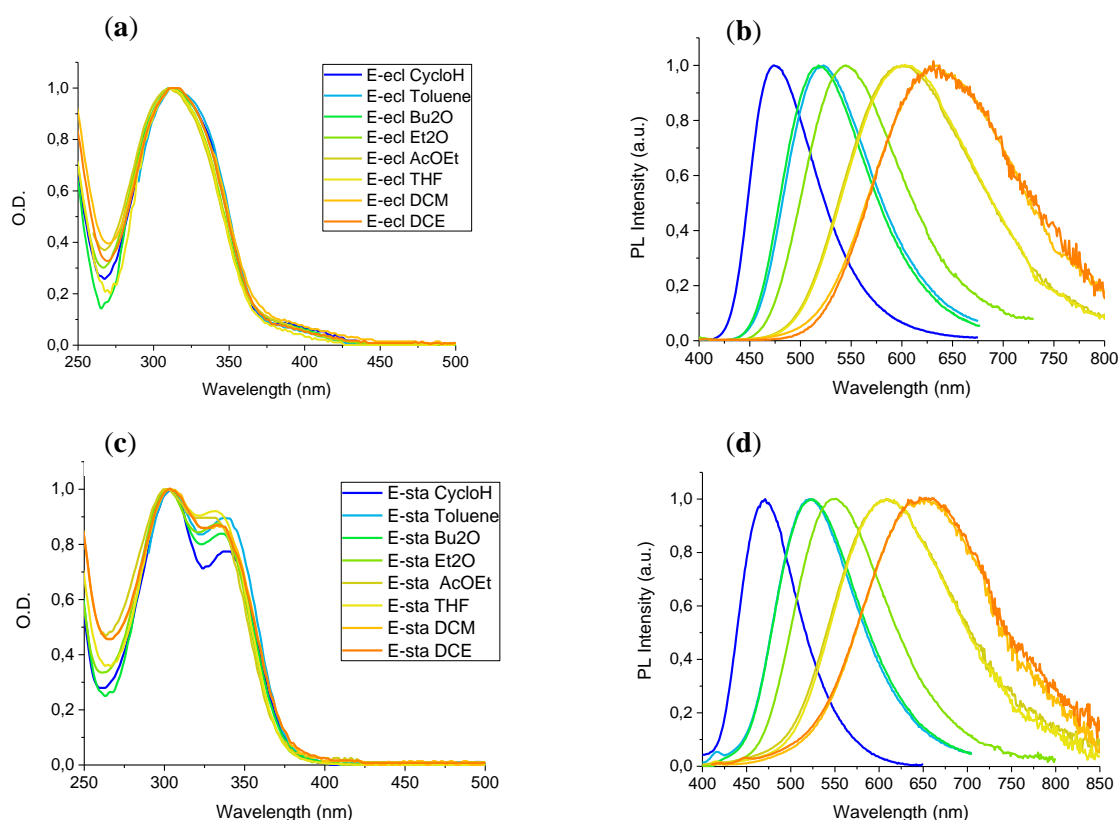


Figure 154: Absorption and emission spectra of **E-ecl** (a and b) and **E-sta** (c and d) in different solvents (CycloH: cyclohexane, Bu₂O: dibutylether, Et₂O: diethylether, AcOEt: ethyl acetate, THF: tetrahydrofuran, DCM: dichloromethane, DCE: dichloroethane)

The absorption spectra of the staggered and eclipsed emitters show little changes with a maximum moving from 301 to 304 nm and from 310 to 315 nm respectively. However, the increase of polarity of the medium leads to a remarkable redshift of the emission band: from 471 nm in cyclohexane to 655 nm in dichloromethane for the staggered, and from 474 to 637 nm for the eclipsed. These important shifts indicate the high polarity of the excited state of both emitters compared to their ground states.

The Bilot-Kawski-Bakshiev¹⁵⁴ formalism was used to estimate experimentally the ground state dipole moment and the values of 0.3 and 0.2 Debye were measured for **E-ecl** and **E-sta** (see Appendix 6 for calculation details) which is slightly smaller than the calculated values but clearly shows that the ground state dipole moment are negligible. The excited state dipole moments were then estimated by using the Lippert-Mataga formalism.¹⁵⁴ In comparison with the ground state, higher values were

calculated such as 19.6 and 20.2 Debye for **E-ecl** and **E-sta**, respectively. Such important shift of dipole moments between ground and excited state is common in donor-acceptor molecules such as TADF molecules, even if usually the polarity of the ground-state is higher than that estimated for **E-ecl** and **E-sta**.¹⁵⁵

b. Time-resolve measurements

In common fluorophores, the lifetime of fluorescence does not exceed 10-20 nanoseconds; it is thus called “prompt fluorescence” (PF). In the case of TADF molecules, an additional emission process named “delayed fluorescence” (DF) occurs and can last for tens or hundreds of microseconds. Therefore, time-resolve studies must be performed in order to identify the luminescence lifetime of each process. It is to be noticed that the singlet real lifetime in DF is not that long but the appearance of such component is due to the RISC process which slowly repopulate the singlet excited state.

To observe both emissions lifetimes, a pulse of excitation light is applied and the luminescence’s intensity *versus* time is then recorded to obtain the spectrum of photoluminescence’s decay. The study of **E-ecl** and **E-sta** was first carried out in non-degassed solvents (toluene and dichloromethane). The photoluminescence’s decay curves are depicted in Figure 155.

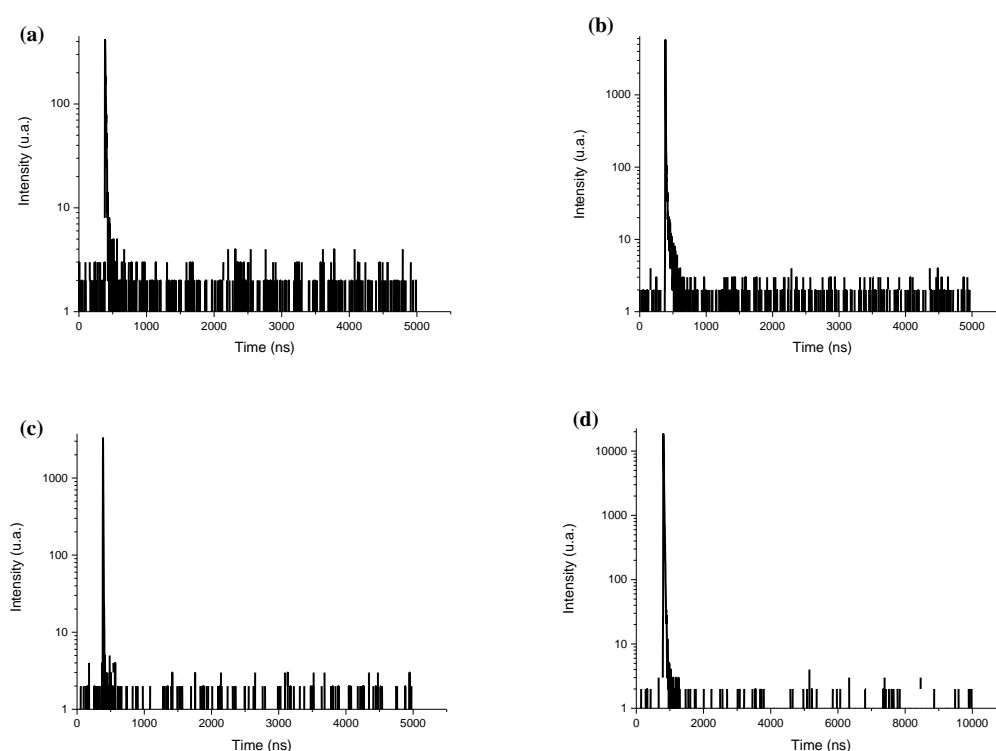


Figure 155: Photoluminescence decay curves of **E-sta** (a, b) and of **E-ecl** (c, d) in non-degassed dichloromethane and toluene

In this figure, each curve shows one single peak representing the prompt fluorescence; no delayed emission could be observed. Additional measurements were then performed on lower time scale (20ns) in order to obtain well resolved curves of prompt fluorescence decays (Figure 156).

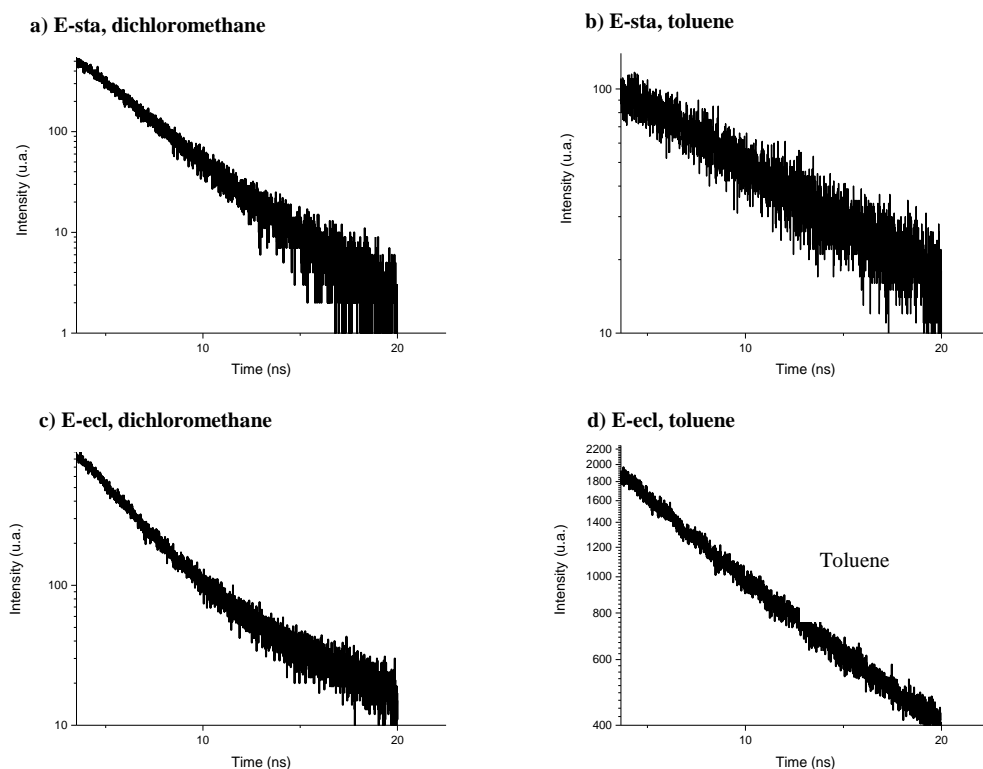


Figure 156: Photoluminescence decay curves of prompt fluorescence of **E-sta** (a, b) and of **E-ecl** (c, d) in non-degassed dichloromethane and toluene

The prompt fluorescence is not affected by the presence of oxygen. It was thus possible to extract the emission lifetimes τ_{PF} in each medium and then to deduce the decay rate constants of prompt fluorescence k_{PF} . The results are summed up in the Table 5.

Solvents	E-ecl		E-sta	
	Dichloromethane	Toluene	Dichloromethane	Toluene
PLQY	2.0	61.1	0.8	2.0
Lifetime τ_{PF} (ns)	2.75	8.83	2.79	8.82
Rate of PF ($k_{PF} = 1/\tau_{PF}$)	$3.6 \cdot 10^8$	$1.1 \cdot 10^8$	$1.1 \cdot 10^8$	$3.6 \cdot 10^8$

Table 5: Lifetimes and decay rate constants of the prompt fluorescence with the associated PLQY

The lifetime values are calculated from an exponential fit of the luminescence's decay. The fit used corresponds to the equation: $y = A_1 \cdot \exp(-x/\tau_{PF})$. In this equation, A_1 is the amplitude of the signal and τ_{PF} corresponds to the lifetime of the luminescence. The results so-obtained are in the same order of magnitude with previous results of prompt fluorescence in TADF-based materials.¹⁵⁶

The same studies was then performed in oxygen-free mediums. For that purpose, the solvents were degassed by bubbling nitrogen for 10 to 20 minutes. The photoluminescence decay curves in these conditions are represented in Figure 157.

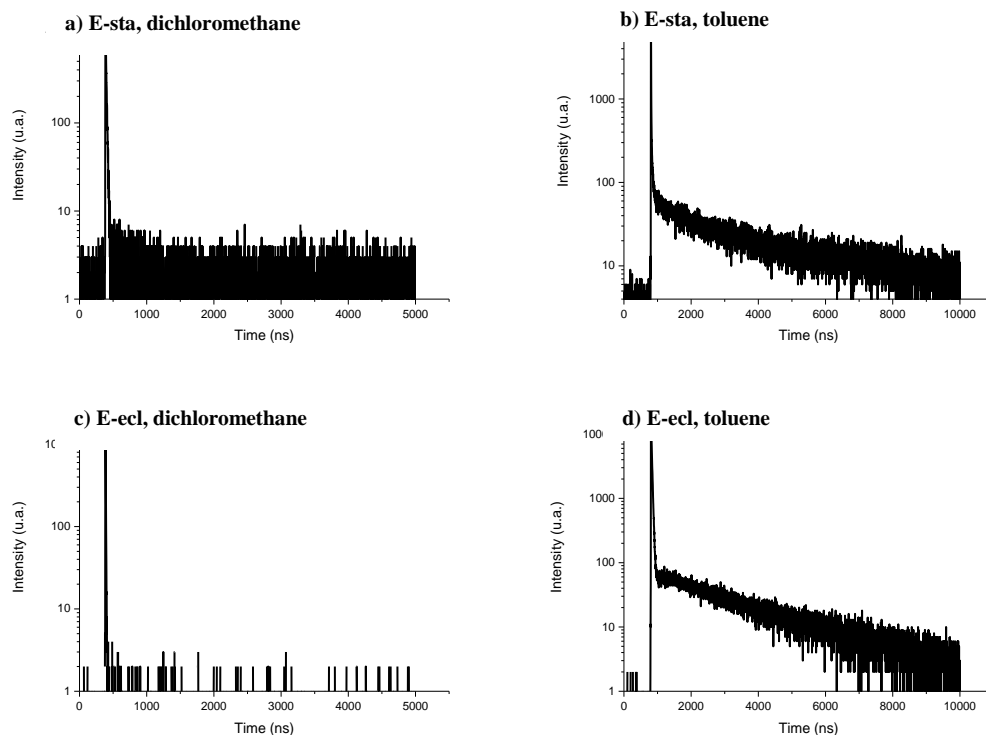


Figure 157: Photoluminescence decay curves of **E-sta** (a, b) and of **E-ecl** (c, d) in degassed dichloromethane and toluene

In oxygen-free media, a different behaviour occurs depending of the solvent. In dichloromethane, no changes were observed: only the prompt fluorescence was recorded as a sharp and intense peak. However in toluene, a clear delayed luminescence can be easily observed with the appearance of a long lifetime in addition to the prompt one. **E-ecl** and **E-sta** thus present a prompt fluorescence ($\tau_{PF} = 8.8$ ns) immediately followed by another emission with a lifetime of 2.30 and 1.65 μ s, respectively. This delayed phenomenon, previously quenched by oxygen, could be assigned to several luminescence processes such as phosphorescence or delayed fluorescence. However, considering that the experiments were performed at room temperature and in solution, the phosphorescence phenomenon was quite unlikely. This second process of luminescence could thus be attributed to thermally activated delayed fluorescence. By fitting the decay curves with mono-exponential functions, the lifetime of these long decays could be estimated in toluene along with the decay rate constants of delayed luminescence, as reported in the Table 6.

	E-ecl	E-sta
Solvents	Toluene	Toluene
Lifetime τ_{DF} (μ s)	2,30	1,65
Rate of DF ($k_{DF} = 1/\tau_{DF}$)	$4.5 \cdot 10^5$	$6.1 \cdot 10^5$

Table 6: Lifetimes and decay rate constants of the delayed luminescence of **E-ecl** and **E-sta**

These first characterisations in solution strongly suggest that the two emitters **E-ecl** and **E-sta** present the properties of TADF. However, further studies such as temperature dependent measurements in solution would be necessary to confirm this hypothesis and to definitely rule out, for instance, the phosphorescence. Moreover, the final objective being the elaboration of OLEDs, additional studies in solid state were then carried out.

2. Studies in solid state

The photophysical studies in solid state are usually performed on thin films prepared by vacuum vapour deposition or solution processing. However, in neat films, the emitting molecules tend to aggregate in such way that part of the emission is quenched through so-called aggregation caused quenching (ACQ) which is due to reabsorption of the emitted light. To avoid this phenomenon, the molecular structures are generally dispersed in a matrix (so-called host) to form a blend. In that case, the emitters (so-called guests) are “diluted” inside the host and isolated from each other, which usually enhances the emission properties by avoiding this reabsorption phenomenon.

a. Measurements on blends

The choice of the host matrix is important in order to have its S_0 - S_1 energy gap larger than that of the guest to allow energy-transfer from the guest to the host. Furthermore, attention must be paid to the HOMO-LUMO gap of the guest compared to the one of the host which could result in the formation of exciplex (electron transfer from the matrix to the emitter or from the emitter to the matrix). In addition, in the case of emitters exhibiting delayed luminescence (TADF, phosphorescence,...), the triplet excited state level of the matrix must be higher than that of the emitter to avoid the triplet quenching (by energy transfer). Finally, the ideal host must also present high charge carrier mobility. The energy diagram of an ideal host matrix and its corresponding emitting guest is displayed in Figure 158.

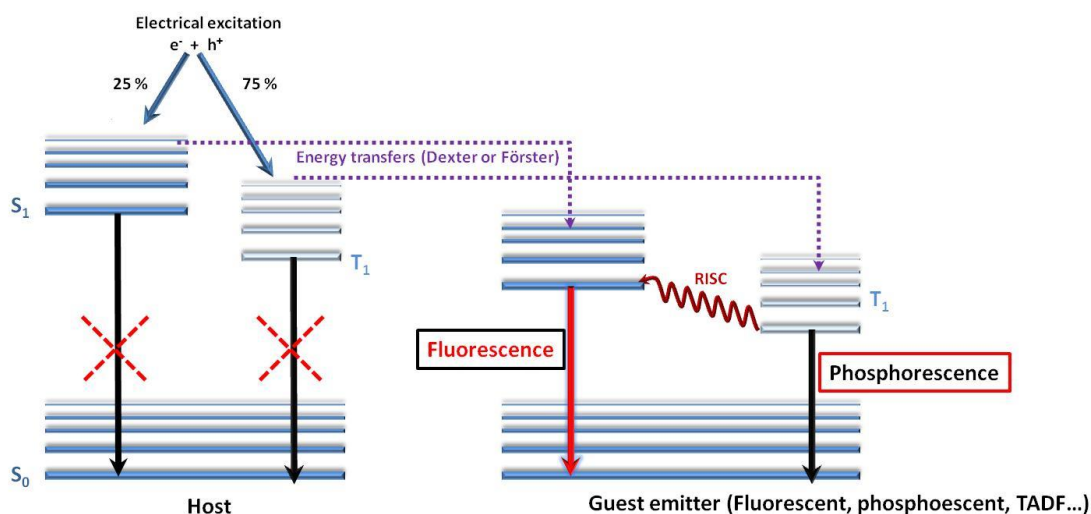


Figure 158: Energy level diagram of an ideal emitting blend

Two blends of the emitter **E-ecl** were prepared using DPEPO (bis[2-(diphenylphosphino)phenyl] ether oxide) and PMMA (polymethylmethacrylate) as matrices. The DPEPO is a common host for blue-TADF emitters and have been used in a large amount of OLED designs because of its good charge transport properties, and also its high S_1 and T_1 energy levels usually preventing the backward excited energy transfer from the guest to the host.¹⁵⁷ In contrast, PMMA presents a very low mobility of charge and an extremely high S_1 energy level: despite its unsuitability for any OLED elaboration, it should be a good host to disperse and study the emitter. However, despite the large HOMO-LUMO energy gap of the DPEPO and PMMA matrices, **E-ecl** still presents a higher LUMO energy level as displayed in the host-guest blend energy diagram in Figure 159.

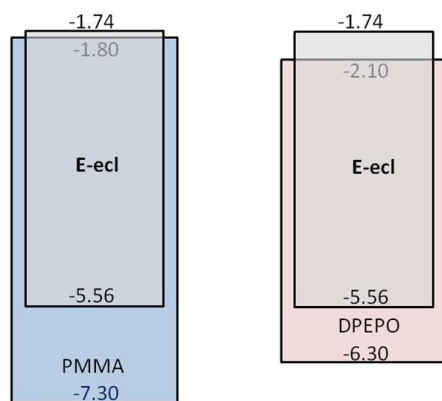


Figure 159: Energy diagram of **E-ecl** blends with DPEPO and PMMA matrices

As a consequence, a quenching of the **E-ecl** emission might occur by the formation of exciplex (electron transfer from the guest to the host). The measurements of PLQYs were then carried out on the two blends DPEPO/**E-ecl** and PMMA/**E-ecl** films from 3 wt% to 80 wt% and the results are depicted in the Table 7.

Weight %	PLQY of PMMA/ E-ecl	PLQY of DPEPO/ E-ecl
100	26.5	26.5
80	21,6	-
60	22,5	27.1
40	20,6	26.9
20	17,9	21.8
10	15,2	18.3
6	13,2	16.8
3	12,9	20.4

Table 7: PLQYs of the DPEPO/**E-ecl** films at different concentration

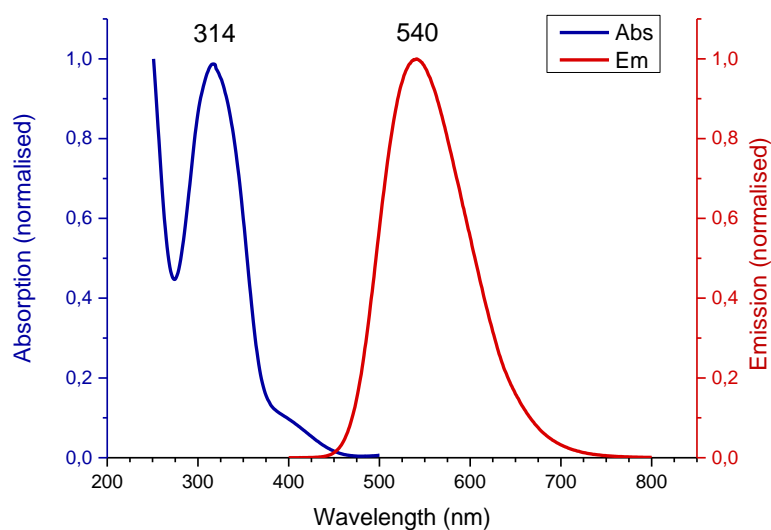
The PLQYs of the blends is clearly lowered when the concentration of emitter decreases. As suspected based on the blend energy diagram, the emission is probably quenched by the host matrix. Despite all our efforts, no suitable matrix was found up to now and we thus focused our work on neat film studies.

b. Measurements on neat films

i. *Steady-state measurements*

Neat films of **E-ecl** and **E-sta** were first deposited on substrates by spin-coating from 1%wt solution (percent of weight) of each emitter in dichloromethane. The absorption and emission spectra were then recorded, and are displayed in Figure 160.

a) **E-ecl**



b) **E-sta**

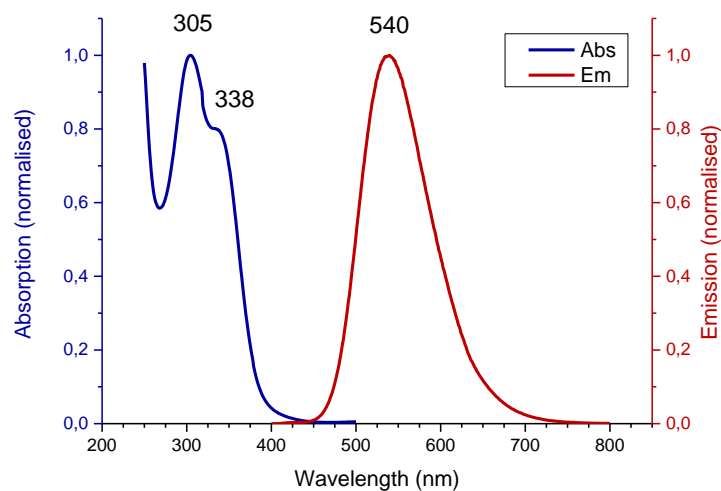


Figure 160: Spectra of absorption (Abs) and emission (Em) of **E-ecl** (a) and **E-sta** (b) in solid state

The absorption spectra are quite similar to those obtained in solution, with λ_{max} peaking at 314 and 305 nm for **E-ecl** and **E-sta**, respectively. From these absorption maxima, it is possible to deduce the theoretical HOMO-LUMO energy gap thus equal to 3.95 and 4.07 eV, which are close to those obtained by theoretical calculations (3.82 and 3.76 eV).¹⁵⁸ In solid state as well, the charge-transfer band is observed only for **E-ecl** ($\lambda = 400$ nm).

The maxima of emission in neat films were detected at 540 nm for both isomers, giving a green-yellow fluorescence with PLQYs measured in inert atmosphere of 26.5 and 11.4 % for the eclipsed and staggered emitters, respectively. Thus, the eclipsed compound appears to be a more efficient emitter than its staggered homologue in both solid and solution phases.

ii. Time-resolved measurements

Time-resolved measurements were performed by using a streak camera apparatus. The streak camera images of the isomer **E-ecl**, recorded at room temperature on a 50 μ s and 20 ns timescales under vacuum, are depicted in Figure 161 (a and b).

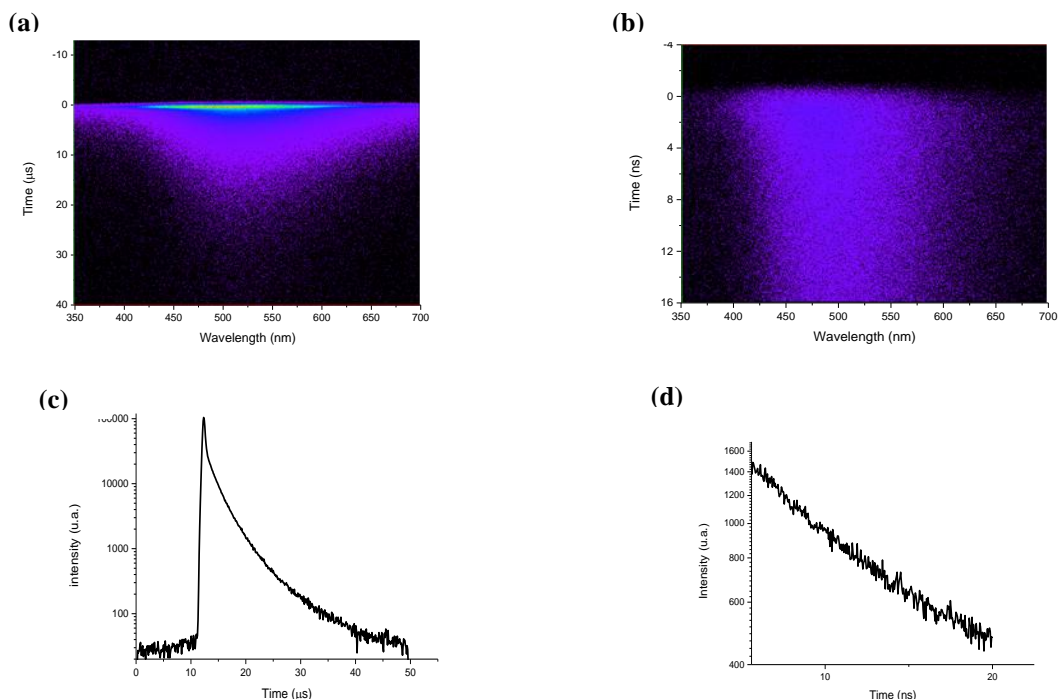


Figure 161: Streak camera images of **E-ecl** at room temperature with timeframes of 50 μ s (**a**) and 20 ns (**b**), and the corresponding photoluminescence decay curves (**c** and **d**)

The streak camera image on 50 μ s timescale (Figure 161a) shows two different decay regimes. First a fast component can be seen just after excitation, followed by a longer component slowly decreasing for 40 μ s. The first component can be assigned to the prompt fluorescence (PF) while the long one to delayed luminescence (DL). The streak camera image (Figure 161b) recorded on 20 ns timeframe shows that the prompt fluorescence only lasts for a few nanoseconds which is a consistent with classical fluorescence phenomenon.

The photoluminescence decay on 50 μ s and 20 ns timescales can be extracted from the previous streak camera images as represented in the Figure 161 (c and d), respectively. The lifetime value τ_{PF} of the prompt fluorescence was calculated by fitting the decay curve of the Figure 161d with a simple exponential fit ($y = A_1 \cdot \exp(-x/\tau_{PF}) + y_0$). However, the delayed luminescence decay in the Figure 161 c) could not be fitted properly with a simple mono-exponential but only with a bi-exponential function. That indicates that the delayed emission presents two delayed components (DL1 and DL2) and the amplitudes A_1 and A_2 are thus representing the contribution of each luminescence phenomenon (DL1 and DL2) to the whole emission.

The Table 8 reports the photoluminescence lifetime values and decay rate constants for the three distinct emissions (one prompt fluorescence (PF) and two delayed luminescences (DL1 and DL2)) of **E-ecl** and **E-sta**.

	E-ecl	E-sta
τ_{PF} (ns)	8.2	9.8
τ_{DL1} (μ s)	2.0	1.8
τ_{DL2} (μ s)	5.2	4.7
k_{PF} (s^{-1})	$1.2 \cdot 10^8$	$1.1 \cdot 10^8$
k_{DL1} (s^{-1})	$5.0 \cdot 10^5$	$5.6 \cdot 10^5$
k_{DL1} (s^{-1})	$1.9 \cdot 10^5$	$2.1 \cdot 10^5$

Table 8: Photoluminescence lifetime values (τ) and decay rate constants ($k=1/\tau$) of the three processes of luminescence (prompt fluorescence PF, and delayed luminescences DL1 and DL2)

The data obtained by the streak camera experiments also allows to extract the photoluminescence spectra of any timescale during the emission. The spectra of prompt fluorescence (from 0 to 50 ns) and delayed luminescence (from 2 to 40 μ s) were recovered and those of **E-ecl** are represented in Figure 162.

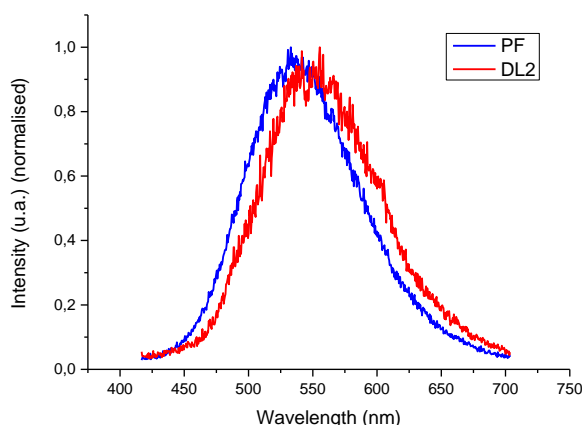


Figure 162: Emission spectra of prompt fluorescence and delayed luminescence of **E-ecl** (normalised)

In this figure, the two emission spectra are not overlapping: the maximum of the delayed emission spectrum is redshifted of about 15 nm compared to that of the prompt fluorescence. These results suggest that a component of the delayed luminescence involves a direct relaxation from the triplet state (phosphorescence), located at lower energy than the singlet state and thus emitting at higher wavelength.

In order to get more insights on the two components of the delayed emission, the time-resolved measurements were performed at 77 K on a 50 μ s timescale, as displayed for **E-ecl** in Figure 163.

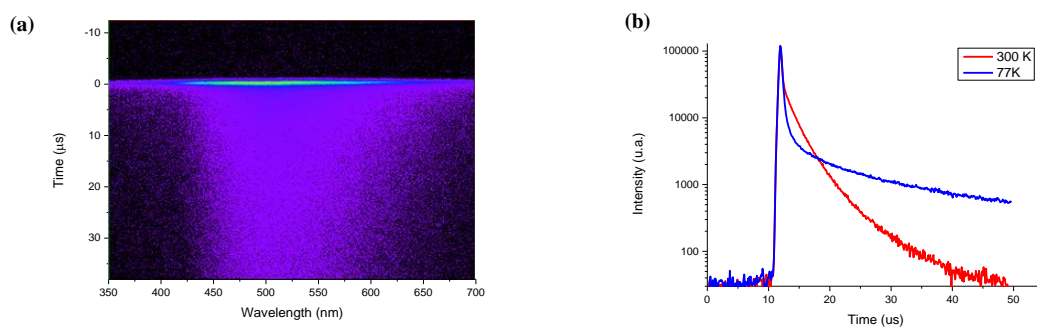


Figure 163: Streak camera image at 77K (a) and the decay curves at 77 K and 300 K (b) of the **E-ecl** neat film on a 50 μ s timeframe

The streak camera image given in Figure 163a shows a drastic increase of the emission at 77 K compared to that at room temperature (300 K). Moreover, the decay curves (at 77 and 300 K) depicted in the Figure 163b presents an interesting increase of lifetime of the delayed luminescence (much slower compound) induced by the decrease of temperature. The global emission is thus enhanced by lowering the temperature.

iii. Temperature-dependent measurements

To better understand this enhancement of emission at low temperature, we performed the time-resolved measurements on a large range of temperature: 300, 250, 200, 150, 100, and 70 K. As the decrease of temperature can lead to drastic modifications of the absorption of organic molecules, we first check the absorption behaviour of the absorption *versus* temperature. Indeed, the oscillator strength of any transition may be enhanced on cooling, leading to an increase of the intensity of the corresponding absorption band. If this phenomenon happens on the emitter **E-ecl**, the luminescence could be consequently enhanced in the same way. The temperature-dependent absorption study was thus carried out at the Institut des NanoSciences de Paris (INSP) in collaboration with Dr. Thierry Barisien and the spectra are displayed in Figure 164.

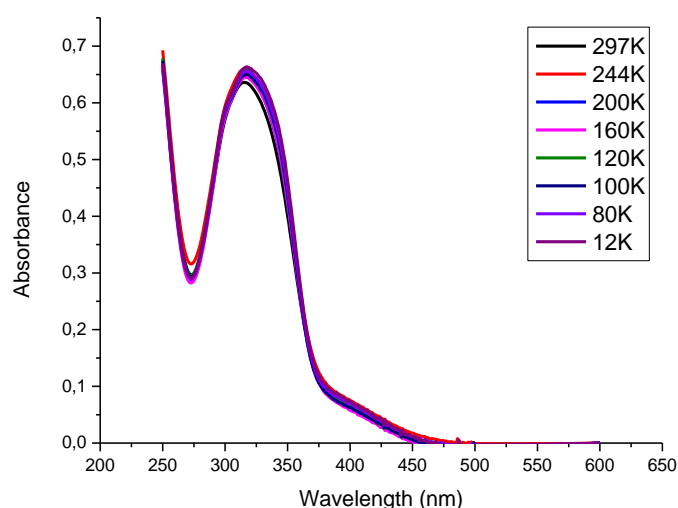


Figure 164: Absorption spectra of **E-ecl** at different temperatures: 297, 244, 200, 160, 120, 100, 80 and 12 K

The absorption spectra at different temperatures show no significant changes. The large absorption band was still centred on 314 nm and no exaltation of the absorption occurred. Consequently, the increase of delayed luminescence's intensity observed on cooling cannot be assigned to an absorption change.

The same temperature-dependent study was performed on the photoluminescence of the dyes in vacuum. The extracted decay curves show an evolution of the luminescence decays *versus* the temperature (Figure 165).

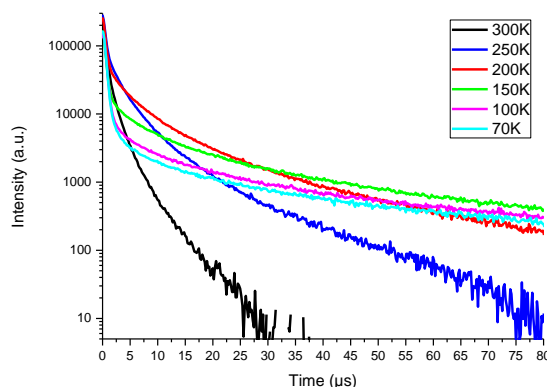


Figure 165: Photoluminescence decay curves of **E-ecl** at 300, 250, 200, 150, 100, and 70 K on a 100 μ s timeframe

For the latter experiment, relevant changes of the lifetimes of the delayed luminescence could be observed. Three series of measurements were thus carried out: one series was performed on a 20 ns timescale in order to obtain the lifetimes of the prompt fluorescence by using mono-exponential fits. Then in a second series, different timescales (from 100 μ s to 10 ms) were used in order to include the whole delayed emission and to extract the lifetime of the second delayed luminescence τ_{DL2} by mono-exponential fit on the most delayed part of the curves. The third and last series was performed on a 100 μ s timescale in order to finally obtain the τ_{DL1} by a bi-exponential fits. This last series (on a 100 μ s timescale) should also give some insights about the contribution of each delayed luminescence by comparing their relative amplitudes A_1 and A_2 . However, considering the small timescale (100 μ s), it is important to mention that the amplitude of the second delayed luminescence (A_2) is strongly underestimated. The temperature dependence of the prompt fluorescence (PF) and delayed luminescence (DL1 and DL2) lifetimes and the amplitudes ratio of A_1 and A_2 are reported in Figure 166.

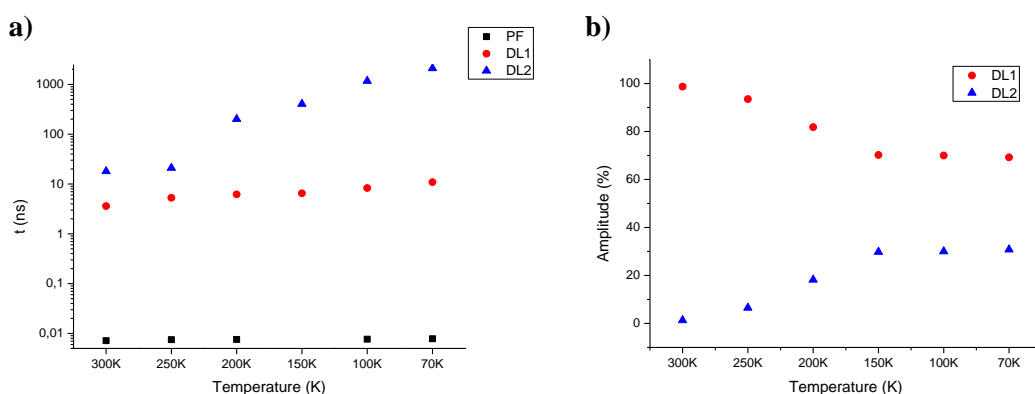


Figure 166: Representation of the lifetime evolutions of the prompt fluorescence (PF) and the delayed luminescences (DL1 and DL2) (a), and the amplitude ratio (A_1 and A_2) of each delayed luminescence (b) *versus* the temperature (300, 250, 200, 150, 100 and 70 K) for **E-ecl**

Observation of the lifetimes (Figure 166a) shows firstly that, as expected, the prompt fluorescence lifetime is not affected by the decrease of the temperature with a constant value of 7.5 ns. Concerning the delayed components, the first delayed luminescence DL1 presents a slight increase of its lifetime on cooling from 3.6 to 10.9 μ s. Finally, the second and longer delayed luminescence DL2 shows a large increase of its lifetime from 18 μ s to 2.1 ms (two orders of magnitude). In addition, the evolution

of the amplitude ratios of delayed luminescence (DL1 and DL2) on cooling shows a concomitant decrease of DL1 and increase of DL2 contributions in the global delayed emission (Figure 166b).

iv. *Potential pathways of deactivation*

Based on the conscientious study of the energy diagram of **E-ecl**, several potential desexcitation processes for the delayed components could therefore be expected as represented in Figure 167.

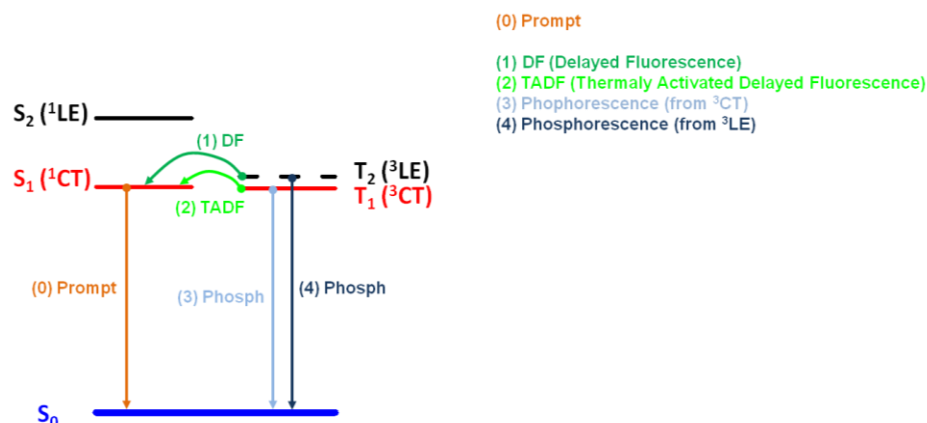


Figure 167: Potential luminescence process for the delayed emission of **E-ecl**

As two delayed components are observed, we can thus propose five different couples of possible processes:

- (1) + (2) \rightarrow DF (3LE) + TADF (3CT)
- (1) + (3) \rightarrow DF (3LE) + Phospho (3CT)
- (1) + (4) \rightarrow DF (3LE) + Phospho (3LE)
- (2) + (3) \rightarrow TADF (3CT) + Phospho (3CT)
- (2) + (4) \rightarrow DF (3LE) + Phospho (3LE)

If (1) + (4) and (2) + (3) would occur, that would mean that two excitation pathways were coming from the same excited state: (3LE) for (1) + (4) option and (3CT) for (2) + (3) option which is not consistent with the two lifetimes obtained by photophysical measurements. This allows the exclusion of both (1) + (4) and (2) + (3). For (2) + (4), this coupled pathway can also be ruled out since it would have been observed by the streak camera experiments. Indeed, the phosphorescence from the 3LE state would have emitted light at higher energy compared to the prompt fluorescence and as we showed in Figure 162, only an emission at higher wavelength was observed in the delayed component.

Thus two potential pathways are remaining: (1) + (2) \rightarrow DF (3LE) + TADF (3CT) and (1) + (3) \rightarrow DF (3LE) + Phospho (3CT). However as previously mentioned, the shift of emission of the delayed luminescence compared to the prompt fluorescence strongly suggests a direct relaxation from the triplet state 3CT (phosphorescence). As a consequence, DL1 corresponding to DF (1) and DL2 corresponding to Phospho (3CT) (3) is the most likely couple of deactivation pathway describing the delayed luminescence of **E-ecl** based on the available data to date. In addition to the low temperature promoting the phosphorescence, this attribution would also explain the longer and more intense DL2 at low temperature.

To conclude this part on the neat film study, an experimental value of ΔE_{ST} can be calculated from the spectra of the prompt and delayed emissions recorded at low temperature. Based on the previous

discussion, the spectra of the prompt and delayed phenomena can be attributed to the deactivation coming from singlet (S_1) and triplet (T_1) states, respectively.

If we consider the spectra of emission at 77 K, represented in Figure 168, the prompt emission is still attributed to the prompt fluorescence while the delayed component is mainly attributed to DL2, and thus probably phosphorescence.

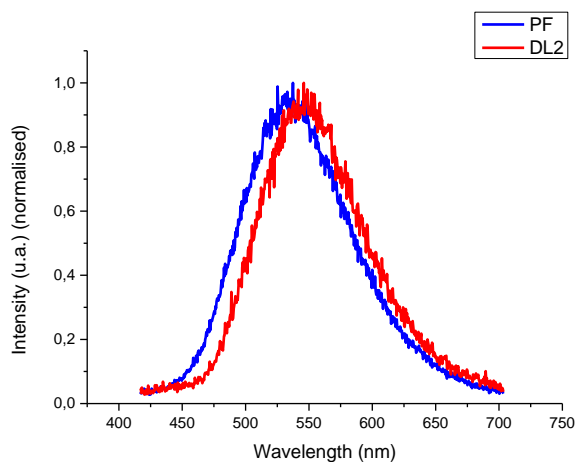


Figure 168: Spectra of emission of the prompt fluorescence and the longer delayed luminescence DL2 (phosphorescence) of **E-ecl** at 77K

Thus, the ΔE_{ST} could be easily calculated by measuring the lowest emission wavelengths of both luminescence spectra. The same experiments were also carried out on the staggered isomer, thus the parameters of both emitters are resumed in the Table 9.

	E-ecl		E-sta	
Wavelength (nm)	$\lambda_S = 458.28$	$\lambda_T = 472.64$	$\lambda_S = 462.17$	$\lambda_T = 476.23$
Energy level (eV)	$E_S = 2.71$	$E_T = 2.63$	$E_S = 2.68$	$E_T = 2.60$
ΔE_{ST} (eV)	0.08		0.08	

Table 9: Singlet and triplet energy levels extracted from the streak camera experiments

The singlet and triplet energy levels were calculated from the highest wavelength of emission (*i.e.* edge of the band) of prompt fluorescence (λ_S) and phosphorescence (λ_T) shown in Figure 168. The ΔE_{ST} of **E-ecl** and **E-sta** were both estimated at 0.08 eV. These results are slightly higher than calculated by the BMK (0.02 eV), but are still in a good agreement with the simulated values.

c. Measurements on OLED

The performance of an OLED containing **E-ecl** was studied. As discussed previously, no blend of **E-ecl** was considered and only devices based on neat films and presenting a PLQY of 26.5 % were elaborated. The HOMO energy level of **E-ecl** was first determined on neat film by photoelectron spectroscopy, as represented in Figure 169.

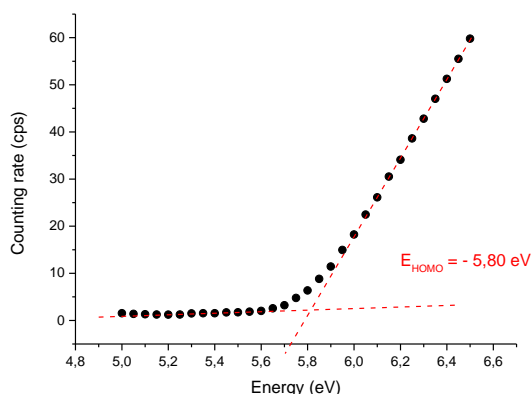


Figure 169: Photoelectron spectrum on the neat film of **E-ecl** (cps: count per second)

The experimental HOMO energy level was found around -5.80 eV which is in the same order of magnitude of the BMK calculations values (-5.56 eV).

The OLED was then fabricated by depositing the organic layers and cathodes on pre-cleaned indium tin oxide (ITO) glass substrate. The structure of the OLED is: ITO/PEDOT:PSS/**E-ecl**/PPT/TPBi/LiF/Al, as represented in Figure 170. The poly(3,4-ethylenedioxythiophene) : poly(styrene sulfonic acid) (PEDOT: PSS) was spin-coated on top of the ITO (the anode) and served as a hole-injecting layer. Then the emissive layer made of **E-ecl** neat film was spin-coated on top of the PEDOT layer, the layer thickness being typically in the range between 50 and 60 nm. The hole blocking layer was composed of a 10 nm thick film of 2,8-bis(dipheylphoshoryl) dibenzo[*b,d*]thiophene (PPT) onto which was deposited a 40 nm thick of the electron transport layer 2,2',2''-(1,3,5-benzinetriyl)-tris(1-phenyl-1-*H*-benzimidazole) (TPBi). Finally, the cathode consisting of a thin LiF layer and a 100 nm thick Al overlayer was prepared on top of the device to produce a good electron injecting contact by thermal evaporation through a shadow mask.

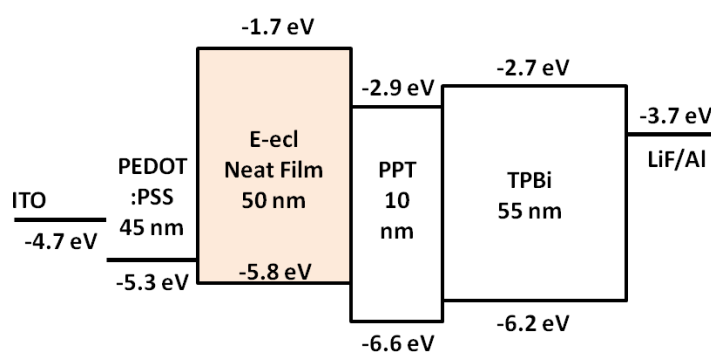


Figure 170: Energy level structure of the OLED based on **E-ecl**

The electroluminescence spectrum was first recorded at different current intensities (1, 10 and 100 mA) to evaluate the device efficiency, as represented in Figure 171 (in addition to the photoluminescence spectrum) along with the pictures of the OLED device (on and off mode).

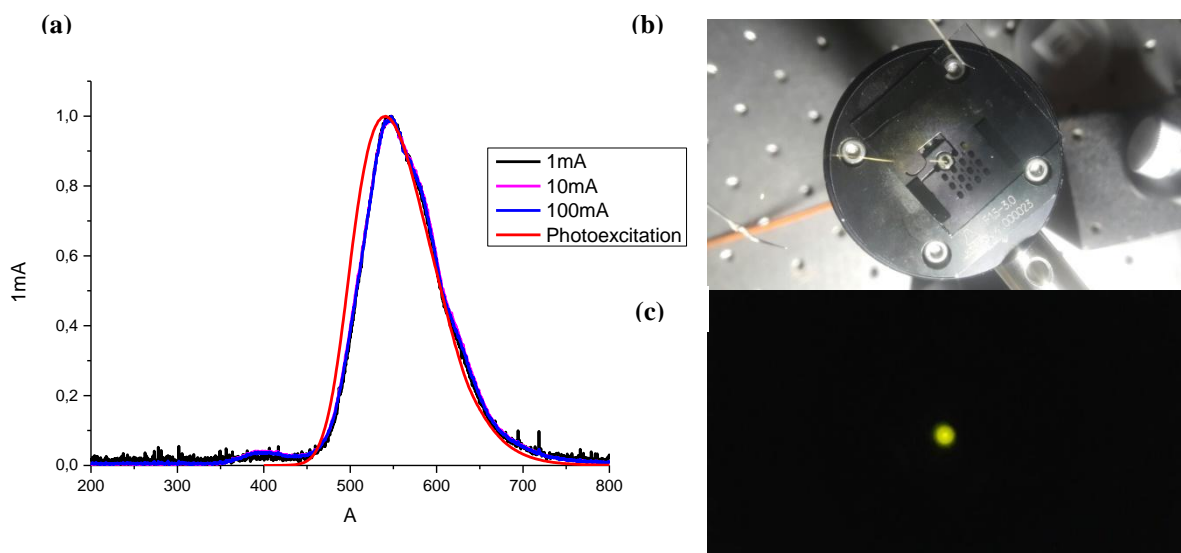


Figure 171: Electroluminescence spectra of the OLED at 1, 10 and 100 mA of current intensity and photoluminescence spectrum of **E-ecl** in neat film (a) and picture of the device in off (b) and on (c) mode

The OLED presents a yellow electroluminescent (Figure 171a) at $\lambda_{\text{max}} = 545$ nm which is consistent with the previous photoluminescence reported on the neat film ($\lambda_{\text{max}} = 540$ nm), confirming that the emission was generated solely from the emitters themselves through the same radiative decay processes.

The Figure 172 presents the electrical characteristics such as the external quantum efficiency (EQE) versus current-plots and the current-density-voltage-luminance (J-V-L) characteristics.

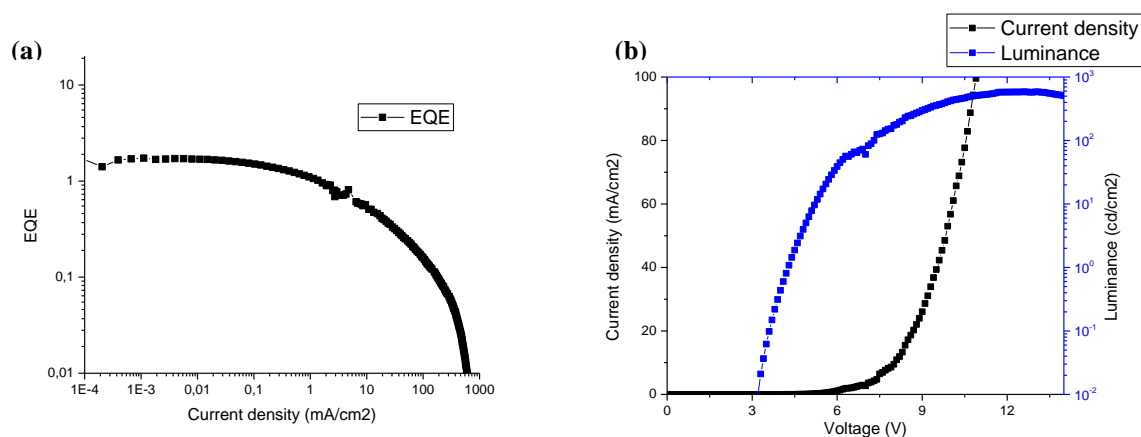


Figure 172: External quantum efficiency (EQE) versus current-plots (a) and the current-density-voltage-luminance (J-V-L) characteristics (b)

The yellow-emitting device displayed an EQE of 2.0 % at low current density, a maximum luminance (L_{max}) of 600 $\text{cd}\cdot\text{cm}^{-2}$ and a turn-on voltage at 1 $\text{cd}\cdot\text{cm}^{-2}$ of 3.5 V. Note that this device is not very efficient yet and several parameters will need to be adjusted in order to increase its efficiency. Indeed, as depicted in the energy diagram (Figure 170), the electron transport bilayer (PPT + TPBi) is not well adapted and presents a very low LUMO energy level compared to the emitter, and induces a non-optimised charge carrier injection. Moreover, this OLED have been prepared using a neat film of **E-ecl**, thus the incorporation of the emitter in a well-adapted matrix with high LUMO energy level should allow to increase the PLQY of the molecule and therefore the EQE of the device.

Conclusion

Two emitting donor-acceptor charge-transfer isomers based on a cyclophane central core were prepared. This design was proposed to induce a small energy gap between the singlet and triplet states and a potential reverse intersystem crossing process, both leading to TADF properties. After having attempted fruitless synthetic routes, the successful synthesis of the two isomers **E-ecl** and **E-sta** was carried out in seven steps with an overall yield of 5 and 5.5 %, respectively. The molecules have been characterised by detailed NMR spectroscopy studies and X-ray crystallography. Theoretical calculation were also performed to estimate various electronic parameters related to the ground and excited states.

The study of the absorption and emission solvatochromic properties of both **E-ecl** and **E-sta** allowed to evaluate the dipole moments of each molecule at the ground state (0.3 and 0.2 Debye) and at the excited state (19.6 and 20.2 Debye) using Bilot-Kawski-Bakshiev and Lippert-Mataga formalisms. Later on, the steady-state measurements showed that the photoluminescence quantum yields were dependant of the presence of oxygen in the medium. As a consequence, the best results were obtained in toluene, with PLQYs increasing with the degassing from 16.6 to 61.1 % for **E-ecl** and from 0.8 to 2.0 % for **E-sta**. This behaviour proved the contribution of the triplet excited state to the whole emission process. The time-resolved measurements were then carried out and both emitters have presented a dual emission of one prompt fluorescence and one delayed luminescence in degassed toluene. The lifetime values of both emission phenomena were thus measured in toluene for **E-ecl** (τ_{PF} = 8.8 ns, τ_{DL} = 2.3 μ s) and **E-sta** (τ_{PF} = 8.8 ns, τ_{DL} = 1.7 μ s). These results described a delayed phenomenon dependant of the triplet excited state. Therefore, the phosphorescence being unlikely in solution and at room temperature, we proposed to attribute this delayed emission to thermally activated delayed fluorescence (from the charge-transfer excited triplet state $T_1(^3CT)$). However, considering the last experiments performed in solid state, the delayed component could also correspond to delayed fluorescence DF (from the locally-excited triplet state $T_2(^3LE)$); additional temperature-dependant measurements should be carried out soon to confirm one desexcitation pathway or the other.

Finally, the two emitters were studied in solid state. Due to that high LUMO level energy the first attempts of dispersing the emitter with DPEPO or PMMA in a blend were inefficient and the photophysic properties had to be measured on neat films. The PLQYs were measured at 26.5% and 11.4% for **E-ecl** and **E-sta**, respectively. The time-resolved experiments demonstrated the presence of one prompt fluorescence and two delayed luminescence phenomena (DL1 and DL2) at room temperature. The lifetime values were then measured for **E-ecl** (τ_{PF} = 8.2 ns, τ_{DL1} = 2.0 μ s, τ_{DL2} = 5.2 μ s) and **E-sta** (τ_{PF} = 9.8 ns, τ_{DL1} = 1.8 μ s, τ_{DL2} = 4.7 μ s). The processes of absorption and emission were then studied *versus* temperature: 300, 250, 200, 150, 100, and 70 K. This study showed on cooling that the first and second delayed component (DL1 and DL2) lifetimes increase and also that the DL1/DL2 ratio decreases significantly. Among the different possible desexcitation pathways, we proposed to attribute the first delayed emission to simple delayed fluorescence (DF) and the second delayed

component to phosphorescence. From these conclusions, we evaluated the ΔE_{ST} of **E-ecl** and **E-sta** (0.08 eV for both emitters) by measuring the shift of maxima of emission at 77 K between prompt and delayed emissions.

Finally, we fabricated a first OLED device based on the eclipsed isomer **E-ecl**. Despite the low efficiency of the device (external quantum yield of 2.0 % and maximum luminance of 600 cd.cm²) the results are encouraging. Further modifications of the different layers of the device should be performed soon in order to increase its efficiency.

The short-term goal of this project is to validate the hypotheses about the mechanism of delayed emission of the eclipsed emitter **E-ecl**, and to carry out the photophysical study in solid state on the staggered isomer **E-sta**. A detailed comparison of both isomers should be performed to explain the influence of the isomerism on the phenomena of emission. The long-term goal should be focused on investigating the electronic properties of the cyclophane core itself in order to explain the different emissions observed, and especially to obtain more insights about the phosphorescence phenomenon observed at room temperature.

¹⁴⁸ Friedman, L.; Shechter, H. *J. Org. Chem.* **1961**, *26*, 2522–2524.

¹⁴⁹ Huang, C. B.; Yi, D. S.; Liu, T. M. *Adv. Mater. Res.* **2012**, *476–478*, 1178–1185.

¹⁵⁰ Jeffrey, G. A. *An introduction to hydrogen bonding*, Oxford university press **1997**.

¹⁵¹ Boese, A. D.; Martin, J. M. L. *J. Chem. Phys.* **2004**, *121*, 3405–3416.

¹⁵² Huang, S.; Zhang, Q.; Shiota, Y.; Nakagawa, T.; Kuwabara, K.; Yoshizawa, K.; Adachi, C. *J. Chem. Theory Comput.* **2013**, *9*, 3872–3877.

¹⁵³ Hirata, S.; Sakai, Y.; Masui, K.; Tanaka, H.; Lee, S. Y.; Nomura, H.; Nakamura, N.; Yasumatsu, M.; Nakanotani, H.; Zhang, Q.; Shizu, K.; Miyazaki, H.; Adachi, C. *Nat. Mater.* **2015**, *14*, 330–336.

¹⁵⁴ Gülseven Sıdır, Y.; Sıdır, İ. *Spectrochim. Acta Part A Mol. Biomol. Spectrosc.* **2013**, *102*, 286–296.

¹⁵⁵ D’Aléo, A.; Sazzad, M. H.; Kim, D. H.; Choi, E. Y.; Wu, J. W.; Canard, G.; Fages, F.; Ribierre, J.-C.; Adachi, C. *Chem. Commun.* **2017**, *2*, 2–5.

¹⁵⁶ Serevičius, T.; Nakagawa, T.; Kuo, M.-C.; Cheng, S.-H.; Wong, K.-T.; Chang, C.-H.; Kwong, R. C.; Xia, S.; Adachi, C. *Phys. Chem. Chem. Phys.* **2013**, *15*, 15850.

¹⁵⁷ Suzuki, K.; Kubo, S.; Shizu, K.; Fukushima, T.; Wakamiya, A.; Murata, Y.; Adachi, C.; Kaji, H. *Angew. Chemie Int. Ed.* **2015**, *54*, 15231–15235.

¹⁵⁸ Bredas, J.-L. *Mater. Horiz.* **2014**, *1*, 17–19.

GENERAL CONCLUSION

The [2.2]paracyclophane and its analogue dithia[3.3]paracyclophane were first satirically described by Cram as constricted molecules with “inherent suicidal tendencies”. After dozens of unsuccessful reactions carried out on the cyclophane unit, I can only agree with the first part of this definition: a constricted molecule indeed, but acting as a rock when it comes to reacting with any chemical. After the first attempts of catalyses in smooth conditions, several harsh reactants were tried out. The cyclophane unit was able to endure sodium hydride, bromine, sulphuric acid or even *n*-butyl lithium treatments and was still standing at the end of the reaction. Therefore, I had to resort to alternative side-routes in order to arrive to the cyclophane precursors, whilst leaving the cyclophane synthesis to the end of the synthetic route. Besides from the targeted Janus tecton **JT**, the synthesis of the pedestal **P1** (and **P2**), the naked pillar **NP** and the two isomers **E-ecl** and **E-sta** were finally carried out with relatively good overall yields, considering the difficulties encountered along the reaction pathways.

The first objective of this PhD thesis was to continue the work of previous students by developing new cyclophane-based molecules capable of self-assembling on surfaces. The whole design, previously described with the molecular clip functions, had to be entirely re-thought in order to create a new “universal” pedestal capable of self-assembling on any substrate by any supramolecular bond. As a consequence, the majority of the previous reactions developed in the lab were unfit for the new design. Thus, developing the synthesis and finding time to actually test the self-assembly on surface proved difficult, and I was able to only spend a few weeks at the CEA of Saclay working with Dr. Fabrice Charra under the STM. However, this gave me the opportunity to work with physicists and thus to learn more about the physical aspects of my work on surfaces. With the help of Dr. Charra, we were able to analyse and understand the peculiar square lattice resulting from the pedestal’s network on HOPG. These preliminary results obtained with the pedestal **P1** are very promising, and the required additional tests using the naked pillar **NP** on HOPG and gold will be carried out soon.

The second objective of this thesis was about exploring a new use of the cyclophane unit in the field of organic emitting materials for OLEDs. This brand new subject was quite challenging because, firstly it was developed in parallel to the first subject, and thus additional reactions were required. Secondly, the required characterisations demanded a quick learning of the theory base of photophysics. As part of this project, I had the great opportunity to work for a few weeks in the laboratory of Prof. Chihaya Adachi (OPERA Laboratory) at Kyushu University in Fukuoka (Japan). In OPERA, I carried out the photophysical experiments by myself using specific apparatus (like the Streak camera) acquiring enough theoretical and practical knowledge to understand the electronic processes involved in the photoluminescence of the emitters **E-ecl** and **E-sta**. In this project, I was able to follow the whole course of the molecules from the molecular design and synthesis to the photophysical investigations and finally the elaboration of the OLED device. Despite the apparent low efficiency of these emitters in the solid state or as part of the device, the results are actually very encouraging. Indeed, these studies are the very first investigations for thermally activated delayed fluorescence performed on cyclophane-based molecules and thus, the parameters of the experiments have not been fully optimised yet. In addition, these emitters also present a rare, room temperature metal-free

phosphorescence in the solid state. There are to date, very few examples of materials presenting this phenomenon and it is of great interest to study these materials further.

To conclude the work undertaken during my PhD, I would like to point out the amount and variety of new skills and knowledge that I acquired during these three years. In addition to the many new reactions that I performed, this project also allowed me to learn a lot about the inner workings in Science, about research in general and also about myself. I arrived in this laboratory as a newly-graduated organic chemist and I have ended up now with new competences in self-assembly on surfaces, theoretical calculations and photophysics. Moreover, I fully understand now the importance of working as part of a team: when the chemistry went wrong, nothing was more useful than the help from colleagues to envisage other approaches and routes.. My PhD journey now comes to an end, and now I am just waiting for a new “easy” subject to work on!

APPENDICES

APPENDIX 1: EXPERIMENTAL DETAILS

All solvents and reactants were purchased from commercial supplier. The reactants were used without further purification. When necessary, the solvent was dried by using a MBraun solvent purification system (MB SPS-800).

The purifications performed by chromatography were either carried out by gravity column chromatography using silica gel (Si 60, 40-63 μm , Merck) or by flash chromatography (Combiflash Companion).

The nuclear magnetic resonance experiments were recorded at 300 or 600 MHz (Bruker, BBFO probe for the 2D-experiments). The proton and carbon chemical shifts (δ) are reported in ppm and are referenced to the residual solvent signal: CDCl_3 (7.26, 77.16) and DMSO (2.50, 39.52). The abbreviations used to describe the multiplicity of the signals are: s for singlet, d for doublet, t for triplet, q for quartet and m for multiplet.

The Infra-red spectra were recorded with a ThermoFisher Nicolet iS10 FT-IR spectrometer.

The UV/Vis spectra were recorded with a Varian Cary WinUV spectrophotometer. The cells were in quartz with two faces (thickness: 1 cm). The photoluminescence spectra were recorded with a Varian Cary Eclipse fluorescence spectrophotometer.

STM images were acquired at the CEA of Saclay in the team of Dr. Fabrice Charra, at room temperature with a homemade digital system. The fast scan axis was kept perpendicular to the sample slope. Images acquired simultaneously in both fast scan directions are systematically recorded and compared. All images are corrected for the drift of the instrument by combining two successive images with downward and upward slow-scan directions. The solvent was phenyl-octane (Aldrich, 98%), which avoids the co-adsorption often observed with linear alkanes. The substrate was HOPG (Goodfellow) and the tips were mechanically formed from a 250 μm Pt-Ir wire (Pt80/Ir20, Goodfellow). The monolayers were formed by drop casting a droplet (ca. 10 μL , in dichloromethane) of solution immediately after cleaving the substrate. The samples were heated at 80°C for 10 minutes before immersing the STM junction in an additional droplet of phenyloctane (ca. 10 μL) and approaching the STM tip.

The AFM images were acquired on an AFM 5100 equipped with a 90 μm Keysight scanner in the MONARIS lab (UPMC) with Dr. Imad Arfaoui. The images were recorded in contact mode using an ultra-thin tip (65 kHz, 0.5 N/m).

The X-ray crystallography was performed on a Bruker APEX-II CCD diffractometer.

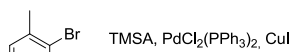
At the INSP, the UV-Vis absorption spectra at low temperature were recorded on a Varian Cary WinUV equipped with a homemade cryostat.

In the lab Pr. Adachi in OPERA, the UV-Vis absorption spectra were recorded on a Shimadzu UV-2501 recording spectrophotometer. PL spectra were recorded on a Hitachi F-4600 fluorescence spectrophotometer. The PL lifetimes were measured by a single photon counting spectrometer from Edinburgh Instruments (FLS920) with a Picosecond Pulsed UV-LASTER (LASTER377) as the excitation source. Absolute PLQYs were obtained using a Quantaurus-QY measurement system (C11347-11, Hamamatsu Photonics) and all the samples were excited at 330 nm. Fluorescence and delayed luminescence characteristics in solid states were measured under vacuum using a streak

camera system (C4334, Hamamatsu Co.). A nitrogen gas laser (MNL200, LASERTECHNIK BERLIN) with an excitation wavelength of 337nm was used. Excitation light was absolutely cut off by putting a 370 nm long band-pass filter (SCF-50S-37L, SIGMA KOKI CO., LTD.) in front of the photo-detector. The current density-voltage-luminance (J-V-L) characteristics of the OLED were measured using a semiconductor parameter analyzer (Agilent Co., HP4155C) with an optical power meter (Newport, Model 1835-C).

APPENDIX 2: PROCEDURES

Synthesis of the 1,4-Bis[(trimethylsilyl)ethynyl]-2,5-dimethylbenzene **1**¹⁵⁹



Under Argon.

In a Schlenk tube were introduced 2,5-dibromo-*p*-xylene (2 g, 7.6 mmol), PdCl₂(PPh₃)₂ (265 mg, 0.4 mmol), CuI (70mg, 0.4 mmol) and triethylamine (40 mL, 300 mmol). Then, trimethylsilylacetylene (3.5 mL, 24 mmol) was added, the Schlenk tube was sealed and the mixture was stirred at 100°C for 8 hours. The solution was diluted with dichloromethane, washed with water and dried over magnesium sulfate. After evaporation *in vacuo*, the residue was purified by flash chromatography (SiO₂, petroleum ether) to afford **1** as a white powder in 91 % yield.

¹H NMR (300 MHz, CDCl₃) δ 7.26 (s, 2H), 2.34 (s, 6H), 0.25 (s, 18 H).

¹³C NMR (300 MHz, CDCl₃) δ 137.66, 132.97, 123.18, 104.03, 99.67, 19.97, 0.18.

Synthesis of the 1,4-Diethynyl-2,5-dimethylbenzene **2**¹⁵⁹

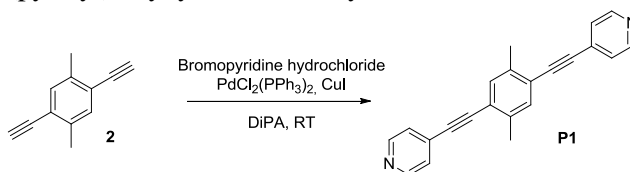


To a solution of **1** (415 mg, 1.4 mmol) in methanol (25 mL) was added potassium fluoride (350 mg, 6.0 mmol). The mixture was stirred overnight and then evaporated *in vacuo*. The residue was purified by chromatography (SiO₂, dichloromethane) to afford **2** as a light yellow powder in 96 % yield.

¹H NMR (300 MHz, CDCl₃) δ 7.26 (s, 2H), 3.33 (s, 2H), 2.34 (s, 6H).

¹³C NMR (300 MHz, CDCl₃) δ 137.91, 133.40, 122.48, 82.33, 82.26, 19.94.

Synthesis of the 1,4-Bis[(pyridyl)ethynyl]-2,5-dimethylbenzene **P1**



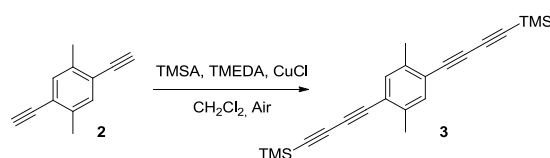
Under Argon.

In a Schlenk tube were introduced **2** (200 mg, 1.3 mmol), *p*-bromopyridine hydrochloride (500 mg, 2.0 mmol), Pd(PPh₃)₂Cl₂ (46 mg, 0.07 mmol) and CuI (13 mg, 0.7 mmol). Then, DiPA (15 mL, 107.0 mmol) was added and the mixture was stirred at RT for 8 hours. The solution was diluted with dichloromethane, washed with water and dried over MgSO₄. After evaporation *in vacuo*, the residue was purified by chromatography (SiO₂, petroleum ether: ethyl acetate 9:1) to afford **P1** as a white powder in 85 % yield.

¹H NMR (300 MHz, CDCl₃) δ 8.63 (m, 4H), 7.40 (m, 6H), 2.49 (s, 6H).

¹³C NMR (300 MHz, CDCl₃) δ 149.89, 138.03, 133.26, 131.59, 125.59, 122.92, 92.75, 92.18, 20.12.

Synthesis of the 1,4-Bis[(trimethylsilyl)butadiynyl]-2,5-dimethylbenzene **3**

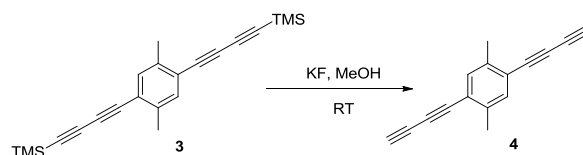


To a solution of copper chloride (2.2 g, 16.2 mmol) in dichloromethane (20 mL) were added TMEDA (4.8 mL, 32.4 mmol). After 1 hour stirring, a solution of TMSA (4.5 mL, 32.4 mmol) and **2** (500 mg, 3.24 mmol) in dichloromethane (30 mL) was added and dried air was bubbled into the solution. After 5 hour, the black solution was evaporated, and the crude was dissolved in petroleum ether. The mixture was filtered off on silica gel to afford **3** as a white powder in 75% yield.

^1H NMR (300 MHz, CDCl_3) δ 7.27 (s, 2H), 2.36 (s, 6H), 0.24 (s, 18 H).

^{13}C NMR (300 MHz, CDCl_3) δ 139.22, 134.02, 122.31, 95.53, 87.85, 79.66, 75.42, 20.08, 0.26.

Synthesis of the 1,4-Dibutadiynyl-2,5-dimethylbenzene **4**



To a solution of **3** (150 mg, 0.4 mmol) in methanol (75 mL) was added potassium fluoride (125 mg, 2.1 mmol). The mixture was stirred overnight and then evaporated *in vacuo*. The residue was purified by chromatography (SiO_2 , dichloromethane) to afford **4** as a light yellow powder in 95 % yield.

^1H NMR (300 MHz, CDCl_3) δ 7.31 (s, 2H), 2.59 (s, 2H), 2.38 (s, 6H).

Synthesis of the 1,4-Bis[(pyridyl)butadiynyl]-2,5-dimethylbenzene **P2**

Under Argon.

In a Schlenk tube were introduced **4** (100 mg, 0.5 mmol), *p*-Iodopyridine (510 mg, 2.5 mmol), $\text{Pd}(\text{PPh}_3)_2\text{Cl}_2$ (35 mg, 0.05 mmol) and CuI (10 mg, 0.5 mmol). Then, DiPA (5 mL, 35.0 mmol) was added and the mixture was stirred at RT for 8 hours. The solution was diluted with dichloromethane, washed with water and dried over MgSO_4 . After evaporation *in vacuo*, the residue was purified by chromatography (SiO_2 , petroleum ether: ethyl acetate 9:1) to afford **P2** as a white powder in 40 % yield.

^1H NMR (300 MHz, CDCl_3) δ 8.62 (m, 4H), 7.37 (m, 6H), 2.43 (s, 6H).

^{13}C NMR (300 MHz, CDCl_3) δ 150.01, 139.36, 134.05, 130.18, 126.16, 122.46, 82.334, 80.14, 78.77, 78.27, 20.10.

Synthesis of the 1,4-Bis[(trimethylsilyl)ethynyl]-2,5-bis(bromomethyl)benzene **5**

Procedure 1:

To a solution of **1** (0.5 g, 1.7 mmol) were added NBS (630 mg, 3.5 mmol) and AIBN (14 mg, 0.08 mmol). The mixture was refluxed overnight and then allowed to cool down to RT. The solvent was evaporated *in vacuo* and the crude was purified by flash chromatography (SiO₂, petroleum ether) to afford **5** as a white powder in 5-37 % yield.

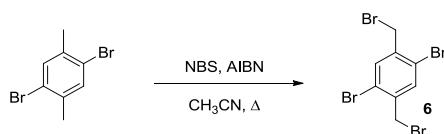
Procedure 2:

To a solution of **1** (1.0 g, 3.4 mmol) were added NBS (2.7 g, 15.0 mmol) and AIBN (55 mg, 0.35 mmol). The mixture was refluxed overnight and then allowed to cool down to RT. The solvent was evaporated *in vacuo* and the crude was purified by flash chromatography (SiO₂, petroleum ether) to afford **5** as a white powder in 12-52 % yield.

¹H NMR (300 MHz, CDCl₃) δ 7.51 (s, 2H), 4.57 (s, 4H), 0.28 (s, 18H).

¹³C NMR (300MHz, CDCl₃) δ 139.79, 133.82, 123.58, 103.31, 101.07, 30.56, 0.10.

Synthesis of the 1,4-dibromo-2,5-bis(bromomethyl)benzene **6**¹⁶⁰



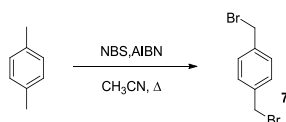
To a solution of 2,5-dibromo-*p*-xylene (5 g, 19 mmol) in acetonitrile (75 mL) was added NBS (7.1 g, 40 mmol) and AIBN (160 mg, 1 mmol). After stirring for 24 hours under reflux, the mixture was evaporated *in vacuo* and washed by hot methanol to afford **6** as a white powder in 60% yield.

Mp = 161 °C

¹H NMR (300 MHz, CDCl₃) δ 7.66 (s, 2H), 4.51 (s, 4H).

¹³C NMR (300MHz, CDCl₃) δ 139.14, 135.50, 123.43, 31.62.

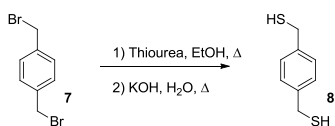
Synthesis of the 1,4-bis(bromomethyl)benzene **7**



To a solution of *p*-xylene (2 g, 19 mmol) in acetonitrile (60 mL) was added NBS (7.1 g, 40 mmol) and AIBN (160 mg, 1 mmol). After stirring for 16 hours under reflux, the mixture was evaporated *in vacuo* and purified by flash chromatography (SiO₂, petroleum ether: dichloromethane 1:1) to afford **7** as a white powder in 87% yield.

¹H NMR (300 MHz, CDCl₃) δ 7.37 (s, 4H), 4.48 (s, 4H).

Synthesis of the 1,4-bis(mercaptomethyl)benzene **8** ¹⁶¹



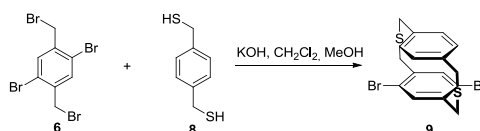
Under Argon.

To a solution of **7** (5 g, 18.9 mmol) in ethanol (75 mL) was added thiourea (3.6 g, 47.4 mmol). The mixture was heated at 80°C for 3h and then cool down to RT. After evaporation *in vacuo*, the residue was dissolved in water (20 mL). Sodium hydroxide was added (2.25 g, 56.7 mmol) and the mixture was heated to 100 °C overnight. The solution was then extracted with diethylether and dried over MgSO₄. Evaporation *in vacuo* gave **8** as colourless crystals in 79% yield.

¹H NMR (300 MHz, CDCl₃) δ 7.27 (s, 2H), 3.72 (d, 4H), 1.75 (t, 2H).

¹³C NMR (300 MHz, CDCl₃) δ 140.07, 128.46, 28.72.

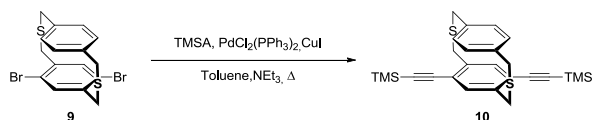
Synthesis of the 5,8-dibromo-2,11-dithia[3.3]paracyclophane **9** ¹⁶²



To a solution of KOH (330 mg, 6.0 mmol) in methanol (1 L) were introduced dropwise (2.5 mL/h) a solution of **6** (2.0 g, 4.7 mmol) and **8** (0.8 g, 4.7 mmol) in dichloromethane (100 mL) and another solution of KOH (330 mg, 6.0 mmol) in methanol (50 mL). At the end of the addition, the mixture was acidified with dilute H₂SO₄, extracted with CH₂Cl₂, washed with water, dried over MgSO₄ and evaporated *in vacuo*. The crude was washed by hot ethanol to afford **9** as a white powder in 89 % yield.

¹H NMR (300 MHz, CDCl₃) δ 7.19 (s, 2H), 7.17 (d, 2H), 7.03 (d, 2H), 4.15-3.57 (m, 8H).

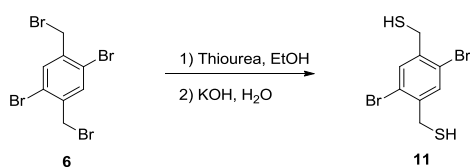
Synthesis of the 5,8-bis(trimethylsilyl)ethynyl-2,11-dithia[3.3]paracyclophane **10** ¹⁶²



Under Argon.

In a Schlenk tube were introduced **9** (400 mg, 0.93 mmol), Pd(PPh₃)₂Cl₂ (65 mg, 0.1 mmol), CuI (27 mg, 0.14 mmol), NEt₃ (5 mL, 35 mmol) and toluene (50 mL) were added. Then TMSA (2 mL, 13.8 mmol) was added and the mixture was stirred at 110°C for 8 hours. The black solution was diluted with dichloromethane, washed with water and dried over MgSO₄. After evaporation *in vacuo*, the residue was purified by chromatography (SiO₂, petroleum ether: dichloromethane 3:1) to afford **10** as a white powder in less than 10% yield. The product could not be completely isolated and thus, no characterisation could be performed.

Synthesis of the 1,4-dibromo-2,5-bis(mercaptomethyl)benzene **11**¹⁶³

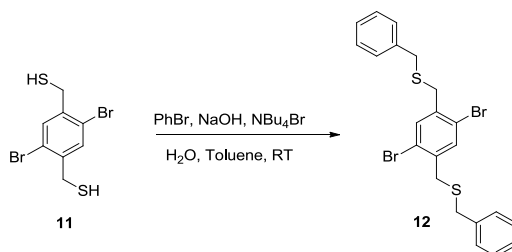


Under Argon.

To a solution of **6** (2 g, 4.8 mmol) in ethanol (15 mL) was added thiourea (0.9 g, 11.9 mmol). The mixture was heated at 80 °C for 3 h and then cool down to RT. After evaporation *in vacuo*, the residue was dissolved in water (15 mL). Sodium hydroxide was added (0.6 g, 14.2 mmol) and the mixture was heated to 100 °C overnight. The solution was then extracted with diethylether and dried over MgSO₄. Evaporation *in vacuo* gave **11** as colourless crystals in 85% yield.

¹H NMR (300 MHz, CDCl₃) δ 7.57 (s, 2H), 3.76 (d, 4H), 1.99 (t, 2H).

Synthesis of the 1,4-dibromo-2,5-bis[(benzylthio)methyl]benzene **12**

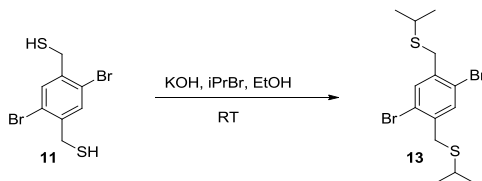


To a solution of **11** (580 mg, 1.20 mmol) in toluene (10 mL) were added tertbutylbromide (50 mg, 15 mmol) and water (10 mL). Benzylbromide (608 mg, 3.70 mmol) was then added and the mixture was stirred for 1 hour. The reaction mixture was poured into water, extracted with dichloromethane and dried over magnesium sulfate and evaporated *in vacuo*. The crude was purified by chromatography (SiO₂, petroleum ether: dichloromethane 1:1) to afford **12** in 5% yield.

¹H NMR (300 MHz, CDCl₃) δ 7.46 (s, 2H), 7.35 (m, 6H), 7.29 (m, 2H), 3.73 (s, 4H), 3.68 (s, 4H).

¹³C NMR (300 MHz, CDCl₃) δ 138.23, 137.70, 134.67, 129.08, 128.69, 127.33, 123.30, 36.53, 35.45.

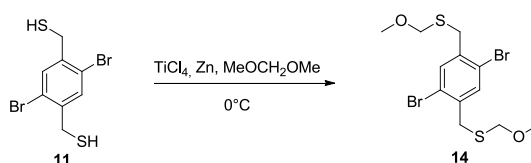
Synthesis of the 1,4-dibromo-2,5-bis[(isopropylthio)methyl]benzene **13**



To a solution of **11** (900 mg, 2.8 mmol) and potassium hydroxide (800 mg, 14.3 mmol) in ethanol (80 mL) was added 2-bromopropane (1 mL, 10 mmol) and the solution was stirred for 18 hours. The mixture was then poured into water, extracted with dichloromethane and dried over MgSO₄. The residue was purified by flash chromatography (SiO₂, petroleum ether: dichloromethane 1:0 to 1:3) to afford **13** as colourless crystals in 23% yield.

¹H NMR (300 MHz, CDCl₃) δ 7.58 (s, 2H), 3.78 (s, 4H), 2.91 (sept, 2H), 1.28 (d, 12H).

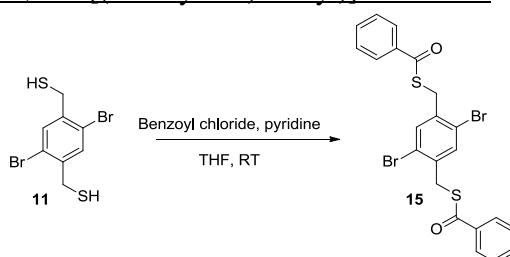
Synthesis of the 1,4-dibromo-2,5-bis[(methoxymethylthio)methyl]benzene **14**



To a solution of Zinc (90 mg, 1.4 mmol) in MOM (25 mL, 280 mmol) were added TiCl_4 (0.1 mL, 0.68 mmol). The solution was stirred for 30 min before adding **11** (200 mg, 0.6 mmol). The mixture was stirred for an additional 2 h and then hydrolyzed. The solution was extracted with AcOEt, dried over MgSO_4 and evaporated *in vacuo*. The residue was purified by chromatography (SiO_2 , petroleum ether: dichloromethane 1:1) to afford **14** as a white powder in 88 % yield.

^1H NMR (300 MHz, CDCl_3) δ 7.56 (s, 2H), 4.57 (s, 4H), 3.81 (s, 4H), 3.37 (s, 6H).

Synthesis of the 1,4-dibromo-2,5-bis[(benzoylthio)methyl]benzene **15**

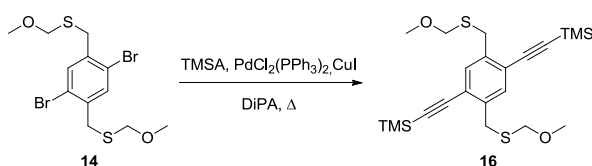


Under Argon.

To a solution of dry pyridine (0.25 mL, 3.35 mmol) in THF (20 mL) was added dry benzoylchloride (0.7 mL, 6.1 mmol). Then, **11** (500 mg, 1.55 mmol) was added and the mixture was stirred for 14 hours. The solution was diluted with methanol and filtrated to afford **15** as a white powder in 95% yield.

^1H NMR (300 MHz, CDCl_3) δ 7.94 (d, $^3J = 7.0$ Hz, 4H), 7.76 (s, 2H), 7.57 (t, $^3J = 7.0$ Hz, 2H), 7.44 (t, $^3J = 7.0$ Hz, 4H), 4.36 (s, 4H).

Synthesis of the 1,4-bis[(trimethylsilyl)ethynyl]-2,5-bis[(methoxymethylthio)methyl]benzene **16**

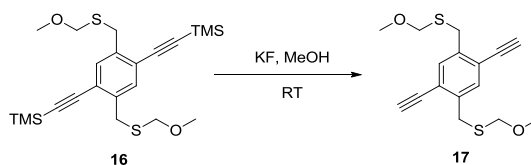


Under Argon.

In a Schlenk tube were introduced **14** (200 mg, 0.4 mmol), $\text{PdCl}_2(\text{PPh}_3)_2$ (40 mg, 0.06 mmol), CuI (10 mg, 0.06 mmol) and DiPA (5 mL, 0.35 mmol). Then, trimethylsilylacetylene (0.8 mL, 5.5 mmol) was added and the mixture was stirred at 100°C overnight. The solution was diluted with dichloromethane, washed with water and dried over magnesium sulfate. After evaporation *in vacuo*, the residue was purified by flash chromatography (SiO_2 , petroleum: dichloromethane 1:1) to afford **16** as a white powder in 84 % yield.

^1H NMR (300 MHz, CDCl_3) δ 7.42 (s, 2H), 4.56 (s, 4H), 3.85 (s, 4H), 3.37 (s, 6H), 0.27 (s, 18H).

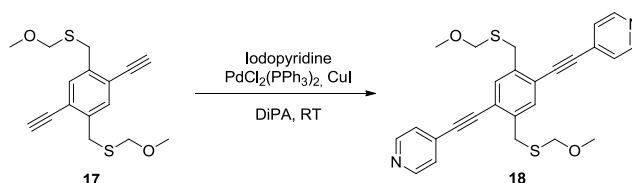
Synthesis of the 1,4-(diethynyl)-2,5-bis[(methoxymethylthio)methyl]benzene **17**



To a solution of **16** (540 mg, 1.3 mmol) in methanol (50 mL) was added potassium fluoride (740 mg, 12.7 mmol). The mixture was stirred overnight and then evaporated *in vacuo*. The residue was purified by chromatography (SiO₂, petroleum ether: dichloromethane 1:1) to afford **17** as a red crystals in 64 % yield.

¹H NMR (300 MHz, CDCl₃) δ 7.48 (s, 2H), 4.57 (s, 4H), 3.89 (s, 4H), 3.42 (s, 2H), 3.36 (s, 6H).

Synthesis of the 1,4-bis[(pyridyl)ethynyl]-2,5-bis[(methoxymethylthio)methyl]benzene **18**

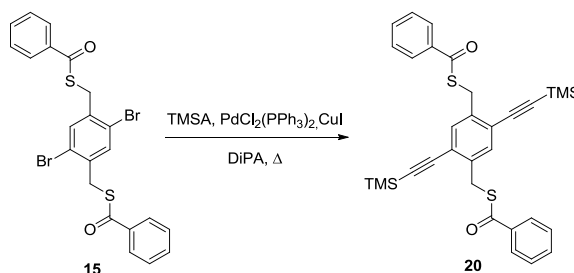


Under Argon.

In a Schlenk tube were introduced **17** (100 mg, 0.36 mmol), Iodopyridine (370 mg, 1.8 mmol), Pd(PPh₃)₂Cl₂ (25 mg, 0.04 mmol) and CuI (8 mg, 0.4 mmol). Then, DiPA (5 mL, 35.0 mmol) was added and the mixture was stirred for 8 hours. The solution was diluted with dichloromethane, washed with water and dried over MgSO₄. After evaporation *in vacuo*, the residue was purified by flash chromatography (SiO₂, petroleum ether: ethyl acetate 9:1 to 1:1) to afford **18** as a yellow powder in 67 % yield.

¹H NMR (300 MHz, CDCl₃) δ 8.63 (s, 4H), 7.52 (s, 2H), 7.42 (d, ³J = 5.2 Hz, 4H), 4.60 (s, 4H), 3.95 (s, 4H), 3.37 (s, 6H).

Synthesis of the 1,4-bis[(trimethylsilyl)ethynyl]-2,5-bis[(benzoylthio)methyl]benzene **20**

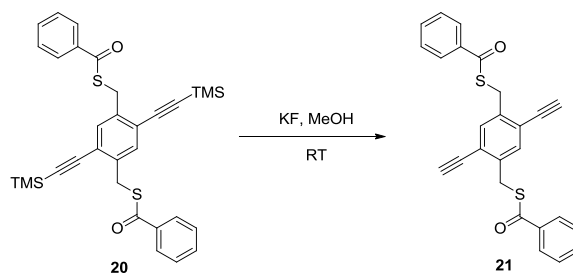


Under Argon.

In a Schlenk tube were introduced **15** (550 mg, 1.0 mmol), PdCl₂(PPh₃)₂ (65 mg, 0.1 mmol), CuI (18 mg, 0.1 mmol), DiPA (1.3 mL, 9.5 mmol) and THF (10 mL). Then, trimethylsilylacetylene (1.3 mL, 9.5 mmol) was added and the mixture was stirred at 100°C overnight. The solution was diluted with dichloromethane, washed with water and dried over MgSO₄. After evaporation *in vacuo*, the residue was purified by flash chromatography (SiO₂, petroleum: dichloromethane 1:0 to 1:1) to afford **20** as white crystals in 31 % yield.

¹H NMR (300 MHz, CDCl₃) δ 7.95 (d, ³J = 7 Hz, 4H), 7.59 (s, 2H), 7.56 (t, ³J = 7 Hz, 2H), 7.43 (t, ³J = 7 Hz, 4H), 4.42 (s, 4H), 0.25 (s, 18H).

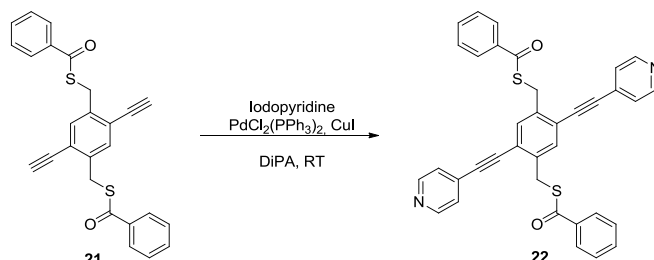
Synthesis of the 1,4-diethynyl-2,5-bis[(benzoylthio)methyl]benzene **21**



To a solution of **20** (110 mg, 0.2 mmol) in methanol (100 mL) was added potassium fluoride (120 mg, 2.0 mmol). The mixture was stirred overnight and then evaporated *in vacuo*. The residue was diluted with dichloromethane and filtrated over silica gel. The filtrate was evaporated *in vacuo* to afford **21** as white crystals in 95 % yield.

^1H NMR (300 MHz, CDCl_3) δ 7.96 (d, $^3J = 7$ Hz, 4H), 7.64 (s, 2H), 7.57 (t, $^3J = 7$ Hz, 2H), 7.44 (t, $^3J = 7$ Hz, 4H), 4.44 (s, 4H), 3.45 (s, 2H).

Synthesis of the 1,4-bis[(pyridyl)ethynyl]-2,5-bis[(benzoylthio)methyl]benzene **22**

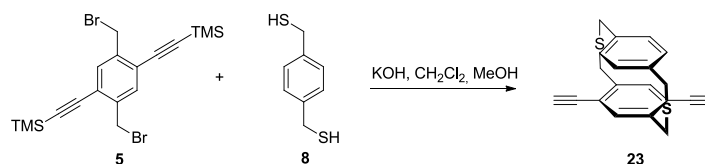


Under Argon.

In a Schlenk tube were introduced **21** (120 mg, 0.3 mmol), Iodopyridine (360 mg, 1.7 mmol), $\text{Pd}(\text{PPh}_3)_2\text{Cl}_2$ (25 mg, 0.04 mmol) and CuI (8 mg, 0.4 mmol). Then, DiPA (10 mL, 70.0 mmol) was added and the mixture was stirred for 20 hours. The solution was diluted with dichloromethane, washed with water and dried over MgSO_4 . After evaporation *in vacuo*, the residue was purified by flash chromatography (SiO_2 , petroleum ether: ethyl acetate 9:1 to 1:1) to afford **22** as a yellow powder in 40 % yield.

^1H NMR (300 MHz, CDCl_3) δ 8.64 (s, 4H), 7.96 (d, $^3J = 7.0$ Hz, 4H), 7.76 (s, 2H), 7.50 (t, $^3J = 7.0$ Hz, 2H), 7.47 (m, 8H), 4.53 (s, 4H).

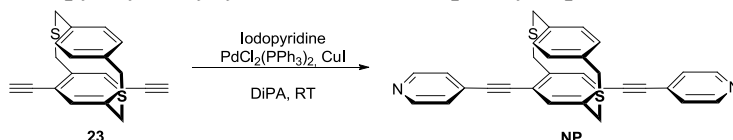
Synthesis of the 5,8-diethynyl-2,11-dithia[3.3]paracyclophane **23** ¹⁶²



To a solution of KOH (100 mg, 1.8 mmol) in methanol (350 mL) were introduced dropwise (4 mL/h) a solution of **5** (500 mg, 1.1 mmol) and **8** (187 mg, 1.1 mmol) in dichloromethane (50 mL) and another solution of KOH (300 mg, 5.4 mmol) in methanol (50 mL). At the end of the addition, the mixture was acidified with dilute H_2SO_4 , extracted with Dichloromethane, washed with water, dried over MgSO_4 and evaporated *in vacuo*. The crude was purified by chromatography (SiO_2 , petroleum ether: dichloromethane 1:1) to afford **23** as a white powder in 43 % yield.

^1H NMR (300 MHz, CDCl_3) δ 7.14 (s, 2H), 7.06 (d, $^3J = 8$ Hz, 2H), 7.02 (d, $^3J = 8$ Hz, 2H), 4.30 (d, $^3J = 15$ Hz, 2H), 3.87 (d, $^3J = 15$ Hz, 2H), 3.78 (d, $^3J = 15$ Hz, 2H), 3.59 (d, $^3J = 15$ Hz, 2H), 3.43 (s, 2H).

Synthesis of the 5,8-bis[(pyridyl)ethynyl]-2,11-dithia[3.3]paracyclophane **NP**

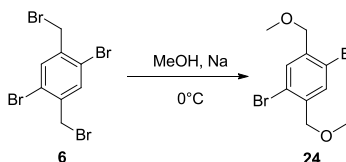


Under Argon.

In a Schlenk tube were introduced **23** (150 mg, 0.5 mmol), Iodopyridine (480 mg, 2.4 mmol), $\text{Pd}(\text{PPh}_3)_2\text{Cl}_2$ (35 mg, 0.05 mmol) and CuI (10 mg, 0.05 mmol). Then, DiPA (1.5 mL, 10.0 mmol) was added and the mixture was stirred for 20 hours. The solution was diluted with dichloromethane, washed with water and dried over MgSO_4 . After evaporation *in vacuo*, the residue was purified by flash chromatography (SiO_2 , petroleum ether: ethyl acetate 9:1 to 1:1) to afford **NP** as a yellow powder in 44 % yield.

^1H NMR (300 MHz, CDCl_3) δ 8.69 (s, 4H), 7.49 (d, $^3J = 5.5$ Hz, 4H), 7.22 (s, 2H), 7.08 (d, $^3J = 8$ Hz, 2H), 7.05 (d, $^3J = 8$ Hz, 2H), 4.32 (d, $^3J = 15$ Hz, 2H), 3.90 (d, $^3J = 15$ Hz, 2H), 3.85 (d, $^3J = 15$ Hz, 2H), 3.72 (d, $^3J = 15$ Hz, 2H).

Synthesis of the 1,4-dibromo-2,5-dimethoxymethylbenzene **24**



Under Argon.

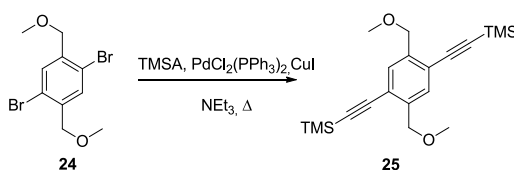
In a Schlenk tube were introduced **6** (1 g, 2.4 mmol), degassed MeOH (20 mL). After stirring for 10 minutes, a solution of sodium (0.14 g, 6.0 mmol) in methanol (20 mL) was added dropwise and the reaction was heated at 90°C overnight. The solution was then poured into water, extracted with dichloromethane and dried over magnesium sulfate. The dichloromethane was removed *in vacuo* to afford **24** as a white powder in quantitative yield.

$\text{Mp} = 70^\circ\text{C}$

^1H NMR (300 MHz, CDCl_3) δ 7.63 (s, 2H), 4.47 (s, 4H), 3.47 (s, 6H).

^{13}C NMR (300 MHz, CDCl_3) δ 138.50, 112.33, 121.30, 73.23, 58.89.

Synthesis of the 1,4-bis[(trimethylsilyl)ethynyl]-2,5-dimethoxymethylbenzene **25**



Under Argon

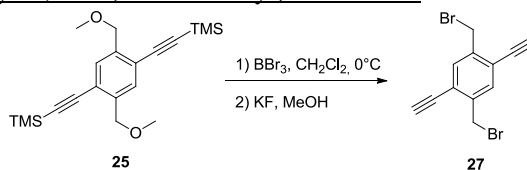
In a Schlenk tube were introduced **24** (1.9g, 6 mmol), $\text{PdCl}_2(\text{PPh}_3)_2$ (200 mg, 0.3 mmol), CuI (0.1 mg, 0.3 mmol) and triethylamine (30 mL, 225 mmol). Then, trimethylsilylacetylene (2.7 mL, 19 mmol) was added, the Schlenk tube was sealed and the mixture was stirred at 100°C for 8 hours. The solution was diluted with dichloromethane, washed with water and dried over magnesium sulfate. After evaporation *in vacuo*, the residue was purified by flash chromatography (SiO_2 , petroleum ether) to afford **25** as a white powder in 84 % yield.

$\text{Mp} = 89^\circ\text{C}$

^1H NMR (300 MHz, CDCl_3) δ 7.53 (s, 2H), 4.57 (s, 4H), 3.44 (s, 6H), 0.24 (s, 18H).

^{13}C NMR (300 MHz, CDCl_3) δ 139.43, 131.23, 122.01, 102.34, 100.96, 72.11, 58.73, 0.07.

Synthesis of the 1,4-diethynyl-2,5-bis(bromomethyl)benzene **27**



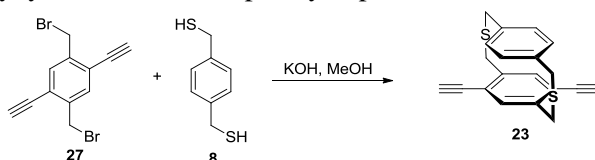
Under Argon.

In a Schlenk tube were introduced **25** (0.45g, 1.2 mmol) and dichloromethane (10 mL). After stirring at 0°C for 10 minutes, a solution of BBr_3 (3.7 mL, 3.7 mmol) in dichloromethane (10 mL) was added dropwise. After stirring for 2 hours, the reaction mixture was poured into water and extracted with dichloromethane. The solution was dried over MgSO_4 and evaporated *in vacuo*. The crude was then dissolved in methanol (80 mL) and potassium fluoride (340 mg, 6 mmol). The solution was stirred overnight at room temperature and then poured in water, extracted with dichloromethane and dried over MgSO_4 . The solution was then evaporated *in vacuo* to afford **27** as a light yellow powder in 47% yield.

^1H NMR (300 MHz, CDCl_3) δ 7.58 (s, 2H), 4.60 (s, 4H), 3.51 (s, 2H).

^{13}C NMR (300 MHz, CDCl_3) δ 140.13, 134.50, 122.98, 85.02, 79.83, 30.15.

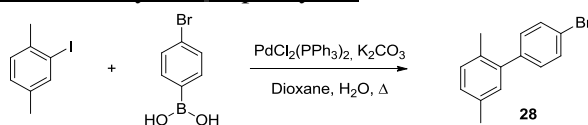
Synthesis of the 5,8-diethynyl-2,11-dithia[3.3]paracyclophane **23**¹⁶²



To a solution of KOH (100 mg, 1.8 mmol) in methanol (350 mL) were introduced dropwise (4 mL/h) a solution of **27** (400 mg, 1.3 mmol) and **8** (200 mg, 1.3 mmol) in dichloromethane (50 mL) and another solution of KOH (200 mg, 3.6 mmol) in methanol (50 mL). At the end of the addition, the mixture was evaporated *in vacuo*. The residue was then dissolved in Dichloromethane, washed with water, dried over MgSO_4 and evaporated again *in vacuo*. The crude was purified by chromatography (SiO_2 , petroleum ether: dichloromethane 1:1) to afford **23** as a white powder in 43 % yield.

^1H NMR (300 MHz, CDCl_3) δ 7.14 (s, 2H), 7.06 (d, $^3J = 8$ Hz, 2H), 7.02 (d, $^3J = 8$ Hz, 2H), 4.30 (d, $^3J = 15$ Hz, 2H), 3.87 (d, $^3J = 15$ Hz, 2H), 3.78 (d, $^3J = 15$ Hz, 2H), 3.59 (d, $^3J = 15$ Hz, 2H), 3.43 (s, 2H).

Synthesis of the 4'-bromo-2,5-dimethyl-1,1'-biphenyl **28**



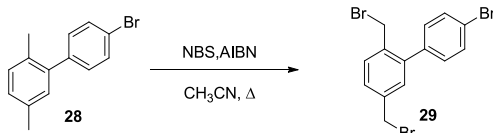
Under Argon.

To *p*-bromophenylboronic acid (860 mg, 4.30 mmol) and $\text{Pd}(\text{PPh}_3)_2\text{Cl}_2$ (175 mg, 0.25 mmol) was added a solution of 2-iodo-*p*-xylene (0.62 mL, 4.30 mmol) in dioxane (20 mL). Then, K_2CO_3 (2 g, 15.00 mmol) in water (5 mL) was added, and the mixture was heated at 110°C for 12 hours. The reaction was allowed to cool down to RT and was poured into water. The mixture was then extracted with dichloromethane, dried over MgSO_4 and evaporated *in vacuo*. The crude was purified by chromatography (SiO_2 , petroleum ether) to afford **28** as a colourless oil in 94% yield.

^1H NMR (300 MHz, CDCl_3) δ 7.61 (d, $^3J = 8.5$ Hz, 2H), 7.27 (d, $^3J = 8.5$ Hz, 2H), 7.25 (d, $^3J = 8.0$ Hz, 1H), 7.18 (d, $^3J = 8.0$ Hz, 1H), 7.12 (s, 1H), 2.45 (s, 3H), 2.31 (s, 3H).

^{13}C NMR (300 MHz, CDCl_3) δ 141.05, 140.56, 135.40, 132.07, 131.26, 130.95, 130.49, 130.38, 128.40, 130.98, 21.01, 20.00.

Synthesis of the 4'-bromo-2,5-bis(bromomethyl)-1,1'-biphenyl **29**

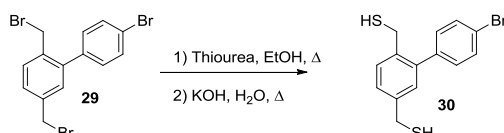


Under Argon.

To a solution of **28** (1 g, 3.8 mmol) in acetonitrile (100 mL) was added NBS (1.4 g, 8.0 mmol) and AIBN (60 mg, 0.4 mmol). After stirring for 14 hours at 90 °C, the mixture was evaporated *in vacuo* and purified by flash chromatography (SiO₂, Petroleum ether) to afford **29** as a white powder in 90% yield.

¹H NMR (300 MHz, CDCl₃) δ 7.60 (d, ³J = 8.5 Hz, 2H), 7.50 (d, ³J = 8.0 Hz, 1H), 7.41 (dd, ³J = 8.0 Hz, ⁴J = 2.0 Hz, 1H), 7.32 (d, ³J = 8.5 Hz, 2H), 7.24 (d, ⁴J = 2.0 Hz, 1H), 4.49 (s, 2H), 4.39 (s, 2H).

Synthesis of the 4'-bromo-2,5-bis(mercaptomethyl)-1,1'-biphenyl **30**

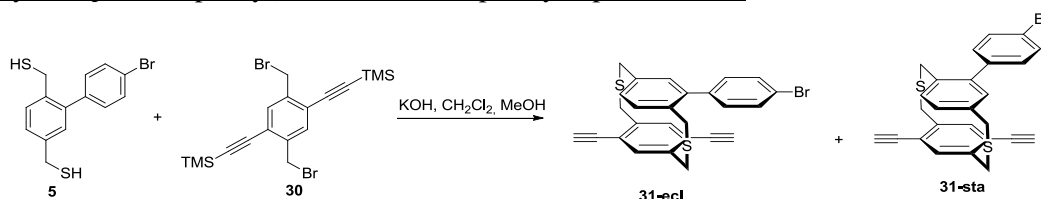


Under Argon.

To a solution of **29** (900 mg, 2.15 mmol) in ethanol (50 mL) was added thiourea (410 mg, 5.35 mmol). The mixture was heated at 80°C in a sealed Schlenk tube for 3h and then cool down to RT. After evaporation *in vacuo*, the residue was dissolved in water (50 mL) and the solution was degassed. Potassium hydroxide was added (1.2 g, 21.5 mmol) and the mixture was heated at 100 °C overnight in a sealed Schlenk tube. The solution was then extracted with diethylether and dried over MgSO₄. The evaporation *in vacuo* gave **30** as colourless crystals in 83% yield.

¹H NMR (300 MHz, CDCl₃) δ 7.55 (d, ³J = 8.5 Hz, 2H), 7.37 (d, ³J = 8.0 Hz, 1H), 7.29 (dd, ³J = 8.0 Hz, ⁴J = 2.0 Hz, 1H), 7.32 (d, ³J = 8.5 Hz, 2H), 7.13 (d, ⁴J = 2.0 Hz, 1H), 3.72 (d, ³J = 7.5 Hz, 2H), 3.62 (d, ³J = 7.5 Hz, 2H), 1.77 (d, ³J = 7.5 Hz, 1H), 1.66 (d, ³J = 7.5 Hz, 1H).

Synthesis of the 5,8-diethynyl-13-(*p*-bromophenyl)-2,11-dithia[3.3]paracyclophane **31-ecl** and the 5,8-diethynyl-14-(*p*-bromophenyl)-2,11-dithia[3.3]paracyclophane **31-sta**



To a solution of KOH (100 mg, 1.8 mmol) in methanol (600 mL) were introduced dropwise (3,5 mL/h) a solution of **5** (420 mg, 0.9 mmol) and **30** (300 mg, 0.9 mmol) in dichloromethane (50 mL) and another solution of KOH (200 mg, 3.7 mmol) in methanol (50 mL). At the end of the addition, the mixture was acidified with dilute H₂SO₄, extracted with Dichloromethane, washed with water, dried over MgSO₄ and evaporated *in vacuo*. The crude was purified by flash chromatography (SiO₂, petroleum ether: dichloromethane 1:0 to 1:1) to afford two structural isomers **31-ecl** and **31-sta** as a white powder in combined yield of 60 %.

¹H NMR (300 MHz, CDCl₃) δ 7.63–7.00 (m, 18H), 4.45–3.46 (m, 16H+ 4H).

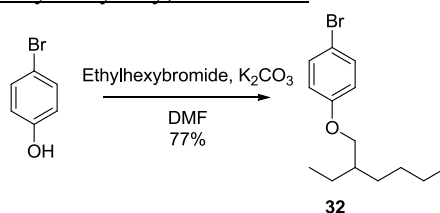
Synthesis of the 5,8-bis[(pyridyl)ethynyl]-13-(*p*-bromophenyl)-2,11-dithia[3.3]paracyclophane **nsNP-sta** and the 5,8-[(pyridyl)ethynyl]-14-(*p*-bromophenyl)-2,11-dithia[3.3]paracyclophane **nsNP-ecl**

Under Argon.

In a Schlenk tube were introduced **31** (170 mg, 0.36 mmol), Iodopyridine (370 mg, 1.8 mmol), Pd(PPh₃)₂Cl₂ (30 mg, 0.04 mmol) and CuI (8 mg, 0.04 mmol). Then, DiPA (1.5 mL, 10.0 mmol) was added and the mixture was stirred for 24 hours. The solution was diluted with dichloromethane, washed with water and dried over MgSO₄. After evaporation *in vacuo*, the residue was purified by flash chromatography (SiO₂, petroleum ether: ethyl acetate 9:1 to 1:1) to afford **nsNP** as two structural isomers (eclipsed **nsNP-ecl** and staggered **nsNP-sta**) as a yellow powder in 84 % yield.

¹H NMR (300 MHz, CDCl₃) δ 8.78–8.65 (m, 8H), 7.61–7.06 (m, 26H), 4.45–3.46 (m, 16H).

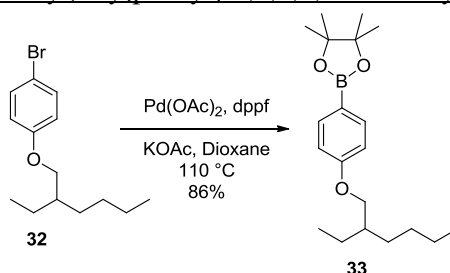
Synthesis of the 1-Bromo-4-(2'-ethylhexyloxy)benzene **32**¹⁶⁴



To a solution of *p*-bromophenol (2 g, 11.5 mmol) and ethylhexylbromide (2.66 g, 13.8 mmol) in dimethylformamide (30 mL) was introduced potassium carbonate (3.2 g, 23 mmol) and the mixture was refluxed overnight. The solution was then poured into water, extracted with petroleum ether and dried over MgSO₄. After evaporation *in vacuo*, the crude was purified by flash chromatography (SiO₂, petroleum ether) to afford **32** in 77 % yield.

¹H NMR (300 MHz, CDCl₃) δ 7.38 (d, ³J = 9.0 Hz, 2H), 6.81 (d, ³J = 9.0 Hz, 2H), 3.81 (d, ³J = 6.0 Hz, 2H), 1.75 (m, 1H), 1.57–1.33 (m, 8H), 0.96 (t, ³J = 7.0 Hz, 6H).

Synthesis of the 2-[4'-[(2''-ethylhexyl)oxy]phenyl]-4,4,5,5-tetramethyl-1,3,2-dioxaborolane **33**¹⁶⁵

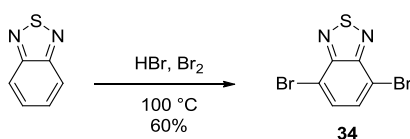


Under Argon.

In a Schlenk tube were introduced **32** (0.5 g, 1.7 mmol), pinacolborane (0.95 g, 3.8 mmol), potassium acetate (1.0 g, 10.1 mmol) and dioxane (10 mL). Pd(OAc)₂ (38 mg, 0.17 mmol) and dppf (390 mg, 0.68 mmol) were then added in THF (5 mL) and the reaction was refluxed 12 hours. The solution was then diluted with dichloromethane, washed with water and dried over MgSO₄. After evaporation *in vacuo*, the residue was purified by flash chromatography (SiO₂, petroleum ether: dichloromethane 1:0 to 1:1) to afford **33** as a light green oil in 62 % yield.

¹H NMR (300 MHz, CDCl₃) δ 7.79 (d, ³J = 9.0 Hz, 2H), 6.93 (d, ³J = 9.0 Hz, 2H), 3.90 (d, ³J = 6.0 Hz, 2H), 1.75 (m, 1H), 1.60–1.33 (m, 20H), 0.96 (t, ³J = 7.0 Hz, 6H).

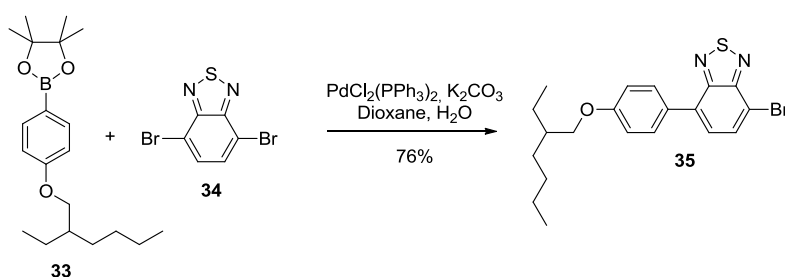
Synthesis of the 4,7-dibromo-2,1,3-benzothiadiazole **34** ¹⁴⁵



A solution of benzothiadiazole (4.0 g, 29.4 mmol) in a mixture of bromine and hydrobromic acid (48 %, 60 mL) was refluxed overnight. The solution was then poured into aqueous sodium thiosulfate and the mixture was filtrated off. The precipitate was recrystallised in ethanol to afford **34** as white needles in 55% yield.

¹H NMR (300 MHz, CDCl₃) δ 7.72 (s, 2H).

Synthesis of the 4-bromo-7-[4'-(2''-ethylhexyloxy)phenyl]-2,1,3-benzothiadiazole **35**

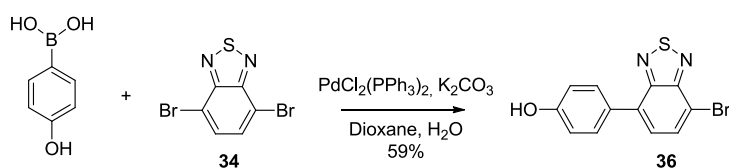


Under Argon.

In a Schlenk tube were introduced **33** (460 mg, 1.4 mmol), **34** (811 mg, 2.8 mmol), Pd(PPh₃)₂Cl₂ (100 mg, 0.15 mmol) and dioxane (20 mL). Then, K₂CO₃ (0.78 g, 5.7 mmol) in water (5 mL) was added, and the mixture was heated at 110°C for 12 hours. The reaction was allowed to cool down to RT and was poured into water. The mixture was then extracted with dichloromethane, dried over MgSO₄ and evaporated *in vacuo*. The crude was purified by flash chromatography (SiO₂, petroleum ether: dichloromethane 1:0 to 1:1) to afford **35** as pale yellow oil in 76% yield.

¹H NMR (300 MHz, CDCl₃) δ 7.88 (d, ³J = 7.0 Hz, 2H), 7.61 (d, ³J = 5.0 Hz, 1H), 7.60 (d, ³J = 5.0 Hz, 1H), 7.07 (d, ³J = 7.0 Hz, 2H), 3.94 (d, ³J = 5.8 Hz, 2H), 1.75 (m, 1H), 1.60-1.33 (m, 8H), 0.96 (t, ³J = 7.0 Hz, 6H).

Synthesis of the 4-(7'-bromo-2',1',3'-benzothiadiazol-4'-yl)-phenol **36**

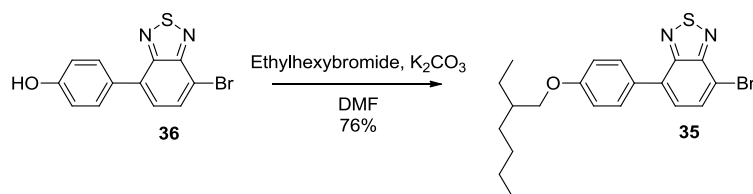


Under Argon.

In a schlenk tube were introduced *p*-hydroxyphenylboronic acid (1 g, 7.25 mmol), **34** (3.2 g, 2.8 mmol), Pd(PPh₃)₂Cl₂ (100 mg, 0.15 mmol) and dioxane (20 mL). Then, K₂CO₃ (0.78 g, 5.7 mmol) in water (5 mL) was added, and the mixture was heated at 110°C for 12 hours. The reaction was allowed to cool down to RT and was poured into water. The mixture was then extracted with dichloromethane, dried over MgSO₄ and evaporated *in vacuo*. The crude was purified by flash chromatography (SiO₂, petroleum ether: dichloromethane 1:0 to 1:1) to afford **36** as pale yellow powder in 76% yield.

¹H NMR (300 MHz, CDCl₃) δ 7.90 (d, ³J = 7.6 Hz, 1H), 7.82 (d, ³J = 8.8 Hz, 2H), 7.52 (d, ³J = 7.6 Hz, 1H), 6.99 (d, ³J = 8.8 Hz, 2H), 4.96 (s, 1H).

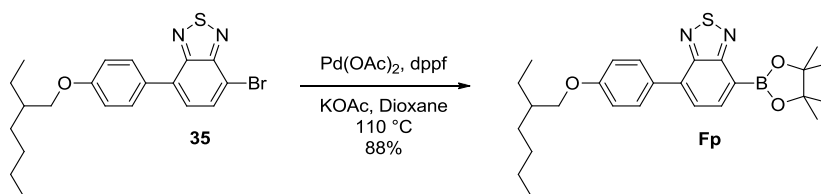
Synthesis of the 4-bromo-7-[4'-(2''-ethylhexyloxy)phenyl]-2,1,3-benzothiadiazole **35**



To a solution of **36** (200 mg, 0.6 mmol) and ethylhexylbromide (0.17 g, 1.0 mmol) in dimethylformamide (40 mL) was introduced potassium carbonate (0.18 g, 1.3 mmol) and the mixture was refluxed overnight. The solution was then poured into water, extracted with petroleum ether and dried over MgSO_4 . After evaporation *in vacuo*, the crude was purified by flash chromatography (SiO_2 , petroleum ether: dichloromethane 1:0 to 1:1) to afford **35** in 76 % yield.

^1H NMR (300 MHz, CDCl_3) δ 7.88 (d, $^3J = 7.0$ Hz, 2H), 7.61 (d, $^3J = 5.0$ Hz, 1H), 7.60 (d, $^3J = 5.0$ Hz, 1H), 7.07 (d, $^3J = 7.0$ Hz, 2H), 3.94 (d, $^3J = 5.8$ Hz, 2H), 1.75 (m, 1H), 1.60-1.33 (m, 8H), 0.96 (t, $^3J = 7.0$ Hz, 6H).

Synthesis of the 2-(7'-[4''-(2'''-ethylhexyloxy)phenyl]-2',1',3'-benzothiadiazole)-4,4,5,5-tetramethyl-1,3,2-dioxaborolane **Fp**



Under Argon.

In a Schlenk tube were introduced **35** (80 mg, 0.2 mmol), pinacolborane (0.15 g, 1.0 mmol), potassium acetate (0.11 g, 1.1 mmol) and dioxane (20 mL). $\text{Pd}(\text{OAc})_2$ (5 mg, 0.02 mmol) and dppf (42 mg, 0.08 mmol) were then added in THF (5 mL) and the reaction was refluxed 12 hours. The solution was then diluted with dichloromethane, washed with water and dried over MgSO_4 . After evaporation *in vacuo*, the residue was purified by flash chromatography (SiO_2 , petroleum ether: dichloromethane 1:0 to 1:1) to afford **Fp** as a light green oil in 88 % yield.

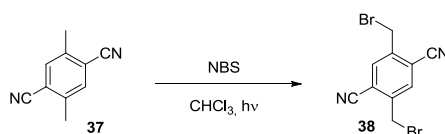
^1H NMR (300 MHz, CDCl_3) δ 7.87 (d, $^3J = 7.8$ Hz, 1H), 7.83 (d, $^3J = 8.8$ Hz, 2H), 7.50 (d, $^3J = 7.8$ Hz, 1H), 7.05 (d, $^3J = 8.8$ Hz, 2H), 3.92 (d, $^3J = 5.6$ Hz, 2H), 1.77 (m, 1H), 1.59-1.26 (m, 20H), 0.92 (t, $^3J = 7.0$ Hz, 6H).

Synthesis of the 2,5-dimethylterephthalonitrile **37** ¹⁶⁶

To a solution of 2,5-dibromo-*p*-xylene (20 g, 76 mmol) in DMF (400 mL) was added CuCN (27.2 g, 304 mmol) and the solution was stirred under reflux overnight. The reaction mixture was poured into water and filtrated. The crude was then solubilised by dichloromethane, washed with water and dried over MgSO_4 to afford **37** as a cotton-light white compound in 91 % yield.

^1H NMR (300 MHz, CDCl_3) δ 7.56 (s, 2H), 2.55 (s, 6H).

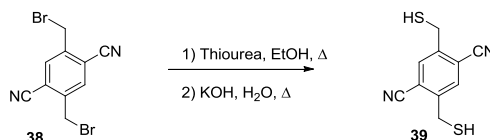
Synthesis of the 2,5-bis(bromomethyl)-terephthalonitrile **38**¹⁴⁹



In a Schlenk tube were introduced **37** (1.0 g, 6,7 mmol), NBS (2.4 g, 13,2 mmol) and CHCl_3 (10 mL). The Schlenk was then sealed with a screwed cap. After 30 minutes under UV, the solution was washed by water and evaporated *in vacuo*. The crude was re-introduced in the schlenk tube with NBS (2.4 g, 13,2 mmol) and CHCl_3 (10 mL), and the tube was sealed once again. After an additional 30 minutes under UV, the reaction mixture was washed by water, evaporated *in vacuo*. The crude was finally purified by flash chromatography (SiO_2 , petroleum ether : dichloromethane 1:0 to 1:1) to afford **38** as white crystals in 52%.

^1H NMR (300 MHz, CDCl_3) δ 7.86 (s, 2H), 4.61 (s, 4H).

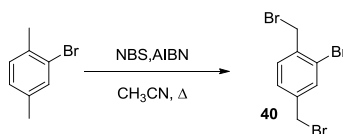
Synthesis of the 2,5-bis(mercaptomethyl)-terephthalonitrile **39**



To a solution of **38** (730 mg, 2.3 mmol) in degassed ethanol (20mL) was added thiourea (390 mg, 5.1 mmol). The mixture was heated at 80°C for 3h and then cool down to RT. The solution was poured into diethylether and the white precipitate was filtered off. The so-obtained powder was dissolved in degassed water (40 mL) and potassium hydroxide (1.3 g, 23 mmol) was added. After stirring at 100°C overnight, the solution was acidified with diluted sulfuric acid, extracted with diethylether and dried over MgSO_4 . Evaporation *in vacuo* afforded **39** as colorless crystals in 90% yield.

^1H NMR (300 MHz, THF) δ 7.97 (s, $^3J = 8.5$ Hz, 2H), 4.06 (d, 4H), 2.35 (t, $^3J = 8.5$ Hz, 2H).

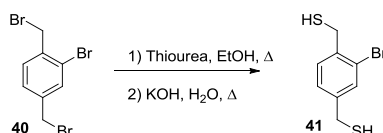
Synthesis of the 2-bromo-1,4-bis(bromomethyl)-benzene **40**¹⁶⁷



To a solution of 2-bromo-*p*-xylene (10 g, 54 mmol) in acetonitrile (300 mL) was added NBS (24 g, 135 mmol) and AIBN (440 mg, 2,7 mmol). After stirring for 20 hours under reflux, the mixture was evaporated *in vacuo* and washed by hot methanol to afford **40** as a white powder in 72% yield.

^1H NMR (300 MHz, CDCl_3) δ 7.60 (d, $^4J = 1.7$ Hz, 1H), 7.42 (d, $^3J = 7.9$ Hz, 1H), 7.31 (dd, $^3J = 7.9$ Hz, $^4J = 1.7$ Hz, 1H), 4.57 (s, 2H), 4.40 (s, 2H).

Synthesis of the 2-bromo-1,4-bis(mercaptomethyl)-benzene **41**



To a solution of **40** (3 g, 8,75 mmol) in ethanol (75mL) was added thiourea (2,7 g, 35 mmol). The mixture was heated at 80°C for 3h and then cool down to RT. After evaporation *in vacuo*, the residue was dissolved in water (15 mL). Sodium hydroxide was added (1,4 g, 35 mmol) and the mixture was heated to 100 °C overnight. The solution was then extracted with diethylether and dried over MgSO₄. Evaporation *in vacuo* afforded **41** as colorless crystals in 50% yield.

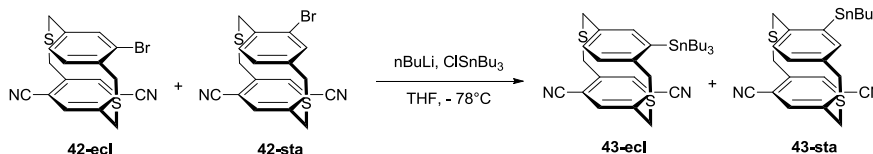
¹H NMR (300 MHz, CDCl₃) δ 7.52 (d, ⁴J = 1.4 Hz, 1H), 7.32 (d, ³J = 7.8 Hz, 1H), 7.23 (dd, ³J = 7.8 Hz, ⁴J = 1.4 Hz, 1H), 3.81 (d, ³J = 8.1 Hz, 2H), 3.68 (d, ³J = 7.7 Hz, 2H), 1.98 (t, ³J = 8.1 Hz, 1H), 1.77 (t, ³J = 7.7 Hz, 1H).

Synthesis of the 5,8-dicyano-13-bromo-2,11-dithia[3.3]paracyclophane **42-ecl** and ,8-dicyano-14-bromo-2,11-dithia[3.3]paracyclophane **42-sta**

To a solution of KOH (110 mg, 2.0 mmol) in methanol (400 mL) were introduced dropwise (1.5 mL/h) a solution of **41** (400 mg, 1,6 mmol) and **38** (500 mg, 1,6 mmol) in dichloromethane (50 mL) and another solution of KOH (110 mg, 2.0 mmol) in methanol (50 mL). At the end of the addition, the mixture was acidified with dilute H₂SO₄, extracted with Dichloromethane, washed with water, dried over MgSO₄ and evaporated *in vacuo*. The crude was washed by hot ethanol to afford a mixture of two structure isomers **42-sta** and **42-ecl** as a white powder in 82 % yield.

¹H NMR (300 MHz, CDCl₃) δ 7.60–7.00 (m, 10H), 4.56–3.61 (m, 16H).

Synthesis of the 5,8-dicyano-13-(tributylstannyl)-2,11-dithia[3.3]paracyclophane **43-ecl** and ,8-dicyano-14-(tributylstannyl)-2,11-dithia[3.3]paracyclophane **43-sta**

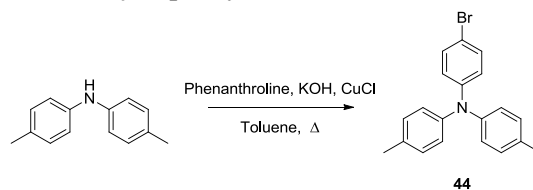


Under argon.

To a -78°C cooled solution of **42** (100mg, 0.26 mmol) in dry THF (5 mL) was added dropwise n-Buli (2.5 M in hexane, 0.11 mL, 0.27 mmol). After stirring for 30 min at -78°C, ClSnBu₃ (0.08mL, 0.3 mmol) was added. The mixture was stirred for an additional 30 min, and the reaction was allowed to reach room temperature. After stirring overnight, the solution was hydrolysed, extracted with dichloromethane, dried over magnesium sulphate and evaporated *in vacuo*. The crude **43** was used for the next reaction without further purification.

¹H NMR (300 MHz, CDCl₃) δ 7.61–7.00 (m, 10H), 4.18–3.76 (m, 16H), 1.62 (m, 6H), 1.28 (m, 12H), 0.92 (t, ³J = 8.2 Hz, 9H).

Synthesis of the 4-bromo-4',4''-dimethyltriphenylamine **44**¹⁶⁸

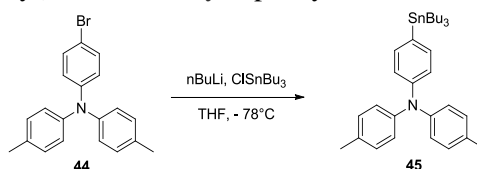


Under argon.

In a schlenk tube were introduced ditolylamine (1 g, 5.05 mmol), 1-iodo-4-bromobenzene (1.56 g, 5.5 mmol) phenanthroline (180 mg, 1 mmol), copper chloride (100 mg, 1 mmol), potassium hydroxide (3.0 g, 4.5 mmol) and degassed toluene (12 mL). The tube was sealed with a screwed cap and the reaction was stirred for 20 hours at 125°C. The mixture was then poured into water, extracted with toluene, dried over magnesium sulphate and evaporated *in vacuo*. The crude was purified by chromatography (SiO₂, petroleum ether) to afford **44** as a white powder in 67% yield.

¹H NMR (300 MHz, CDCl₃) δ 7.26 (d, ³J = 8.7 Hz, 2H), 7.06 (d, ³J = 8.3 Hz, 4H), 6.97 (d, ³J = 8.3 Hz, 4H), 6.88 (d, ³J = 8.7 Hz, 2H), 2.31 (s, 6H).

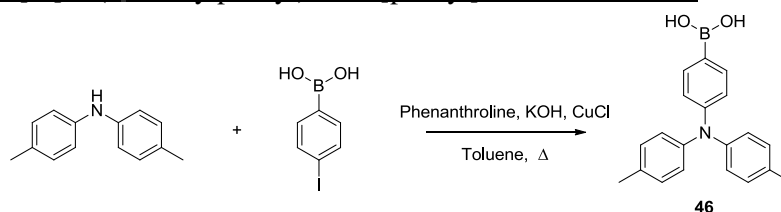
Synthesis of the 4-(tributylstannyl)-4',4''-dimethyltriphenylamine **45**



To a -78°C cooled solution of **44** (980 mg, 2.78 mmol) in dry THF (8 mL) were added dropwise n-BuLi (1.6 M in hexane, 1.91 mL, 3.06 mmol). After stirring for 30 min at -78°C, ClSnBu₃ (0.91 mL, 3.34 mmol) was added. The mixture was stirred for an additional 30 min, and the reaction was allowed to reach room temperature. After stirring overnight, the solution was hydrolysed, extracted with dichloromethane, dried over magnesium sulphate and evaporated *in vacuo*. The crude **45** was used for the next reaction without further purification.

¹H NMR (300 MHz, CDCl₃) δ 7.28 (d, ³J = 8.3 Hz, 2H), 7.03 (d, ³J = 8.4 Hz, 4H), 7.01 (d, ³J = 8.4 Hz, 4H), 6.99 (d, ³J = 8.3 Hz, 2H), 2.33 (s, 6H), 1.55 (m, 6H), 1.34 (m, 12H), 1.05 (t, ³J = 8.2 Hz, 9H).

Synthesis of the *B*-[4-[bis(4'-methylphenyl)amino]phenyl]boronic acid **46**¹⁶⁹



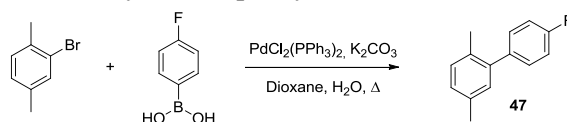
Under argon.

In a schlenk tube were introduced ditolylamine (1 g, 5.05 mmol), *p*-iodophenylboronic acid (1.5 g, 5.5 mmol) phenanthroline (180 mg, 1 mmol), copper iodide (190 mg, 1 mmol), potassium hydroxide (3.0 g, 4.5 mmol) and degassed toluene (12 mL). The tube was sealed with a screwed cap and the reaction was stirred for 18 hours at 125°C. The mixture was then poured into water, extracted with toluene, dried over magnesium sulphate and evaporated *in vacuo*. The crude was purified by chromatography (SiO₂, petroleum ether) to afford **46** as a white powder in 25% yield.

¹H NMR (300 MHz, CDCl₃) δ 7.22 (d, ³J = 7.3 Hz, 2H), 7.19 (d, ³J = 7.4 Hz, 4H), 7.08-6.94 (m, 10H), 2.32 (s, 6H).

¹³C NMR (300 MHz, CDCl₃) δ 148.47, 145.66, 132.44, 129.98, 129.16, 124.63, 123.14, 121.87, 20.92.

Synthesis of the 4'-fluoro-2,5-dimethyl-1,1'-biphenyl **47**¹⁷⁰

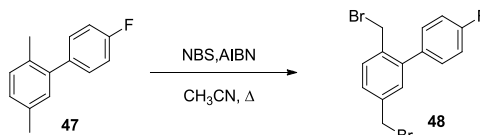


Under Argon.

To *p*-fluorophenylboronic acid (2 g, 14.3 mmol) and $\text{Pd}(\text{PPh}_3)_2\text{Cl}_2$ (230 mg, 0.33 mmol) was added a solution of 2-iodobromo-*p*-xylene (1.8 mL, 13.0 mmol) in dioxane (50 mL). Then, K_2CO_3 (9 g, 65 mmol) in water (20 mL) was added, and the mixture was heated at 110°C for 12 hours. The reaction was then allowed to cool down to RT and was poured into water. The mixture was extracted with dichloromethane, dried over MgSO_4 and evaporated *in vacuo*. The crude was purified by chromatography (SiO_2 , petroleum ether) to afford **47** as a colourless oil in quantitative yield.

^1H NMR (300 MHz, CDCl_3) δ 7.29 (m, 2H), 7.10 (m, 5H), 2.36 (s, 3H), 2.22 (s, 3H).

Synthesis of the 4'-fluoro-2,5-bis(bromomethyl)-1,1'-biphenyl **48**

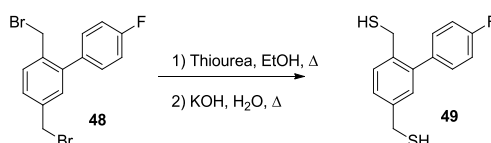


Under Argon.

To a solution of **47** (2 g, 10 mmol) in acetonitrile (80 mL) was added NBS (3.74 g, 21 mmol) and AIBN (160 mg, 1 mmol). After stirring for 13 hours at 90 °C, the mixture was evaporated *in vacuo* and purified by flash chromatography (SiO_2 , Petroleum ether) to afford **48** as a white powder in 66% yield.

^1H NMR (300 MHz, CDCl_3) δ 7.51 (d, $^3J = 8.0$ Hz, 1H), 7.42 (m, 3H), 7.26 (s, 1H), 7.15 (m, 2H), 4.49 (s, 2H), 4.40 (s, 2H).

Synthesis of the 4'-fluoro-2,5-bis(mercaptomethyl)-1,1'-biphenyl **49**

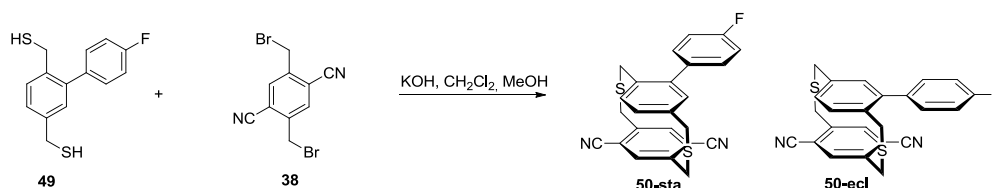


Under Argon.

To a solution of **48** (2.38 g, 6.7 mmol) in ethanol (625 mL) was added thiourea (1.26 g, 16.6 mmol). The mixture was heated at 80°C in a sealed Schlenk tube for 3h and then cool down to RT. After evaporation *in vacuo*, the residue was dissolved in water (60 mL) and the solution was degassed. Potassium hydroxide was added (3.9 g, 70.0 mmol) and the mixture was heated at 100 °C overnight in a sealed Schlenk tube. The solution was then extracted with diethylether and dried over MgSO_4 . Evaporation *in vacuo* gave **49** as colourless crystals in 73% yield.

^1H NMR (300 MHz, CDCl_3) δ 7.42-7.28 (m, 4H), 7.19 – 7.08 (m, 3H), 3.74 (t, $^3J = 6.6$ Hz, 2H), 3.65 (d, $^3J = 7.3$ Hz, 2H), 1.79 (t, $^3J = 7.6$ Hz, H), 1.68 (t, $^3J = 7.3$ Hz, 1H).

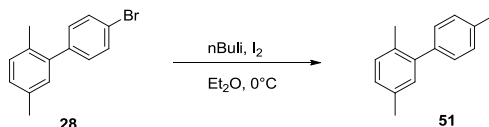
Synthesis of the 5,8-dicyano-13-(4'-fluorophenyl)-2,11-dithia[3.3]paracyclophane **50-ecl** and ,8-dicyano-14-(4'-fluorophenyl)-2,11-dithia[3.3]paracyclophane **50-sta**



To a solution of KOH (100 mg, 1,8 mmol) in methanol (350 mL) were introduced dropwise (4 mL/h) a solution of **49** (168 mg, 0.64 mmol) and **38** (200 mg, 0.64 mmol) in dichloromethane (50 mL) and another solution of KOH (100 mg, 1.8 mmol) in methanol (50 mL). At the end of the addition, the mixture evaporated *in vacuo* and the crude was purified by flash chromatography (SiO₂, dichloromethane) to afford **50** as a white powder in 52 % yield.

¹H NMR (300 MHz, CDCl₃) δ 7.68 – 6.86 (m, 18H), 4.35 – 3.42 (m, 8H).

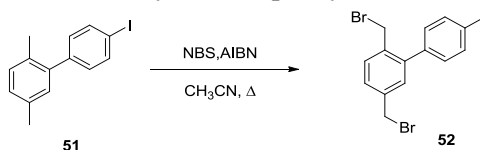
Synthesis of the 4'-iodo-2,5-dimethyl-1,1'-biphenyl **51**



To a 0°C cooled solution of **28** (1.9 g, 7.1 mmol) in dry diethylether (40 mL) was added dropwise n-Buli (1.6 M in hexane, 5.3 mL, 8.5 mmol). After stirring for 30 min at 0°C, iodine (2.7 g, 10.6 mmol) was added. The mixture was stirred for an additional 30 min, and the reaction was allowed to reach room temperature. After stirring overnight, the solution was hydrolysed, extracted with dichloromethane, dried over magnesium sulphate and evaporated *in vacuo*. The crude was purified by chromatography (SiO₂, petroleum ether) to afford **51** as a colorless oil in quantitative yield.

¹H NMR (300 MHz, CDCl₃) δ 7.69 (d, ³J = 8.2 Hz, 2H), 7.11 (d, ³J = 7.7 Hz, 1H), 7.01 (m, 3H), 2.30 (s, 3H), 2.17 (s, 3H).

Synthesis of the 4'-iodo-2,5-bis(bromomethyl)-1,1'-biphenyl **52**

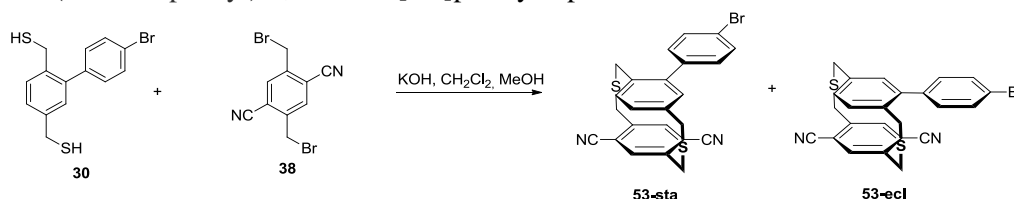


Under Argon.

To a solution of **51** (1 g, 3.25 mmol) in acetonitrile (80 mL) was added NBS (1.5 g, 8.1 mmol) and AIBN (50 mg, 0.32 mmol). After stirring for 24 hours at 90 °C, the mixture was evaporated *in vacuo* and purified by flash chromatography (SiO₂, pPetroleum ether) to afford **52** as a white powder in 74% yield.

¹H NMR (300 MHz, CDCl₃) δ 7.82 (d, ³J = 8.1 Hz, 2H), 7.53 (d, ³J = 8.0 Hz, 1H), 7.40 (dd, ³J = 8.0 Hz, ⁴J = 1.7 Hz, 1H), 7.26 (d, ⁴J = 1.7 Hz, 1H), 7.21 (d, ³J = 8.1 Hz, 2H), 4.51 (s, 2H), 4.41 (s, 2H).

Synthesis of the 5,8-dicyano-13-(4'-bromophenyl)-2,11-dithia[3.3]paracyclophane **53-ecl** and ,8-dicyano-14-(4'-bromophenyl)-2,11-dithia[3.3]paracyclophane **53-sta**



To a solution of KOH (100 mg, 1,8 mmol) in methanol (600 mL) were introduced dropwise (3 mL/h) a solution of **30** (620 mg, 1,9 mmol) and **38** (600 mg, 1,9 mmol) in dichloromethane (60 mL) and another solution of KOH (200 mg, 3,6 mmol) in methanol (60 mL). At the end of the addition, the mixture was acidified with dilute H₂SO₄, extracted with Dichloromethane, washed with water, dried over MgSO₄ and evaporated *in vacuo*. The crude was purified by flash chromatography (SiO₂, petroleum ether:dichloromethane 1:0 to 1:1) to afford **53** as a mixture of two isomers staggered (**53-sta**) and eclipsed (**53-ecl**), with respectively 30% in 12 % yield.

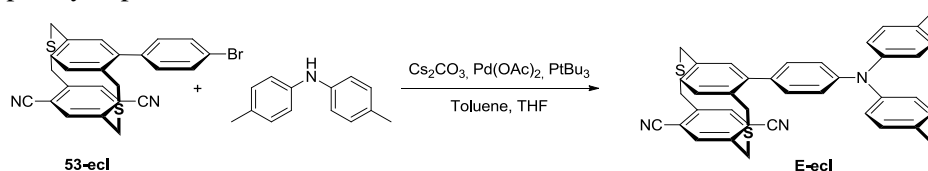
53-sta:

¹H NMR (300 MHz, CDCl₃) δ 7.57 (d, ³J = 8.5 Hz, 2H), 7.54 (s, 1H), 7.29 (d, ³J = 8.5 Hz, 2H), 7.14 (m, 2H), 7.04 (d, ⁴J = 1.5 Hz, 1H), 6.97 (d, ³J = 8.0 Hz, 1H), 4.21 (d, ³J = 14.8 Hz, 1H), 4.01-3.65 (m, 6H), 3.59 (d, ³J = 15.8 Hz, 1H).

53-ecl:

¹H NMR (300 MHz, CDCl₃) δ 7.60 (d, ³J = 8.6 Hz, 1H), 7.56 (s, 1H), 7.52 (s, 1H), 7.26 (m, 2H), 7.12 (d, ⁴J = 1.8 Hz, 1H), 7.01 (dd, ³J = 7.8 Hz, ⁴J = 1.8 Hz, 1H), 4.29 (d, ²J = 15.6 Hz, 1H), 4.13 (d, ²J = 15.8 Hz, 1H), 3.99 (d, ²J = 15.2 Hz, 1H), 3.92-3.82 (m, 4H), 3.68 (d, ²J = 15.2 Hz, 1H).

Synthesis of the 5,8-dicyano-13-(4'-[bis(4''-methylphenyl)amino]phenyl)-2,11-dithia[3.3]paracyclophane **E-ecl**



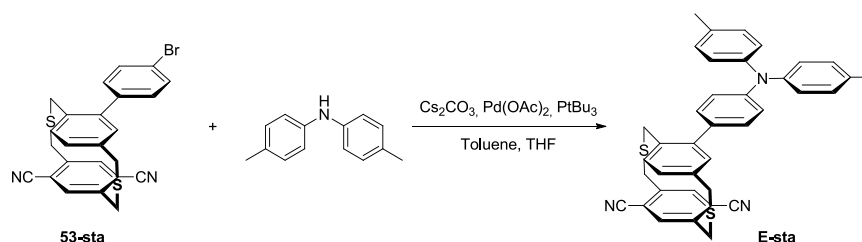
Under argon.

In a schlenk tube were introduced **53-ecl** (270 mg, 0.52 mmol), ditolylamine (120 mg, 0.60 mmol), cesium carbonate (235 mg, 0.73 mmol) and degassed toluene (40 mL). A solution of palladium acetate (16 mg, 0.03 mmol) and tri-tert-butylphosphine (24 μL, 0.12 mmol) in THF (5 mL) was then added and the tube was sealed with a screwed cap. After stirring for 18 hours at 120°C, the mixture was evaporated *in vacuo* and the crude was purified by chromatography (SiO₂, petroleum ether:dichloromethane 1:1) to afford **E-ecl** as a yellow powder in 97% yield.

¹H NMR (600 MHz, DMSO) δ 7.73 (s, 1H), 7.63 (s, 1H), 7.30 (d, ³J = 8.5 Hz, 2H), 7.16 (d, ³J = 8.0 Hz, 1H), 7.13 (d, ³J = 8.2 Hz, 4H), 7.07 (d, ⁴J = 1.3 Hz, 1H), 6.98 (d, ³J = 8.3 Hz, 4H), 6.95 (dd, ³J = 8.0 Hz, ⁴J = 1.3 Hz, 1H), 6.93 (d, ³J = 8.6 Hz, 2H), 4.09 (d, ²J = 15.4 Hz, 2H), 4.05 (d, ²J = 15.2 Hz, 2H), 3.99 (d, ²J = 15.0 Hz, 1H), 3.98 (d, ²J = 14.7 Hz, 1H), 3.91 (d, ²J = 14.9 Hz, 1H), 3.85 (d, ²J = 14.6 Hz, 1H), 2.28 (s, 6H).

¹³C NMR (600 MHz, DMSO) δ 146.6, 144.6, 141.2, 140.6, 135.5, 134.8, 134.2, 132.7, 137.3, 131.6, 131.4, 130.2, 130.0, 129.9, 127.0, 124.4, 121.0, 116.7, 116.2, 115.5, 114.6, 36.5, 35.4, 34.5, 34.2, 20.3.

Synthesis of the 5,8-dicyano-14-(4'-[bis(4''-methylphenyl)amino]phenyl)-2,11-dithia[3.3]paracyclophane **E-sta**



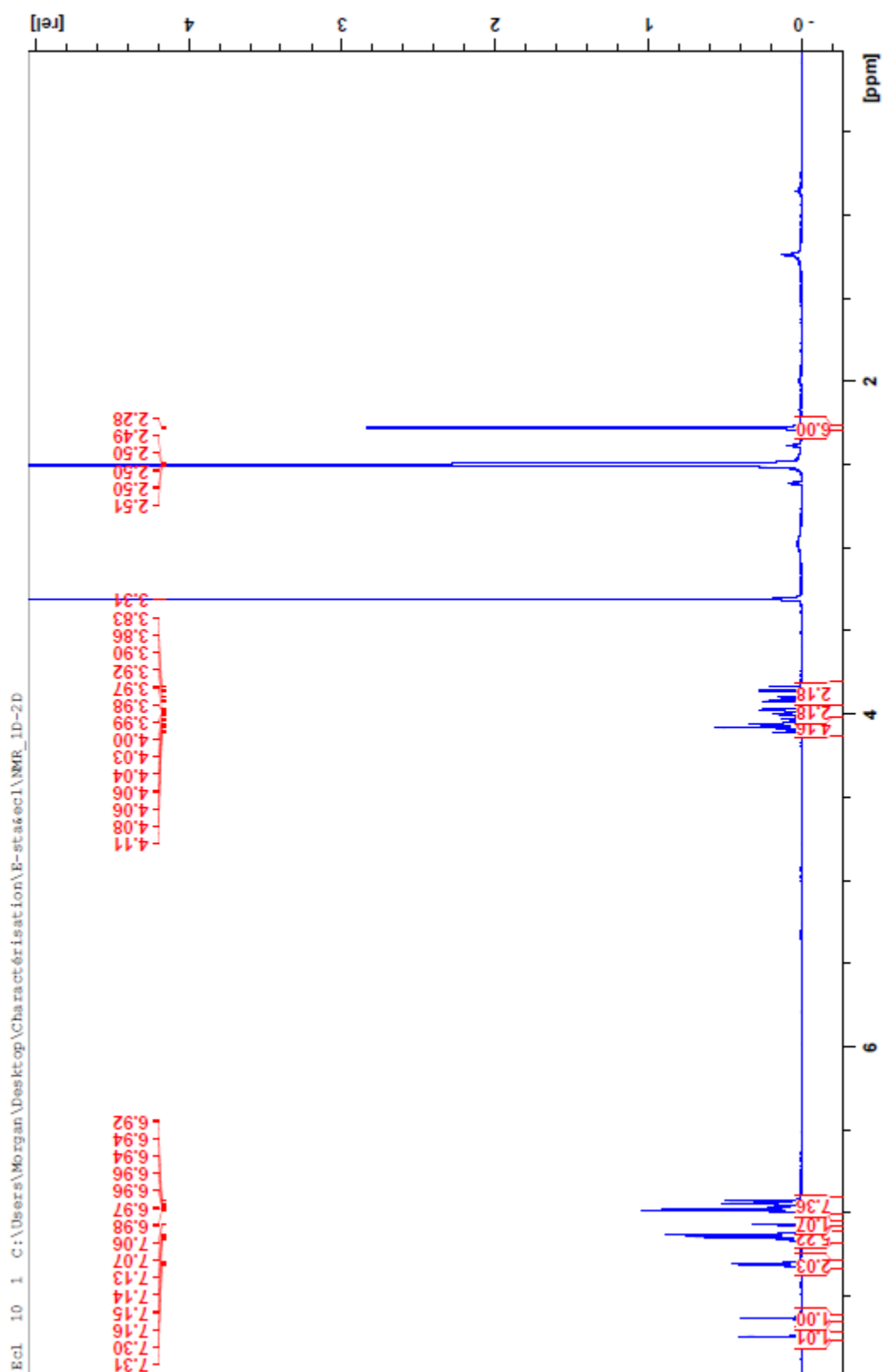
Under argon.

In a schlenk tube were introduced **53-sta** (300 mg, 0.63 mmol), ditolylamine (150 mg, 0.76 mmol), cesium carbonate (290 mg, 0.88 mmol) and degassed toluene (40 mL). A solution of palladium (tri-tert-butylphosphine)₂ (16 mg, 0.03 mmol) in THF (5 mL) was then added and the tube was sealed with a screwed cap. After stirring for 24 hours at 120°C, the mixture was evaporated *in vacuo* and the crude was purified by chromatography (SiO₂, petroleum ether:dichloromethane 1:1) to afford **E-sta** as a yellow powder in 35% yield.

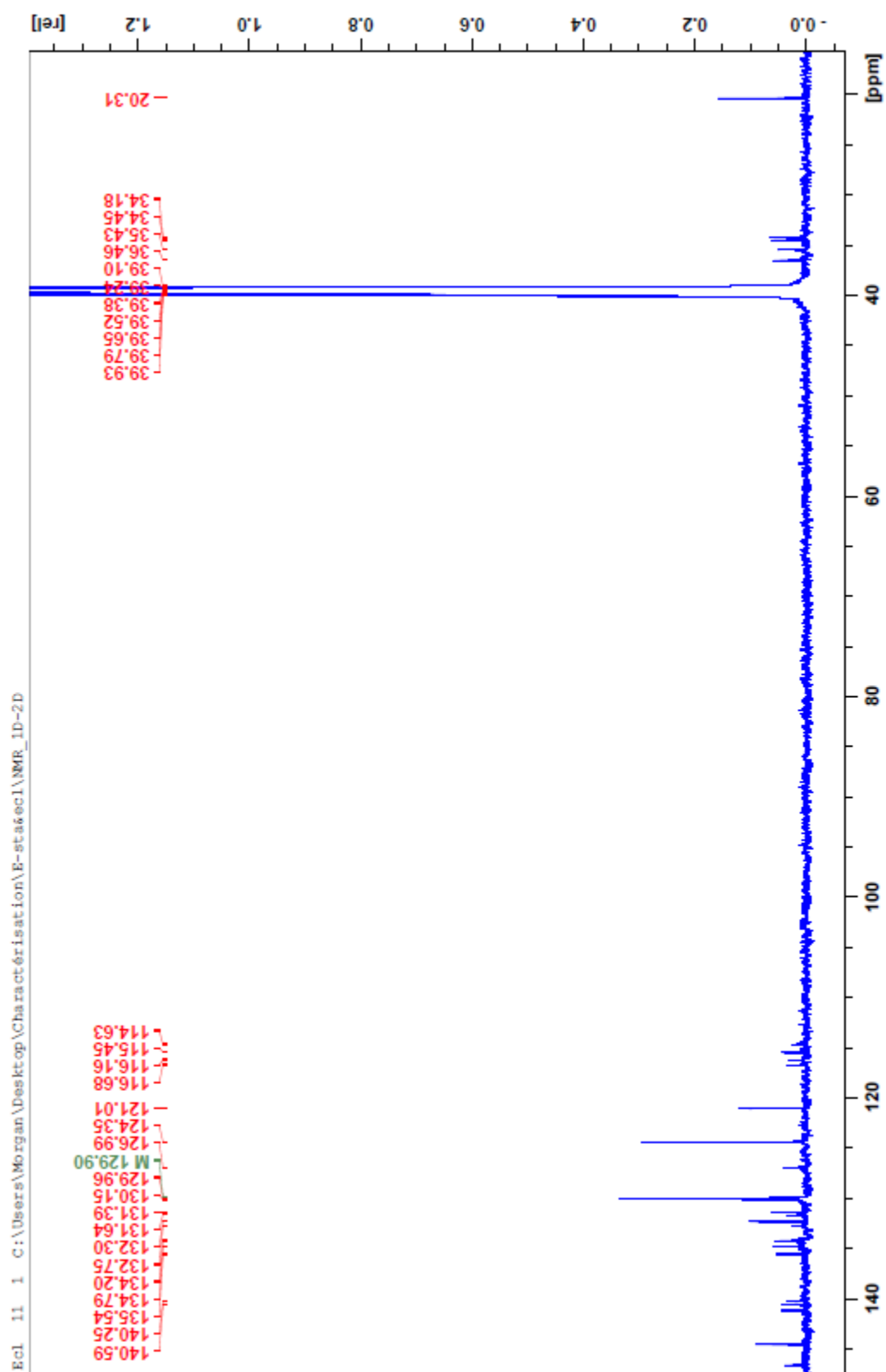
¹H NMR (600 MHz, DMSO) δ 7.82 (s, 1H), 7.35 (s, 1H), 7.32 (d, ³J = 8.5 Hz, 2H), 7.20 (d, ³J = 7.8 Hz, 1H), 7.17 (d, ³J = 8.2 Hz, 4H), 7.05 (d, ⁴J = 1.2 Hz, 1H), 7.01 (d, ³J = 8.3 Hz, 4H), 6.95 (d, ³J = 8.6 Hz, 2H), 6.87 (d, ³J = 7.6 Hz, 1H), 4.10 (d, ²J = 14.7 Hz, 1H), 4.01 (d, ²J = 14.7 Hz, 1H), 4.00-3.90 (m, 5H), 3.88 (d, ²J = 15.2 Hz, 1H), 2.29 (s, 6H).

¹³C NMR (600 MHz, DMSO) δ 146.8, 144.5, 141.0, 140.8, 140.2, 135.5, 135.2, 133.7, 132.8, 132.7, 132.1, 130.3, 130.1, 129.5, 129.4, 128.4, 124.8, 120.7, 116.9, 116.4, 115.6, 115.4, 79.2, 78.9, 78.7, 36.1, 35.5, 34.3, 34.2, 20.4.

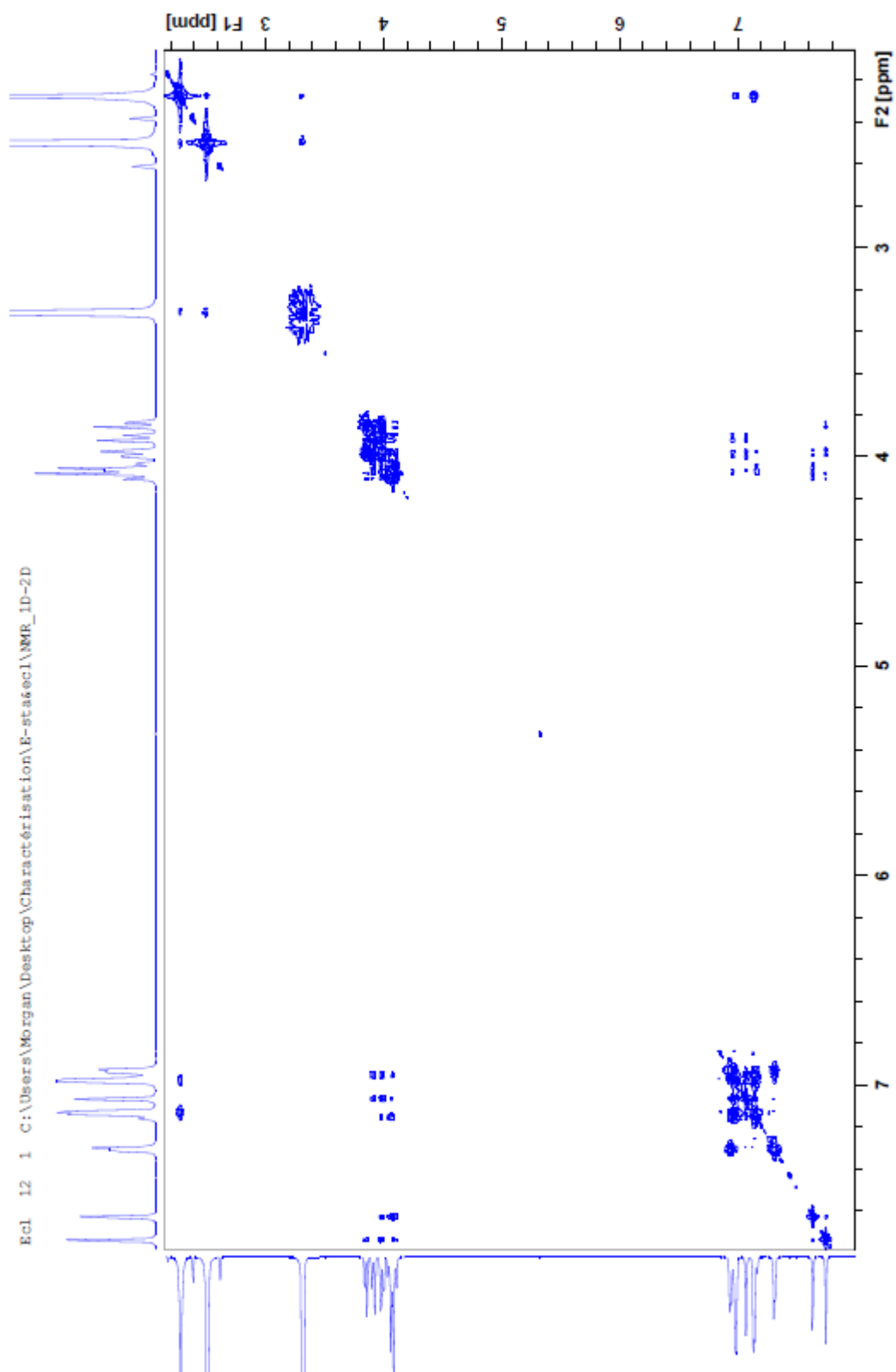
APPENDIX 3: E-ecl, NMR experiments (600 MHz, DMSO-*d*₆) **¹H NMR (E-ecl)**



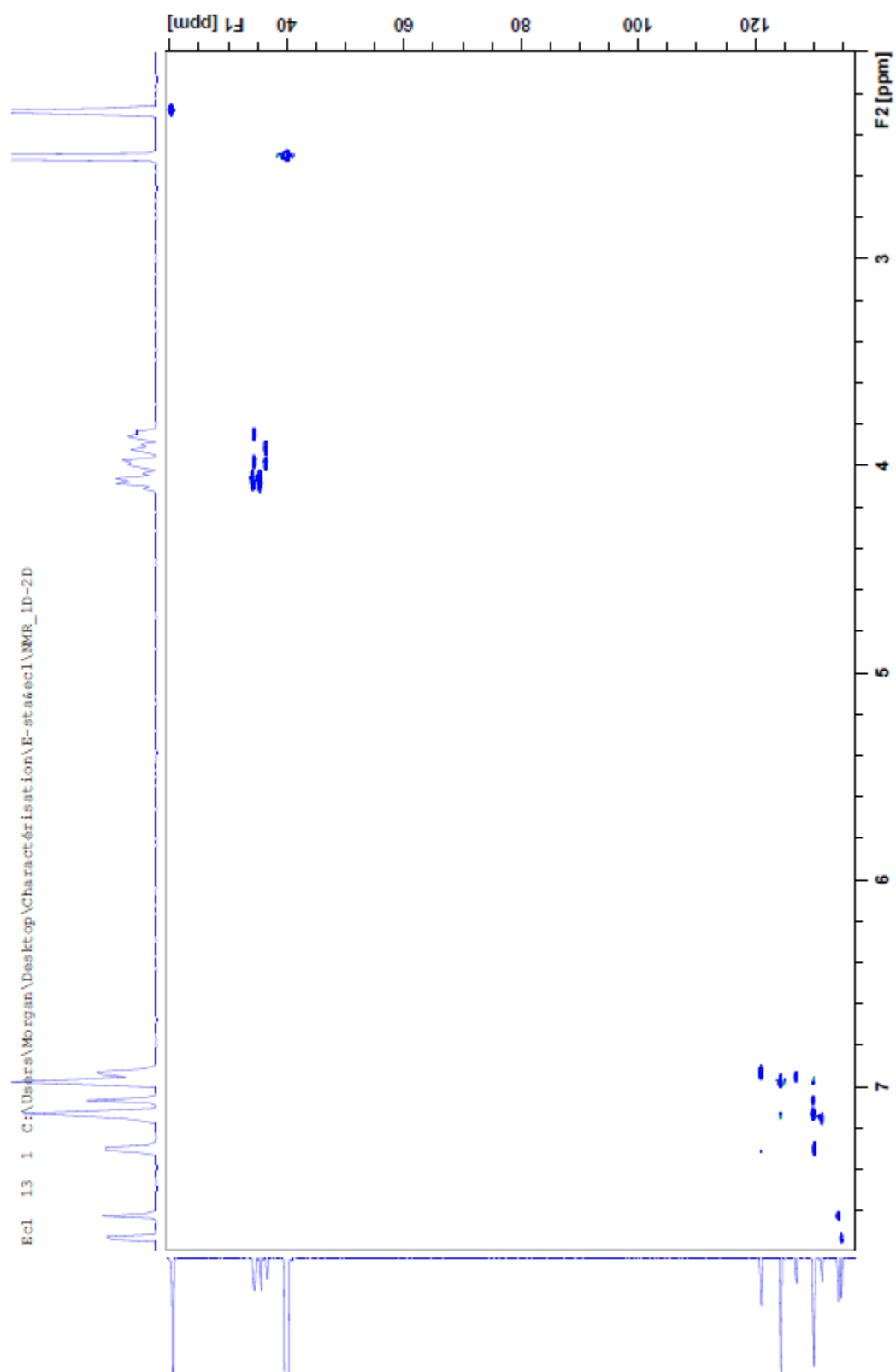
^{13}C NMR (E-ecl)



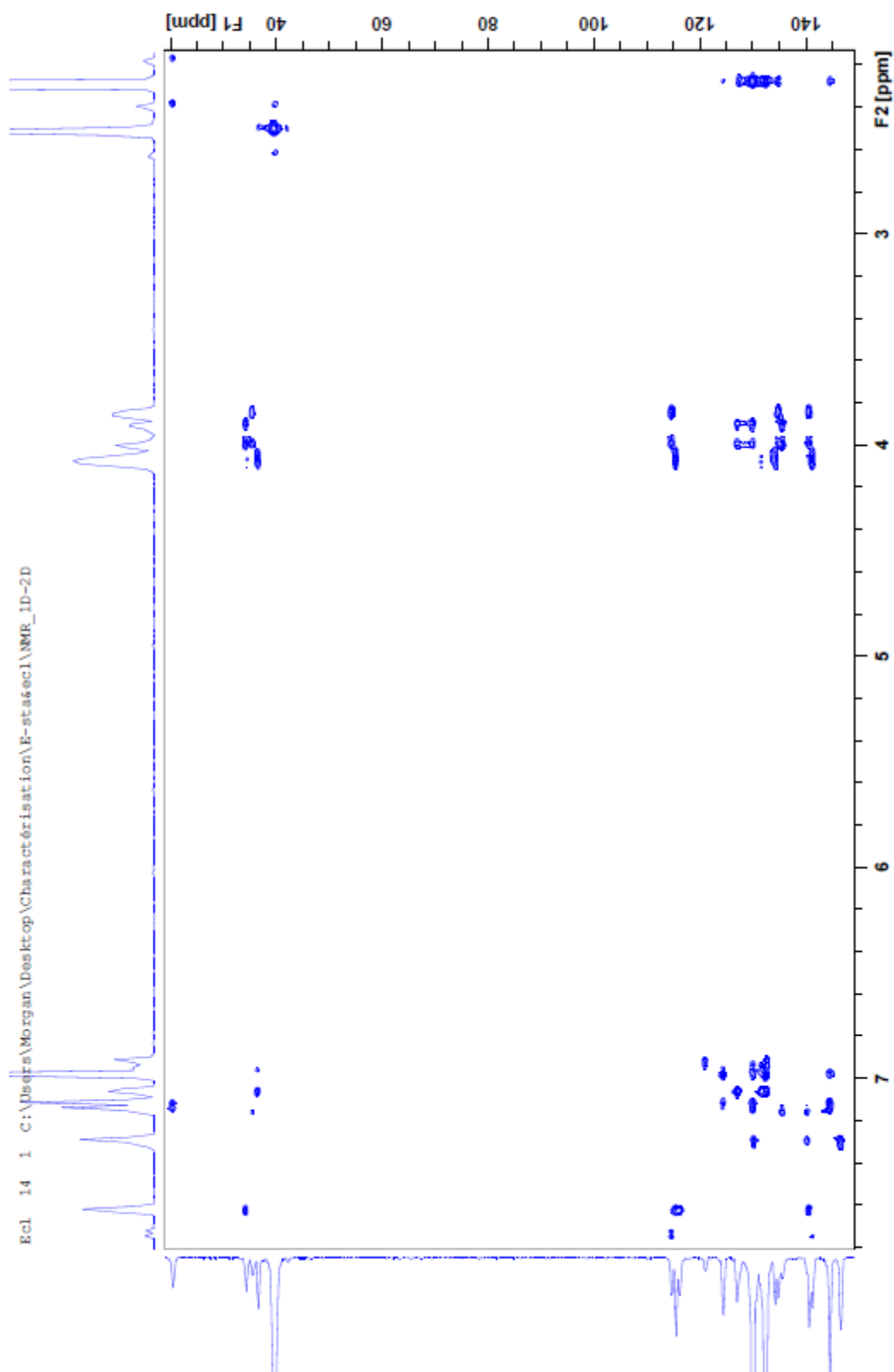
COSY NMR (E-ecl)



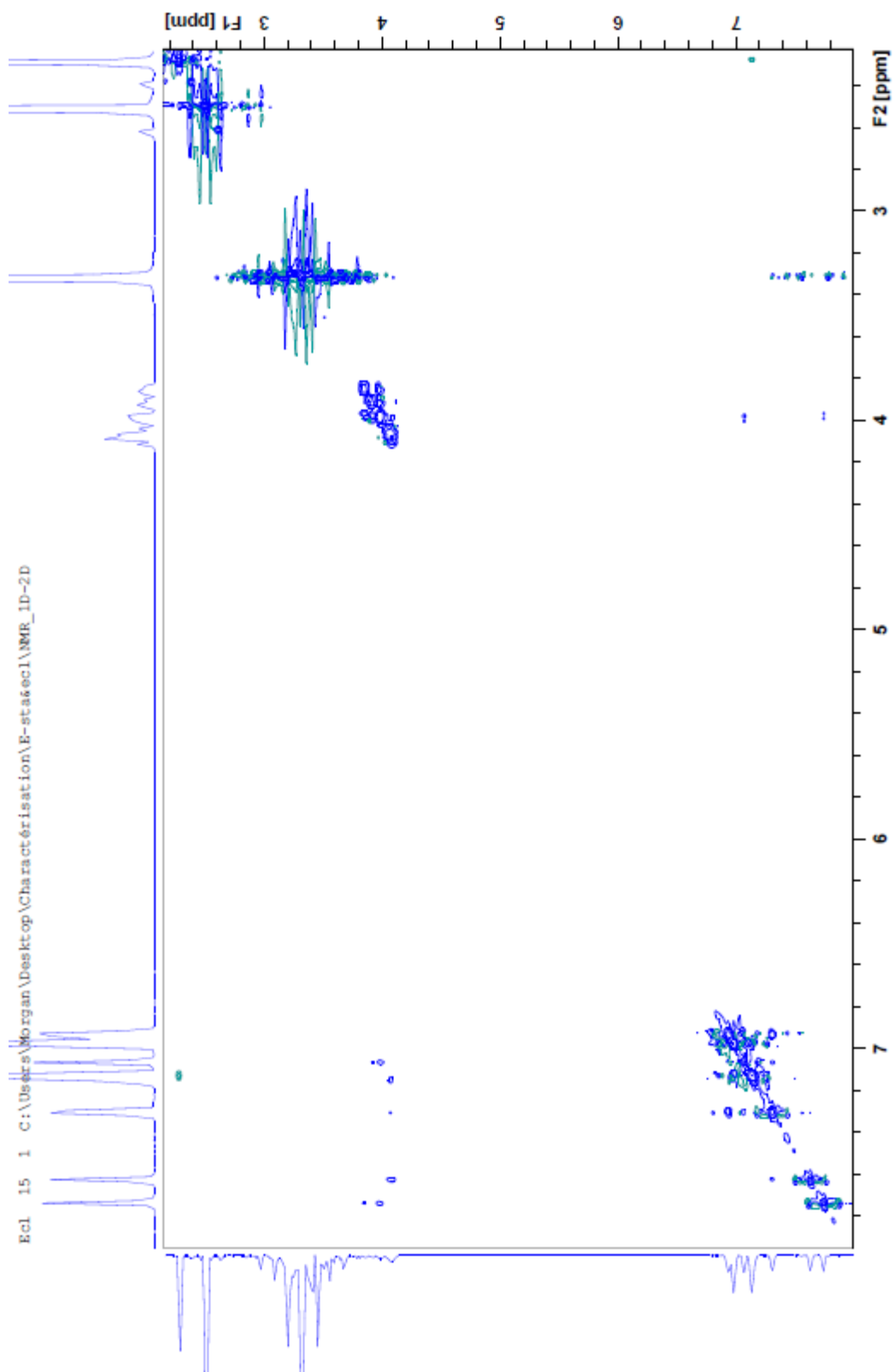
HSQC NMR (E-ecl)



HMBC NMR (E-ecl)

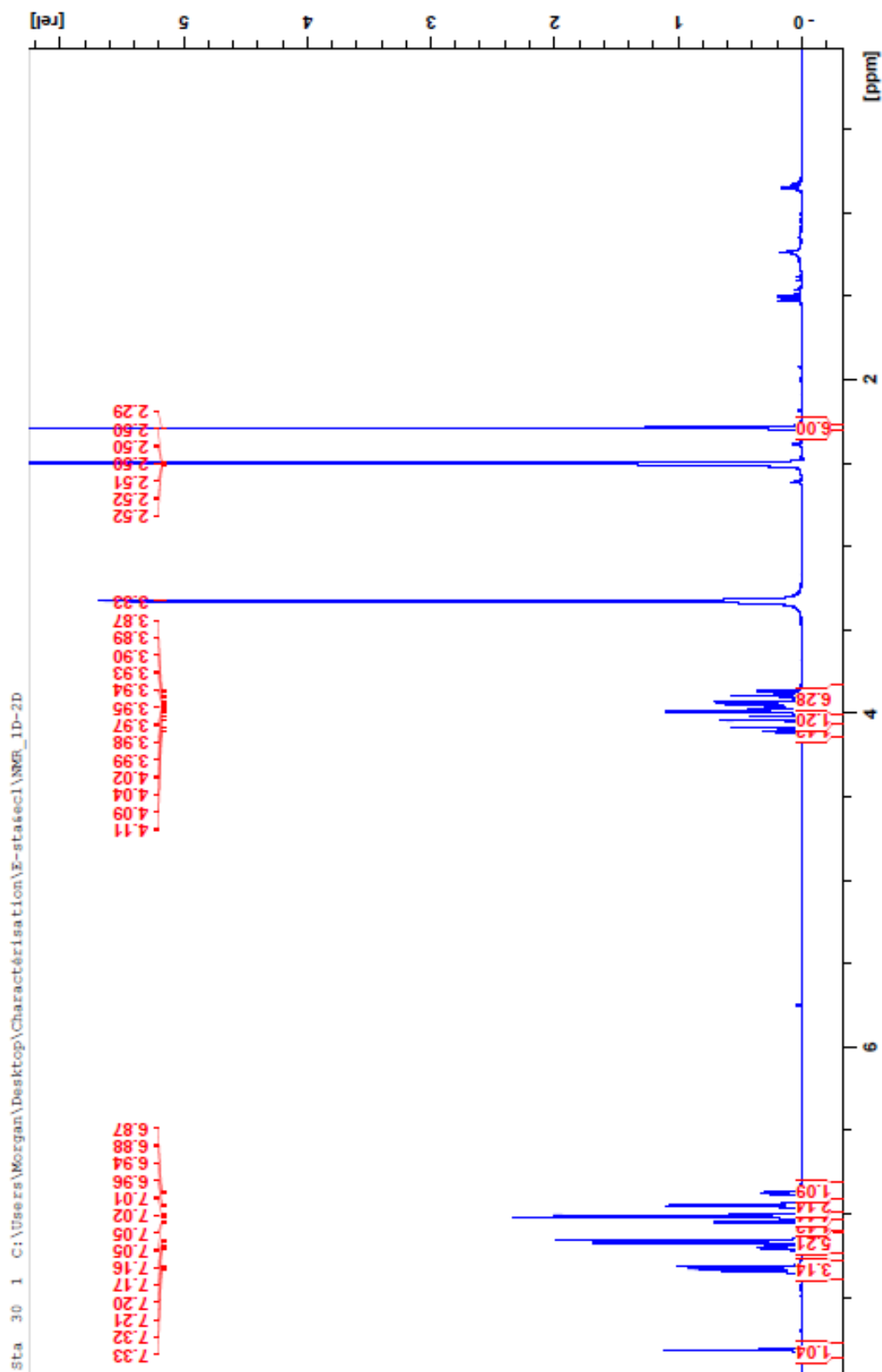


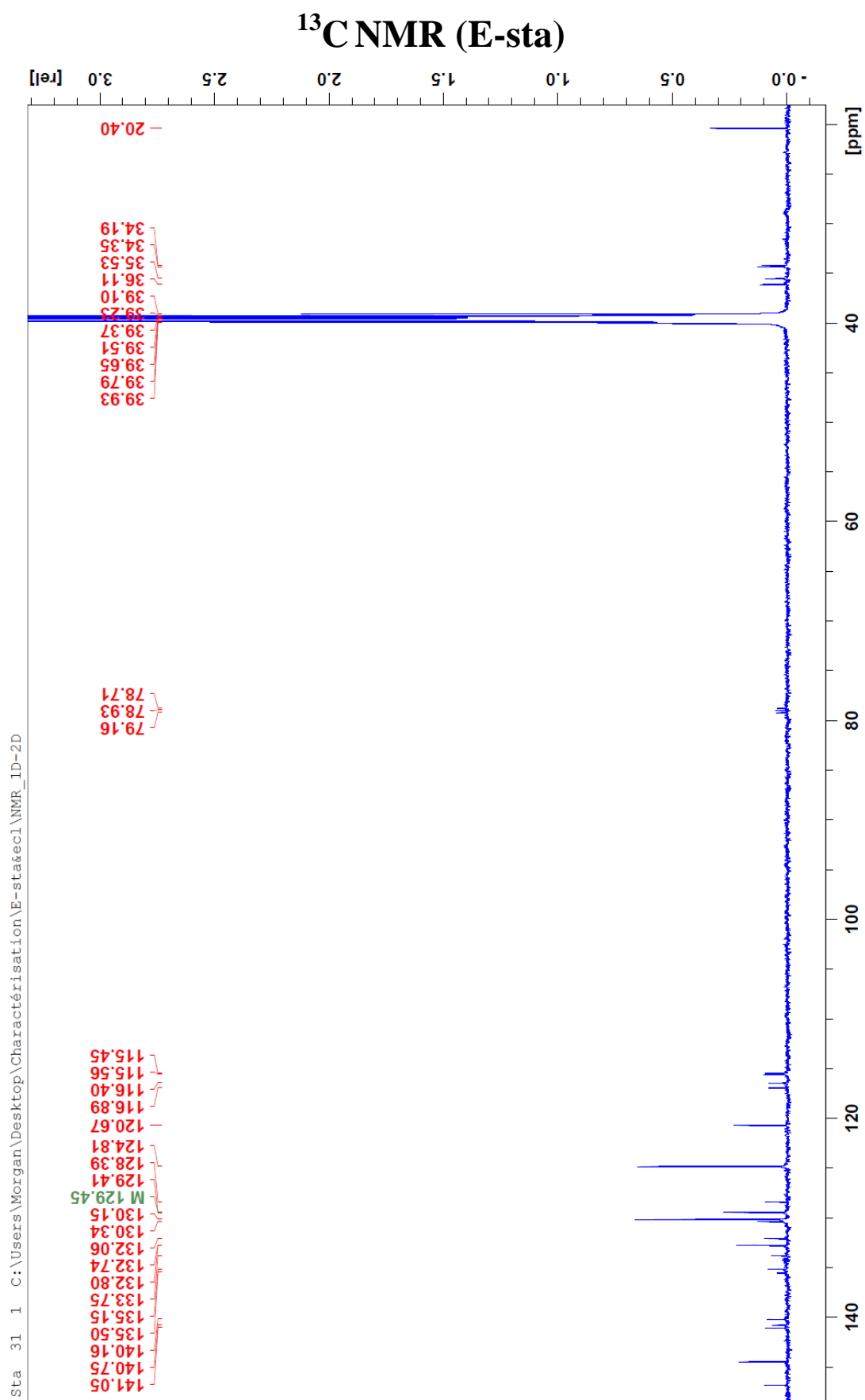
NOESY NMR (E-ecl)



APPENDIX 4: E-sta, NMR experiments (600 MHz, DMSO-*d*₆)

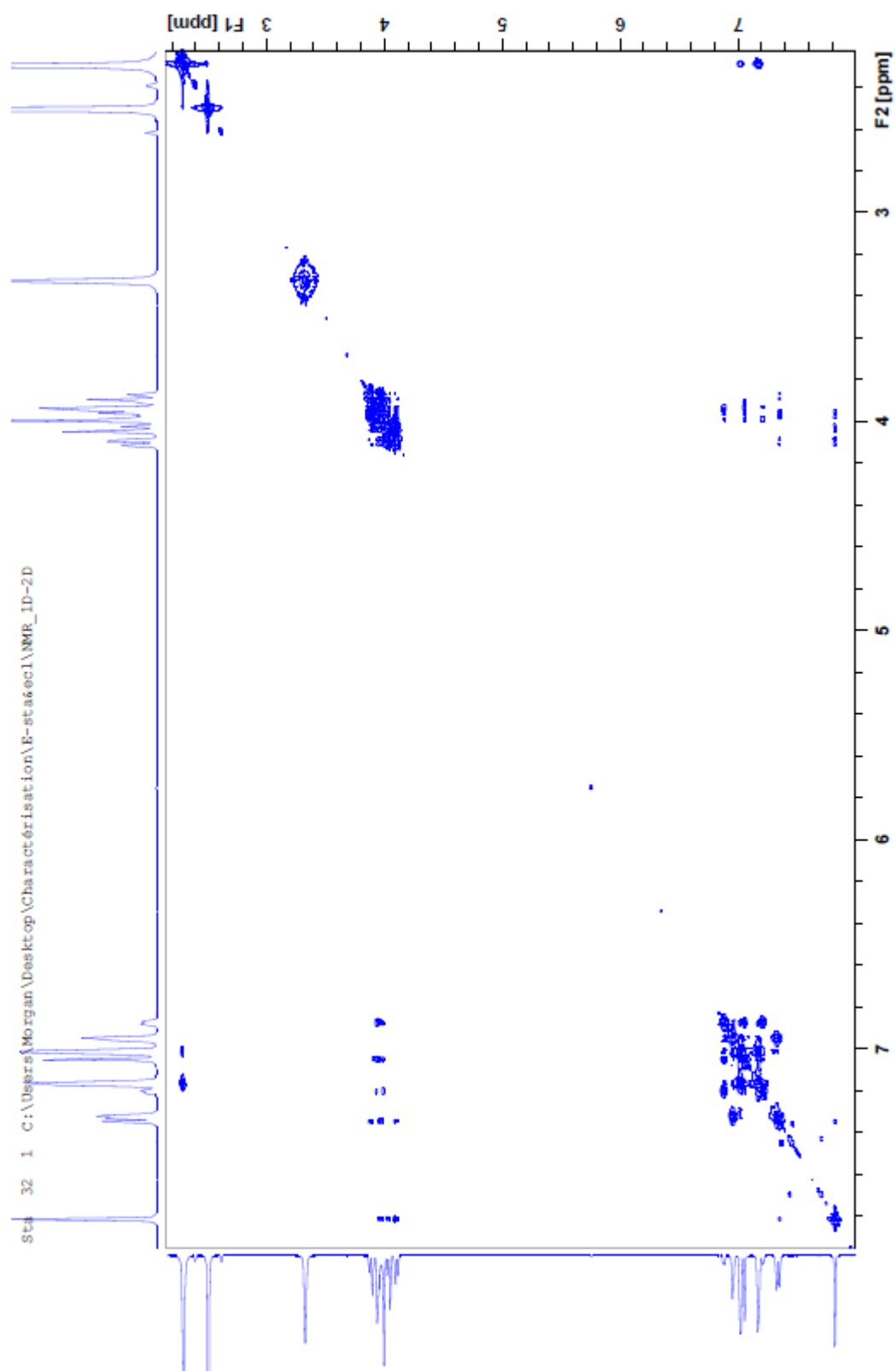
¹H NMR (E-sta)



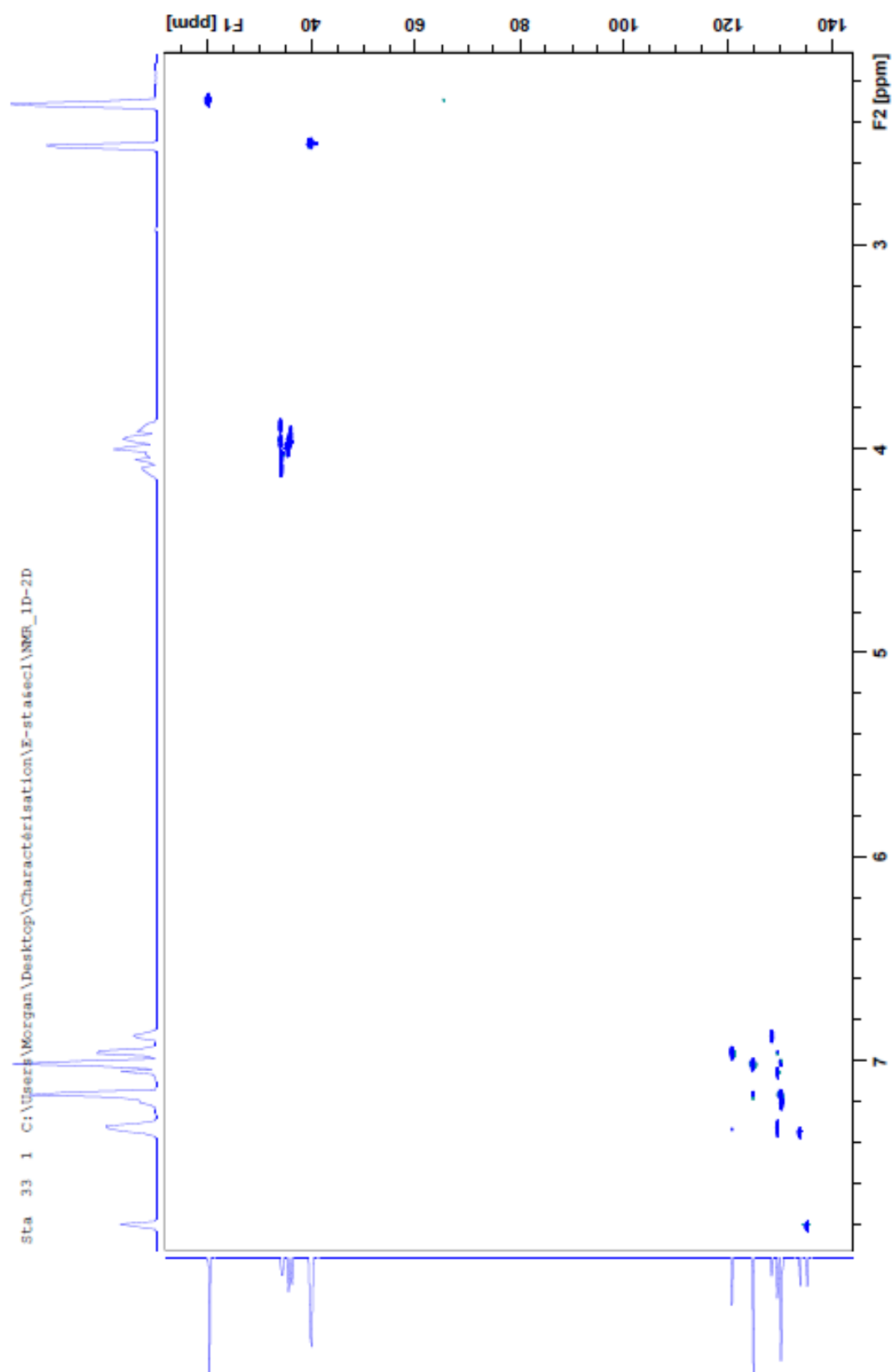


Sta 31 1 C:\Users\Morgan\Desktop\Characterisation\E-sta\ec1\NMR_ID-2D

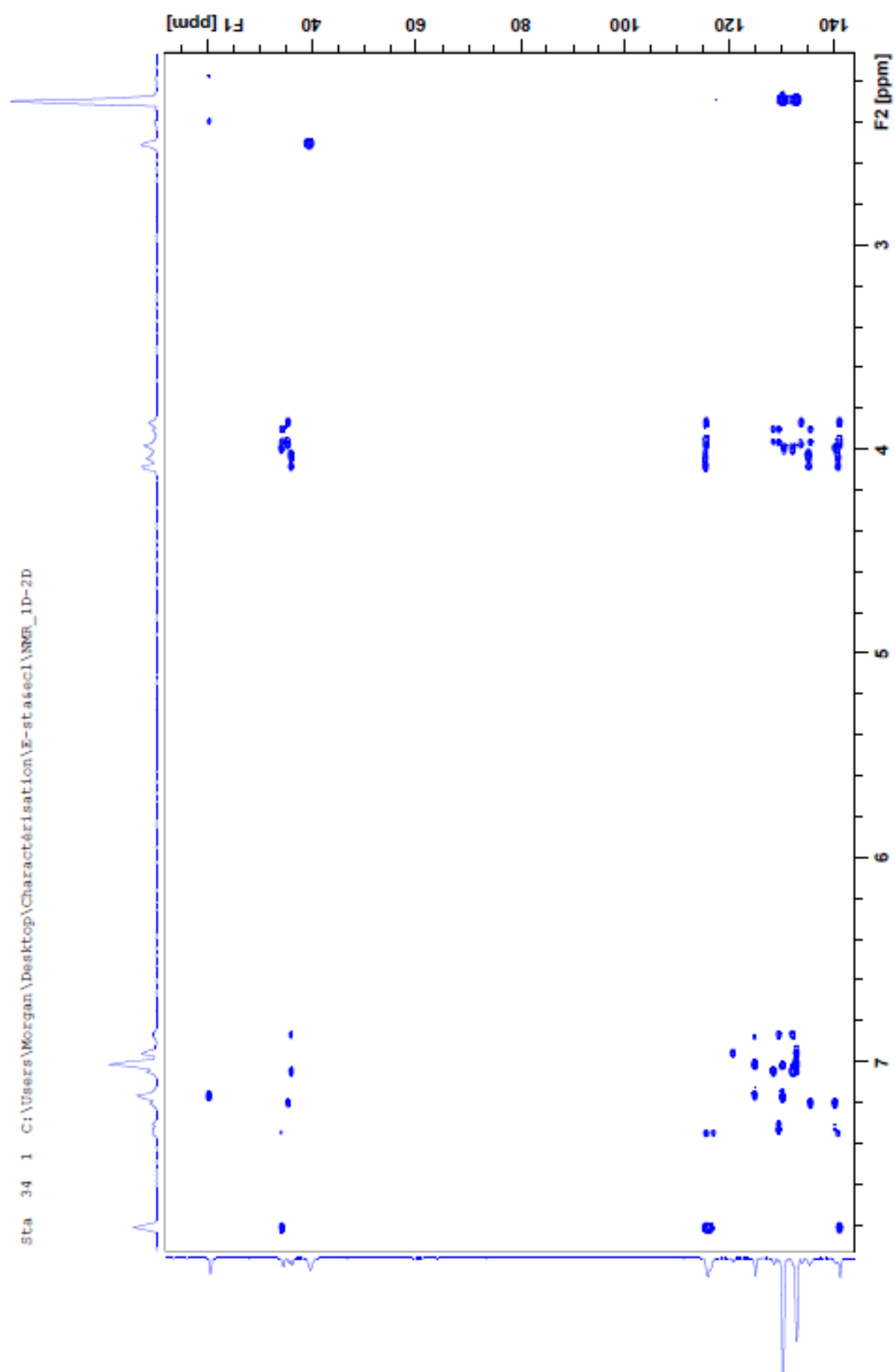
COSY NMR (E-sta)



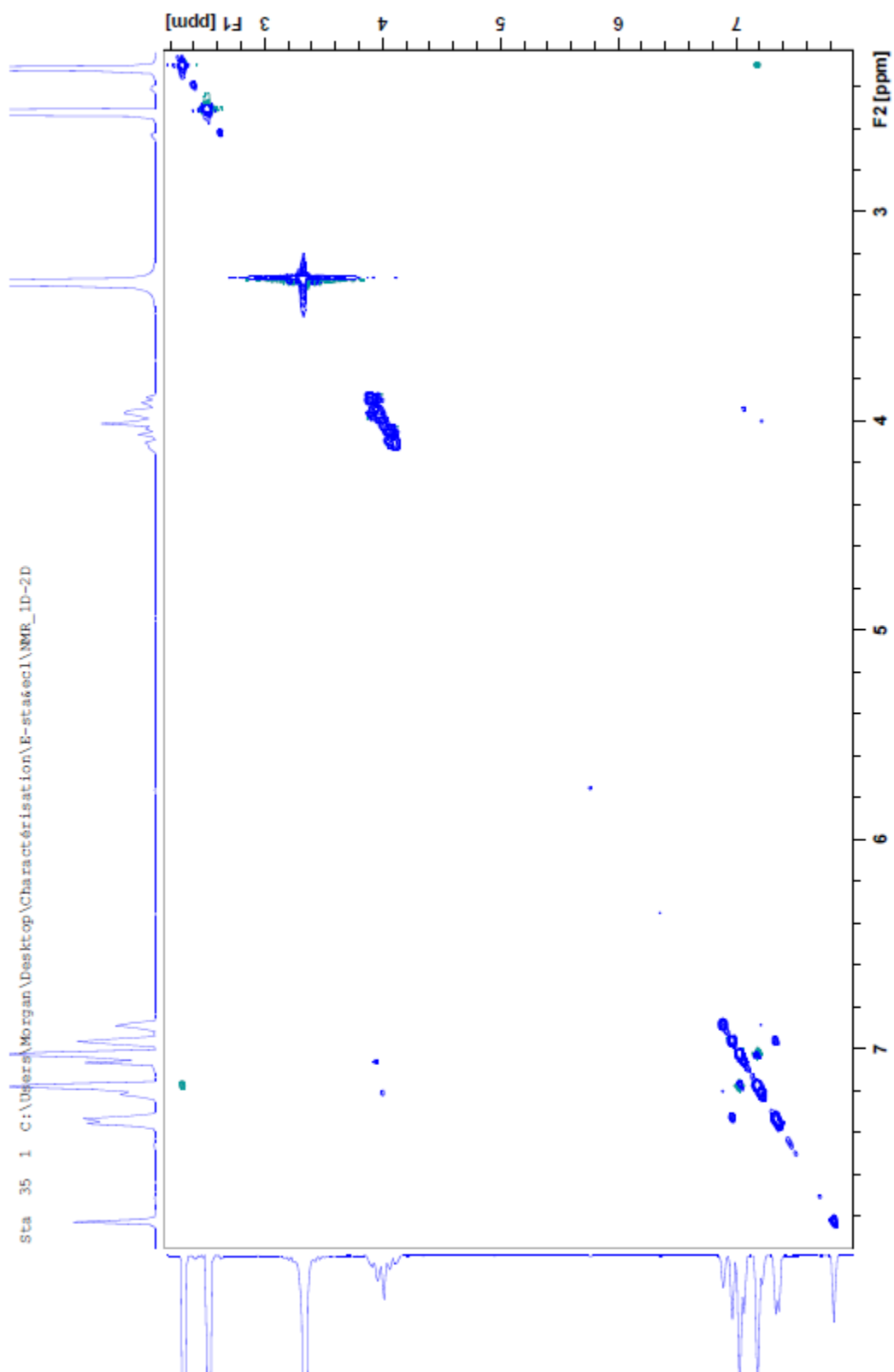
HSQC NMR (E-sta)



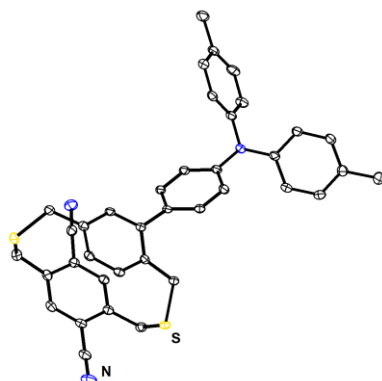
HMBC NMR (E-sta)



NOESY NMR (E-sta)



APPENDIX 5: E-sta, X-ray data



Empirical formula	C ₃₈ H ₃₁ N ₃ S ₂
Formula weight	593.78
Temperature (K)	120(1)
Wavelength (Å)	1.54178
Crystal system	Monoclinic
Space group	C 2/c
Unit cell dimensions	a = 25.2831(7) Å
	b = 10.3041(3) Å
	c = 23.9742(5) Å
	α = 90°
	β = 13.010(2)°
	γ = 90°
Cell volume	6085.4(3) Å ³
Z	8
Crystal dimensions	0.11 x 0.09 x 0.02
Density	1.296
F(000)	2496
Absorption coefficient	1.827
Min. and max. transmission	0.79 and 1.00
θ range for data collection	3.79° to 66.61°
Index ranges	-30 ≤ h ≤ 29
	-11 ≤ k ≤ 12
	-27 ≤ l ≤ 28
Reflection collected	19716
R(int)	4.02 %
Data / parameters / restraints	5375 / 390 / 0
Goodness-of-fit F ²	1.032
Final R indices [I > 2σ(I)]	R ₁ = 4.08 %
	wR ₂ = 9.99 %
Final R indices (all data)	R ₁ = 5.74 %
	wR ₂ = 10.77 %

APPENDIX 6: DIPOLE MOMENTS CALCULATIONS

By employing the simplest quantum-mechanical second order perturbation theory, Bilot and Kowski have obtained expressions for solvent spectral shift given by:

$$\nu_a - \nu_f = m^1 f(\varepsilon, n) + \text{constant} \quad (1)$$

$$\nu_a + \nu_f = -m^2 [f(\varepsilon, n) + 2g(n)] + \text{constant} \quad (2)$$

where ν_a is the absorption maximum and ν_f is the fluorescence maximum, both in wavenumber. ε is the permittivity and n is the refractive index. m^1 and m^2 represent the slope plotting relation (1) and (2) using Bakshiev polarity function $f(\varepsilon, n)$ and Kowski-Chamma-Viallet polarity function $g(n)$:

$$f(\varepsilon, n) = \frac{2n^2 + 1}{n^2 + 2} \left(\frac{\varepsilon - 1}{\varepsilon + 2} - \frac{n^2 - 1}{n^2 + 2} \right) \quad (3)$$

$$g(n) = \frac{3}{2} \left(\frac{n^4 - 1}{(n^2 + 2)} \right) \quad (4)$$

Following the Onsager theory, m^1 and m^2 can be expressed as following:

$$m^1 = \frac{2(\mu_e - \mu_g)^2}{hca^3} \quad (5)$$

$$m^2 = \frac{2(\mu_e^2 - \mu_g^2)}{hca^3} \quad (6)$$

where h is the Planck constant ($h = 6.63 \cdot 10^{-34}$ J.s), c is the velocity of light in vacuum ($c = 3 \cdot 10^8$ m.s⁻¹) and a is the Onsager's radius with μ_g the ground state dipole moment and μ_e the excited state dipole moment.

Therefore the ground state dipole moment can be found by using the following equation:

$$\mu_g = \frac{m^2 - m^1}{2} \left(\frac{hca^3}{2m^1} \right)^{1/2} \quad (7)$$

In this equation, the Onsager radius a is calculated using the equation (8):

$$a = \left(\frac{3M}{4\pi\delta N_A} \right)^{1/3} \quad (8)$$

where δ is the density of the considered dye ($\delta = 1.296$ for **E-sta**, obtained by X-ray radio-crystallography, and we considered that **E-ecl** would have the same density), M is the molecular weight of the dye (593.78 g.mol⁻¹) and N_A is the Avogadro's constant ($6.022 \cdot 10^{23}$ mol⁻¹). The Onsager radius a is thus equal to 5.66 Å.

In addition to these calculations from Bilot and Kowski, Lippert and Mataga proposed the following equation to determine the excited state dipole moment μ_e :

$$\nu_a - \nu_f = m^3 \Delta f' + \text{constant} \quad (9)$$

with $\Delta f'$ and m^3 defined as following:

$$\Delta f' = \frac{\varepsilon - 1}{2\varepsilon + 1} - \frac{n^2 - 1}{2(n^2 + 1)} \quad (10)$$

$$m^3 = \frac{2(\mu_e - \mu_g)^2}{hca^3} \quad (11)$$

The plotting of (1), (2) and (9) for **E-ecl** and **E-sta** is represented in Figure 173.

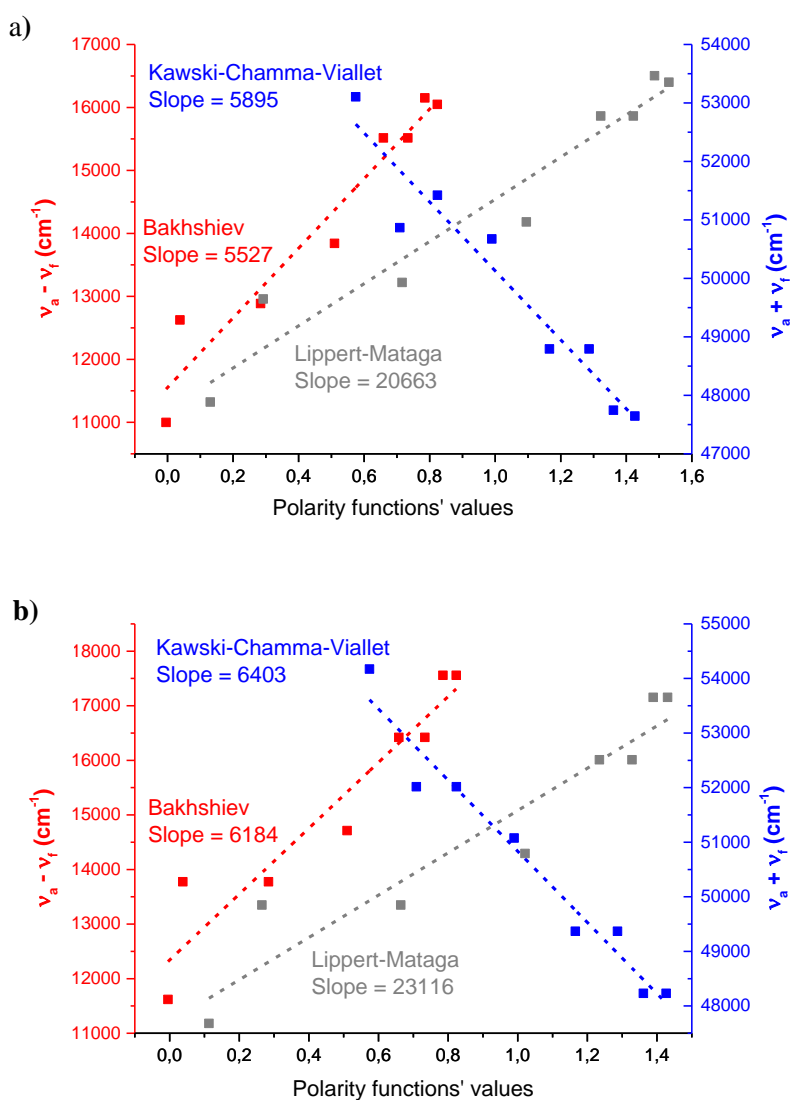


Figure 173: Solvent polarity functions of a) **E-ecl** and b) **E-sta**

The slope of (1) and (2) represents m^1 and m^2 , which used in (7) allowed to determined the ground state dipole moments of **E-ecl** ($\mu_g = 0.3$ Debye) and **E-sta** ($\mu_g = 0.2$ Debye). Then the slope of (9) gives m^3 which reported in (11) along with the values of μ_g allows to calculate the excited state dipole moment of **E-ecl** ($\mu_e = 19.6$ Debye) and **E-sta** ($\mu_e = 20.2$ Debye).

-
- ¹⁵⁹ Takahashi, S.; Kuroyama, Y.; Sonogashira, K.; Hagihara, N. *Synthesis (Stuttg)*. **1980**, 1980, 627–630.
- ¹⁶⁰ Blum, J.; Zimmerman, M. *Tetrahedron* **1972**, 28, 275–280.
- ¹⁶¹ Zaborova, E.; Six, A.; Amokrane, H.; Charra, F.; Mathevet, F.; Attias, A.-J.; Kreher, D. *Pure Appl. Chem.* **2016**, 88, 1005–1025.
- ¹⁶² Xia, J.-L.; Zhang, C.; Zhu, X.; Ou, Y.; Jin, G.-J.; Yu, G.; Liu, S. H. *New J. Chem.* **2011**, 35, 97–102.
- ¹⁶³ Pretula, J.; Kaluzynski, K.; Wisniewski, B.; Szymanski, R.; Loontjens, T.; Penczek, S. *J. Polym. Sci. Part a-Polymer Chem.* **2008**, 46, 830–843.
- ¹⁶⁴ Vilbrandt, N.; Gassmann, A.; Von Seggern, H.; Rehahn, M. *Macromolecules* **2016**, 49, 1674–1680.
- ¹⁶⁵ Lo, S.-C.; Namdas, E. B.; Burn, P. L.; Samuel, I. D. W. *Macromolecules* **2003**, 36, 9721–9730.
- ¹⁶⁶ Osoda, K.; Pannecoucke, X.; Narasaka, K. *Chem. Lett.* **1995**, 24, 1119–1120.
- ¹⁶⁷ Lin, S.-T.; Yang, Y.-C.; Lin, S.-F.; Hwang, L.-J. *J. Chem. Res.* **2005**, 2005, 708–711.
- ¹⁶⁸ Anémian, R.; Cupertino, D. C.; Mackie, P. R.; Yeates, S. G. *Tetrahedron Lett.* **2005**, 46, 6717–6721.
- ¹⁶⁹ Dai, F.-R.; Zhan, H.-M.; Liu, Q.; Fu, Y.-Y.; Li, J.-H.; Wang, Q.-W.; Xie, Z.; Wang, L.; Yan, F.; Wong, W.-Y. *Chem. - A Eur. J.* **2012**, 18, 1502–1511.
- ¹⁷⁰ Bell, H. C.; Kalman, J. R.; Pinhey, J. T.; Sternhell, S. *Tetrahedron Lett.* **1974**, 15, 857–860.

Abstracts

In this work and due to their unique electronic properties, 3D-dithia[3.3]paracyclophane-based molecules have been studied for surface nanostructuration applications and as new fluorophore.

First, the supramolecular self-assembly of molecules is used to create well-organised 2D-networks on conducting surfaces. However, the use of such substrates tends to quench any electronic properties of the adsorbed molecules. In this context, 3D-dithia[3.3]paracyclophane-based molecules were employed to lift up the active moiety from the surface. In this work, new pyridyl end-capped molecules were designed to self-assemble on any substrate. Preliminary characterisations were performed to study the supramolecular self-assembly of such molecules alone or with co-adsorbers, and the first images of organised 2D-networks on graphite and gold have been obtained by scanning probe microscopy.

Second, the design of new and efficient emitter is a hot topic for the fabrication of OLED devices. A new type of compounds is currently investigated for their high electroluminescence efficiency due to thermally activated delayed fluorescence (TADF). This phenomenon is expected from molecules showing low electronic gap between singlet and triplet excited states, which is related to a low overlap of the HOMO and LUMO, localised on the electron-donor and acceptor moieties of the molecule, respectively. In this sense, we propose a new design of donor-acceptor molecules where the HOMO (donor) and LUMO (acceptor) are separated by a cyclophane core. We synthesised a couple of emitters and their photophysics properties were studied in solution and in solid state.

Key words: cyclophane, supramolecular self-assembly, surface nanostructuration, thermally activated delayed fluorescence, photophysics.

Dans ce travail, des dérivés du dithia[3.3]paracyclophane sont étudiés pour des applications en nanostructuration de surfaces et comme nouveaux fluorophores.

Dans un premier temps, l'auto-assemblage supramoléculaire de molécules est utilisé pour créer des réseaux 2D sur surface. Cependant, l'utilisation de tels substrats a tendance à annihiler les propriétés électroniques des composés adsorbés. Par conséquent, des dérivés 3D du dithia[3.3]paracyclophane sont employées afin d'éloigner le composant actif de la surface. Dans cet optique, de nouvelles molécules à base de groupements pyridine ont été conçues pour s'auto-assembler sur différents substrats. Les caractérisations préliminaires ont été effectuées afin d'étudier les propriétés d'auto-assemblage de telles molécules seules ou co-adsorbées, et les premières images de réseaux 2D auto-organisés sur graphite et or ont été obtenues par microscopie à sonde locale.

Dans un second temps, de nouveaux composés sont actuellement étudiés pour électroluminescence à haute rendement à partir de la fluorescence retardée à activation thermique (TADF). Ce phénomène est généralement observé pour des molécules montrant un faible gap électronique entre ses états excités singulet et triplet, lié au faible recouvrement des orbitales HOMO et LUMO localisées sur le donneur et l'accepteur, respectivement. Dans ce contexte, nous proposons un nouveau design de molécules de type donneur-accepteur où HOMO (donneur) et LUMO (accepteur) sont séparées par un cœur cyclophane. Nous avons synthétisé deux émetteurs et leurs propriétés photo-physiques ont été étudiées en solution et à l'état solide.

Mots clés : cyclophane, auto-assemblage supramoléculaire, nanostructuration de surface, fluorescence retardée à activation thermique, photo-physique.